Rational Numerical Method
for Analyzing Micro Behavior in Macro Deformation

by

Tsuyoshi Higo

A dissertation submitted in partial fulfillment
of the requirements for the degree of
Doctor of Philosophy
(Mechanical Engineering)
in The University of Michigan
2009

Doctoral Committee:

Professor Noboru Kikuchi, Chair
Professor Sherif El-Tawil
Professor Scott J. Hollister
Professor Shixin Jack Hu

To My Family

Acknowledgements

I would like to take this opportunity to thank the many people who have contributed to the achievement of my doctorate research. First, I would especially like to express my sincere gratitude and greatest respect to my advisor, Professor Noboru Kikuchi, who has provided generous guidance and supervision for my doctoral studies at the University of Michigan, Ann Arbor. I am also especially grateful to my doctoral committee members for their insightful advice and help with my doctral research: Professor Shixin Jack Hu supported my research in the metal forming process, Professor Scott J. Hollister gave prescious instruction in multiscale analysis, and Professor Sherif El-Tawil contributed numerous suggestions in the FE simulation.

I also would like to acknowledge every member at the Computational Mechanics Laboratory at the University of Michigan: Dr. Atsushi Koguchi, Dr. Minako Sekiguchi, Mr. Kazuki Kuwabara, Dr. Ikjoong Lee, Dr. Youngwon Hahn, Dr. Jangho Shin, Mr. Jeonghun Seo, Dr. Sachiko Masuda, Mr. Seiji Yamada and Mr. Shin-ichiro Aoe. I would also like to thank Mr. Kazutoshi Nobukawa, Mr. Akira Saito, Dr. Shingo Takeuchi and Mr. Eiji Saito, who are my close friends and helped with my adjustments to life in the United States. I also really appreciate the help of Dr. Peter Nagourney as well as of Professor Leslie A. Olsen in preparing my dissertation.

I would like to acknowledge that my study at the University of Michigan was generously supported by Nippon Steel Corporation and two of its manegers were especially helpful in my studies. Dr. Shigeru Ogawa, General Manager for the steel rolling R&D division, strongly recommended me and gave me the great opportunity of studying abroad. Mr. Kenji Yamada, Chief Researcher, helped me clarify the methodology for my research. In addition, I would like to thank Dr. Katsuyuki Suzuki, Associate Professor at the University of Tokyo, as well as Dr. Syogo Nakasumi, Researcher for National Institute of Advanced Industrial Science and Technology in Japan, who made valuable suggestions on my research through the discussion with me.

Last, my special thanks go to my parents and sister in Japan for their continuous patience and to my wife, Ms. Noriko Higo, for her generous patience, inspiring kind words, and trustful support.

Table of Contents

List of Figures

Figure

List of Tables

Table

List of Appendices

Appendix

Chapter 1

Introduction

Recently, the progress of computing speed and capacity has resulted in a reduction in computing costs. Therefore, many numerical approaches have been achieved to investigate material deformation behavior. One of the most important features of numerical simulation is that any value at any place at any time can be obtained. For example, experimental measurement of internal forces during the forging process is very difficult, although they are easily obtained through numerical simulation. Another feature of numerical simulation is that any one parameter's quantitative influence for deformation behavior is precisely obtained. For instance, the effect of material work hardening for deformation behavior is easily clarified through numerical simulation using different work hardening indices. However, finding two or more materials whose properties are the same except for the work hardening index is almost impossible. Therefore, numerical simulation can be regarded as an experiment under ideal conditions. Because of these features, numerical simulation helps to clarify deformation mechanisms.

Thus, computer aided engineering (CAE) plays a significant role in engineering by providing a guiding principle based on the deformation mechanism, including quantitative prediction of deformation behaviors such as displacement, strain, stress, load and torque. Moreover, CAE helps to improve existing processes as well as to develop innovative processes. Of all numerical simulation methods, the finite element method (FEM) seems to be the most practical one. In fact, innumerable FE analyses for material deformation behavior have been performed. For example, a three-dimensional elasto-plastic numerical simulation program for the metal forming processes was developed, and width spread during the slab rolling was compared with an experimental one[1)]. Furthermore, fracture initiation[2),3)], or microstructure evolution[4),5)] during various metal forming processes was predicted. Even crack growth, which requires representing the discontinuity of the displacement field at the interface, was analyzed[6)].

Recently, demand for obtaining micro deformation behavior under the actual loading conditions has increased. In order to satisfy this demand, multiscale analysis should be performed. Here, multiscale analysis has two meanings; one is the theory which connects atomic and/or dislocation behavior with the continuum mechanics[7]; the other is the theory that connects two or more different scale problems, both of which are based on the continuum mechanics. This research focuses on the latter, the continuum-based multiscale analysis. The continuum mechanics theory[8),9)], which is the base theory of FEM formulations, is said to be effective if the scale of the object is much larger than the scale at which micro discontinuity can not be neglected. Hence, for example, when the deformation behavior of the polycrystalline metal is performed, the continuum mechanics would be effective if the scale of the object is much larger than the crystal scale (10^{-6}m). Therefore, FEM formulations are effective not only for the macro scale model but also for the micro scale model when the resolution of the micro scale model is much larger than the crystal scale.

If the microscale model has structural periodicity, the homogenization method[10)] is one of the most practical ways to connect the microscale and macroscale models. For example, S. Jansson[11)] investigated the homogenized behavior of a fiber reinforced metal matrix composite. However, if the micro scale model that is focused on has no structural periodicity, scratches or defects for example, the homogenization method is not effective any more.

Multiscale analysis for simulating the local area deformation can be performed even by using the conventional FEM. Actually, the deformation behaviors of a plane strain rigid-plastic plane with an inclusion were performed[12)]. However, computing a multiscale problem whose scale is widely distributed is practically impossible because element size must be changed gradually[13)]. In order to allocate small elements adjacent a large element, nonconforming elements[14)~18)], in which the slave nodes are constrained on the master element boundaries, are proposed. A commercial FE code[19)] has already installed similar constraints, named *NODAL TIES*. These methods, however, limit the FE mesh discretization since the slave nodes are required to be on the master element boundary.

The zooming method[20] is also often used for multiscale analysis, even in some commercial FE codes[19]. For instance, surface roughness transcription between the tool and material during the forging process was computed[21]. Oxide scale deformation behavior at the entry of the roll bite during the hot rolling process was performed[22]. Moreover, the deformation characteristics of the inclusions during the hot rolling process were demonstrated[23]. This method, however, is an uncoupled analysis of the macro model and the micro model. That is, when displacement boundary conditions of the micro model are given from the macro model's results, forces obtained by each model do not coincide, and vice versa. Displacement boundary conditions give more accurate results for some problems, while force boundary conditions give more reasonable results for others. Therefore, the analyst must have knowledge about selecting appropriate boundary conditions. Although an improved zooming method was suggested[24] that iterates computation until the macro and micro boundary conditions converge, it does not seem to be practical due to its long computing time.

For computing micro scale deformation behavior under macro scale deformation, the mesh overlay method, known as the *s-version FEM*[25], is very effective. The most important feature of the mesh overlay method is superimposing a fine model, which is called "the local model," over a part of a whole model, which is called "the global model." Due to its efficiency, enormous amounts of research have been performed, including center-holed plane stress tension problems[26] and crack problems[27]. It has also been demonstrated that the mesh overlay method can be applied to composite material problems[28].

However, there are three issues to be conquered in order to achieve a practically useful mesh overlay analysis. That is, (1) the accuracy of the linear equation solver, (2) the application for the three-dimensional analysis, and (3) the extension to nonlinear analysis. First, let us consider the accuracy of the linear equation solver for the mesh overlay analysis. Recently, the iterative method, the conjugate gradient method for example, is often applied to solve the stiffness equations. In fact, S. Wang et al.[29] concluded that the iterative method is suitable due to its shorter computer memory usage since the band width of the stiffness matrix increases in the mesh overlay formulations. M. Yoshida et al.[30] investigated the effectiveness of preconditions for the conjugate

gradient method. However, contrary conclusions have been also derived. For example, Y. Okuno et al.[31] reported that the convergence speed is slow when the iterative method is applied to the mesh overlay analysis. Moreover, J. W. Park et al.[32] showed that the multi-frontal solver, one of the direct methods, is the best to solve the linear equations in the mesh overlay method. However, these considerations are about the convergence speed. Since the mesh overlay analysis is a coupled analysis of the global and local models, the displacement at a point on the local region is expressed as the summation of the global displacement and the local displacement for elastic problems, and for plastic problems the velocity is treated as the same manner. Hence, the order of the solutions of the mesh overlay method, nodal displacements for elastic analysis, or nodal velocities for plastic analysis, would widely vary. Therefore, the criterion to judge its convergence should be carefully determined, although there seem to be no reports that investigate the relation between solution accuracy and the criterion of convergence for the iterative method to solve the stiffness equations.

Second, let us think about the mesh overlay applications for the three-dimensional analysis. There are few reports that apply the mesh overlay method for three-dimensional problems[33),34)]. One reason may be the difficulty of finding the element the Gauss point belongs to under three-dimensions. Finding this element is required to construct the coupling effect of the global and local models. In fact, N. Takano et al.[35] demonstrated a three-dimensional mesh overlay analysis by using the voxel element[36], which allows easy determination of the positional relation between a point and a plane due to its orthogonal and uniform mesh discretization. An interesting mesh overlay method was proposed in which the shell elements are used for the global model and the solid elements are used for the local model[37),38)]. However, if the bending deformation can be neglected, the shell elements do not have to be used.

Finally, let us consider applying the mesh overlay analysis for the nonlinear analysis. The number of reports that applied the mesh overlay method for nonlinear problems, which are demanded in various practical situations to clarify their behaviors, is still small[25),39)]. An interesting method to analyze the elasto-plastic problem using the mesh overlay method was developed[40]. In this method, the local model covers at least the plastic deformation region. That is, deformation in the region covered only by the

global model is limited to elastic deformation. Therefore, although the local model is analyzed based on the elasto-plastic theory, the constitutive equations for the global model are based on the elastic theory. Due to this treatment, the calculating algorithm becomes simple. However, when plastic deformation occurs in most regions, this method is no longer functional. Moreover, these methods omit the iteration for constructing the stiffness equations by assuming linearity at each time step. Hence, as the number of the time steps increases, the accumulated error may become too large to ignore, and negatively influence the solutions.

The purpose of this research is to develop a rational numerical method for analyzing micro behavior in macro deformation. In other words, this report devotes fundamental research to applying the mesh overlay method for the metal forming process with the goal of enhancing its practicality. First, the formulations of the mesh overlay method for the elastic problem is reviewed in Chapter 2. Then, the validity of the linear equation solver is examined from the viewpoint of its accuracy. Moreover, some numerical examples, including a combination of the mesh overlay method and the homogenization method, are performed in order to verify its practicality and effectiveness. Additionally, an efficient three-dimensional analysis that applies the mesh overlay method is proposed.

Then, the mesh overlay method is extended into the rigid-plastic analysis in Chapter 3. First, the formulations of the mesh overlay method based on the rigid-plastic theory are newly derived. Since plastic deformation behavior is nonlinear, the formulations are shown as a rate form, and the iterative method must be adopted to acquire the converged solutions at each time step. Numerical examples are shown to verify the accuracy of the rigid-plastic mesh overlay formulations derived in this report. Then, an efficient three-dimensional analysis is also applied to the rigid-plastic analysis.

Conclusions of this report and future issues are presented in Chapter 4.

Chapter 2

Mesh Overlay Method for Elastic Problems

2.1 Introduction

The basic concept of the mesh overlay method was originally proposed by T. Belytschko et al[41]. The purpose of the research was to describe high gradient strain localization. J. Fish[25] improved its formulations and named it the *s-version FEM*. The most important feature of the mesh overlay method is superimposing a fine model, which is called "the local model," over a part of a whole model, which is called "the global model." Due to the efficiency of this method, enormous amounts of research have been performed, including center-holed plane stress tension problems[26], crack problems[27] and composite material problems[28]. Additionally, a method was proposed in which the local model is moved according to the result of the topology optimization[29]. Moreover, extension to multi local models was also demonstrated[33),42].

In this chapter, the formulations are reviewed first. The linear equation solver for the mesh overlay analysis is also investigated. Then, numerical examples are shown to confirm the accuracy of the mesh overlay analysis. In order to enhance its practicality, the mesh overlay method is adopted to the homogenization problem, and a highly efficient three-dimensional analysis is proposed utilizing the mesh overlay method.

2.2 Formulations (Review)

2.2.1 Stiffness Equations

Two models, named the global and local models, constitute the whole computational model in the mesh overlay method. The global model covers the whole region Ω, whereas the local model covers only the local region Ω^L, which overlays the global model, as shown in **Fig. 2.1**. Usually, the resolution of the global model is coarser than that of the local model. In other words, the element size of the global model is larger than that of the local model. The region where only the global model covers is named the global region Ω^G, and the boundary between the global region Ω^G and the local region Ω^L is named the global-local boundary Γ^{GL} in this report.

$$\Omega = \Omega^G \cup \Omega^L \tag{2.1a}$$

$$\Omega^G \cap \Omega^L = 0 \tag{2.1b}$$

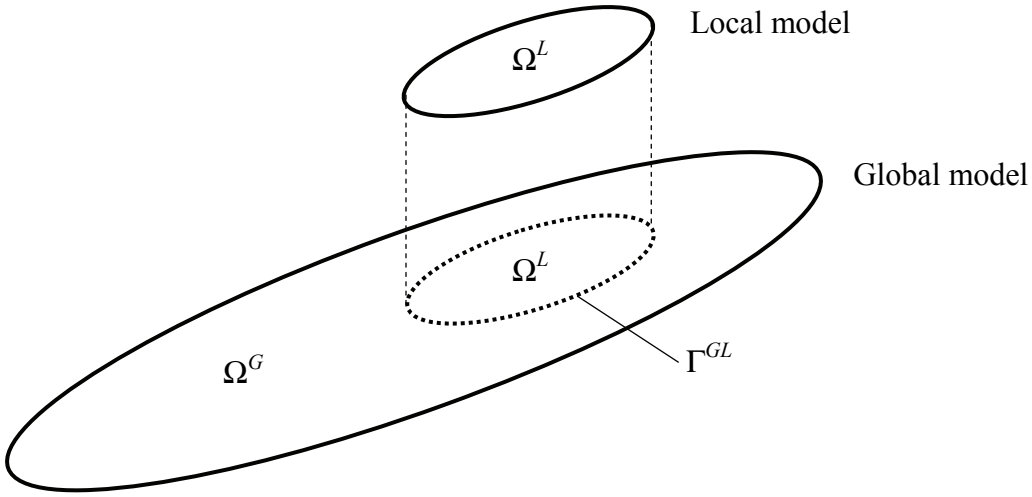

Fig. 2.1 Schematic figure of global and local models

In the mesh overlay method, displacement u_i is defined by eq. (2.2)[25].

$$u_i \equiv \begin{cases} u^G{}_i & in \quad \Omega^G \\ u^G{}_i + u^L{}_i & in \quad \Omega^L \end{cases} \tag{2.2}$$

The global displacement $u^G{}_i$ and the local displacement $u^L{}_i$ are obtained from the global and local models, respectively. In order to satisfy the C^0 continuity of displacement u_i, the local displacement $u^L{}_i$ is set to be zero on the global-local boundary Γ^{GL} [25].

$$u^L{}_i = 0 \qquad on \quad \Gamma^{GL} \tag{2.3}$$

Then, strain tensor ε_{ij} is expressed by eq. (2.4).

$$\varepsilon_{ij} = \begin{cases} \dfrac{\partial u^G{}_i}{\partial x_j} \equiv \varepsilon^G{}_{ij} & in \quad \Omega^G \\ \dfrac{\partial u^G{}_i}{\partial x_j} + \dfrac{\partial u^L{}_i}{\partial x_j} \equiv \varepsilon^G{}_{ij} + \varepsilon^L{}_{ij} & in \quad \Omega^L \end{cases} \tag{2.4}$$

Summation convention is assumed in this report unless “no sum” is written explicitly.

Stress tensor σ_{ij} is expressed by eq. (2.5) where $D^G{}_{ijkl}$ and $D^L{}_{ijkl}$ denote the elastic deformation tensor for the global and local elements, respectively.

$$\sigma_{ij} = \begin{cases} D^G{}_{ijkl}\varepsilon^G{}_{kl} & in \quad \Omega^G \\ D^L{}_{ijkl}(\varepsilon^G{}_{kl} + \varepsilon^L{}_{kl}) & in \quad \Omega^L \end{cases} \tag{2.5}$$

In accordance with FEM formulations[43),44)], the global and local displacements $u^G{}_i$ and $u^L{}_i$ at arbitrary points are expressed by the nodal displacement $d^G{}_i$ and $d^L{}_i$ for the global and local nodes, and the shape function matrix $N^G{}_{ij}$ and $N^L{}_{ij}$ for the global and local elements, respectively.

$$u^G{}_i = N^G{}_{ij} d^G{}_j \tag{2.6a}$$

$$u^L{}_i = N^L{}_{ij} d^L{}_j \tag{2.6b}$$

or, in the matrix description:

$$\{u^G\} = [N^G]\{d^G\} \tag{2.7a}$$

$$\{u^L\} = [N^L]\{d^L\} \tag{2.7b}$$

Although the global strain tensor ε^G_{ij} is a 3×3 matrix, the number of the independent components is only six. As opposed to the more complex matrix equation, the global strain vector ε^G_i is defined as a vector form in this report:

$$\begin{cases} \varepsilon^G{}_1 = \varepsilon^G{}_x \\ \varepsilon^G{}_2 = \varepsilon^G{}_y \\ \varepsilon^G{}_3 = \varepsilon^G{}_z \\ \varepsilon^G{}_4 = 2\varepsilon^G{}_{xy} \\ \varepsilon^G{}_5 = 2\varepsilon^G{}_{yz} \\ \varepsilon^G{}_6 = 2\varepsilon^G{}_{zx} \end{cases} \tag{2.8a}$$

or, in the matrix description:

$$\{\varepsilon^G\} \equiv \{\varepsilon^G{}_x \quad \varepsilon^G{}_y \quad \varepsilon^G{}_z \quad 2\varepsilon^G{}_{xy} \quad 2\varepsilon^G{}_{yz} \quad 2\varepsilon^G{}_{zx}\}^T \tag{2.8b}$$

The local strain vector ε^L_i is also expressed as a vector form:

$$\begin{cases} \varepsilon^L{}_1 = \varepsilon^L{}_x \\ \varepsilon^L{}_2 = \varepsilon^L{}_y \\ \varepsilon^L{}_3 = \varepsilon^L{}_z \\ \varepsilon^L{}_4 = 2\varepsilon^L{}_{xy} \\ \varepsilon^L{}_5 = 2\varepsilon^L{}_{yz} \\ \varepsilon^L{}_6 = 2\varepsilon^L{}_{zx} \end{cases} \tag{2.9a}$$

or, in the matrix description:

$$\{\varepsilon^L\} \equiv \{\varepsilon^L{}_x \quad \varepsilon^L{}_y \quad \varepsilon^L{}_z \quad 2\varepsilon^L{}_{xy} \quad 2\varepsilon^L{}_{yz} \quad 2\varepsilon^L{}_{zx}\}^T \tag{2.9b}$$

The global strain vector ε^G_i is expressed by the global strain-nodal displacement matrix B^G_{ij} and the global nodal displacement d^G_j.

$$\varepsilon^G{}_i = B^G{}_{ij} d^G{}_j \tag{2.10a}$$

or, in the matrix description:

$$\{\varepsilon^G\} = [B^G]\{d^G\} \tag{2.10b}$$

Similarly, the local strain vector $\varepsilon^L{}_i$ is represented by the local strain-nodal displacement matrix $B^L{}_{ij}$ and the local nodal displacement $d^L{}_j$.

$$\varepsilon^L{}_i = B^L{}_{ij} d^L{}_j \tag{2.11a}$$

or, in the matrix description:

$$\{\varepsilon^L\} = [B^L]\{d^L\} \tag{2.11b}$$

The stress vector σ_i is also defined as follows:

$$\sigma_i = \begin{cases} D^G{}_{ij}\varepsilon^G{}_j & in \quad \Omega^G \\ D^L{}_{ij}(\varepsilon^G{}_j + \varepsilon^L{}_j) & in \quad \Omega^L \end{cases} \tag{2.12a}$$

where $D^G{}_{ij}$ and $D^L{}_{ij}$ denote the elastic deformation matrix for the global and local elements, respectively. In the matrix description:

$$\{\sigma\} = \begin{cases} [D^G]\{\varepsilon^G\} & in \quad \Omega^G \\ [D^L](\{\varepsilon^G\} + \{\varepsilon^L\}) & in \quad \Omega^L \end{cases} \tag{2.12b}$$

Here,

$$\{\sigma\} \equiv \{\sigma_x \quad \sigma_y \quad \sigma_z \quad \tau_{xy} \quad \tau_{yz} \quad \tau_{zx}\}^T \tag{2.13}$$

$$[D^G] = \frac{E^G}{(1+\nu^G)(1-2\nu^G)} \begin{bmatrix} 1-\nu^G & \nu^G & \nu^G & 0 & 0 & 0 \\ \nu^G & 1-\nu^G & \nu^G & 0 & 0 & 0 \\ \nu^G & \nu^G & 1-\nu^G & 0 & 0 & 0 \\ 0 & 0 & 0 & \dfrac{1-2\nu^G}{2} & 0 & 0 \\ 0 & 0 & 0 & 0 & \dfrac{1-2\nu^G}{2} & 0 \\ 0 & 0 & 0 & 0 & 0 & \dfrac{1-2\nu^G}{2} \end{bmatrix} \tag{2.14a}$$

$$[D^L]=\frac{E^L}{(1+\nu^L)(1-2\nu^L)}\begin{bmatrix} 1-\nu^L & \nu^L & \nu^L & 0 & 0 & 0 \\ \nu^L & 1-\nu^L & \nu^L & 0 & 0 & 0 \\ \nu^L & \nu^L & 1-\nu^L & 0 & 0 & 0 \\ 0 & 0 & 0 & \frac{1-2\nu^L}{2} & 0 & 0 \\ 0 & 0 & 0 & 0 & \frac{1-2\nu^L}{2} & 0 \\ 0 & 0 & 0 & 0 & 0 & \frac{1-2\nu^L}{2} \end{bmatrix} \tag{2.14b}$$

Now, the principle of minimum potential energy is applied to derive the stiffness equation when the body force b_i acts on the region Ω and the external force t_i acts on the boundary Γ_t. According to this principle, the global nodal displacement $d^G{}_i$ and the local nodal displacement $d^L{}_i$ are determined by minimizing the total energy Π of the system. Therefore, the global nodal displacement $d^G{}_i$ and the local nodal displacement $d^L{}_i$ should satisfy eq. (2.15).

$$\begin{cases} \dfrac{\partial \Pi}{\partial d^G{}_i}=0 \\ \dfrac{\partial \Pi}{\partial d^L{}_i}=0 \end{cases} \tag{2.15}$$

As one of the components of the total energy Π, the elastic strain energy Π_e, shown in eq. (2.16), is considered.

$$\begin{aligned} \Pi_e &= \frac{1}{2}\int_\Omega \varepsilon_i \sigma_i d\Omega \\ &= \frac{1}{2}\int_{\Omega^G} \varepsilon^G{}_i \sigma_i d\Omega + \frac{1}{2}\int_{\Omega^L} (\varepsilon^G{}_i + \varepsilon^L{}_i)\sigma_i d\Omega \\ &= \frac{1}{2}\int_{\Omega^G} \varepsilon^G{}_i D^G{}_{ij} \varepsilon^G{}_j d\Omega + \frac{1}{2}\int_{\Omega^L} (\varepsilon^G{}_i + \varepsilon^L{}_i) D^L{}_{ij} (\varepsilon^G{}_j + \varepsilon^L{}_j) d\Omega \\ &= \frac{1}{2}\int_{\Omega^G} d^G{}_k B^G{}_{ik} D^G{}_{ij} B^G{}_{jl} d^G{}_l d\Omega \\ &\quad + \frac{1}{2}\int_{\Omega^L} (d^G{}_k B^G{}_{ik} + d^L{}_k B^L{}_{ik}) D^L{}_{ij} (B^G{}_{jl} d^G{}_l + B^L{}_{jl} d^L{}_l) d\Omega \end{aligned} \tag{2.16}$$

Here, eqs. (2.10) ~ (2.12) were used to modify the equation.

Second, the energy generated by the body force b_i is also considered. The body force energy Π_b is represented in eq. (2.17).

$$\begin{aligned}\Pi_b &= -\int_{\Omega} u_i b_i d\Omega \\ &= -\int_{\Omega^G} u^G{}_i b_i d\Omega - \int_{\Omega^L} (u^G{}_i + u^L{}_i) b_i d\Omega \\ &= -\int_{\Omega^G} N^G{}_{ij} d^G{}_j b_i d\Omega - \int_{\Omega^L} (N^G{}_{ij} d^G{}_j + N^L{}_{ij} d^L{}_j) b_i d\Omega \\ &= -\int_{\Omega^G} N^G{}_{ij} b_i d\Omega d^G{}_j - \int_{\Omega^L} N^G{}_{ij} b_i d\Omega d^G{}_j - \int_{\Omega^L} N^L{}_{ij} b_i d\Omega d^L{}_j \end{aligned} \tag{2.17}$$

Here, eq. (2.6) was adopted to derive the equation.

Finally, Π_t, the energy generated by the external force t_i, is considered as shown in eq. (2.18).

$$\begin{aligned}\Pi_t &= -\int_{\Gamma_t^G} u^G{}_i t_i d\Gamma - \int_{\Gamma_t^L} (u^G{}_i + u^L{}_i) t_i d\Gamma \\ &= -\int_{\Gamma_t^G} N^G{}_{ij} d^G{}_j t_i d\Gamma - \int_{\Gamma_t^L} (N^G{}_{ij} d^G{}_j + N^L{}_{ij} d^L{}_j) t_i d\Gamma \\ &= -\int_{\Gamma_t^G} N^G{}_{ij} t_i d\Gamma d^G{}_j - \int_{\Gamma_t^L} N^G{}_{ij} t_i d\Gamma d^G{}_j - \int_{\Gamma_t^L} N^L{}_{ij} t_i d\Gamma d^L{}_j \end{aligned} \tag{2.18}$$

Equation (2.6) was adopted to derive this equation, too.

The total energy Π is given as follows:

$$\Pi = \Pi_e + \Pi_b + \Pi_t \tag{2.19}$$

Equation (2.20) denotes the partial derivative of the elastic strain energy, eq. (2.16), by the global nodal displacement.

$$\begin{aligned}\frac{\partial \Pi_e}{\partial d^G{}_i} &= \frac{\partial}{\partial d^G{}_i}\left(\frac{1}{2}\int_{\Omega^G} d_m{}^G B^G{}_{km} D^G{}_{kl} B^G{}_{ln} d^G{}_n d\Omega\right) \\ &\quad + \frac{\partial}{\partial d^G{}_i}\left\{\frac{1}{2}\int_{\Omega^L} (d_m{}^G B^G{}_{km} + d_m{}^L B^L{}_{km}) D^L{}_{kl} (B^G{}_{ln} d^G{}_n + B^L{}_{ln} d^L{}_n) d\Omega\right\} \\ &= \int_{\Omega^G} B^G{}_{ki} D^G{}_{kl} B^G{}_{ln} d^G{}_n d\Omega + \int_{\Omega^L} B^G{}_{ki} D^L{}_{kl} (B^G{}_{ln} d^G{}_n + B^L{}_{ln} d^L{}_n) d\Omega \\ &= \int_{\Omega^G} B^G{}_{ki} D^G{}_{kl} B^G{}_{ln} d\Omega d^G{}_n \\ &\quad + \int_{\Omega^L} B^G{}_{ki} D^L{}_{kl} B^G{}_{ln} d\Omega d^G{}_n + \int_{\Omega^L} B^G{}_{ki} D^L{}_{kl} B^L{}_{ln} d\Omega d^L{}_n \end{aligned} \tag{2.20}$$

In order to simplify the calculation, eq. (2.21) is assumed[28], in which the global elastic deformation matrix D^G_{ij} is used instead of the local elastic deformation matrix D^L_{ij}.

$$\int_{\Omega^L} B^G{}_{ki} D^L{}_{kl} B^G{}_{ln} d\Omega \cong \int_{\Omega^L} B^G{}_{ki} D^G{}_{kl} B^G{}_{ln} d\Omega \tag{2.21}$$

Substitution of eq. (2.21) into eq. (2.20) yields eq. (2.22) where $\Omega = \Omega^G + \Omega^L$ is used.

$$\begin{aligned}\frac{\partial \Pi_e}{\partial d^G{}_i} &\cong \int_{\Omega^G} B^G{}_{ki} D^G{}_{kl} B^G{}_{ln} d\Omega d^G{}_n + \int_{\Omega^L} B^G{}_{ki} D^G{}_{kl} B^G{}_{ln} d\Omega d^G{}_n \\ &\quad + \int_{\Omega^L} B^G{}_{ki} D^L{}_{kl} B^L{}_{ln} d\Omega d^L{}_n \\ &= \int_{\Omega} B^G{}_{ki} D^G{}_{kl} B^G{}_{ln} d\Omega d^G{}_n + \int_{\Omega^L} B^G{}_{ki} D^L{}_{kl} B^L{}_{ln} d\Omega d^L{}_n \end{aligned} \tag{2.22}$$

In this report, when the region of integral is denoted as Ω or Γ_t, the integral is evaluated by the global model even in the local region Ω^L. Due to this arrangement, the resolution of the region covered by the local model becomes coarse because the global Gauss points, instead of the local Gauss points, are used to evaluate the integrated terms in the local region Ω^L.

Equation (2.23) describes the partial derivative of the elastic strain energy, eq. (2.16), by the local nodal displacement.

$$\begin{aligned}\frac{\partial \Pi_e}{\partial d^L{}_i} &= \frac{\partial}{\partial d^L{}_i}\left(\frac{1}{2}\int_{\Omega^G} d_m{}^G B^G{}_{km} D^G{}_{kl} B^G{}_{ln} d^G{}_n d\Omega\right) \\ &\quad + \frac{\partial}{\partial d^L{}_i}\left\{\frac{1}{2}\int_{\Omega^L} (d_m{}^G B^G{}_{km} + d_m{}^L B^L{}_{km}) D^L{}_{kl} (B^G{}_{ln} d^G{}_n + B^L{}_{ln} d^L{}_n) d\Omega\right\} \\ &= \int_{\Omega^L} B^L{}_{ki} D^L{}_{kl} (B^G{}_{ln} d^G{}_n + B^L{}_{ln} d^L{}_n) d\Omega \\ &= \int_{\Omega^L} B^L{}_{ki} D^L{}_{kl} B^G{}_{ln} d\Omega d^G{}_n + \int_{\Omega^L} B^L{}_{ki} D^L{}_{kl} B^L{}_{ln} d\Omega d^L{}_n \end{aligned} \tag{2.23}$$

The partial derivative of the body force energy, eq. (2.17), by the global nodal displacement is denoted in eq. (2.24).

$$\frac{\partial \Pi_b}{\partial d^G{}_i} = -\int_{\Omega^G} N^G{}_{ki} b_k d\Omega - \int_{\Omega^L} N^G{}_{ki} b_k d\Omega \tag{2.24}$$

Similarly, in order to simplify the computation, the second term on the right is evaluated by the global model instead of the local model. Since $\Omega = \Omega^G + \Omega^L$, eq. (2.24) is modified as follows:

$$\frac{\partial \Pi_b}{\partial d^G{}_i} \cong -\int_{\Omega} N^G{}_{ki} b_k d\Omega \tag{2.25}$$

Equation (2.26) expresses the partial derivative of the body force energy, eq. (2.17), by the local nodal displacement.

$$\frac{\partial \Pi_b}{\partial d^L{}_i} = -\int_{\Omega^L} N^L{}_{ki} b_k d\Omega \tag{2.26}$$

The partial derivative of the external force energy, eq. (2.18), by the global nodal displacement is derived.

$$\frac{\partial \Pi_t}{\partial d^G{}_i} = -\int_{\Gamma_t^G} N^G{}_{ki} t_k d\Gamma - \int_{\Gamma_t^L} N^G{}_{ki} t_k d\Gamma \tag{2.27}$$

The second term on the right is also evaluated by the global model instead of the local model for simplifying the calculation. Since $\Gamma_t = \Gamma_t^G + \Gamma_t^L$, eq. (2.27) is modified as follows:

$$\frac{\partial \Pi_t}{\partial d^G{}_i} \cong -\int_{\Gamma_t} N^G{}_{ki} t_k d\Gamma \tag{2.28}$$

Equation (2.29) denotes the partial derivative of the external force energy, eq. (2.18), by the local nodal displacement.

$$\frac{\partial \Pi_t}{\partial d^L{}_i} = -\int_{\Gamma_t^L} N^L{}_{ki} t_k d\Gamma \tag{2.29}$$

According to eqs. (2.19), (2.22), (2.25) and (2.28), the partial derivative of the total energy by the global nodal displacement is shown in eq. (2.30a).

$$\begin{aligned} \frac{\partial \Pi}{\partial d^G{}_i} = & \int_{\Omega} B^G{}_{ki} D^G{}_{kl} B^G{}_{ln} d\Omega d^G{}_n + \int_{\Omega^L} B^G{}_{ki} D^L{}_{kl} B^L{}_{ln} d\Omega d^L{}_n \\ & - \int_{\Omega} N^G{}_{ki} b_k d\Omega - \int_{\Gamma_t} N^G{}_{ki} t_k d\Gamma \end{aligned} \tag{2.30a}$$

Similarly, applying eqs. (2.19), (2.23), (2.26) and (2.29), eq. (2.30b) is derived.

$$\frac{\partial \Pi}{\partial d^L{}_i} = \int_{\Omega^L} B^L{}_{ki} D^L{}_{kl} B^G{}_{ln} d\Omega d^G{}_n + \int_{\Omega^L} B^L{}_{ki} D^L{}_{kl} B^L{}_{ln} d\Omega d^L{}_n - \int_{\Omega^L} N^L{}_{ki} b_k d\Omega - \int_{\Gamma_t^L} N^L{}_{ki} t_k d\Gamma \tag{2.30b}$$

Therefore, the minimizing conditions of the total energy, eq. (2.15), are modified as follows:

$$\int_{\Omega} B^G{}_{ki} D^G{}_{kl} B^G{}_{ln} d\Omega d^G{}_n + \int_{\Omega^L} B^G{}_{ki} D^L{}_{kl} B^L{}_{ln} d\Omega d^L{}_n - \int_{\Omega} N^G{}_{ki} b_k d\Omega - \int_{\Gamma_t} N^G{}_{ki} t_k d\Gamma = 0 \tag{2.31a}$$

$$\int_{\Omega^L} B^L{}_{ki} D^L{}_{kl} B^G{}_{ln} d\Omega d^G{}_n + \int_{\Omega^L} B^L{}_{ki} D^L{}_{kl} B^L{}_{ln} d\Omega d^L{}_n - \int_{\Omega^L} N^L{}_{ki} b_k d\Omega - \int_{\Gamma_t^L} N^L{}_{ki} t_k d\Gamma = 0 \tag{2.31b}$$

or, in the matrix description,

$$\int_{\Omega} [B^G]^T [D^G][B^G] d\Omega \{d^G\} + \int_{\Omega^L} [B^G]^T [D^L][B^L] d\Omega \{d^L\} - \int_{\Omega} [N^G]^T \{b\} d\Omega - \int_{\Gamma_t} [N^G]^T \{t\} d\Gamma = 0 \tag{2.32a}$$

$$\int_{\Omega^L} [B^L]^T [D^L][B^G] d\Omega \{d^G\} + \int_{\Omega^L} [B^L]^T [D^L][B^L] d\Omega \{d^L\} - \int_{\Omega^L} [N^L]^T \{b\} d\Omega - \int_{\Gamma_t^L} [N^L]^T \{t\} d\Gamma = 0 \tag{2.32b}$$

As a result, the minimizing conditions of the total energy, eq. (2.15), can be modified as follows in the matrix description:

$$[K^G]\{d^G\} + [K^{GL}]\{d^L\} = \{f^G\} \tag{2.33a}$$

$$[K^{LG}]\{d^G\} + [K^L]\{d^L\} = \{f^L\} \tag{2.33b}$$

Here,

$$[K^G] = \int_{\Omega} [B^G]^T [D^G][B^G] d\Omega \tag{2.34a}$$

$$[K^{GL}]=[K^{LG}]^T=\int_{\Omega^L}[B^G]^T[D^L][B^L]d\Omega \tag{2.34b}$$

$$[K^L]=\int_{\Omega^L}[B^L]^T[D^L][B^L]d\Omega \tag{2.34c}$$

$$\{f^G\}=\int_{\Omega}[N^G]^T\{b\}d\Omega+\int_{\Gamma_t}[N^G]^T\{t\}d\Omega \tag{2.34d}$$

$$\{f^L\}=\int_{\Omega^L}[N^L]^T\{b\}d\Omega+\int_{\Gamma^L_t}[N^L]^T\{t\}d\Omega \tag{2.34e}$$

Of course, these stiffness equations are also able to be derived by applying the principle of virtual work. That procedure is presented in Appendix A.

If the coupled stiffness matrix $[K^{GL}]$ is a zero matrix, eqs. (2.33a) ~ (2.33b) show the conventional stiffness equations for the global and local models, respectively. In other words, the coupled stiffness matrix $[K^{GL}]$ is the key component of the mesh overlay method. Moreover, the global stiffness matrix $[K^G]$ and the global force vector $\{f^G\}$ are constructed only by the parameters on the global model. Similarly, the local stiffness matrix $[K^L]$ and the local force vector $\{f^L\}$ are constructed only by the parameters on the local model. Therefore, by modifying eqs. (2.33a) ~ (2.33b) as follows, a commercial FE code is also able to be applied for the mesh overlay analysis[26].

$$[K^G]\{d^G\}=\{f^G\}-[K^{GL}]\{d^L\} \tag{2.35a}$$

$$[K^L]\{d^L\}=\{f^L\}-[K^{LG}]\{d^G\} \tag{2.35b}$$

In this case, the analyst is just required to build a user subroutine that constructs the coupled stiffness matrix $[K^{GL}]$ to evaluate the second term on the right side of eq. (2.35a) or (2.35b). These stiffness equations can be solved by adopting the block-Gauss-Siedel method[45)~47)].

2.2.2 Two-dimensional Case

For two-dimensional analysis, the number of the independent components of the stress vector $\{\sigma\}$ and the strain vector $\{\varepsilon\}$ becomes three, respectively.

$$\{\sigma\} \equiv \{\sigma_x \quad \sigma_y \quad \tau_{xy}\}^T \tag{2.36}$$

$$\{\varepsilon\} \equiv \{\varepsilon_x \quad \varepsilon_y \quad 2\varepsilon_{xy}\}^T \tag{2.37}$$

Hence, the deformation matrix [D] for the plane strain condition, ε_z=0, is modified as follows:

$$[D] = \frac{E}{(1+\nu)(1-2\nu)} \begin{bmatrix} 1-\nu & \nu & 0 \\ \nu & 1-\nu & 0 \\ 0 & 0 & \dfrac{1-2\nu}{2} \end{bmatrix} \tag{2.38}$$

The z-directional stress σ_z is computed in eq. (2.39).

$$\sigma_z = \nu(\sigma_x + \sigma_y) \tag{2.39}$$

On the other hand, the deformation matrix [D] for the plane stress condition, σ_z=0, is expressed as follows:

$$[D] = \frac{E}{(1-\nu^2)} \begin{bmatrix} 1 & \nu & 0 \\ \nu & 1 & 0 \\ 0 & 0 & \dfrac{1-\nu}{2} \end{bmatrix} \tag{2.40}$$

The z-directional strain ε_z is computed in eq. (2.41).

$$\varepsilon_z = -\frac{\nu}{E}(\sigma_x + \sigma_y) \tag{2.41}$$

2.2.3 Coupled Stiffness Matrix Construction

In the mesh overlay method, in order to compute the coupled stiffness matrix $[K^{GL}]$, not only the strain-nodal displacement matrix for the local element $[B^L]$ but also the one for the global element $[B^G]$ should be evaluated at every evaluation point for the local model. Therefore, the following procedures are required: (1) find the global element that the local evaluation point belongs to, and (2) obtain the natural coordinates of the local evaluation point for the global element.

The verification algorithm, whether the point is above, on or below the plane, is famous as the *ORIENT3D* for a three-dimensional, or *ORIENT2D* for a two-dimensional problem. It is well-known that the following equation is satisfied when the point $D(x_D, y_D, z_D)$ is on the plane defined by the points $A(x_A, y_A, z_A)$, $B(x_B, y_B, z_B)$ and $C(x_C, y_C, z_C)$.

$$\det\begin{bmatrix} x_A - x_D & y_A - y_D & z_A - z_D \\ x_B - x_D & y_B - y_D & z_B - z_D \\ x_C - x_D & y_C - y_D & z_C - z_D \end{bmatrix} = 0 \tag{2.42}$$

In addition, if the signature of the determinant in eq. (2.42) is positive (negative), the point D is above (below) the plane ABC. However, due to the round off error of the floating point, this algorithm sometimes fails when the verified point D is close to the plane ABC, even if double precision arithmetic is adopted[48].

Therefore, in this research, whether the point is in the element or not is verified by the following procedures. Let us consider the quadrilateral element shown in **Fig. 2.2**. The nodes are numbered from *1* to *4* in a counterclockwise direction. Absolute coordinates for each node are given as (x_i, y_i).

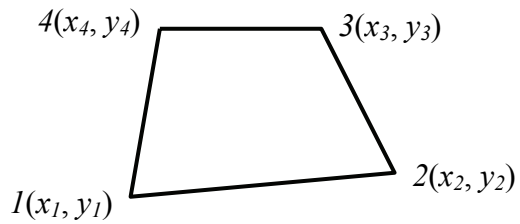

Fig. 2.2 Schematic figure of quadrilateral element

First, the segment *1-2* is defined as $f_{12}(x, y)=0$:

$$f_{12}(x,y)=\begin{cases}\dfrac{1}{|y_2-y_1|}\{(y_2-y_1)x+(x_1-x_2)y+(x_2y_1-x_1y_2)\} & if\ y_1\neq y_2\\ \dfrac{1}{|x_1-x_2|}\{(x_1-x_2)y+(x_2y_1-x_1y_2)\} & if\ y_1=y_2\end{cases} \tag{2.43}$$

Here, if the absolute value of $f_{12}(x, y)$ is less than 10^{-6}, $f_{12}(x, y)$ is assumed to be zero in this research. Similarly, the segment *4-3* is defined as $f_{43}(x, y)=0$:

$$f_{43}(x,y)=\begin{cases}\dfrac{1}{|y_3-y_4|}\{(y_3-y_4)x+(x_4-x_3)y+(x_3y_4-x_4y_3)\} & if\ y_3\neq y_4\\ \dfrac{1}{|x_4-x_3|}\{(x_4-x_3)y+(x_3y_4-x_4y_3)\} & if\ y_3=y_4\end{cases} \tag{2.44}$$

Therefore, if the product of $f_{12}(x_0, y_0)$ and $f_{43}(x_0, y_0)$ becomes negative, the point(x_0, y_0) is between the segments *1-2* and *4-3*. Similarly, the segments *2-3* and *1-4* can be also defined as $f_{23}(x, y)=0$ and $f_{14}(x, y)=0$. When the product of $f_{23}(x_0, y_0)$ and $f_{14}(x_0, y_0)$ also becomes negative, the point(x_0, y_0) is in the quadrilateral element defined by the points (x_1, y_1) to (x_4, y_4).

The absolute coordinates of the evaluation point $\{x\}$ can be easily obtained through the absolute coordinates of all nodes of the local element $\{X^e\}$ and its shape function matrix $[N^L]$.

$$\{x\}=[N^L]\{X^e\} \tag{2.45}$$

Therefore, by applying this procedure for all global elements, the global element that overlays the evaluating point would be found.

Finally, the natural coordinates for the global element (ξ^G, η^G), which overlays the evaluating point, should be computed. In order to find them, the iterative calculation is adopted.

In order to increase the accuracy of the integration, a scheme using sub elements has been proposed[27),33),42),49)]. In this research, however, the approximate

procedure[25),26),35)] based on the Gauss-Legendre quadrature is adopted to compute eqs. (2.34a) ~ (2.34e) due to its simple algorithms. Hence, when a global element partially overlaps a local element, the integration in eq. (2.34b) may error. In order to reduce the error, the contain number of Gauss points for the local elements should be increased.

2.2.4 Flow of Analysis (Stiffness Matrix Construction)

The construction of the stiffness matrix is depicted as follows. Gauss points for each element are given. If the Gauss point is for a global element, construct the global stiffness matrix $[K^G]$, and go to the next Gauss point. On the other hand, if the Gauss point is for a local element, the coupled stiffness matrix $[K^{LG}]$ and $[K^{GL}]$, as well as the local stiffness matrix $[K^L]$, should be calculated. In order to construct the coupled stiffness matrix $[K^{LG}]$, the strain-nodal displacement matrix for the global element $[B^G]$ of the local Gauss point is necessary, as shown in eq. (2.34b). The strain-nodal displacement matrix for the global element $[B^G]$ of the local Gauss point can be computed according to the procedure for computing the natural coordinates for the overlaid global element of the local Gauss point, shown in the previous subsection. Hence, the coupled stiffness matrix $[K^{LG}]$ can be computed. The transposed matrix of the coupled stiffness matrix $[K^{LG}]$ equals the other components, $[K^{GL}]$. Then, go to the next Gauss point. The flow for two-dimensional problems is shown in **Fig. 2.3**.

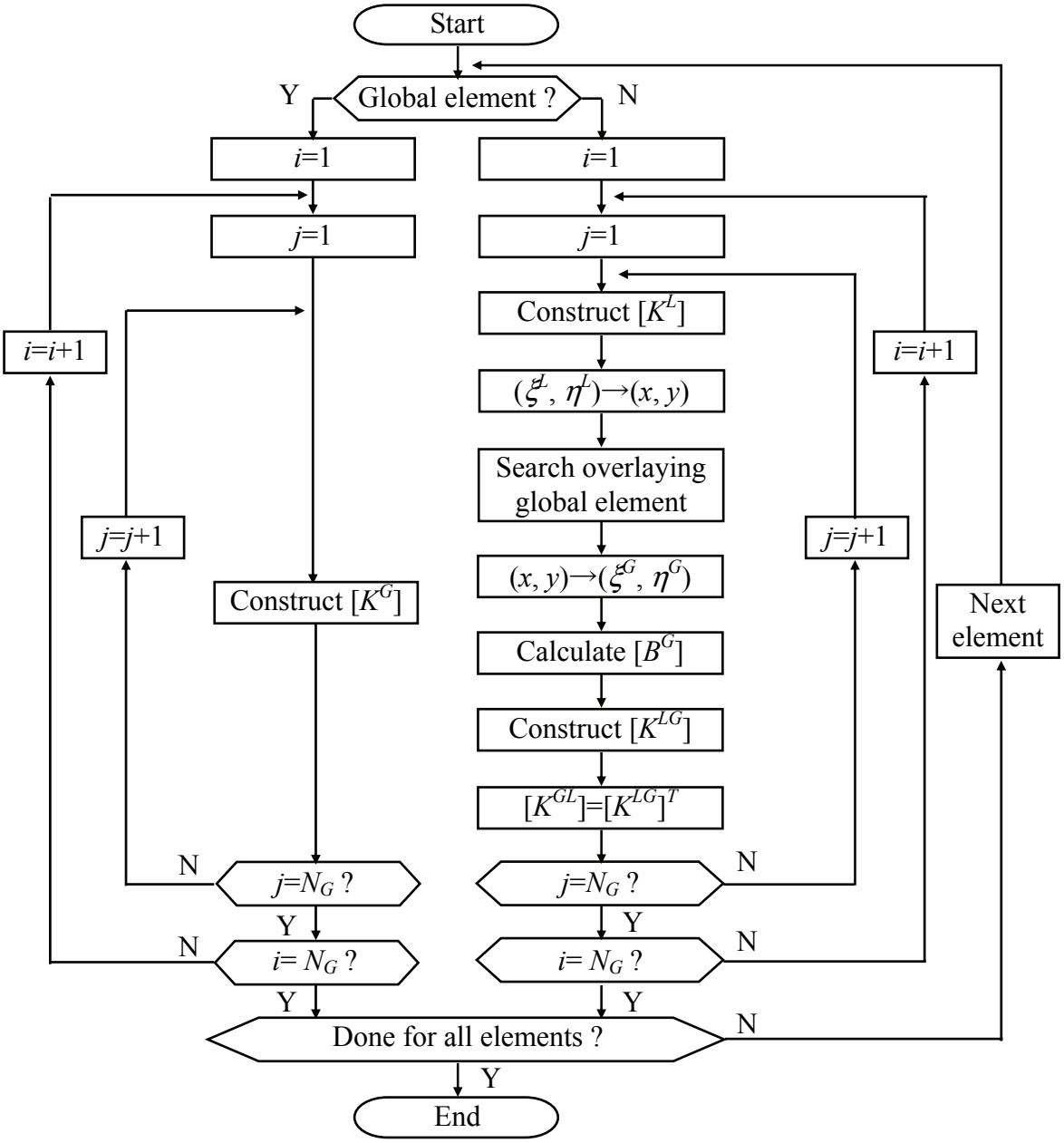

Fig. 2.3 Flow for constructing stiffness matrix [K] for two-dimensional problems (N_G: No. of Gauss points along an axis per element)

2.2.5 Summary

The mesh overlay formulations for elastic problems were reviewed. In the mesh overlay method, a fine model called “the local model” overlays a part of a whole model called “the global model.” In order to satisfy the C^0 continuity of displacement, the local displacement is set to be zero on the global-local boundary. Therefore, strain is also expressed as the summation of the global strain and the local strain in the local region. Because of this constraint, the global-local boundary does not have to be placed on the global element boundary. Hence, the mesh discretization can be flexibly applied. As shown in the stiffness equations, the coupled stiffness matrix, which has an important role for coupling the global analysis and the local analysis, is the key component of the mesh overlay method.

2.3 Linear Equation Solver

2.3.1 Introduction

Recently, the iterative method, the conjugate gradient method for example, is applied to solve simultaneous linear equations due to its shorter computing time. The iterative method is also applied to solve the stiffness equations for the mesh overlay analysis. For instance, S. Wang et al.[29] concluded that the iterative method is suitable due to large bandwidth of the stiffness matrix in the mesh overlay formulations. M. Yoshida et al.[30] investigated the effectiveness of preconditions for the conjugate gradient method. However, contrary conclusions also have been derived. For example, Y. Okuno et al.[31] reported that the convergence speed is slow when the iterative method is applied to the mesh overlay analysis. Moreover, J. W. Park et al.[32] showed that the multi-frontal solver, one of the direct methods, is the best to solve the linear equations in the mesh overlay method. These considerations, however, seem to focus on the convergence speed.

The mesh overlay analysis is a coupled analysis of the global and local models. In the mesh overlay method, the displacement at a point on the local region is expressed as the summation of the global displacement and the local displacement, as shown in eq. (2.2). Hence, the order of nodal displacements, which are the solutions of the mesh overlay method, would widely distribute.

In the iterative method, the solutions are assumed first. Then, the error is evaluated. If the error is not acceptable, the assumed solutions are modified and the error is evaluated again. These procedures are repeated until the error becomes small enough. Therefore, the criterion that judges its convergence should be carefully determined. However, there seem to be no reports that investigate the relation between solution accuracy and convergence criterion for the iterative method to solve the stiffness equations when the order of the solutions is extensively spread. In fact, the applied criterion to judge its convergence is widely distributed in past reports, even for the conventional FE analysis. Some research decided that the converged solutions are obtained when the relative residual becomes 10^{-4} or less[50]; another research considered

its convergence when the error norm reaches 10^{-8} or less[51]. Hence, how to set the convergence condition does not seem to have been clarified yet.

This section investigates the relation of the convergence criterion for the iterative method that solves the stiffness equations to the accuracy of the obtained solutions. It also discusses the validity of adopting the iterative method to solve the stiffness equations for the mesh overlay method.

2.3.2 Computational Conditions

Figure 2.4 shows a system consisting of N_S elastic springs. Currently, this system is in equilibrium, where each length of the spring is L_i, and the spring constant is k_i. Now, one end is fixed, and the unit displacement will be applied on the other end.

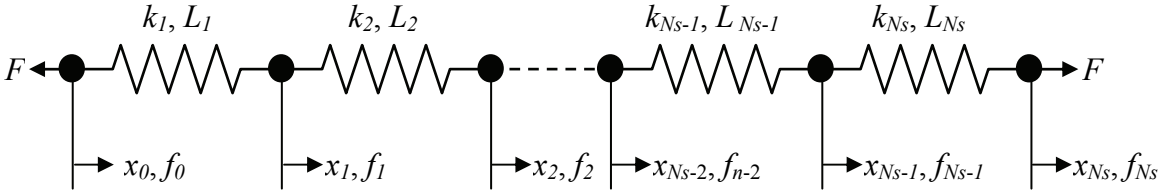

Fig. 2.4 Elastic spring system for investigating linear equation solver

The stiffness equations are shown in eq. (2.46). The stiffness matrix becomes a tri-diagonal matrix.

$$\begin{bmatrix} k_1 & -k_1 & 0 & \cdots & 0 & 0 & 0 \\ -k_1 & k_1+k_2 & -k_2 & \cdots & 0 & 0 & 0 \\ 0 & -k_2 & k_2+k_3 & \cdots & 0 & 0 & 0 \\ \vdots & \vdots & \vdots & \ddots & \vdots & \vdots & \vdots \\ 0 & 0 & 0 & \cdots & k_{N_S-2}+k_{N_S-1} & -k_{N_S-1} & 0 \\ 0 & 0 & 0 & \cdots & -k_{N_S-1} & k_{N_S-1}+k_{N_S} & -k_{N_S} \\ 0 & 0 & 0 & \cdots & 0 & -k_{N_S} & k_{N_S} \end{bmatrix} \begin{Bmatrix} x_0 \\ x_1 \\ x_2 \\ \vdots \\ x_{N_S-2} \\ x_{N_S-1} \\ x_{N_S} \end{Bmatrix} = \begin{Bmatrix} f_0 \\ f_1 \\ f_2 \\ \vdots \\ f_{N_S-2} \\ f_{N_S-1} \\ f_{N_S} \end{Bmatrix} \tag{2.46}$$

In order to simplify the problem, each spring is considered as an elastic bar. The elastic modulus of each bar has the same value, E_0, and the area of the cross section is

also the same, A_0. Hence, the spring constant k_i is derived by eq. (2.47).

$$k_i = \frac{E_0 A_0}{L_i} \tag{2.47}$$

Let us investigate the relation between the accuracy of the solutions obtained by the iterative method and its convergence criterion. Specifically, the number of elements N_S is set to 10. The length of the left three elements L_1~L_3 is the same, and that of the others L_4~L_{10} is also the same. Here, L_1~L_3 are widely chosen from 1 to 10000; L_4~L_{10} are always set to 1, as shown in **Table 2.1**.

Table 2.1 Computational conditions for investigating linear equation solver

Case	L_1~L_3	L_4~L_{10}
A	1	1
B	10	1
C	100	1
D	1000	1
E	10000	1

As the boundary conditions, the displacement of the left end x_0 is zero, and the displacement of the right end x_{Ns} is assigned to unity. The penalty method is adopted to satisfy these boundary conditions. The penalty constant is set to 10^5 for the present problem.

The stiffness equations, eq. (2.46), are solved by two types of the iterative method: (1) the conjugate gradient (CG) method, and (2) the pre-conditioned conjugate gradient (PCCG) method. The scaling is not applied in the CG method; it is adopted in the PCCG method. Here, in this research, the scaling matrix [W] of the PCCG method is a diagonal matrix where each diagonal component is the same as the diagonal component of the stiffness matrix. The convergence criterion Δ is set to 10^{-8}. In order to find the definition of the scaling matrix [W] or the convergence criterion Δ, please see Appendix B.

Moreover, (3) the Gauss-Jordan method is also applied to solve eq. (2.46) as the functions as the direct method. The reference solutions (4) are derived by eq. (2.48) since this system is assumed to be a uniform bar.

$$x_i = \frac{\sum_{k=1}^{i} L_k}{\sum_{k=1}^{n} L_k} \tag{2.48}$$

2.3.3 Numerical Results (Case A: L_1~L_3=L_4~L_{10}=1)

Let us first examine when all elements' length is the same. The obtained solutions are shown in **Table 2.2**. In this case, the solutions obtained by the CG method, the PCCG method and the Gauss-Jordan method coincide. The small differences between these solutions and the reference solutions are due to the penalty method, although these errors would have no negative influence on the solutions. The number of the iterations to acquire the converged solutions for the PCCG method were less than those needed with the CG method, although it is not shown here. Therefore, it is confirmed that the scaling has a positive effect on faster convergence.

Table 2.2 Nodal displacements when L_1~L_3=1 and L_4~L_{10}=1

	Reference	Gauss-Jordan	CG	PCCG
x_0	0.000000×10^{0}	1.000018×10^{-6}	1.000018×10^{-6}	1.000018×10^{-6}
x_1	1.000000×10^{-1}	1.000018×10^{-1}	1.000018×10^{-1}	1.000018×10^{-1}
x_2	2.000000×10^{-1}	2.000026×10^{-1}	2.000026×10^{-1}	2.000026×10^{-1}
x_3	3.000000×10^{-1}	3.000034×10^{-1}	3.000034×10^{-1}	3.000034×10^{-1}
x_4	4.000000×10^{-1}	4.000042×10^{-1}	4.000042×10^{-1}	4.000042×10^{-1}
x_5	5.000000×10^{-1}	5.000050×10^{-1}	5.000050×10^{-1}	5.000050×10^{-1}
x_6	6.000000×10^{-1}	6.000058×10^{-1}	6.000058×10^{-1}	6.000058×10^{-1}
x_7	7.000000×10^{-1}	7.000066×10^{-1}	7.000066×10^{-1}	7.000066×10^{-1}
x_8	8.000000×10^{-1}	8.000074×10^{-1}	8.000074×10^{-1}	8.000074×10^{-1}
x_9	9.000000×10^{-1}	9.000082×10^{-1}	9.000082×10^{-1}	9.000082×10^{-1}
x_{10}	1.000000×10^{0}	1.000009×10^{0}	1.000009×10^{0}	1.000009×10^{0}

2.3.4 Numerical Results (Case B: L_1~L_3=10, L_4~L_{10}=1)

Next, the case when the left three elements' length L_1~L_3 is ten times longer than the others is considered. The nodal displacements are shown in **Table 2.3**. In this case, the same tendency noted in the previous section is confirmed.

Table 2.3 Nodal displacements when L_1~L_3=10 and L_4~L_{10}=1

	Reference	Gauss-Jordan	CG	PCCG
x_0	0.000000×10^{0}	2.702749×10^{-6}	2.702749×10^{-6}	2.702749×10^{-6}
x_1	2.702703×10^{-1}	2.702749×10^{-1}	2.702749×10^{-1}	2.702749×10^{-1}
x_2	5.405405×10^{-1}	5.405470×10^{-1}	5.405470×10^{-1}	5.405470×10^{-1}
x_3	8.108108×10^{-1}	8.108192×10^{-1}	8.108192×10^{-1}	8.108192×10^{-1}
x_4	8.378378×10^{-1}	8.378464×10^{-1}	8.378464×10^{-1}	8.378464×10^{-1}
x_5	8.648649×10^{-1}	8.648736×10^{-1}	8.648736×10^{-1}	8.648736×10^{-1}
x_6	8.918919×10^{-1}	8.919009×10^{-1}	8.919009×10^{-1}	8.919009×10^{-1}
x_7	9.189189×10^{-1}	9.189281×10^{-1}	9.189281×10^{-1}	9.189281×10^{-1}
x_8	9.459459×10^{-1}	9.459553×10^{-1}	9.459553×10^{-1}	9.459553×10^{-1}
x_9	9.729730×10^{-1}	9.729825×10^{-1}	9.729825×10^{-1}	9.729825×10^{-1}
x_{10}	1.000000×10^{0}	1.000010×10^{0}	1.000010×10^{0}	1.000010×10^{0}

2.3.5 Numerical Results (Case C: L_1~L_3=100, L_4~L_{10}=1)

Let us now investigate if the left three elements' length L_1~L_3 is 100 times longer than the others. The obtained solutions are shown in **Table 2.4**. In this case, the same tendency from the previous section is also confirmed, although there are small differences between the CG method and the PCCG method. Furthermore, since the PCCG method gives the same solutions to the Gauss-Jordan method, the scaling seems to have a role in achieving more accurate results. However, the differences may be too small to have any influences on the accuracy of the solutions.

Table 2.4 Nodal displacements when L_1~L_3=100 and L_4~L_{10}=1

	Reference	Gauss-Jordan	CG	PCCG
x_0	0.000000×10^{0}	3.257383×10^{-6}	3.257385×10^{-6}	3.257383×10^{-6}
x_1	3.257329×10^{-1}	3.257383×10^{-1}	3.257383×10^{-1}	3.257383×10^{-1}
x_2	6.514658×10^{-1}	6.514734×10^{-1}	6.514734×10^{-1}	6.514734×10^{-1}
x_3	9.771987×10^{-1}	9.772085×10^{-1}	9.772086×10^{-1}	9.772085×10^{-1}
x_4	9.804560×10^{-1}	9.804659×10^{-1}	9.804656×10^{-1}	9.804659×10^{-1}
x_5	9.837134×10^{-1}	9.837232×10^{-1}	9.837235×10^{-1}	9.837232×10^{-1}
x_6	9.869707×10^{-1}	9.869806×10^{-1}	9.869803×10^{-1}	9.869806×10^{-1}
x_7	9.902280×10^{-1}	9.902379×10^{-1}	9.902382×10^{-1}	9.902379×10^{-1}
x_8	9.934853×10^{-1}	9.934953×10^{-1}	9.934951×10^{-1}	9.934953×10^{-1}
x_9	9.967427×10^{-1}	9.967526×10^{-1}	9.967527×10^{-1}	9.967526×10^{-1}
x_{10}	1.000000×10^{0}	1.000010×10^{0}	1.000010×10^{0}	1.000010×10^{0}

2.3.6 Numerical Results (Case D: L_1~L_3=1000, L_4~L_{10}=1)

Next, let us consider when the left three elements' length L_1~L_3 is 1000 times longer than the others. **Table 2.5** shows the obtained nodal displacements. In this case, there are significant differences between the solutions by the iterative method and the direct method, when the nodal displacement x_1 or x_2 is observed. The reason is as follows: the exact value of the nodal displacement x_1 or x_2 is much larger than the solutions obtained by the iterative method in this case, as shown in the reference solutions. However, the iterative method evaluates its convergence by the magnitude of the residual vector, which is the inner product of the stiffness matrix and the nodal displacement vector. Since the components of the stiffness matrix that are related to the nodal displacement x_1 or x_2 are much smaller under this condition, the magnitude of the residual vector becomes small enough even though the error contained in the nodal displacement x_1 or x_2 could not be ignored. Therefore, when the order of each solution and/or the one of the components of the coefficient matrix widely spreads, the obtained solutions by the iterative method could contain some errors.

Table 2.5 Nodal displacements when L_1~L_3=1000 and L_4~L_{10}=1

	Reference	Gauss-Jordan	CG	PCCG
x_0	0.000000×10^{0}	3.325629×10^{-6}	0.000000×10^{0}	0.000000×10^{0}
x_1	3.325574×10^{-1}	3.325629×10^{-1}	9.930586×10^{-17}	0.000000×10^{0}
x_2	6.651147×10^{-1}	6.651225×10^{-1}	1.986117×10^{-8}	0.000000×10^{0}
x_3	9.976721×10^{-1}	9.976821×10^{-1}	9.930586×10^{-1}	9.930586×10^{-1}
x_4	9.980047×10^{-1}	9.980146×10^{-1}	9.940516×10^{-1}	9.940516×10^{-1}
x_5	9.983372×10^{-1}	9.983472×10^{-1}	9.950447×10^{-1}	9.950447×10^{-1}
x_6	9.986698×10^{-1}	9.986798×10^{-1}	9.960378×10^{-1}	9.960378×10^{-1}
x_7	9.990023×10^{-1}	9.990123×10^{-1}	9.970308×10^{-1}	9.970308×10^{-1}
x_8	9.993349×10^{-1}	9.993449×10^{-1}	9.980239×10^{-1}	9.980239×10^{-1}
x_9	9.996674×10^{-1}	9.996774×10^{-1}	9.990169×10^{-1}	9.990169×10^{-1}
x_{10}	1.000000×10^{0}	1.000010×10^{0}	1.000010×10^{0}	1.000010×10^{0}

Additionally, the difference is also notable even by the PCCG method. Therefore, scaling to increase solution accuracy for the present problem is not effective any more.

2.3.7 Numerical Results (Case E: L_1~L_3=10000, L_4~L_{10}=1)

Finally, consider when the left three elements' length L_1~L_3 is 10000 times longer than the others. The obtained solutions are shown in **Table 2.6**. The error of the iterative method, that is to say, the CG method and the PCCG method, becomes large. However, the direct method gives almost accurate results.

Table 2.6 Nodal displacements when L_1~L_3=10000 and L_4~L_{10}=1

	Reference	Gauss-Jordan	CG	PCCG
x_0	0.000000×10^{0}	3.332611×10^{-6}	0.000000×10^{0}	0.000000×10^{0}
x_1	3.332556×10^{-1}	3.332611×10^{-1}	9.993105×10^{-19}	0.000000×10^{0}
x_2	6.665111×10^{-1}	6.665189×10^{-1}	1.998621×10^{-9}	0.000000×10^{0}
x_3	9.997667×10^{-1}	9.997767×10^{-1}	9.993105×10^{-1}	9.993105×10^{-1}
x_4	9.998000×10^{-1}	9.998100×10^{-1}	9.994104×10^{-1}	9.994104×10^{-1}
x_5	9.998334×10^{-1}	9.998434×10^{-1}	9.995103×10^{-1}	9.995103×10^{-1}
x_6	9.998667×10^{-1}	9.998767×10^{-1}	9.996103×10^{-1}	9.996103×10^{-1}
x_7	9.999000×10^{-1}	9.999100×10^{-1}	9.997102×10^{-1}	9.997102×10^{-1}
x_8	9.999333×10^{-1}	9.999433×10^{-1}	9.998101×10^{-1}	9.998101×10^{-1}
x_9	9.999667×10^{-1}	9.999767×10^{-1}	9.999101×10^{-1}	9.999101×10^{-1}
x_{10}	1.000000×10^{0}	1.000010×10^{0}	1.000010×10^{0}	1.000010×10^{0}

In order to improve the accuracy, stricter convergence criterion, $\Delta=10^{-12}$, is adopted. The obtained solutions are shown in **Table 2.7**. When the convergence criterion becomes stricter, the iterative method gives results almost accurate as the direct method. Hence, the convergence criterion should be strict when the solutions, nodal displacements for the presented problem, widely distribute.

Table 2.7 Nodal displacements when L_1~L_3=10000and L_4~L_{10}=1: $\Delta=10^{-12}$

	Reference	Gauss-Jordan	CG	PCCG
x_0	0.000000×10^{0}	3.332611×10^{-6}	3.332606×10^{-6}	3.332611×10^{-6}
x_1	3.332556×10^{-1}	3.332611×10^{-1}	3.332606×10^{-1}	3.332611×10^{-1}
x_2	6.665111×10^{-1}	6.665189×10^{-1}	6.665187×10^{-1}	6.665189×10^{-1}
x_3	9.997667×10^{-1}	9.997767×10^{-1}	9.997643×10^{-1}	9.997767×10^{-1}
x_4	9.998000×10^{-1}	9.998100×10^{-1}	9.997981×10^{-1}	9.998100×10^{-1}
x_5	9.998334×10^{-1}	9.998434×10^{-1}	9.998323×10^{-1}	9.998434×10^{-1}
x_6	9.998667×10^{-1}	9.998767×10^{-1}	9.998668×10^{-1}	9.998767×10^{-1}
x_7	9.999000×10^{-1}	9.999100×10^{-1}	9.999020×10^{-1}	9.999100×10^{-1}
x_8	9.999333×10^{-1}	9.999433×10^{-1}	9.999376×10^{-1}	9.999433×10^{-1}
x_9	9.999667×10^{-1}	9.999767×10^{-1}	9.999736×10^{-1}	9.999767×10^{-1}
x_{10}	1.000000×10^{0}	1.000010×10^{0}	1.000010×10^{0}	1.000010×10^{0}

In this case, the length L_1~L_3 is 10000 times longer than the others. Therefore, the ratio of the largest diagonal component of the stiffness matrix and the smallest one is 10000. However, considering the three-dimensional analysis, when the length of the smallest element is only $10000^{1/3}$=21.5 times shorter than the largest element length, the ratio of the stiffness matrix components will become 10000. Hence, this example is not impractical, especially for the mesh overlay analysis.

2.3.8 Summary

This section investigated the relation between the solutions and the convergence criterion when the iterative method is applied to solve simultaneous linear equations. Through the present computations, the following results were achieved:

(1) The convergence criterion should be strict when the solutions (the components of the stiffness matrix) distribute widely.

(2) The pre-conditioned conjugate gradient (PCCG) method gives faster convergence than the conjugate gradient (CG) method owing to its scaling. However, scaling does not seem to have enough effect on increasing the accuracy of the solutions.

Therefore, if the convergence criterion is carefully selected, the iterative method will give accurate results even for the mesh overlay analysis. However, it is not clear how the convergence criterion should be decided according to the distribution range of the solutions and/or the components of the stiffness matrix. Moreover, when applied to nonlinear analysis, which is analyzed in Chapter 3, the stiffness matrix may not become a positive definite matrix if the assumed velocity fields are not appropriate. In that case, the algorithm of the conjugate gradient method becomes more complicated.

According to these considerations, this research has concluded that the direct method is more accurate for the mesh overlay analysis. Hence, the direct method is adopted to solve the stiffness equations in this research.

Some reports have investigated the relation between the accuracy of the mesh overlay solutions and the dimensional ratio of the global and local elements[34),35),52)]. The relationship between the convergence criterion of the iterative method and the accuracy of the solutions may be one of the reasons why the accuracy of the mesh overlay analysis degrades when the local elements become much smaller than the global elements.

2.4 Numerical Example (Plane Strain Tension with Inclusion)

2.4.1 Introduction

A numerical simulation code for elastic problems was developed based upon the aforementioned formulations in this research. Now, numerical simulation is performed in order to verify the formulations reviewed in the previous section, and to grasp the features of the mesh overlay solutions concretely. In this section, plane strain tension with an inclusion is analyzed first.

2.4.2 Computational Conditions

A plane strain elastic plate with an inclusion at the center is considered. **Figure 2.5** shows the dimension of the plate. The plate length is $2L$ and the width is $2W$. The inclusion length is $2a$ and the width is $2b$. The lateral displacement U is given and no shear forces are applied on this boundary. Elastic moduli for the matrix and the inclusion are E_0 and E_1, respectively. Poisson's ratio for the matrix and the inclusion are ν_0 and ν_1, respectively. **Table 2.8** shows the computational conditions. Body forces $\{b\}$ are ignored.

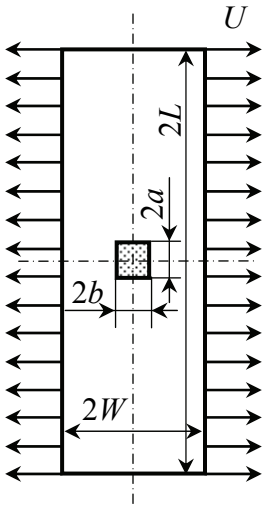

Fig. 2.5 Computational model of plane strain elastic plate tension with inclusion

Table 2.8 Computational conditions of plane strain elastic plate tension with inclusion

Aspect ratio of the plate	L/W	3	
Aspect ratio of the inclusion	a/b	1	
Normalized width of the inclusion	b/W	0.2	
Normalized displacement	U/W	0.1	
Elastic modulus of the matrix	E_0	100	GPa
Elastic modulus of the inclusion	E_1	10	GPa
Poisson's ratio of the matrix	ν_0	0.30	
Poisson's ratio of the inclusion	ν_1	0.30	

Because of the symmetry of deformation, one quarter of the model is considered in the calculation. The mesh discretization for the global model is (a) 1×3 and (b) 3×9, whereas that for the local model, which covers one-third of the whole area, is 10×10. Moreover, a calculation using conventional FE analysis is also performed as a reference solution. The mesh discretization for the conventional analysis is 10×30. The number of Gauss points for the mesh overlay analysis is 4×4 per element for the local model and 2×2 per element for the global model, respectively. That for the conventional analysis is also 2×2. In both analyses, four-node linear isoparametric quadrilateral elements are used.

Figures 2.6~2.7 show the boundary conditions of the global and local models for this problem, respectively. Although the boundary conditions for the global model are the same as those for the conventional analysis, those for the local model are set as follows: lateral displacements of the nodes on the surface, where the lateral displacement U is prescribed, are set to be zero whereas the longitudinal displacements for these nodes are not constrained. The grayed meshes, 2×2 elements near the origin, show the inclusion. It is also noted that the global model does not consider the inclusion.

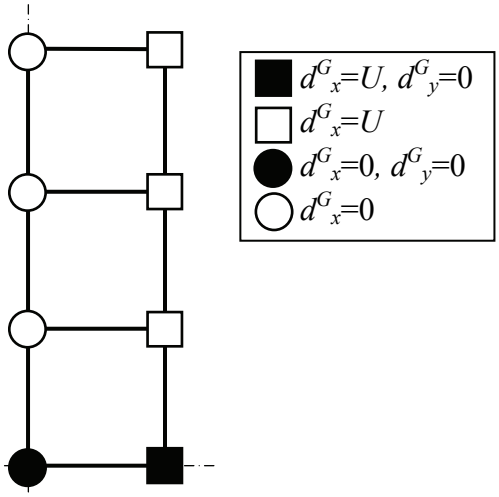

Fig. 2.6 Boundary conditions for the global model of plane strain elastic plate tension with inclusion

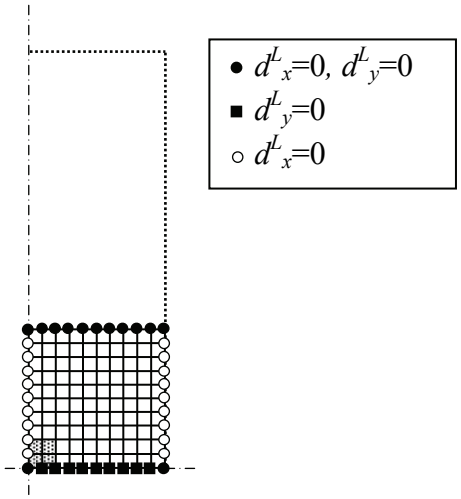

Fig. 2.7 Boundary conditions for the local model of plane strain elastic plate tension with inclusion

2.4.3 Computational Results

Obtained results are shown as follows. First of all, let us check whether the summation expressed by eq. (2.4) is correctly followed in this simulation. **Figure 2.8** shows the distributions of (a) the global lateral strain ε^G_x, (b) the local lateral strain ε^L_x and (c) the lateral strain ε_x.

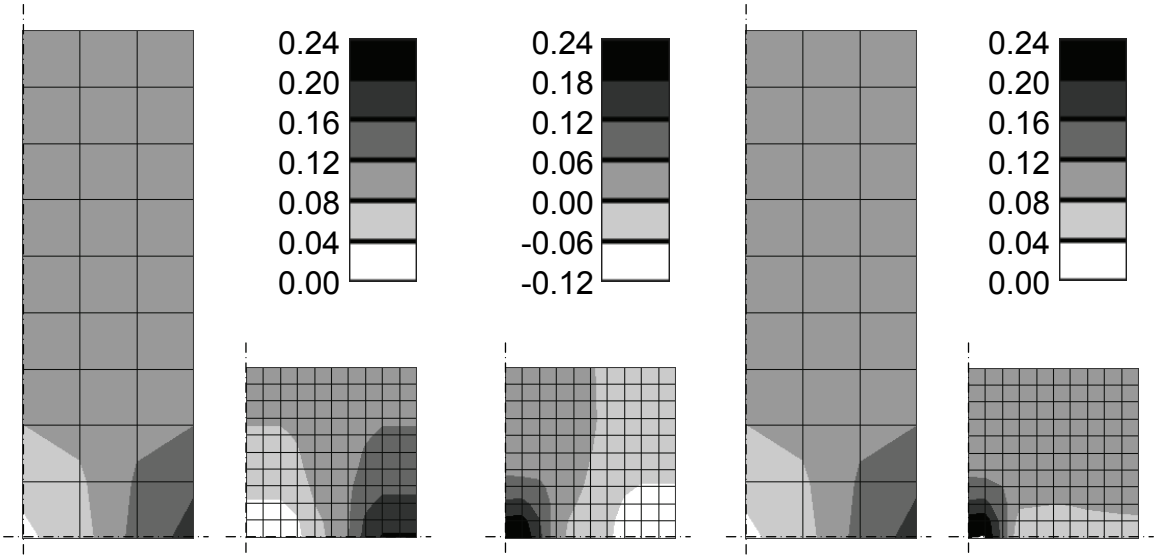

(a) Global lateral strain ε^G_x (b) Local lateral strain ε^L_x (c) Lateral strain ε_x

Fig. 2.8 Strain distributions of plane strain elastic plate tension with inclusion

It is confirmed that the lateral strain ε_x is precisely calculated as the summation of the global lateral strain ε^G_x and the local lateral strain ε^L_x in this simulation. Here, it is noted that the lateral global strain ε^G_x tends to be zero at the region where the material constants are different between the global and local models[40),53)]. The reason why the global strain becomes zero in this region will be investigated in Chapter 3. The longitudinal strain and the shear strain were also computed in a similar way although their distributions are not shown here.

It has been reported that the global and local displacement fields become indeterminate when the pattern of the global and local mesh discretizations are similar[30),32),46),49),53),54)]. However, such a situation does not occur even when the global

and local mesh patterns are the same as those shown in these computational models, since the local model contains a region where the material constants for the global model and those for the local model differ. Therefore, there are no countermeasures to the indefiniteness in the present formulations.

Figure 2.9 shows the strain distributions obtained by the mesh overlay method with (a) 1×3 global meshes and (b) 3×9 global meshes, and by (c) the conventional analysis. Each plot displays the lateral strain ε_x on the right side and the equivalent strain $\bar{\varepsilon}$ on the left side as a mirror image.

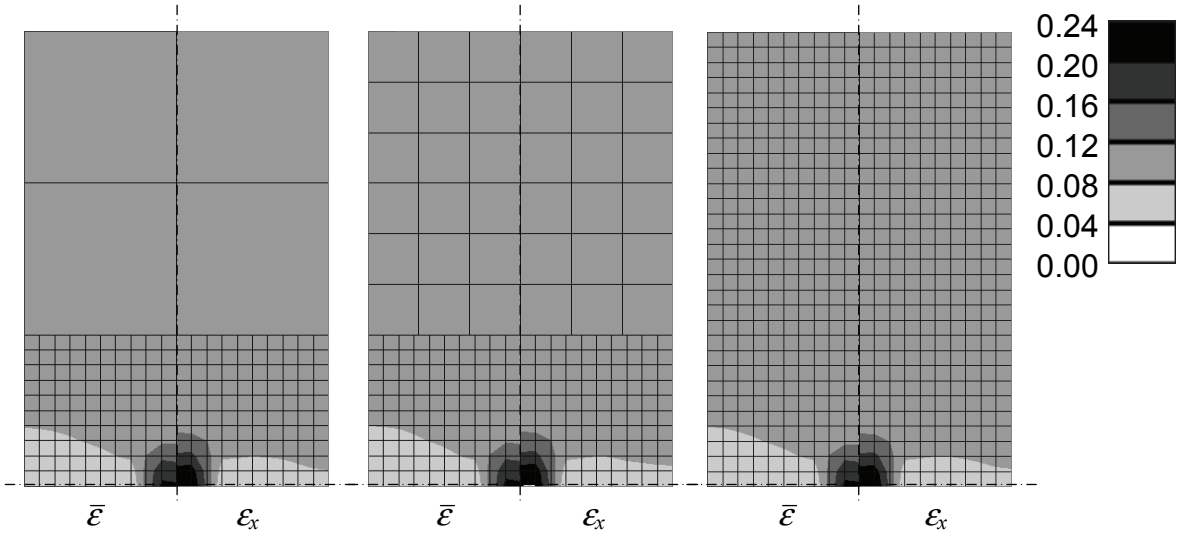

(a) Mesh overlay (Coarse global model) (b) Mesh overlay (Fine global model) (c) Conventional

Fig. 2.9 Lateral strain ε_x (right side) and equivalent strain $\bar{\varepsilon}$ (left side) distributions of plane strain elastic plate tension with inclusion

The strain distributions obtained by the mesh overlay method and the ones by the conventional method show good agreement even though resolution of the global model is coarse. Hence, it is no exaggeration to say that the mesh overlay method gives excellent approximate results. However, if the local model is too small, the results obtained by the mesh overlay method will not show good agreement with the results obtained by the conventional one. Although H. Okada et al.[33] reported the guidelines of the local model area and its resolution for plane tension problems with a hole, the generalized guidelines

have not been proposed yet. Therefore, a universal criterion to decide the size of the local model is strongly needed.

2.4.4 Summary

In this section, the mesh overlay analysis was achieved for the deformation behavior of a plate with an inclusion at the center under plane strain tension. It was confirmed that the strain in the local region is correctly expressed as the summation of the global strain and local strain. Obtained numerical examples showed that the solution by the mesh overlay analysis agrees with that by conventional analysis, even for the composite material deformation. Additionally, the global strain tends to become zero in the region where the global material and local material are different.

2.5 Numerical Example (Plane Strain Tension with Hole)

2.5.1 Introduction

Another feature of the mesh overlay method is flexibility of the mesh discretization since the boundary of the local model does not have to be set on the global element boundaries. In order to show this feature, another numerical example is performed as follows.

2.5.2 Computational Conditions

A plane strain elastic plate, which has a hole at the center, is considered. **Figure 2.10** shows the dimension of the plate. The plate length is $2L$ and the width is $2W$. Radius of the center hole is r. Displacement along longitudinal direction U is given and no shear forces are applied on this boundary. Elastic modulus of the plate is E and Poisson's ratio is ν. **Table 2.9** shows the computational conditions. Body forces $\{b\}$ are ignored.

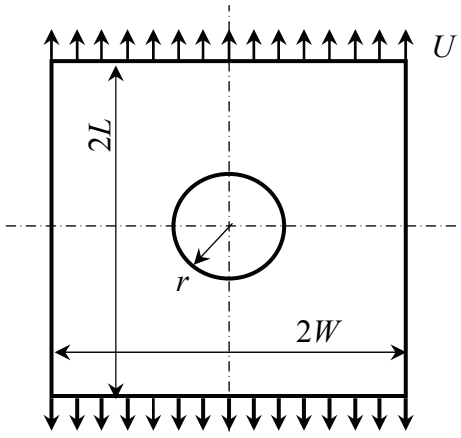

Fig. 2.10 Computational model of center holed plane strain elastic plate tension

Table 2.9 Computational conditions of center holed plane strain elastic plate tension

Aspect ratio of the plate	L/W	1
Hole diameter / plate width	r/W	0.3333
Nominal displacement	U/L	0.001
Elastic modulus	E	210 GPa
Poisson's ratio	ν	0.3333

Because of the symmetry of deformation, one quarter of the model is considered in the calculation. Mesh discretization for the global model is (a) 3×3, (b) 6×6 and (c) 10×10; that for the local model, which covers the circle region of radius 2r, is 18(angular direction)×20(radial direction). Furthermore, calculation using conventional FEM is also performed as a reference solution. **Figure 2.11** shows mesh discretization for (a) the mesh overlay method with 3×3 global mesh and (b) the conventional analysis. Although the mesh discretization of the global model for 6×6 or 10×10 is not shown here, the mesh discretization for the local model is the same. In addition, resolution of the local model and that of the conventional analysis in the vicinity of the center hole are the same. Here, four-node linear isoparametric quadrilateral elements are applied. The number of the Gauss points for the local model is 4×4 per element, whereas that for the global model as well as that for the conventional method is 2×2.

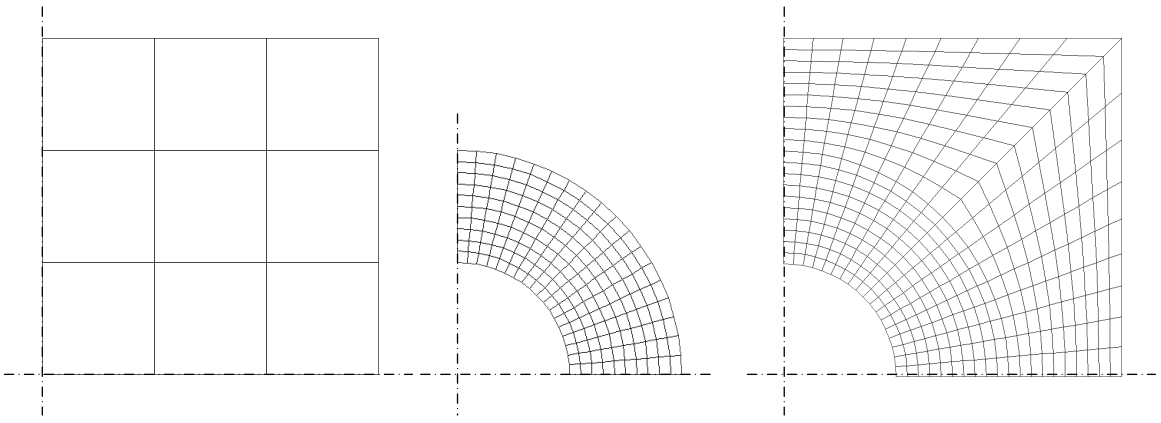

(a) Mesh overlay (b) Conventional

Fig. 2.11 Mesh discretization of center holed plane strain elastic plate tension

The nodes on the local model boundaries do not have to be put on the global element boundaries in the mesh overlay method. Hence, the flexibility of mesh discretization can be seen. Now, local nodes on the edge of the hole should not be constrained except for the symmetric constraints. It is also noted that the hole is not represented on the global model.

2.5.3 Computational Results

Figure 2.12 shows the stress distributions by the mesh overlay method where the global model mesh discretization is (a) 3×3, (b) 6×6 and (c) 10×10, and by (d) the conventional analysis. Each plot displays the longitudinal stress σ_y on the right side and the equivalent stress $\bar{\sigma}$ on the left side as a mirror image.

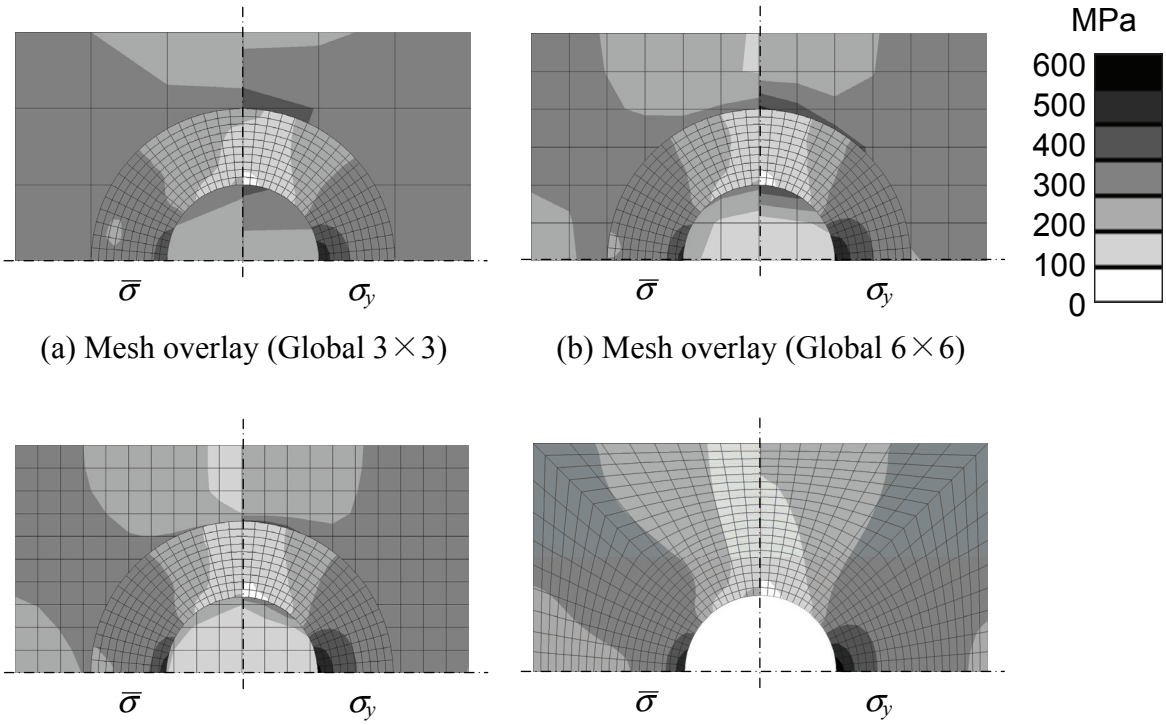

(a) Mesh overlay (Global 3×3) (b) Mesh overlay (Global 6×6)

(c) Mesh overlay (Global 10×10) (d) Conventional

Fig. 2.12 Longitudinal stress σ_y (right side) and equivalent stress $\bar{\sigma}$ (left side) distributions of center holed plane strain elastic plate tension

The stress distributions of the local model obtained by the mesh overlay method and that of the corresponding region obtained by the conventional analysis show good agreement. Moreover, their distributions are very similar between the global model and the corresponding region obtained by the conventional analysis, except the vicinity of the global-local boundary Γ^{GL}. Of results obtained by the mesh overlay method, the finest resolution global model (c) gives the most accurate solution. However, the discrepancy between each result by the mesh overlay method and that by the conventional analysis seems to be small. Additionally, the tendency that the global stress tends to be zero in the hole is also verified.

Now, **Figs. 2.13~2.14** show the longitudinal stress σ_y distribution and the equivalent stress $\bar{\sigma}$ distribution along the edge of the hole and the cross section of the minimum width point (on the *x*-axis). The horizontal axis shows the position from the origin along width (along the *x*-axis) *x* and the vertical axis shows the longitudinal stress σ_y and the equivalent stress $\bar{\sigma}$, respectively. The stress concentration is represented well both in the mesh overlay analysis and the conventional analysis. Moreover, it is found that the discrepancy between the results obtained by the mesh overlay method and the one obtained by the conventional method is small even though resolution of the global model is coarse. Now, stress oscillation is observed where position along width *x* is small. This oscillation is caused by inaccuracy of the integration quadrature of the coupled stiffness matrix $[K^{GL}]$. If reduction of this oscillation is needed, the number of the local Gauss points should be increased. Other suitable treatment such as smoothing may be also effective to reduce this error.

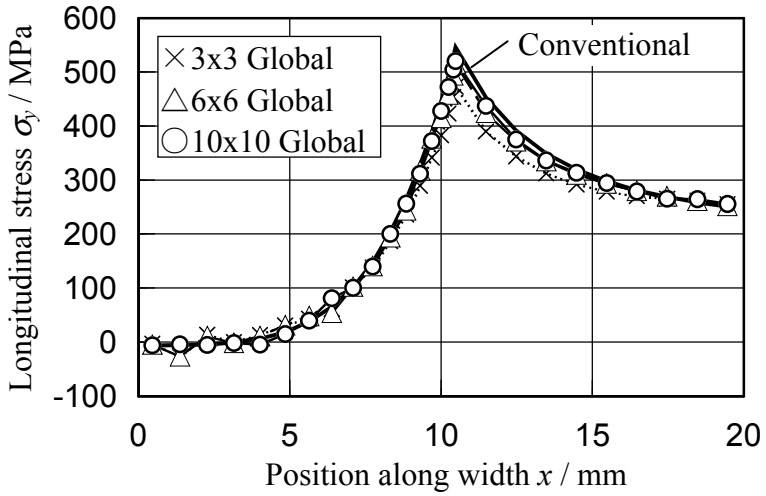

Fig. 2.13 Longitudinal stress σ_y distribution of center holed plane strain elastic plate tension

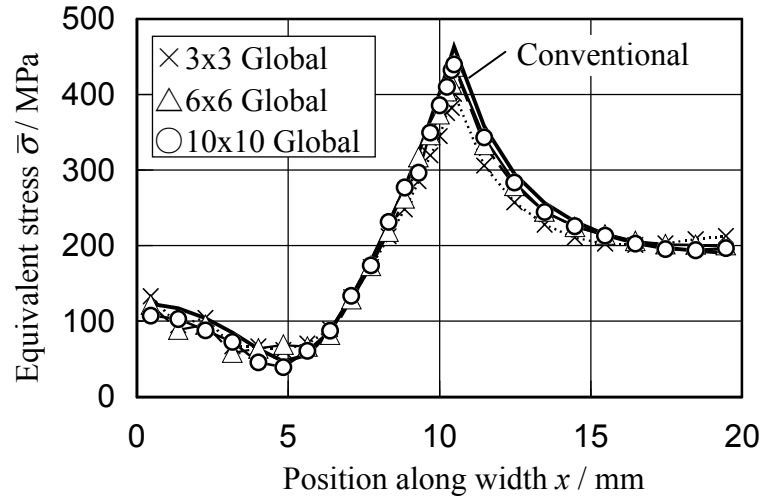

Fig. 2.14 Equivalent stress $\bar{\sigma}$ distribution of center holed plane strain elastic plate tension

2.5.4 Summary

A plane strain plate tension with a circular hole at the center was investigated to verify the features of the mesh overlay method, especially the flexibility of the mesh discretization in this section. Because of the flexibility of the mesh discretization, the orthogonal grid pattern was applied for the global mesh, and the circular mesh pattern was adopted for the local model. It was clarified that satisfactory approximate results can be obtained through the mesh overlay method, especially when the resolution of the global model is high. Furthermore, high accurate results were obtained even when the hole was not considered in the global model. Additionally, the tendency of global stress to become zero at the hole was also confirmed.

2.6 Numerical Example (Application for Homogenization Problem)

2.6.1 Introduction

In this section, as an example to enhance the features of the mesh overlay method, the trial that applies the mesh overlay method for the homogenization method[10] is considered. This idea does not always optimize computing time because adoption of the mesh overlay method is not effective when the inclusion is large compared with the size of the unit cell. However, this example can quantify the advantage of the mesh overlay method for reducing computing costs. The detail of the homogenization method is described in Appendix C.

2.6.2 Computational Conditions

A plane strain elastic plate, which includes an inclusion at the center, is considered. **Figure 2.15** shows the dimension of the plate. The plate length is $2L$ and the width is $2W$. The inclusion length is $2a$ and the width is $2b$. Elastic moduli of the matrix and the inclusion are E_0 and E_1, respectively. Poisson's ratio of the matrix and the inclusion are ν_0 and ν_1, respectively. **Table 2.10** shows the computational conditions. Body forces $\{b\}$ are ignored.

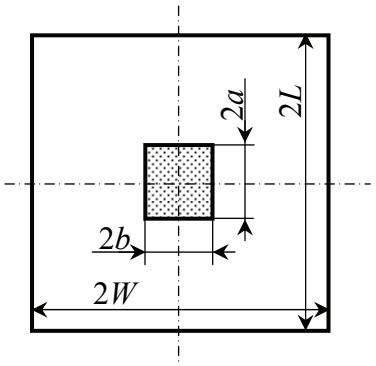

Fig. 2.15 Computational model for homogenization problem of plane strain unit cell with inclusion

Table 2.10 Computational conditions for homogenization problem of plane strain unit cell with inclusion

Aspect ratio of the plate	L/W	1	
Aspect ratio of the inclusion	a/b	1	
Normalized length of the inclusion	a/L	0.2	
Elastic modulus of the matrix	E_0	100	GPa
Elastic modulus of the inclusion	E_1	10	GPa
Poisson's ratio of the matrix	ν_0	0.30	
Poisson's ratio of the inclusion	ν_1	0.30	

Figure 2.16 shows the mesh discretization for (a) the conventional method and (b) the mesh overlay method. Here, the grayed elements express the inclusion. In the conventional analysis, the mesh discretization is 20×20. On the other hand, the global model is divided into 4×4, and the local model is divided into 10×10 in the mesh overlay analysis. According to eq. (C.4) in Appendix C, the periodic boundary condition is adopted. In the mesh overlay method, the number of Gauss points is 4×4 per element for the local element, whereas that for the global element is 2×2. That for the conventional analysis is also 2×2. Both analyses apply four-node linear isoparametric quadrilateral elements.

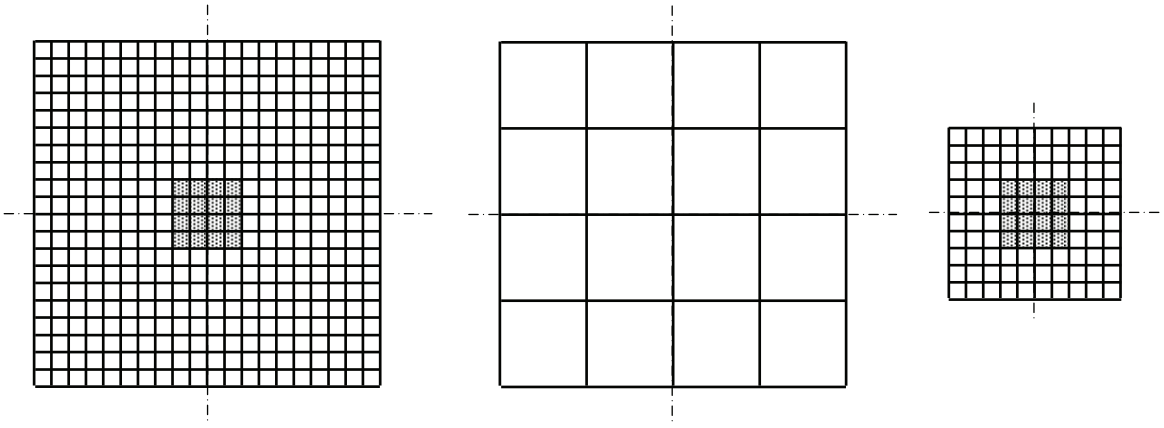

(a) Conventional FEM (b) Mesh overlay method

Fig. 2.16 Mesh discretization for homogenization problem of plane strain unit cell with inclusion

The local model for the mesh overlay method covering the inclusion and its vicinity is discretized as finely as that of the conventional analysis, while element size of the remainder for the mesh overlay method is coarser than that of the conventional analysis. Hence, a reduction in computing costs is expected.

2.6.3 Computational Results

Figures 2.17~2.1**8** show the distributions of (a) the lateral strain ε_x, (b) the longitudinal strain ε_y, (c) the shear strain ε_{xy} and (d) the equivalent strain $\bar{\varepsilon}$ for unit macro strain E_x=1 and $2E_{xy}$=1, respectively. The result obtained by the mesh overlay method is shown on the right side, and the one obtained by the conventional analysis is shown on the left side. The strain distributions for unit macro strain E_y=1 are not shown here because they can be easily obtained due to structure similarity between the *x*- and *y*-coordinate.

Good agreement is observed, although the strain distribution obtained by the conventional method is steeper than the one obtained by the mesh overlay method.

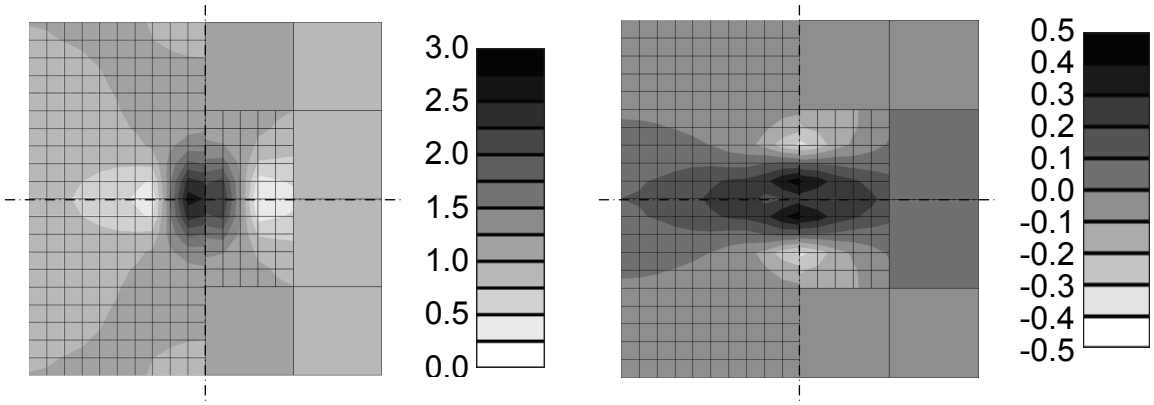

(a) Lateral strain ε_x (b) Longitudinal strain ε_y

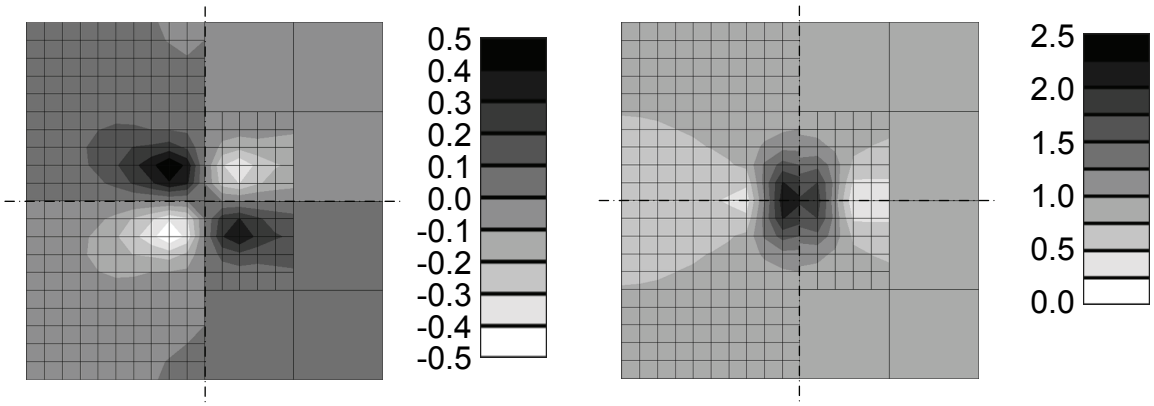

(c) Shear strain ε_{xy} (d) Equivalent strain $\bar{\varepsilon}$

Fig. 2.17 Strain distributions for unit macro strain E_x=1 for homogenization problem of plane strain unit cell with inclusion
(Mesh overlay: right side, conventional: left side)

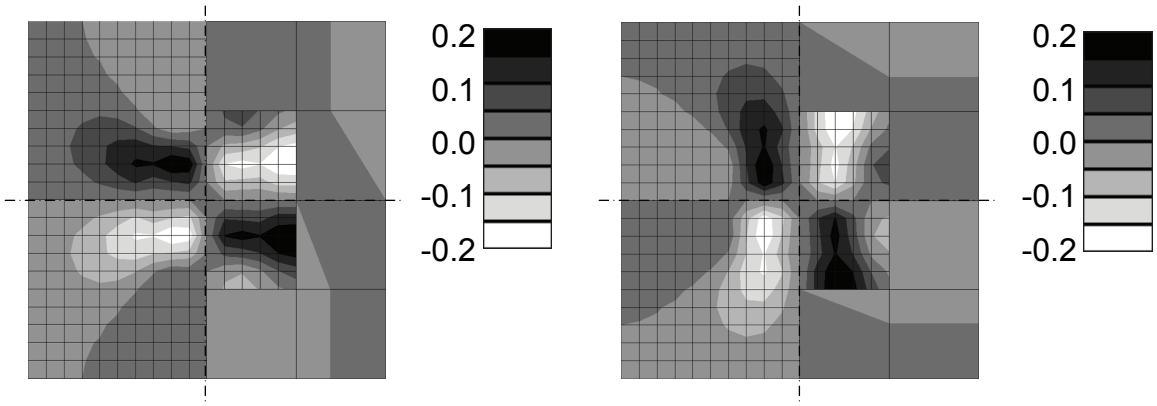

(a) Lateral strain ε_x (b) Longitudinal strain ε_y

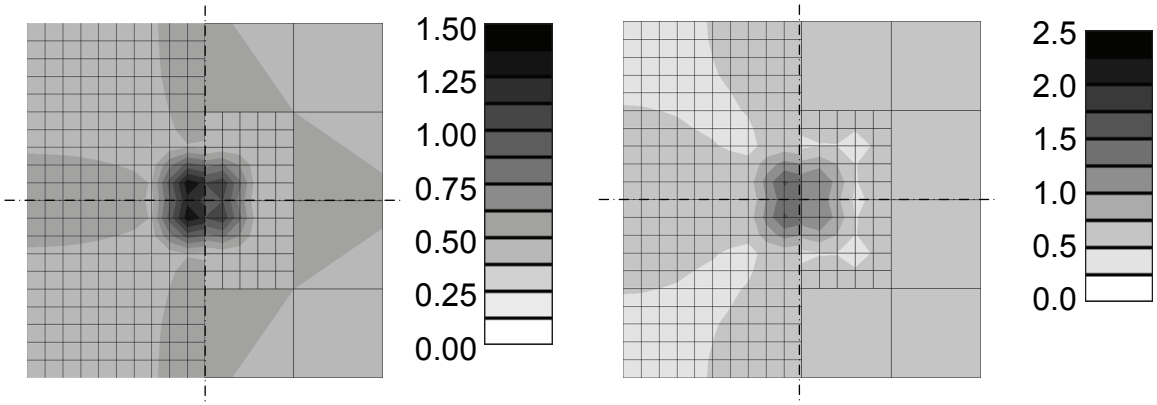

(c) Shear strain ε_{xy} (d) Equivalent strain $\bar{\varepsilon}$

Fig. 2.18 Strain distributions for unit macro strain $2E_{xy}$=1 for homogenization problem of plane strain unit cell with inclusion
(Mesh overlay: right side, conventional: left side)

Since the model structure of the x- and y-coordinate are the same, the longitudinal strain ε_y distribution for unit macro strain E_y is the same as the 90-degree rotated lateral strain ε_x distribution for unit macro strain E_x. The same relations are observed between the lateral strain ε_x distribution for unit macro strain E_y and the longitudinal strain ε_y distribution for unit macro strain E_x; between the shear strain ε_{xy} distribution for unit macro strain E_x and the one for unit macro strain E_y; and between both the longitudinal strain ε_y distribution and the lateral strain ε_x distribution for unit macro strain $2E_{xy}$.

The most important result of the homogenization problems is the homogenized

deformation matrix. The homogenized deformation matrix $[D^H]$ by the conventional analysis is shown in eq. (2.49) as the reference.

$$[D^H] = \begin{bmatrix} 122.42 & 50.949 & 0 \\ 50.949 & 122.42 & 0 \\ 0 & 0 & 34.816 \end{bmatrix} \tag{2.49}$$

Equation (2.50) gives the homogenized deformation matrix $[D^{H*}]$ obtained by the combined method of the homogenization method and the mesh overlay method.

$$[D^{H*}] = \begin{bmatrix} 123.92 & 51.708 & 0 \\ 51.708 & 123.92 & 0 \\ 0 & 0 & 35.455 \end{bmatrix} \tag{2.50}$$

On the other hand, if elastic modulus of the inclusion E_1 is regarded as the same as that of the matrix E_0, which means that the inclusion is ignored, the deformation matrix $[D^0]$ is given by eq. (2.51).

$$[D^0] = \begin{bmatrix} 134.62 & 57.692 & 0 \\ 57.692 & 134.62 & 0 \\ 0 & 0 & 38.462 \end{bmatrix} \tag{2.51}$$

Moreover, based on the volume fraction theory, the deformation matrix $[D^{H'}]$ is given by eq. (2.52).

$$[D^{H'}] = \begin{bmatrix} 129.77 & 52.615 & 0 \\ 52.615 & 129.77 & 0 \\ 0 & 0 & 37.077 \end{bmatrix} \tag{2.52}$$

Of these results, the homogenized deformation matrix $[D^{H*}]$ obtained by the present method can be recognized as the best approximate solution although each component is slightly larger than that of the reference, eq. (2.49). Additionally, the homogenization method gives more flexibility than the volume fraction theory in this condition. Since the discrepancy between the reference, eq. (2.49), and eqs. (2.51) ~ (2.52) is not small, it is concluded that the accurate deformation matrix is not able to be obtained without using

the homogenization method.

Now, let us compare calculating time because one of the most important features of the mesh overlay method is a reduction in computing costs. **Figure 2.19** shows the computing time for this example by the mesh overlay method and by the conventional analysis. The vertical axis shows calculating time normalized by that of the conventional one. The mesh overlay method calculates about five times faster than the conventional analysis for this problem. Although actual computing time for this problem is very short (a few seconds) because this problem is a two-dimensional elastic problem, this feature could become very effective when a three-dimensional or nonlinear problem is considered.

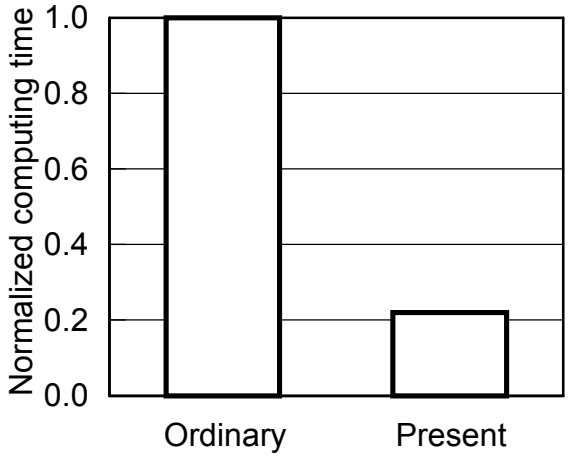

Fig. 2.19 Computing time for homogenization problem of plane strain unit cell with inclusion

2.6.4 Summary

In this section, the mesh overlay method was applied to the homogenization problem. The homogenized deformation matrix of the unit cell with an inclusion at the center under the plane strain condition was investigated. The homogenized deformation matrix obtained by the mesh overlay method gave a better approximation than the simplified approximations such as the volume fraction theory. Moreover, the computing speed vastly increased due to the adoption of the mesh overlay method.

2.7 Efficient Three-dimensional Approach

2.7.1 Introduction

The mesh overlay analysis is found to supply properly accurate solutions with reasonable computing time through numerical examples under two-dimensional conditions. There are, however, a few reports that apply the mesh overlay method for three-dimensional problems[33),34)], although three-dimensional approaches are often demanded in many practical situations. One of the reasons may be the difficulty of finding the global element that each local Gauss point belongs to under three-dimensions, called *ORIENT3D*, in order to construct the coupled stiffness matrix $[K^{GL}]$, which expresses the coupling effect between the global and local models. In fact, N. Takano et al.[35)] demonstrated three-dimensional mesh overlay analysis by using the voxel element[36)], which allows easy solving of the *ORIENT3D* problem due to its orthogonal and uniform mesh discretization.

Let us consider the simple forging process of a bulk metal that contains an inclusion or void. Since the inclusion or void degrades the quality of the metal products, analyzing its deformation behavior is one of the most interesting themes for metal forming researchers. In fact, the closure characteristic of the void in a cylindrical column under the axial symmetric condition was investigated[55)]. However, there are not so many processes that can assume the axial symmetric condition. Moreover, if the void is not on the center of the axle, the axial symmetric condition is not satisfied any more. On the other hand, quasi-static pressure in a void during the plate rolling process was analyzed[56),57)]. However, in this report, since two-dimensional analysis was applied, the void was not a sphere but a penetrated hole along the width direction. In order to simulate this problem more precisely, a three-dimensional approach was also performed[58),59)]. This approach[58)], however, is not quite practical since the diameter of the void is 6mm, whereas the thickness of the plate is 28.1mm.

An interesting mesh overlay method was proposed to acquire the stress distribution of the laminated composites along the thickness direction in which the shell elements are used for the global model; the solid elements are used for the local model[37)]. A similar

method was applied for the analysis of a through crack in a sheet[38]. However, the global shear strain was assumed to be zero in order to prevent the shear locking, and Poisson's ratio was set to zero in order to remove the adverse effects due to ignoring the vertical deformation in the shell element[60]. If the bending deformation can be neglected, the shell elements do not have to be used. In fact, there are many metal forming processes in which those macro metal flows can be represented as two-dimensional, such as simple forging or the sheet rolling process. From this point of view, the method combining a three-dimensional model for the local deformation behavior with a two-dimensional model for the macro one can achieve a good balance between high accuracy and high efficiency.

In this section, in order to enhance the features of the mesh overlay method, the mesh overlay analysis that applies a three-dimensional solid element local model with a two-dimensional solid element global model, as shown in **Fig. 2.20**, is performed.

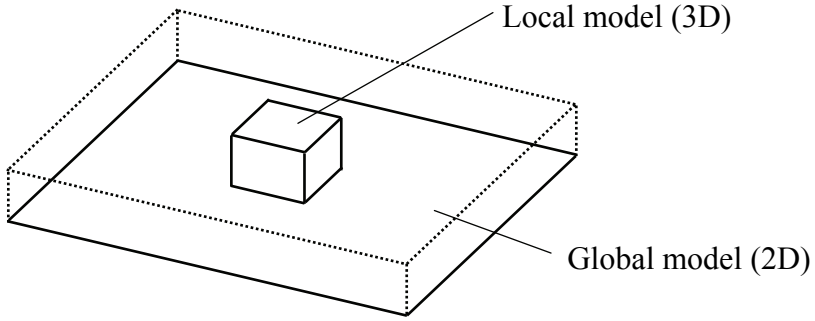

Fig. 2.20 Schematic image of present mesh overlay method that couples three-dimensional local model with two-dimensional global model

2.7.2 Formulations

Let assume that the global model is a two-dimensional model, and the local model is a three-dimensional model. In the mesh overlay formulations, the displacement $\{u\}$ at any point is expressed as the summation of the global displacement $\{u^G\}$ and the local displacement $\{u^L\}$. Therefore, the following relations are obtained:

$$u_i = u^G{}_i(x,y) + u^L{}_i(x,y,z) \tag{2.53}$$

Hence, each component of the strain vector is expressed as follows:

$$\varepsilon_i = \varepsilon^G{}_i(x,y) + \varepsilon^L{}_i(x,y,z) \tag{2.54}$$

Especially when the global model assumes the plane strain condition, eq. (2.53) is modified as follows due to the z-directional global displacement $u^G{}_z$=0:

$$u_x = u^G{}_x(x,y) + u^L{}_x(x,y,z) \tag{2.55a}$$

$$u_y = u^G{}_y(x,y) + u^L{}_y(x,y,z) \tag{2.55b}$$

$$u_z = u^L{}_z(x,y,z) \tag{2.55c}$$

Moreover, eq. (2.54) is also modified as follows:

$$\varepsilon_x = \varepsilon^G{}_x(x,y) + \varepsilon^L{}_x(x,y,z) \tag{2.56a}$$

$$\varepsilon_y = \varepsilon^G{}_y(x,y) + \varepsilon^L{}_y(x,y,z) \tag{2.56b}$$

$$\varepsilon_z = \varepsilon^L{}_z(x,y,z) \tag{2.56c}$$

$$\varepsilon_{xy} = \varepsilon^G{}_{xy}(x,y) + \varepsilon^L{}_{xy}(x,y,z) \tag{2.56d}$$

$$\varepsilon_{yz} = \varepsilon^L{}_{yz}(x,y,z) \tag{2.56e}$$

$$\varepsilon_{zx} = \varepsilon^{L}{}_{zx}(x, y, z) \tag{2.56f}$$

Although the formulations were already derived in section 2.2, constructing the coupled stiffness matrix [K^{LG}] is cumbersome. Hence, the flow of this computation is shown in the following subsection.

2.7.3 Flow of Analysis (Stiffness Matrix Construction)

The global stiffness matrix [K^{G}] and the local stiffness matrix [K^{L}] can be constructed like conventional FE analyses. However, construction of the coupled stiffness matrix [K^{LG}], the most important point of the mesh overlay method, becomes awkward due to different dimensions of the global and local models. Here, the flow of stiffness matrix construction is depicted as follows.

Gauss points for each element are given. If Gauss point is for a global element, construct the global stiffness matrix [K^{G}] and go to the next Gauss point. If the Gauss point is for a local element, construct the coupled stiffness matrix [K^{LG}] and [K^{GL}] as well as the local stiffness matrix [K^{L}]. In order to construct the coupled stiffness matrix [K^{LG}], the strain-nodal displacement matrix for the global element [B^{G}] of the local Gauss point is necessary as shown in eq. (2.34b). The strain-nodal displacement matrix for the global element [B^{G}] is calculated according to the following steps. First, find the global element that the Gauss point overlays. Here, the z-coordinate is not needed since the global model is a two-dimensional model. Next, calculate (ξ^{G}, η^{G}), the natural coordinates of the local Gauss point for the overlaid global element. Since the natural coordinates are obtained, the strain-nodal displacement matrix for the global element [B^{G}] that is computed for the local Gauss point can be calculated. Hence, the coupled stiffness matrix [K^{LG}] can be computed. The transposed matrix of the coupled stiffness matrix [K^{LG}] is [K^{GL}]. Then, go to the next Gauss point. The flow is shown in **Fig. 2.21**.

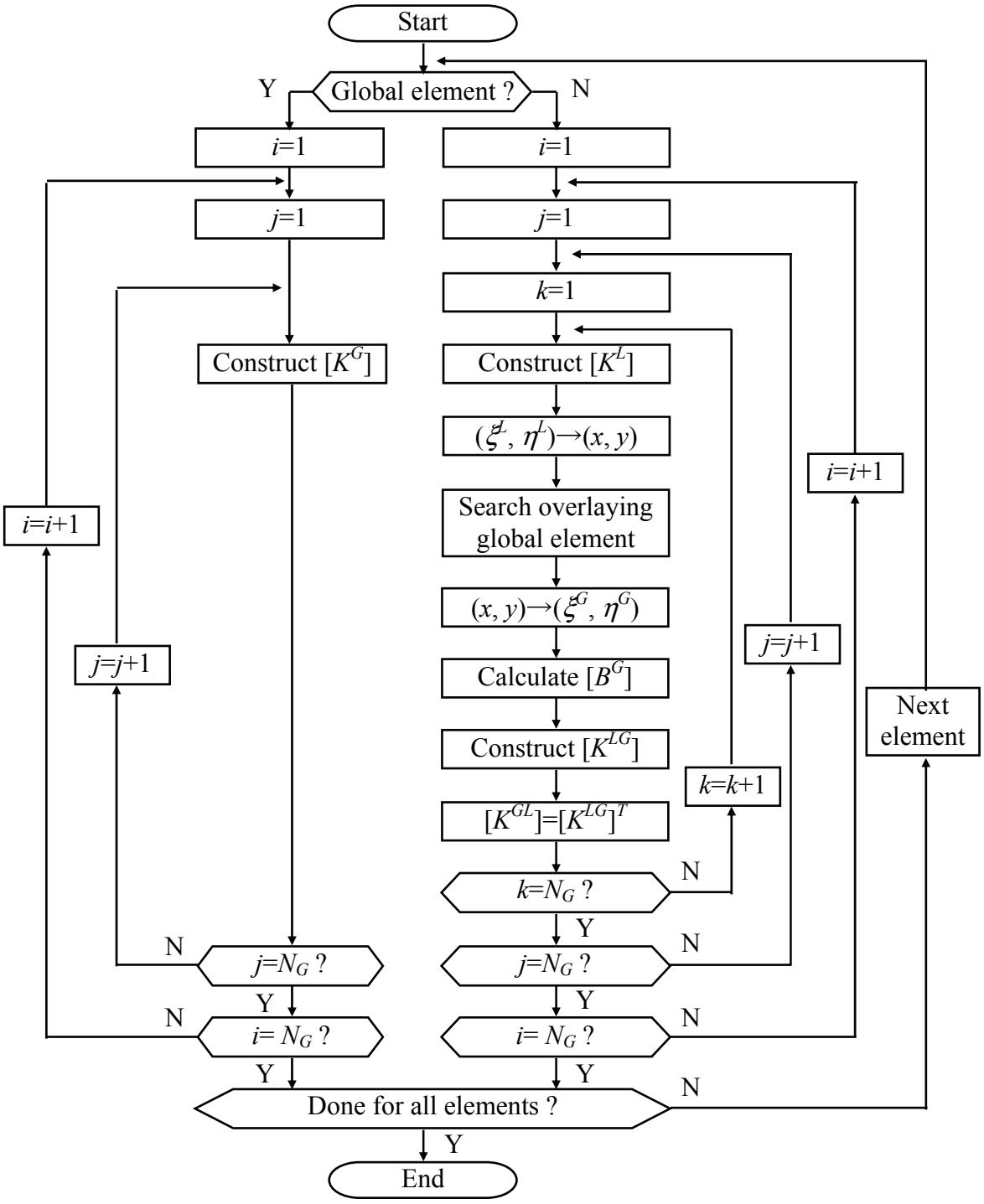

Fig. 2.21 Flow for constructing stiffness matrix [K] for present analysis (N_G: No. of Gauss points along an axis per element)

2.7.4 Computational Conditions

In order to verify the present method, a cube with a spherical inclusion at the center is considered, as shown in **Fig. 2.22**. The inclusion has one-tenth shorter diameter than the side of the cube and one-tenth smaller Young's modulus than the matrix. A uniform longitudinal displacement is given and no shear forces are applied on the boundary, $y=\pm L$. The z-directional displacement $u_z=0$ is also imposed at $z=\pm L$. The computational conditions are shown in **Table 2.11**.

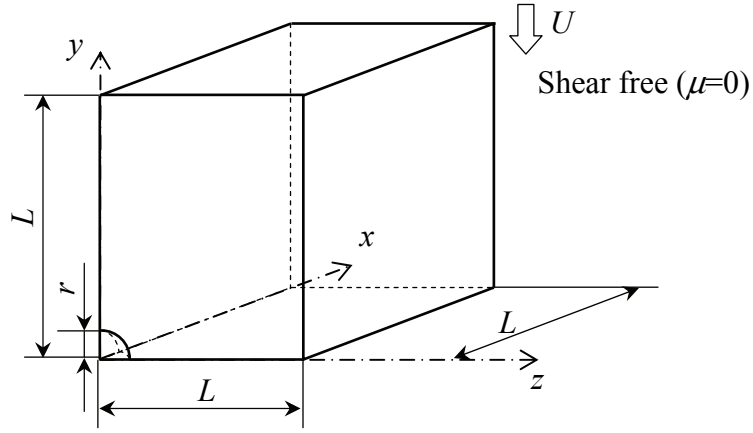

Fig. 2.22 Computational model of elastic block compression with spherical inclusion

Table 2.11 Computational conditions of elastic block compression with spherical inclusion

Normalized length of inclusion	r/L	0.10	
Nominal longitudinal displacement	U/L	0.001	
Young's modulus of matrix	E_0	205.8	GPa
Young's modulus of inclusion	E_1	20.6	GPa
Poisson's ratio	ν	0.3	

The global model has 2×2 mesh discretization with four-node linear isoparametric quadrilateral elements, and the local model has $10\times10\times10$ mesh discretization with

eight-node linear isoparametric hexahedral elements for the mesh overlay analysis, as shown in **Fig. 2.23**. **Figure 2.24** shows the mesh discretization for the conventional analysis that applies with 20×20×20 meshes with eight-node linear isoparametric hexahedral elements. Here, the grayed mesh means the inclusion. The local element for the mesh overlay analysis has the same dimensions as the element of the conventional analysis. Therefore, the local model covers only one-eighth the volume of the whole system. The number of Gauss points is 2×2 per element for the global model and 4×4 ×4 for the local model, respectively. That for the conventional analysis is 2×2 per element.

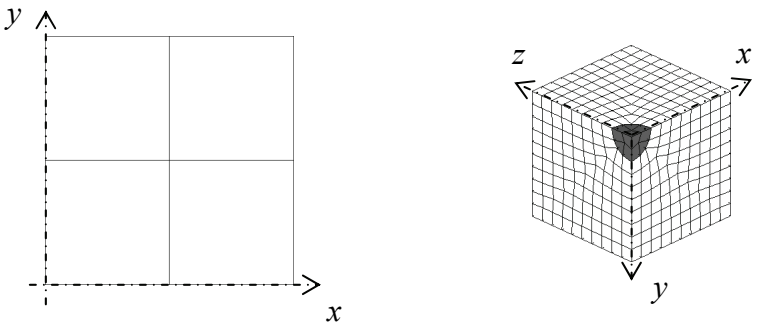

(a) Global model (b) Local model

Fig. 2.23 Mesh discretization for mesh overlay method of elastic block compression with spherical inclusion

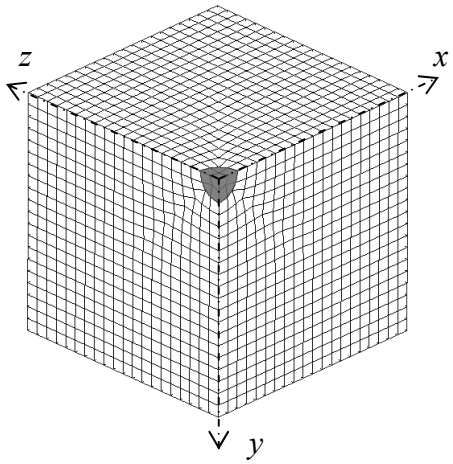

Fig. 2.24 Mesh discretization for conventional method of elastic block compression with spherical inclusion

A plane strain condition along the z-direction is assumed for the global model, and the boundary conditions, the local displacements $d_x^L=d_y^L=d_z^L=0$ on the global-local boundary for the local model, are imposed. For the conventional analysis, the boundary conditions, the z-displacement $d_z=0$ on $z=\pm L$, are also imposed although each element can deform along the z-direction.

2.7.5 Computational Results

Figure 2.25 shows the x-directional strain ε_x distributions by (a) the conventional analysis and (b) the mesh overlay analysis, respectively. Only the local model is shown in the distributions of the mesh overlay analysis. These figures only show $x\geq 0$, $y\geq 0$ and $z\geq 0$ due to the symmetry of the deformation, and the direction of view is from (-1, -1, -1) toward (0, 0, 0). Therefore, the top shown at the center of the figures is the origin. Here, $2\times 2\times 2$ elements near the origin express the inclusion that has one-tenth lower Young's modulus than the matrix.

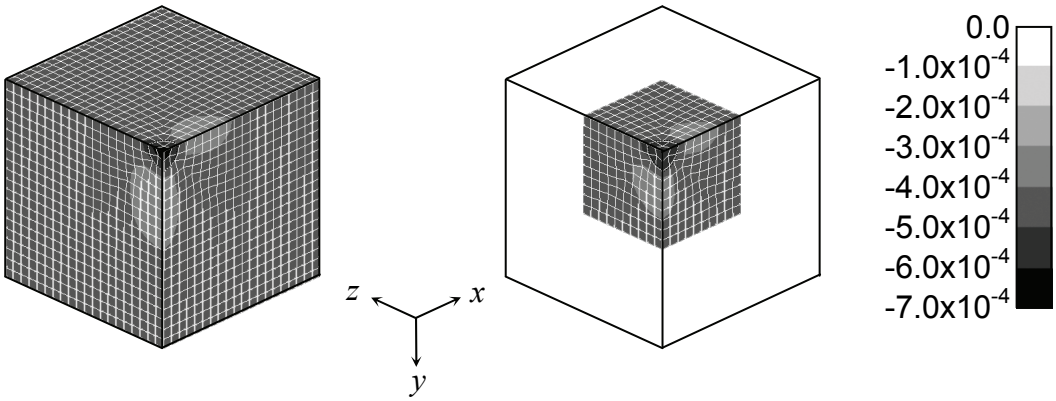

(a) Conventional (b) Mesh overlay

Fig. 2.25 x-directional strain ε_x distributions of elastic block compression with spherical inclusion

Both results represent features of the deformation. That is, strain concentrates at the inclusion and its vicinity. Additionally, due to the deformation concentration, smaller strain area can also be seen near the inclusion along the x-axis and y-axis. The strain distribution obtained by the mesh overlay analysis is close to that by the conventional analysis.

In order for quantitative comparison, the standard deviation of each strain component, $\Delta\varepsilon_i$, in the local area is defined by eq. (2.57).

$$\Delta\varepsilon_i = \sqrt{\frac{\sum_{j=1}^{N_L}\{\varepsilon_i(j)-\varepsilon_i^*(j)\}^2}{N_L}} \tag{2.57}$$

Here, $\varepsilon_i(j)$ and $\varepsilon_i^*(j)$ express the i-th component of the strain vector at the j-th element by the mesh overlay analysis and the one at the corresponding element by the conventional analysis, respectively. N_L is the number of elements in the local model for the mesh overlay analysis.

The standard deviation of the x-directional strain $\Delta\varepsilon_x$ is 4.0×10^{-6}; the average is -4.3×10^{-4}. Hence, high accuracy of the present analysis is also verified.

The distributions of the y-directional strain ε_y by (a) the conventional analysis and (b) the mesh overlay analysis are shown in **Fig. 2.26**, respectively. Both results are close and show the feature of the deformation. That is, strain concentrates at the inclusion, and a smaller strain area can be also seen at the vicinity of the inclusion along the y-axis. The standard deviation of the y-directional strain $\Delta\varepsilon_y$ is 6.3×10^{-6}, which is small compared to its average, 1.0×10^{-3}.

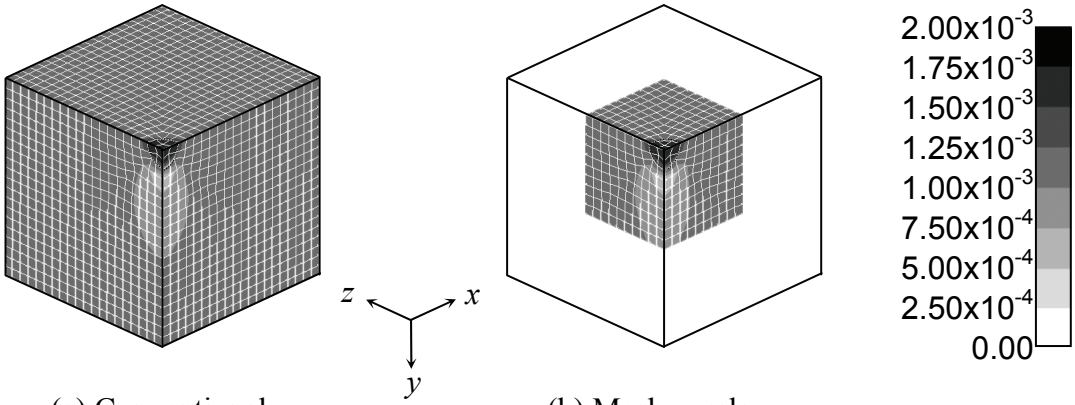

(a) Conventional (b) Mesh overlay

Fig. 2.26 y-directional strain ε_y distributions of elastic block compression with spherical inclusion

Figure 2.27 represents the z-directional strain ε_z distributions by (a) the conventional analysis and (b) the mesh overlay analysis, respectively. Both results describe a positive z-directional strain concentration at the inclusion and its vicinity along the y-axis, and a negative one along the z-axis to compensate for deformation at the inclusion. The distribution by the mesh overlay analysis shows good agreement with that by the conventional analysis, although the standard deviation of the z-directional strain $\Delta\varepsilon_z$ is not small, 2.3×10^{-6}, compared to the average of its magnitude, 5.6×10^{-6}.

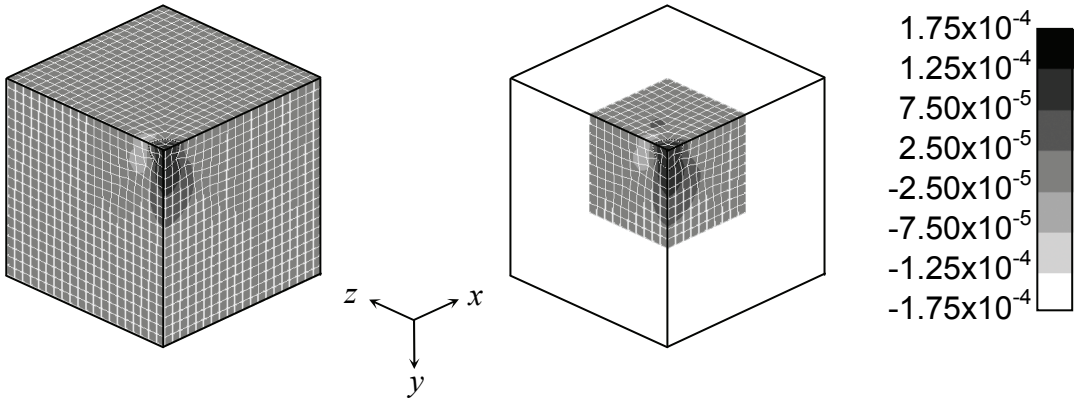

(a) Conventional (b) Mesh overlay

Fig. 2.27 z-directional strain ε_z distributions of elastic block compression with spherical inclusion

The xy-shear strain ε_{xy} distributions are shown in **Fig. 2.28** by (a) the conventional analysis and (b) the mesh overlay analysis, respectively. Positive xy-shear strain ε_{xy} is shown at the adjacent region of the inclusion along the x-axis and negative xy-shear strain ε_{xy} is also observed along the y-axis. The standard deviation of the xy-shear strain $\Delta\varepsilon_{xy}$ is 4.4×10^{-6}, and the average of its magnitude is 1.3×10^{-5}.

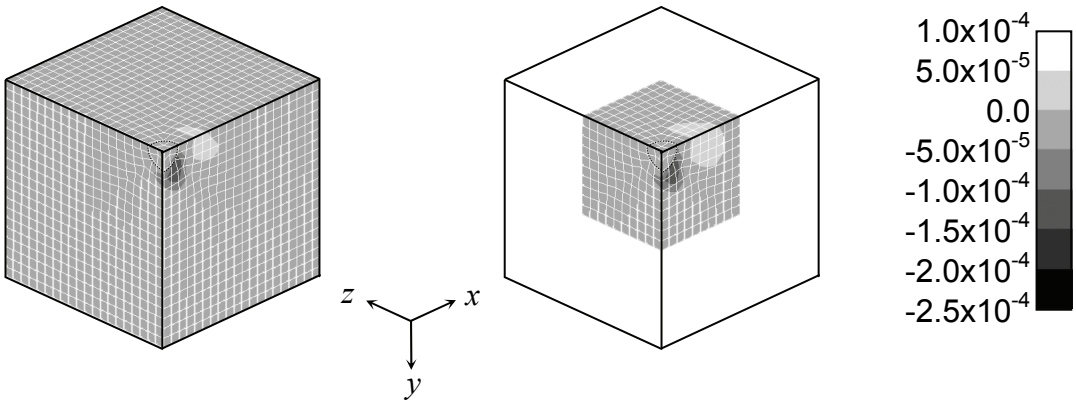

(a) Conventional (b) Mesh overlay

Fig. 2.28 *xy*-shear strain ε_{xy} distributions of elastic block compression with spherical inclusion

Figure 2.29 expresses the *yz*-shear strain ε_{yz} distributions by (a) the conventional analysis and (b) the mesh overlay analysis, respectively. Negative *yz*-shear strain ε_{yz} is represented at the adjacent region of the inclusion on the *yz*-plane. The standard deviation of the *yz*-shear strain $\Delta\varepsilon_{yz}$ is 5.6×10^{-6}, while the average of its magnitude is 1.4×10^{-5}.

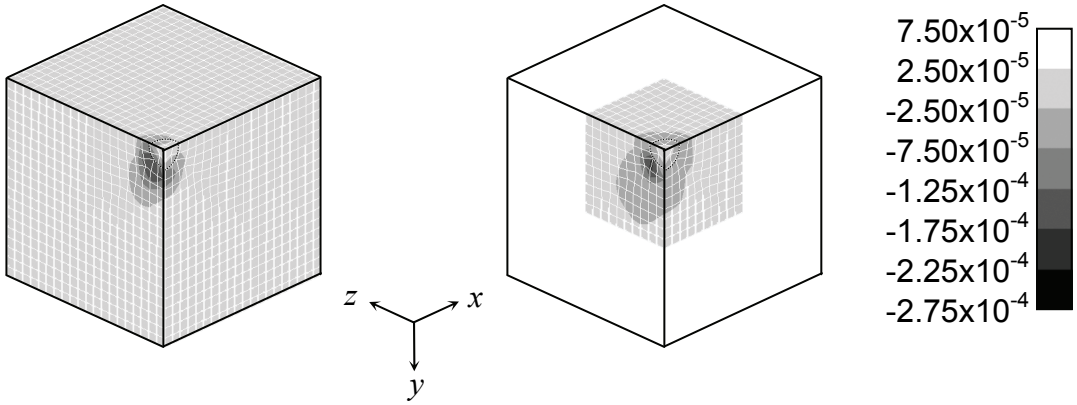

(a) Conventional (b) Mesh overlay

Fig. 2.29 *yz*-shear strain ε_{yz} distributions of elastic block compression with spherical inclusion

Figure 2.30 shows the *zx*-shear strain ε_{zx} distributions by (a) the conventional analysis and (b) the mesh overlay analysis, respectively. Positive *zx*-shear strain ε_{zx} is

represented at the adjacent region of the inclusion on the *zx*-plane. Negative *zx*-shear strain ε_{zx} is observed at its adjacent region on the *xy*-plane and *yz*-plane. The standard deviation of the *zx*-shear strain $\Delta\varepsilon_{zx}$ is 3.0×10^{-6}, and the average of its magnitude is 7.0×10^{-6}.

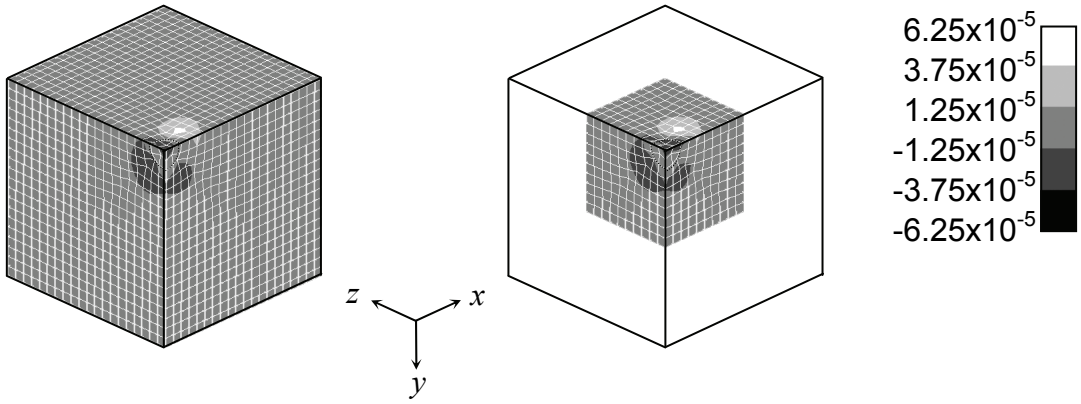

(a) Conventional (b) Mesh overlay

Fig. 2.30 *zx*-shear strain ε_{zx} distributions of elastic block compression with spherical inclusion

The equivalent strain $\bar{\varepsilon}$ distributions by (a) the conventional analysis and (b) the mesh overlay analysis are represented in **Fig. 2.31**, respectively. Both results represent the feature of the deformation, strain concentration at and around the inclusion. The standard deviation of the equivalent strain $\Delta\bar{\varepsilon}$ is 5.8×10^{-6}, and its average is 9.0×10^{-4}.

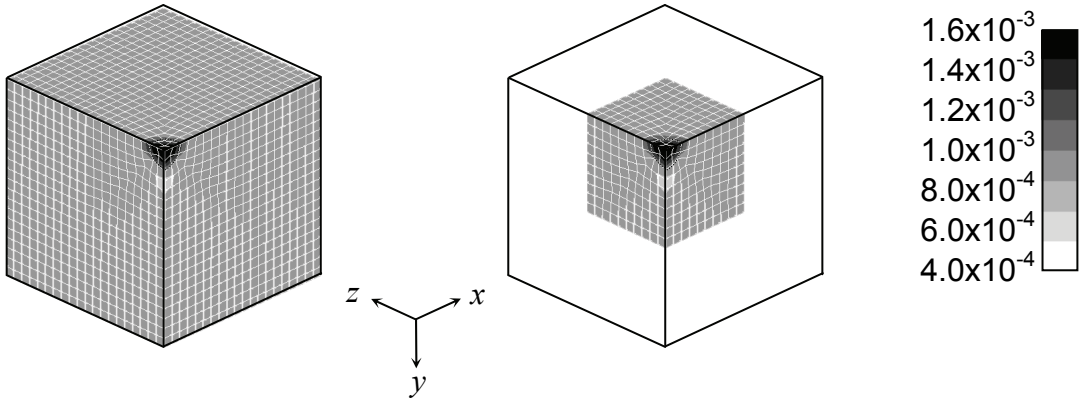

(a) Conventional (b) Mesh overlay

Fig. 2.31 Equivalent strain $\bar{\varepsilon}$ distributions of elastic block compression with spherical inclusion

However, the mesh overlay method gives milder strain distributions than the conventional FE analysis, as shown in Figs. 2.25~2.31. The reason why the mesh overlay analysis can not represent steeper strain distributions may be the local model size and/or the global model resolution. Hence, if a larger local model and/or a finer global model is adopted, the accuracy of the mesh overlay analysis will increase.

2.7.6 Summary

In this section, the mesh overlay method that applies a three-dimensional local model with a two-dimensional global model was proposed as an efficient three-dimensional analysis. Although the formulations are the same as the two-dimensional case, the flows of computations may be difficult to encode. Hence, the flow of the stiffness matrix construction was shown in detail.

A simple compression problem of a block that contains a small spherical inclusion at the center was considered to verify the present method, since the inclusion is not a long bar along the *z*-direction but a small sphere that requires a three-dimensional analysis. That is, the local model, a three-dimensional model, covers the inclusion and its vicinity only, whereas the global model, a two-dimensional model, covers whole system. The numerical simulation shows that the present mesh overlay analysis gives results close to conventional three-dimensional FE analysis. Therefore, the present mesh overlay method that combines a two-dimensional global model and a three-dimensional local model can be regarded as an efficient three-dimensional analytical method.

2.8 Conclusions

Formulations of the mesh overlay method for elastic problems were reviewed. The main features of the mesh overlay method are (1) the coupled analysis between the global and local models, and (2) the flexibility of mesh discretization.

Before performing the mesh overlay analysis, the relation between solution accuracy and convergence criterion when the iterative method is applied to solve the stiffness equations was investigated. The computations achieved the following results:

(1) The pre-conditioned conjugate gradient method gives faster convergence than the conjugate gradient method due to its scaling. However, scaling does not significantly increase solution accuracy.

(2) The iterative method may fail to achieve accurate results if the convergence criterion is not strict. Therefore, the convergence criterion should be carefully selected especially when the order of the solutions as well as the components of the coefficient matrix distribute widely like the mesh overlay analysis. However, it is not clear how the convergence criterion should be decided in advance.

Moreover, from the view points of the nonlinear analysis, if the assumed velocity fields are not suitable, the stiffness matrix may not become positive definite. According to these considerations, this research concluded that the direct method is most suitable for the mesh overlay analysis. Hence, the direct method is adopted to solve the stiffness equations in this research.

Then, the features of the mesh overlay method were verified through the numerical examples as follows:

(1) Adequate approximate results can be obtained through the mesh overlay method.

(2) The inclination to diminish the global strain and the global stress in the region where the local material constants differ from the global material constants

(3) The mesh overlay method and the homogenization method, the objective of which is to obtain the effective (homogenized) value of a parameter for heterogeneous media, were combined to verify one of the most important features of the mesh overlay method, computing cost reduction.

In addition,

(4) The mesh overlay method that applies a three-dimensional local model with a two-dimensional global model was proposed as an efficient three-dimensional analysis. A simple compression problem of a block that contains a small inclusion at the center was considered to verify the present method, since the inclusion is not a long bar along the *z*-direction but a small sphere that requires a three-dimensional analysis. That is, the local model, a three-dimensional model, covers the inclusion and its vicinity only, while the global model, a two-dimensional model, covers whole system. According to the numerical simulation, it was shown that the present mesh overlay analysis gives results close to conventional FE analysis.

However, in order to decide (1) the size of the local model and (2) the resolution of the global model, a certain amount of trial and error is still required. Therefore, some advance guidelines are needed for deciding an appropriate constraint and for estimating their accuracy following the analysis. These are future areas for this research.

Chapter 3

Mesh Overlay Method for Rigid-plastic Problems

3.1 Introduction

The formulations and numerical results obtained in the previous chapter were derived based on elastic theory. However, most concerns about material deformation during the metal forming process involve plastic deformation. Therefore, extending the mesh overlay method into plastic analysis is demanded for practical applications to the metal forming processes.

Before considering the application of the mesh overlay method into plastic analysis, I will review the methods for investigating plastic deformation behavior. There are two numerical analytical theories for plastic deformation behavior[61]. One is the elasto-plastic theory (the solid formulation), and the other is the rigid-plastic theory (the flow formulation). The elasto-plastic theory considers both elastic and plastic deformation. In contrast, the rigid-plastic theory ignores elastic deformation. If the strain during deformation is comparable to the elastic strain, elastic deformation must be considered in the analysis. For example, consider the skin pass (temper) rolling process, the purpose of which is to reduce the stretcher-strain and/or to temper mechanical characteristics. Since its reduction is only 0.5~2.0%, it is impossible to ignore elastic deformation behavior during the skin pass rolling process. Therefore, an elasto-plastic analysis is required to investigate the deformation behavior of the stock during the skin pass rolling. However, elastic strain is negligible when the strain during deformation becomes large. In this situation, the rigid-plastic theory, which has shorter computing time due to its ability to adopt larger time increments, is applicable. In fact, rigid-plastic analysis is still used to clarify the deformation behavior of the stock during the metal forming processes[62),63)]. Since large plastic deformation will be focused on, this research applies the rigid-plastic theory. A large number of research studies have been

dedicated to improving various aspects of the metal forming conditions and clarifying the deformation characteristics of the stock for the metal forming process.

However, recent concerns for the metal forming process, surface quality of the products for example, require finer resolution in relatively large computational models. For instance, the mechanism of the surface roughness transcription during the rolling process was also investigated through the FE simulations[21]. A numerical simulation of the oxide scale deformation behavior at the entry of the roll bite during the hot rolling process was also performed[22]. However, they assumed two-dimensional conditions, although surface configurations, in general, have three-dimensional shapes. In addition, they applied the zooming method. As described before, since the zooming method is an uncoupled analysis between the macro and micro models, the obtained solution will have some errors.

The mesh overlay method seems to be an effective theory to simulate such problems requiring coupling of the macro and micro models, especially when there are large differences between the scales of the two models. However, few reports applied the mesh overlay method for nonlinear problems[25),39]. An interesting method to analyze an elasto-plastic problem using the mesh overlay method was proposed[40]. In this method, the local model covers at least the plastic deformation region. That is, deformation in the region covered only by the global model is limited to elastic deformation. Therefore, although the local model is analyzed based on the elasto-plastic theory, the constitutive equations for the global model are based on the elastic theory. Due to this treatment, the calculating algorithm becomes simple. However, when plastic deformation occurs in most areas, this method is no longer functional. Moreover, these analyses assumed linearity at each time step in order to omit the iteration required to obtain the converged solutions.

In this chapter, the extension of the mesh overlay method into the rigid-plastic analysis is considered. First, the formulations of the mesh overlay method based on the rigid-plastic theory are derived. Since plastic deformation behavior is nonlinear, an iterative method should be adopted to calculate plastic deformation behavior. Hence, the formulations are shown as a rate form. Numerical examples are shown to verify the

accuracy of the rigid-plastic mesh overlay formulations. Finally, the combined analysis of a two-dimensional global model and a three-dimensional local model, as described in the previous chapter, is also performed for the rigid-plastic problems.

3.2 Formulations of Rigid-Plastic Mesh Overlay Method

3.2.1 Global Stiffness Matrix Evaluation

In Chapter 2, the mesh overlay formulations for elastic materials were derived. In the numerical example shown in Fig.2.8, the global strain tends to be zero where the material constants for the global model and those for the local model are different. S. Nakasumi et al.[40] has already demonstrated this phenomenon through numerical examples, and verified its cause by using the equilibrium of the normal stress at the boundary between the different materials. In this research, certification based on the equilibrium of the strain energy is derived.

In the mesh overlay formulations, the following assumption, already shown as eqs. (2.20) ~ (2.22), is adopted:

$$\begin{aligned}\frac{\partial \Pi_E}{\partial d^G{}_i} &= \int_{\Omega^G} B^G{}_{ki} D^G{}_{kl} B^G{}_{ln} d\Omega d^G{}_n \\ &\quad + \int_{\Omega^L} B^G{}_{ki} D^L{}_{kl} B^G{}_{ln} d\Omega d^G{}_n + \int_{\Omega^L} B^G{}_{ki} D^L{}_{kl} B^L{}_{ln} d\Omega d^L{}_n \\ &\cong \int_{\Omega} B^G{}_{ki} D^G{}_{kl} B^G{}_{ln} d\Omega d^G{}_n + \int_{\Omega^L} B^G{}_{ki} D^L{}_{kl} B^L{}_{ln} d\Omega d^L{}_n \end{aligned} \tag{3.1}$$

In order to satisfy this simplification, the following relation is required.

$$\int_{\Omega^L} B^G{}_{ki} D^L{}_{kl} B^G{}_{ln} d\Omega d^G{}_n = \int_{\Omega^L} B^G{}_{ki} D^G{}_{kl} B^G{}_{ln} d\Omega d^G{}_n \tag{3.2}$$

Equation (3.2) can be modified as follows:

$$\int_{\Omega^L} B^G{}_{ki} D^L{}_{kl} \varepsilon^G{}_l d\Omega - \int_{\Omega^L} B^G{}_{ki} D^G{}_{kl} \varepsilon^G{}_l d\Omega = 0 \tag{3.3}$$

That is,

$$\int_{\Omega^L} B^G{}_{ki} (D^L{}_{kl} - D^G{}_{kl}) \varepsilon^G{}_l d\Omega = 0 \tag{3.4}$$

If the local elastic deformation matrix $D^L{}_{ij}$ is the same as the global elastic deformation matrix $D^G{}_{ij}$, eq. (3.4) is always satisfied. Therefore, the global strain $\varepsilon^G{}_i$ does not have to be zero. However, if the local elastic deformation matrix $D^L{}_{ij}$ and the

global elastic deformation matrix D^G_{ij} disagree, the global strain ε^G_i should be zero to satisfy the eq. (3.4). Therefore, the global strain ε^G_i tends to be zero where the material constants for the local element and those for the overlaid global element are different.

Now, let us consider the rigid-plastic problems. The deformation matrix [D] is a function of the equivalent strain rate $\dot{\bar{\varepsilon}}$ and the equivalent stress $\bar{\sigma}$ in the rigid-plastic formulations. Of course, the equivalent stress $\bar{\sigma}$ is also a function of the equivalent strain rate $\dot{\bar{\varepsilon}}$, the equivalent strain $\bar{\varepsilon}$ and the material constants: the deformation resistance K, the strain hardening index n and the strain rate sensitivity index m. Clearly, the equivalent strain rate $\dot{\bar{\varepsilon}}$, the equivalent strain $\bar{\varepsilon}$ and the equivalent stress $\bar{\sigma}$ for the global model and those for the local model are, in general, different. Therefore, the local deformation matrix [D^L] and the global deformation matrix [D^G] for the overlaid element become also different. Hence, the global strain rate $\dot{\varepsilon}^G_i$ would tend to be zero in the local region Ω^L, which invites numerical instability due to the zero-dividing. This occurs because the denominator of the deformation matrix includes the equivalent strain rate $\dot{\bar{\varepsilon}}$, if the simplification that uses the global deformation matrix [D^G] in the local region Ω^L instead of the local deformation matrix [D^L] was applied in the mesh overlay formulations for the rigid-plastic problems. In other words, it is concluded that the global stiffness matrix [K^G] in the local region Ω^L should be evaluated by the local model in order to avoid this tendency. Additionally, because of this arrangement, the possibility of the negative strain energy occurrence[53] is also dissolved. Therefore, the mesh overlay method can be applied without any concerns even when the local model is harder than the global model.

There are some reports that do not apply the simplification in the mesh overlay formulations. For example, S. Wang et al.[29] avoids the simplifications to increase the accuracy of the integration at the global-local boundary for structural optimization for elastic materials. Moreover, N. Takano et al.[35] shows the mesh overlay formulations for elastic problems that do not apply the simplification, although the reason why the simplifications are not applied has not been described, and their later reports[64] adopt the simplifications. However, there seem to be no suggestions that shows this simplification should not be applied for nonlinear mesh overlay analyses.

3.2.2 Stiffness Equations

In this subsection, the formulations of the mesh overlay method based on the rigid-plastic theory are derived. The definitions of the symbols are the same as those in the previous chapter.

Since the rigid-plastic formulations are shown as a rate form due to its nonlinearity, the velocity v_i is defined as the summation of the global velocity $v^G{}_i$ and the local velocity $v^L{}_i$ in the mesh overlay method, as shown in eq. (3.5).

$$v_i \equiv \begin{cases} v^G{}_i & in \quad \Omega^G \\ v^G{}_i + v^L{}_i & in \quad \Omega^L \end{cases} \tag{3.5}$$

Here, the global velocity $v^G{}_i$ and the local velocity $v^L{}_i$ are obtained from the global and local models, respectively. In order to satisfy the C^0 continuity of velocity v_i, the local velocity $v^L{}_i$ is set to be zero on the global-local boundary Γ^{GL}.

$$v^L{}_i = 0 \quad on \quad \Gamma^{GL} \tag{3.6}$$

In accordance with the FEM formulations[43),44)], the global velocity $v^G{}_i$ is expressed in eq. (3.7) by using the global nodal velocity $\dot{d}^G{}_j$ and the global shape function matrix $N^G{}_{ij}$.

$$v^G{}_i = N^G{}_{ij} \dot{d}^G{}_j \tag{3.7}$$

Similarly, the local velocity $v^L{}_i$ is represented by the local nodal velocity $\dot{d}^L{}_j$ and the local shape function matrix $N^L{}_{ij}$:

$$v^L{}_i = N^L{}_{ij} \dot{d}^L{}_j \tag{3.8}$$

Then, strain rate $\dot{\varepsilon}_{ij}$ is described by eq. (3.9) in the mesh overlay method. In eq. (3.9), the global strain rate $\dot{\varepsilon}^G{}_{ij}$ and the local strain rate $\dot{\varepsilon}^L{}_{ij}$ are also defined.

$$\dot{\varepsilon}_{ij} = \begin{cases} \dfrac{\partial v^G{}_i}{\partial x_j} \equiv \dot{\varepsilon}^G{}_{ij} & in \quad \Omega^G \\ \dfrac{\partial v^G{}_i}{\partial x_j} + \dfrac{\partial v^L{}_i}{\partial x_j} \equiv \dot{\varepsilon}^G{}_{ij} + \dot{\varepsilon}^L{}_{ij} & in \quad \Omega^L \end{cases} \tag{3.9}$$

Although the global strain rate $\dot{\varepsilon}_{ij}$ is a 3×3 matrix, the number of the independent components is only six. As opposed to the more complex matrix equation, the global strain rate vector $\dot{\varepsilon}^G{}_i$ is defined as a vector form in this report:

$$\begin{cases} \dot{\varepsilon}^G{}_1 = \dot{\varepsilon}^G{}_x \\ \dot{\varepsilon}^G{}_2 = \dot{\varepsilon}^G{}_y \\ \dot{\varepsilon}^G{}_3 = \dot{\varepsilon}^G{}_z \\ \dot{\varepsilon}^G{}_4 = 2\dot{\varepsilon}^G{}_{xy} \\ \dot{\varepsilon}^G{}_5 = 2\dot{\varepsilon}^G{}_{yz} \\ \dot{\varepsilon}^G{}_6 = 2\dot{\varepsilon}^G{}_{zx} \end{cases} \tag{3.10a}$$

or, in the matrix description:

$$\{\dot{\varepsilon}^G\} \equiv \{\dot{\varepsilon}^G{}_x \quad \dot{\varepsilon}^G{}_y \quad \dot{\varepsilon}^G{}_z \quad 2\dot{\varepsilon}^G{}_{xy} \quad 2\dot{\varepsilon}^G{}_{yz} \quad 2\dot{\varepsilon}^G{}_{zx}\}^T \tag{3.10b}$$

The local strain rate vector $\dot{\varepsilon}^L{}_i$ is also expressed as a vector form:

$$\begin{cases} \dot{\varepsilon}^L{}_1 = \dot{\varepsilon}^L{}_x \\ \dot{\varepsilon}^L{}_2 = \dot{\varepsilon}^L{}_y \\ \dot{\varepsilon}^L{}_3 = \dot{\varepsilon}^L{}_z \\ \dot{\varepsilon}^L{}_4 = 2\dot{\varepsilon}^L{}_{xy} \\ \dot{\varepsilon}^L{}_5 = 2\dot{\varepsilon}^L{}_{yz} \\ \dot{\varepsilon}^L{}_6 = 2\dot{\varepsilon}^L{}_{zx} \end{cases} \tag{3.11a}$$

or, in the matrix description:

$$\{\dot{\varepsilon}^L\} \equiv \{\dot{\varepsilon}^L{}_x \quad \dot{\varepsilon}^L{}_y \quad \dot{\varepsilon}^L{}_z \quad 2\dot{\varepsilon}^L{}_{xy} \quad 2\dot{\varepsilon}^L{}_{yz} \quad 2\dot{\varepsilon}^L{}_{zx}\}^T \tag{3.11b}$$

The global strain rate vector $\dot{\varepsilon}^G{}_i$ is expressed by the global strain rate-nodal velocity matrix $B^G{}_{ij}$ and the global nodal velocity $\dot{d}^G{}_j$.

$$\dot{\varepsilon}^G{}_i = B^G{}_{ij}\dot{d}^G{}_j \tag{3.12a}$$

or, in the matrix description:

$$\{\dot{\varepsilon}^G\} = [B^G]\{\dot{d}^G\} \tag{3.12b}$$

Similarly, the local strain rate vector $\dot{\varepsilon}^L{}_i$ is represented by the local strain rate-nodal velocity matrix $B^L{}_{ij}$ and the local nodal velocity $\dot{d}^L{}_j$.

$$\dot{\varepsilon}^L{}_i = B^L{}_{ij}\dot{d}^L{}_j \tag{3.13a}$$

or, in the matrix description:

$$\{\dot{\varepsilon}^L\} = [B^L]\{\dot{d}^L\} \tag{3.13b}$$

The global volumetric strain rate $\dot{\varepsilon}_V{}^G$ is defined as follows:

$$\begin{aligned}\dot{\varepsilon}_V{}^G &= \dot{\varepsilon}^G{}_x + \dot{\varepsilon}^G{}_y + \dot{\varepsilon}^G{}_z \\ &= B^G{}_{1i}\dot{d}^G{}_i + B^G{}_{2i}\dot{d}^G{}_i + B^G{}_{3i}\dot{d}^G{}_i \\ &= (B^G{}_{1i} + B^G{}_{2i} + B^G{}_{3i})\dot{d}^G{}_i \\ &\equiv C^G{}_i\dot{d}^G{}_i\end{aligned} \tag{3.14a}$$

or, in the matrix description:

$$\dot{\varepsilon}_V{}^G = \{C^G\}^T\{\dot{d}^G\} \tag{3.14b}$$

Similarly, the local volumetric strain rate $\dot{\varepsilon}_V{}^L$ is defined as follows:

$$\begin{aligned}\dot{\varepsilon}_V{}^L &= \dot{\varepsilon}^L{}_x + \dot{\varepsilon}^L{}_y + \dot{\varepsilon}^L{}_z \\ &= B^L{}_{1i}\dot{d}^L{}_i + B^L{}_{2i}\dot{d}^L{}_i + B^L{}_{3i}\dot{d}^L{}_i \\ &= (B^L{}_{1i} + B^L{}_{2i} + B^L{}_{3i})\dot{d}^L{}_i \\ &\equiv C^L{}_i\dot{d}^L{}_i\end{aligned} \tag{3.15a}$$

or, in the matrix description:

$$\dot{\varepsilon}_V{}^L = \{C^L\}^T\{\dot{d}^L\} \tag{3.15b}$$

Equation (3.16) defines the equivalent strain rate $\dot{\bar{\varepsilon}}$.

$$\dot{\bar{\varepsilon}} \equiv \sqrt{\frac{2}{3}\dot{\varepsilon}_{ij}\dot{\varepsilon}_{ij}} \tag{3.16a}$$

or, using the strain rate vector:

$$\dot{\bar{\varepsilon}}^2 \equiv \dot{\varepsilon}_i D'_{ij} \dot{\varepsilon}_j \tag{3.16b}$$

or, in the matrix description:

$$\dot{\bar{\varepsilon}}^2 \equiv \{\dot{\varepsilon}\}^T [D'] \{\dot{\varepsilon}\} \tag{3.16c}$$

where,

$$[D'] \equiv \frac{1}{3}\begin{bmatrix} 2 & 0 & 0 & 0 & 0 & 0 \\ 0 & 2 & 0 & 0 & 0 & 0 \\ 0 & 0 & 2 & 0 & 0 & 0 \\ 0 & 0 & 0 & 1 & 0 & 0 \\ 0 & 0 & 0 & 0 & 1 & 0 \\ 0 & 0 & 0 & 0 & 0 & 1 \end{bmatrix} \tag{3.17}$$

Substituting eqs. (3.9), (3.12) and (3.13) into eq. (3.16b) yields eq. (3.18).

$$\dot{\bar{\varepsilon}}^2 \equiv \begin{cases} B^G{}_{ik}\dot{d}^G{}_k D'_{ij} B^G{}_{jl}\dot{d}^G{}_l & in \quad \Omega^G \\ (B^G{}_{ik}\dot{d}^G{}_k + B^L{}_{ik}\dot{d}^L{}_k) D'_{ij} (B^G{}_{jl}\dot{d}^G{}_l + B^L{}_{jl}\dot{d}^L{}_l) & in \quad \Omega^L \end{cases} \tag{3.18}$$

In order to modify the derived equation later in this subsection, the derivative of the equivalent strain rate by the global and local nodal velocities will be derived in advance. The partial derivative of the square of the equivalent strain rate by the global nodal velocity is modified by the chain rule as follows:

$$\begin{aligned} \frac{\partial(\dot{\bar{\varepsilon}}^2)}{\partial \dot{d}^G{}_i} &= \frac{\partial(\dot{\bar{\varepsilon}}^2)}{\partial \dot{\bar{\varepsilon}}} \frac{\partial \dot{\bar{\varepsilon}}}{\partial \dot{d}^G{}_i} \\ &= 2\dot{\bar{\varepsilon}} \frac{\partial \dot{\bar{\varepsilon}}}{\partial \dot{d}^G{}_i} \end{aligned} \tag{3.19}$$

Hence, the partial derivative of the equivalent strain rate by the global nodal velocity is expressed in eq. (3.20).

$$\frac{\partial \dot{\bar{\varepsilon}}}{\partial \dot{d}^G{}_i} = \frac{1}{2\dot{\bar{\varepsilon}}} \frac{\partial (\dot{\bar{\varepsilon}}^2)}{\partial \dot{d}^G{}_i} \tag{3.20}$$

On the other hand, the partial derivative of the square of the equivalent strain rate is also derived from eq. (3.18), as shown in eq. (3.21).

$$\frac{\partial (\dot{\bar{\varepsilon}}^2)}{\partial \dot{d}^G{}_i} = \begin{cases} 2B^G{}_{ki} D'_{kl} B^G{}_{lm} \dot{d}^G{}_m & in \quad \Omega^G \\ 2B^G{}_{ki} D'_{kl} (B^G{}_{lm} \dot{d}^G{}_m + B^L{}_{lm} \dot{d}^L{}_m) & in \quad \Omega^L \end{cases} \tag{3.21}$$

Substitution of eq. (3.21) into eq. (3.20) yields eq. (3.22).

$$\frac{\partial \dot{\bar{\varepsilon}}}{\partial \dot{d}^G{}_i} = \begin{cases} \frac{1}{\dot{\bar{\varepsilon}}} B^G{}_{ki} D'_{kl} B^G{}_{lm} \dot{d}^G{}_m & in \quad \Omega^G \\ \frac{1}{\dot{\bar{\varepsilon}}} B^G{}_{ki} D'_{kl} (B^G{}_{lm} \dot{d}^G{}_m + B^L{}_{lm} \dot{d}^L{}_m) & in \quad \Omega^L \end{cases} \tag{3.22}$$

Similarly, eq. (3.23) expresses the partial derivative of the equivalent strain rate by the local nodal velocity.

$$\frac{\partial \dot{\bar{\varepsilon}}}{\partial \dot{d}^L{}_i} = \begin{cases} 0 & in \quad \Omega^G \\ \frac{1}{\dot{\bar{\varepsilon}}} B^L{}_{ki} D'_{kl} (B^G{}_{lm} \dot{d}^G{}_m + B^L{}_{lm} \dot{d}^L{}_m) & in \quad \Omega^L \end{cases} \tag{3.23}$$

In this report, the variational principle is applied to derive the stiffness equation. According to the variational principle, the global nodal velocity $\dot{d}^G{}_i$ and the local nodal velocity $\dot{d}^L{}_i$ are determined by minimizing the variation of the functional. Therefore, the global nodal velocity $\dot{d}^G{}_i$ and the local nodal velocity $\dot{d}^L{}_i$ should satisfy eq. (3.24).

$$\begin{cases} \frac{\partial (\delta\Phi)}{\partial \dot{d}^G{}_i} = 0 \\ \frac{\partial (\delta\Phi)}{\partial \dot{d}^L{}_i} = 0 \end{cases} \tag{3.24}$$

As one of the components of the functional, the potential energy is considered. The variation of the potential energy $\delta\Phi_P$ is expressed in eq. (3.25).

$$\delta\Phi_P = \int_{\Omega^G}\int_0^{\dot{\bar{\varepsilon}}} \bar{\sigma} d\dot{\bar{\varepsilon}} d\Omega + \int_{\Omega^L}\int_0^{\dot{\bar{\varepsilon}}} \bar{\sigma} d\dot{\bar{\varepsilon}} d\Omega \tag{3.25}$$

The energy generated by the external force is also considered as a component of the functional. The variation of the external force energy $\delta\Phi_F$ is shown in eq. (3.26).

$$\delta\Phi_F = -\int_{\Gamma_t^G} t_i v^G{}_i d\Gamma - \int_{\Gamma_t^L} t_i (v^G{}_i + v^L{}_i) d\Gamma \tag{3.26}$$

Since plastic deformation is incompressible, the volume constancy condition should be imposed. In this research, the volume constancy condition is described in eq. (3.27).

$$\begin{cases} \dot{\varepsilon}_V{}^G = 0 & in \quad \Omega \\ \dot{\varepsilon}_V{}^G + \dot{\varepsilon}_V{}^L = 0 & in \quad \Omega^L \end{cases} \tag{3.27}$$

The volume constancy constraint is imposed on the whole global model in order to give some restriction for the deformation of the global element that the local model covers in the present method. This is one feature of the present method. In order to achieve the volume constancy, the following variation of the functional $\delta\Phi_V$ is considered.

$$\delta\Phi_V = \frac{\lambda}{2}\left\{\int_\Omega (\dot{\varepsilon}_V{}^G)^2 d\Omega + \int_{\Omega^L} (\dot{\varepsilon}_V{}^G + \dot{\varepsilon}_V{}^L)^2 d\Omega\right\} \tag{3.28}$$

Here, λ denotes the penalty constant, which has a large positive value. In this research, the selective reduced integration method[43),65)] is applied, in which the volume strain rate is evaluated by 1×1 Gauss point in order to prevent excessive constraints, whereas other strain components are evaluated by using more Gauss points.

The variation of the total functional is given as follows:

$$\delta\Phi = \delta\Phi_P + \delta\Phi_F + \delta\Phi_V \tag{3.29}$$

Equation (3.30) denotes the partial derivative of the variation of the potential energy, eq. (3.25), by the global nodal velocity.

$$\begin{aligned}\frac{\partial(\delta\Phi_P)}{\partial \dot{d}^G{}_i} &= \frac{\partial}{\partial \dot{d}^G{}_i}\left(\int_{\Omega^G}\int_0^{\dot{\bar{\varepsilon}}} \bar{\sigma} d\dot{\bar{\varepsilon}} d\Omega\right) + \frac{\partial}{\partial \dot{d}^G{}_i}\left(\int_{\Omega^L}\int_0^{\dot{\bar{\varepsilon}}} \bar{\sigma} d\dot{\bar{\varepsilon}} d\Omega\right) \\ &= \int_{\Omega^G}\left\{\frac{\partial}{\partial \dot{\bar{\varepsilon}}}\left(\int_0^{\dot{\bar{\varepsilon}}} \bar{\sigma} d\dot{\bar{\varepsilon}}\right)\frac{\partial \dot{\bar{\varepsilon}}}{\partial \dot{d}^G{}_i}\right\} d\Omega + \int_{\Omega^L}\left\{\frac{\partial}{\partial \dot{\bar{\varepsilon}}}\left(\int_0^{\dot{\bar{\varepsilon}}} \bar{\sigma} d\dot{\bar{\varepsilon}}\right)\frac{\partial \dot{\bar{\varepsilon}}}{\partial \dot{d}^G{}_i}\right\} d\Omega \\ &= \int_{\Omega^G} \bar{\sigma}\frac{\partial \dot{\bar{\varepsilon}}}{\partial \dot{d}^G{}_i} d\Omega + \int_{\Omega^L} \bar{\sigma}\frac{\partial \dot{\bar{\varepsilon}}}{\partial \dot{d}^G{}_i} d\Omega \end{aligned} \tag{3.30}$$

By using eq. (3.22), eq. (3.31) is derived.

$$\begin{aligned}\frac{\partial(\delta\Phi_P)}{\partial \dot{d}^G{}_i} &= \int_{\Omega^G}\frac{\bar{\sigma}}{\dot{\bar{\varepsilon}}} B^G{}_{ki} D'_{kl} B^G{}_{lm} d\Omega\, \dot{d}^G{}_m + \int_{\Omega^L}\frac{\bar{\sigma}}{\dot{\bar{\varepsilon}}} B^G{}_{ki} D'_{kl} B^G{}_{lm} d\Omega\, \dot{d}^G{}_m \\ &\quad + \int_{\Omega^L}\frac{\bar{\sigma}}{\dot{\bar{\varepsilon}}} B^G{}_{ki} D'_{kl} B^L{}_{lm} d\Omega\, \dot{d}^L{}_m \end{aligned} \tag{3.31}$$

Here, as described in the previous subsection, the second term on the right should be evaluated by the local model to apply the mesh overlay method for the rigid-plastic problems, although this term is evaluated by the global model for elastic problems to simplify the calculation.

Equation (3.32) describes the partial derivative of the variation of the potential energy, eq. (3.25), by the local nodal velocity.

$$\begin{aligned}\frac{\partial(\delta\Phi_P)}{\partial \dot{d}^L{}_i} &= \frac{\partial}{\partial \dot{d}^L{}_i}\left(\int_{\Omega^L}\int_0^{\dot{\bar{\varepsilon}}} \bar{\sigma} d\dot{\bar{\varepsilon}} d\Omega\right) \\ &= \int_{\Omega^L}\left\{\frac{\partial}{\partial \dot{\bar{\varepsilon}}}\left(\int_0^{\dot{\bar{\varepsilon}}} \bar{\sigma} d\dot{\bar{\varepsilon}}\right)\frac{\partial \dot{\bar{\varepsilon}}}{\partial \dot{d}^G{}_i}\right\} d\Omega \\ &= \int_{\Omega^L} \bar{\sigma}\frac{\partial \dot{\bar{\varepsilon}}}{\partial \dot{d}^L{}_i} d\Omega \\ &= \int_{\Omega^L}\frac{\bar{\sigma}}{\dot{\bar{\varepsilon}}} B^L{}_{ki} D'_{kl} B^G{}_{lm} d\Omega\, \dot{d}^G{}_m + \int_{\Omega^L}\frac{\bar{\sigma}}{\dot{\bar{\varepsilon}}} B^L{}_{ki} D'_{kl} B^L{}_{lm} d\Omega\, \dot{d}^L{}_m \end{aligned} \tag{3.32}$$

Equation (3.33) denotes the partial derivative of the variation of the external force energy, eq. (3.26), by the global nodal velocity.

$$\begin{aligned}\frac{\partial(\delta\Phi_F)}{\partial \dot{d}^G{}_i} &= -\frac{\partial}{\partial \dot{d}^G{}_i}\left(\int_{\Gamma_t^G} t_k v^G{}_k d\Gamma\right) - \frac{\partial}{\partial \dot{d}^G{}_i}\left\{\int_{\Gamma_t^L} t_k (v^G{}_k + v^L{}_k) d\Gamma\right\} \\ &= -\int_{\Gamma_t^G} t_k \frac{\partial v^G{}_k}{\partial \dot{d}^G{}_i} d\Gamma - \int_{\Gamma_t^L} t_k \frac{\partial v^G{}_k}{\partial \dot{d}^G{}_i} d\Gamma \\ &= -\int_{\Gamma_t^G} N^G{}_{ki} t_k d\Gamma - \int_{\Gamma_t^L} N^G{}_{ki} t_k d\Gamma \end{aligned} \tag{3.33}$$

The partial derivative of the variation of the external force energy, eq. (3.26), by the local nodal velocity is expressed by eq. (3.34).

$$\begin{aligned}\frac{\partial(\delta\Phi_F)}{\partial \dot{d}^L{}_i} &= -\frac{\partial}{\partial \dot{d}^L{}_i}\left\{\int_{\Gamma_t^L} t_k (v^G{}_k + v^L{}_k) d\Gamma\right\} \\ &= -\int_{\Gamma_t^L} t_k \frac{\partial v^L{}_k}{\partial \dot{d}^L{}_i} d\Gamma \\ &= -\int_{\Gamma_t^L} N^L{}_{ki} t_k d\Gamma \end{aligned} \tag{3.34}$$

Equation (3.35) shows the partial derivative of the variation of the incompressibility functional, eq. (3.28), by the global nodal velocity.

$$\begin{aligned}\frac{\partial(\delta\Phi_V)}{\partial \dot{d}^G{}_i} &= \lambda\left\{\int_{\Omega^G} \dot{\varepsilon}_V{}^G \frac{\partial \dot{\varepsilon}_V{}^G}{\partial \dot{d}^G{}_i} d\Omega + \int_{\Omega^L} (\dot{\varepsilon}_V{}^G + \dot{\varepsilon}_V{}^L) \frac{\partial \dot{\varepsilon}_V{}^G}{\partial \dot{d}^G{}_i} d\Omega\right\} \\ &= \lambda\Bigg(\int_{\Omega^G} C^G{}_i C^G{}_k d\Omega \, \dot{d}^G{}_k \\ &\qquad + \int_{\Omega^L} C^G{}_i C^G{}_k d\Omega \, \dot{d}^G{}_k + \int_{\Omega^L} C^G{}_i C^L{}_k d\Omega \, \dot{d}^L{}_k\Bigg) \end{aligned} \tag{3.35}$$

That by the local nodal velocity is described by eq. (3.36).

$$\begin{aligned}\frac{\partial(\delta\Phi_V)}{\partial \dot{d}^L{}_i} &= \lambda\int_{\Omega^L} (\dot{\varepsilon}_V{}^G + \dot{\varepsilon}_V{}^L) \frac{\partial \dot{\varepsilon}_V}{\partial \dot{d}^L{}_i} d\Omega \\ &= \lambda\left(\int_{\Omega^L} C^L{}_i C^G{}_k d\Omega \, \dot{d}^G{}_k + \int_{\Omega^L} C^L{}_i C^L{}_k d\Omega \, \dot{d}^L{}_k\right) \end{aligned} \tag{3.36}$$

As a result, the stationary conditions of the variation of the functional, eq. (3.24), can be modified as follows in the matrix description:

$$[K^G]\{\dot{d}^G\}+[K^{GL}]\{\dot{d}^L\}=\{f^G\} \tag{3.37a}$$

$$[K^{GL}]^T\{\dot{d}^G\}+[K^L]\{\dot{d}^L\}=\{f^L\} \tag{3.37b}$$

Here,

$$[K^G]=\int_{\Omega^G}\frac{\overline{\sigma}}{\dot{\overline{\varepsilon}}}[B^G]^T[D'][B^G]d\Omega+\int_{\Omega^L}\frac{\overline{\sigma}}{\dot{\overline{\varepsilon}}}[B^G]^T[D'][B^G]d\Omega + \lambda\int_{\Omega}\{C^G\}\{C^G\}^T d\Omega+\lambda\int_{\Omega^L}\{C^G\}\{C^G\}^T d\Omega \tag{3.38a}$$

$$[K^{GL}]=\int_{\Omega^L}\frac{\overline{\sigma}}{\dot{\overline{\varepsilon}}}[B^G]^T[D'][B^L]d\Omega+\lambda\int_{\Omega^L}\{C^G\}\{C^L\}^T d\Omega \tag{3.38b}$$

$$[K^L]=\int_{\Omega^L}\frac{\overline{\sigma}}{\dot{\overline{\varepsilon}}}[B^L]^T[D'][B^L]d\Omega+\lambda\int_{\Omega^L}\{C^L\}\{C^L\}^T d\Omega \tag{3.38c}$$

$$\{f^G\}=\int_{\Gamma_t^G}[N^G]^T\{t\}d\Gamma+\int_{\Gamma_t^L}[N^G]^T\{t\}d\Gamma \tag{3.38d}$$

$$\{f^L\}=\int_{\Gamma_t^L}[N^L]^T\{t\}d\Gamma \tag{3.38e}$$

3.2.3 Newton-Raphson Method

In order to solve eqs. (3.37a)~(3.37b), the successive substitution method can be used. However, although its convergence algorithm is stable, its convergence speed is, in general, slow. Therefore, a faster convergence algorithm is often adopted to solve the stiffness equations. According to the Newton-Raphson method, which is one of the most popular faster convergence algorithms, the following equations are derived:

$$\begin{bmatrix}\dfrac{\partial^2(\delta\Phi)}{\partial\dot{d}^G{}_i\partial\dot{d}^G{}_j} & \dfrac{\partial^2(\delta\Phi)}{\partial\dot{d}^G{}_i\partial\dot{d}^L{}_j}\\ \dfrac{\partial^2(\delta\Phi)}{\partial\dot{d}^L{}_i\partial\dot{d}^G{}_j} & \dfrac{\partial^2(\delta\Phi)}{\partial\dot{d}^L{}_i\partial\dot{d}^L{}_j}\end{bmatrix}\begin{Bmatrix}\Delta\dot{d}^G{}_j\\ \Delta\dot{d}^L{}_j\end{Bmatrix}=\begin{Bmatrix}-\dfrac{\partial(\delta\Phi)}{\partial\dot{d}^G{}_i}\\ -\dfrac{\partial(\delta\Phi)}{\partial\dot{d}^L{}_i}\end{Bmatrix} \tag{3.39}$$

Here, $\Delta\dot{d}^G{}_j$ and $\Delta\dot{d}^L{}_j$ denote the correction of the assumed global and local nodal velocities for the current iteration at the current time step. That is, after the current iteration, say the *n*-th iteration, the assumed global nodal velocity $\dot{d}^{G}{}_i^{<n>}$ and the assumed local nodal velocity $\dot{d}^{L}{}_i^{<n>}$ are revised as shown in eq. (3.40).

$$\begin{cases} \dot{d}^{G}{}_i^{<n+1>} \leftarrow \dot{d}^{G}{}_i^{<n>} + \Delta\dot{d}^{G}{}_i \\ \dot{d}^{L}{}_i^{<n+1>} \leftarrow \dot{d}^{L}{}_i^{<n>} + \Delta\dot{d}^{L}{}_i \end{cases} \tag{3.40}$$

The first derivative of the total functional by the global nodal velocity is expressed in eq. (3.41).

$$\begin{aligned} \frac{\partial(\delta\Phi)}{\partial\dot{d}^{G}{}_i} = & \int_{\Omega^G} \frac{\overline{\sigma}}{\dot{\overline{\varepsilon}}} B^{G}{}_{ki} D'_{kl} \dot{\varepsilon}^{G}{}_l d\Omega + \int_{\Omega^L} \frac{\overline{\sigma}}{\dot{\overline{\varepsilon}}} B^{G}{}_{ki} D'_{kl} (\dot{\varepsilon}^{G}{}_l + \dot{\varepsilon}^{L}{}_l) d\Omega \\ & - \int_{\Gamma_t^G} N^{G}{}_{ki} t_k d\Gamma - \int_{\Gamma_t^L} N^{G}{}_{ki} t_k d\Gamma \\ & + \lambda \left\{ \int_{\Omega^G} C^{G}{}_i \dot{\varepsilon}_V{}^{G} d\Omega + \int_{\Omega^L} C^{G}{}_i (\dot{\varepsilon}_V{}^{G} + \dot{\varepsilon}_V{}^{L}) d\Omega \right\} \end{aligned} \tag{3.41}$$

The first derivative of the total functional by the local nodal velocity is expressed in eq. (3.42).

$$\begin{aligned} \frac{\partial(\delta\Phi)}{\partial\dot{d}^{L}{}_i} = & \int_{\Omega^L} \frac{\overline{\sigma}}{\dot{\overline{\varepsilon}}} B^{L}{}_{ki} D'_{kl} (\dot{\varepsilon}^{G}{}_l + \dot{\varepsilon}^{L}{}_l) d\Omega \\ & - \int_{\Gamma_t^L} N^{L}{}_{ki} t_k d\Gamma + \lambda \int_{\Omega^L} C^{L}{}_i (\dot{\varepsilon}_V{}^{G} + \dot{\varepsilon}_V{}^{L}) d\Omega \end{aligned} \tag{3.42}$$

Before deriving each component of the second-order partial derivatives of the functional by the global and local nodal velocities, eq. (3.39), consider the second-order partial derivatives of the equivalent strain rate by the global and local nodal velocities. In the global region Ω^G, the second-order partial derivatives of the equivalent strain by the global and local nodal velocities are derived by using eqs. (3.12), (3.13), (3.22), and (3.23).

$$\frac{\partial^2 \dot{\bar{\varepsilon}}}{\partial \dot{d}^G{}_i \partial \dot{d}^G{}_j} = \frac{\partial}{\partial \dot{d}^G{}_j}\left(\frac{\partial \dot{\bar{\varepsilon}}}{\partial \dot{d}^G{}_i}\right)$$
$$= \frac{\partial}{\partial \dot{d}^G{}_j}\left(\frac{1}{\dot{\bar{\varepsilon}}} B^G{}_{ki} D'_{kl} B^G{}_{lm} \dot{d}^G{}_m\right)$$
$$= \frac{1}{\dot{\bar{\varepsilon}}} \frac{\partial}{\partial \dot{d}^G{}_j}\left(B^G{}_{ki} D'_{kl} B^G{}_{lm} \dot{d}^G{}_m\right) + \frac{\partial (1/\dot{\bar{\varepsilon}})}{\partial \dot{d}^G{}_j} B^G{}_{ki} D'_{kl} B^G{}_{lm} \dot{d}^G{}_m$$
$$= \frac{1}{\dot{\bar{\varepsilon}}} B^G{}_{ki} D'_{kl} B^G{}_{lj} - \frac{1}{\dot{\bar{\varepsilon}}^2} B^G{}_{ki} D'_{kl} B^G{}_{lm} \dot{d}^G{}_m \frac{\partial \dot{\bar{\varepsilon}}}{\partial \dot{d}^G{}_j}$$
$$= \frac{1}{\dot{\bar{\varepsilon}}} B^G{}_{ki} D'_{kl} B^G{}_{lj} - \frac{1}{\dot{\bar{\varepsilon}}^3} B^G{}_{ki} D'_{kl} B^G{}_{lm} \dot{d}^G{}_m B^G{}_{pj} D'_{pq} B^G{}_{qr} \dot{d}^G{}_r$$
$$= \frac{1}{\dot{\bar{\varepsilon}}}\left(B^G{}_{ki} D'_{kl} B^G{}_{lj} - \frac{1}{\dot{\bar{\varepsilon}}^2} B^G{}_{ki} D'_{kl} \dot{\varepsilon}^G{}_l B^G{}_{pj} D'_{pq} \dot{\varepsilon}^G{}_q\right) \tag{3.43a}$$

$$\frac{\partial^2 \dot{\bar{\varepsilon}}}{\partial \dot{d}^G{}_i \partial \dot{d}^L{}_j} = 0 \tag{3.44a}$$

$$\frac{\partial^2 \dot{\bar{\varepsilon}}}{\partial \dot{d}^L{}_i \partial \dot{d}^L{}_j} = 0 \tag{3.45a}$$

In the local region Ω^L,

$$\frac{\partial^2 \dot{\bar{\varepsilon}}}{\partial \dot{d}^G{}_i \partial \dot{d}^G{}_j} = \frac{\partial}{\partial \dot{d}^G{}_j}\left(\frac{\partial \dot{\bar{\varepsilon}}}{\partial \dot{d}^G{}_i}\right)$$
$$= \frac{\partial}{\partial \dot{d}^G{}_j}\left\{\frac{1}{\dot{\bar{\varepsilon}}} B^G{}_{ki} D'_{kl} (B^G{}_{lm} \dot{d}^G{}_m + B^L{}_{lm} \dot{d}^L{}_m)\right\}$$
$$= \frac{1}{\dot{\bar{\varepsilon}}} \frac{\partial}{\partial \dot{d}^G{}_j}\left\{B^G{}_{ki} D'_{kl} (B^G{}_{lm} \dot{d}^G{}_m + B^L{}_{lm} \dot{d}^L{}_m)\right\}$$
$$+ \frac{\partial (1/\dot{\bar{\varepsilon}})}{\partial \dot{d}^G{}_j} B^G{}_{ki} D'_{kl} (B^G{}_{lm} \dot{d}^G{}_m + B^L{}_{lm} \dot{d}^L{}_m)$$
$$= \frac{1}{\dot{\bar{\varepsilon}}} B^G{}_{ki} D'_{kl} B^G{}_{lj} - \frac{1}{\dot{\bar{\varepsilon}}^2} B^G{}_{ki} D'_{kl} (B^G{}_{lm} \dot{d}^G{}_m + B^L{}_{lm} \dot{d}^L{}_m) \frac{\partial \dot{\bar{\varepsilon}}}{\partial \dot{d}^G{}_j}$$
$$= \frac{1}{\dot{\bar{\varepsilon}}} B^G{}_{ki} D'_{kl} B^G{}_{lj} - \frac{1}{\dot{\bar{\varepsilon}}^3} B^G{}_{ki} D'_{kl} (B^G{}_{lm} \dot{d}^G{}_m + B^L{}_{lm} \dot{d}^L{}_m)$$
$$B^G{}_{pj} D'_{pq} (B^G{}_{qr} \dot{d}^G{}_r + B^L{}_{qr} \dot{d}^L{}_r)$$
$$= \frac{1}{\dot{\bar{\varepsilon}}}\left\{B^G{}_{ki} D'_{kl} B^G{}_{lj} - \frac{1}{\dot{\bar{\varepsilon}}^2} B^G{}_{ki} D'_{kl} (\dot{\varepsilon}^G{}_l + \dot{\varepsilon}^L{}_l) B^G{}_{pj} D'_{pq} (\dot{\varepsilon}^G{}_q + \dot{\varepsilon}^L{}_q)\right\} \tag{3.43b}$$

$$\frac{\partial^2 \dot{\bar{\varepsilon}}}{\partial \dot{d}^G{}_i \partial \dot{d}^L{}_j} = \frac{\partial}{\partial \dot{d}^L{}_j}\left(\frac{\partial \dot{\bar{\varepsilon}}}{\partial \dot{d}^G{}_i}\right)$$

$$= \frac{\partial}{\partial \dot{d}^L{}_j}\left\{\frac{1}{\dot{\bar{\varepsilon}}} B^G{}_{ki} D'_{kl} (B^G{}_{lm} \dot{d}^G{}_m + B^L{}_{lm} \dot{d}^L{}_m)\right\}$$

$$= \frac{1}{\dot{\bar{\varepsilon}}} \frac{\partial}{\partial \dot{d}^L{}_j}\left\{B^G{}_{ki} D'_{kl} (B^G{}_{lm} \dot{d}^G{}_m + B^L{}_{lm} \dot{d}^L{}_m)\right\}$$

$$+ \frac{\partial\left(1/\dot{\bar{\varepsilon}}\right)}{\partial \dot{d}^L{}_j} B^G{}_{ki} D'_{kl} (B^G{}_{lm} \dot{d}^G{}_m + B^L{}_{lm} \dot{d}^L{}_m)$$

$$= \frac{1}{\dot{\bar{\varepsilon}}} B^G{}_{ki} D'_{kl} B^L{}_{lj} - \frac{1}{\dot{\bar{\varepsilon}}^2} B^G{}_{ki} D'_{kl} (B^G{}_{lm} \dot{d}^G{}_m + B^L{}_{lm} \dot{d}^L{}_m) \frac{\partial \dot{\bar{\varepsilon}}}{\partial \dot{d}^L{}_j}$$

$$= \frac{1}{\dot{\bar{\varepsilon}}} B^G{}_{ki} D'_{kl} B^L{}_{lj} - \frac{1}{\dot{\bar{\varepsilon}}^3} B^G{}_{ki} D'_{kl} (B^G{}_{lm} \dot{d}^G{}_m + B^L{}_{lm} \dot{d}^L{}_m)$$

$$B^L{}_{pj} D'_{pq} (B^G{}_{qr} \dot{d}^G{}_r + B^L{}_{qr} \dot{d}^L{}_r)$$

$$= \frac{1}{\dot{\bar{\varepsilon}}}\left\{B^G{}_{ki} D'_{kl} B^L{}_{lj} - \frac{1}{\dot{\bar{\varepsilon}}^2} B^G{}_{ki} D'_{kl} (\dot{\varepsilon}^G{}_l + \dot{\varepsilon}^L{}_l) B^L{}_{pj} D'_{pq} (\dot{\varepsilon}^G{}_q + \dot{\varepsilon}^L{}_q)\right\} \quad (3.44b)$$

$$\frac{\partial^2 \dot{\bar{\varepsilon}}}{\partial \dot{d}^L{}_i \partial \dot{d}^L{}_j} = \frac{\partial}{\partial \dot{d}^L{}_j}\left(\frac{\partial \dot{\bar{\varepsilon}}}{\partial \dot{d}^L{}_i}\right)$$

$$= \frac{\partial}{\partial \dot{d}^L{}_j}\left\{\frac{1}{\dot{\bar{\varepsilon}}} B^L{}_{ki} D'_{kl} (B^G{}_{lm} \dot{d}^G{}_m + B^L{}_{lm} \dot{d}^L{}_m)\right\}$$

$$= \frac{1}{\dot{\bar{\varepsilon}}} \frac{\partial}{\partial \dot{d}^L{}_j}\left\{B^L{}_{ki} D'_{kl} (B^G{}_{lm} \dot{d}^G{}_m + B^L{}_{lm} \dot{d}^L{}_m)\right\}$$

$$+ \frac{\partial(1/\dot{\bar{\varepsilon}})}{\partial \dot{d}^L{}_j} B^L{}_{ki} D'_{kl} (B^G{}_{lm} \dot{d}^G{}_m + B^L{}_{lm} \dot{d}^L{}_m)$$

$$= \frac{1}{\dot{\bar{\varepsilon}}} B^L{}_{ki} D'_{kl} B^L{}_{lj} - \frac{1}{\dot{\bar{\varepsilon}}^2} B^L{}_{ki} D'_{kl} (B^G{}_{lm} \dot{d}^G{}_m + B^L{}_{lm} \dot{d}^L{}_m) \frac{\partial \dot{\bar{\varepsilon}}}{\partial \dot{d}^L{}_j}$$

$$= \frac{1}{\dot{\bar{\varepsilon}}} B^L{}_{ki} D'_{kl} B^L{}_{lj} - \frac{1}{\dot{\bar{\varepsilon}}^3} B^L{}_{ki} D'_{kl} (B^G{}_{lm} \dot{d}^G{}_m + B^L{}_{lm} \dot{d}^L{}_m)$$

$$B^L{}_{pj} D'_{pq} (B^G{}_{qr} \dot{d}^G{}_r + B^L{}_{qr} \dot{d}^L{}_r)$$

$$= \frac{1}{\dot{\bar{\varepsilon}}}\left\{B^L{}_{ki} D'_{kl} B^L{}_{lj} - \frac{1}{\dot{\bar{\varepsilon}}^2} B^L{}_{ki} D'_{kl} (\dot{\varepsilon}^G{}_l + \dot{\varepsilon}^L{}_l) B^L{}_{pj} D'_{pq} (\dot{\varepsilon}^G{}_q + \dot{\varepsilon}^L{}_q)\right\} \quad (3.45b)$$

Let us derive the second-order partial derivatives of the functional. The second-order partial derivative of the potential energy by the global nodal velocity is expressed as follows:

$$
\begin{aligned}
\frac{\partial^2(\delta\Phi_P)}{\partial\dot{d}^G{}_i\partial\dot{d}^G{}_j} &= \frac{\partial}{\partial\dot{d}^G{}_j}\left\{\frac{\partial(\delta\Phi_P)}{\partial\dot{d}^G{}_i}\right\} \\
&= \frac{\partial}{\partial\dot{d}^G{}_j}\left(\int_{\Omega^G}\overline{\sigma}\frac{\partial\dot{\bar{\varepsilon}}}{\partial\dot{d}^G{}_i}d\Omega+\int_{\Omega^L}\overline{\sigma}\frac{\partial\dot{\bar{\varepsilon}}}{\partial\dot{d}^G{}_i}d\Omega\right) \\
&= \int_{\Omega^G}\left\{\overline{\sigma}\frac{\partial}{\partial\dot{d}^G{}_j}\left(\frac{\partial\dot{\bar{\varepsilon}}}{\partial\dot{d}^G{}_i}\right)+\frac{\partial\overline{\sigma}}{\partial\dot{d}^G{}_j}\frac{\partial\dot{\bar{\varepsilon}}}{\partial\dot{d}^G{}_i}\right\}d\Omega \\
&\quad+\int_{\Omega^L}\left\{\overline{\sigma}\frac{\partial}{\partial\dot{d}^G{}_j}\left(\frac{\partial\dot{\bar{\varepsilon}}}{\partial\dot{d}^G{}_i}\right)+\frac{\partial\overline{\sigma}}{\partial\dot{d}^G{}_j}\frac{\partial\dot{\bar{\varepsilon}}}{\partial\dot{d}^G{}_i}\right\}d\Omega \\
&= \int_{\Omega^G}\left(\overline{\sigma}\frac{\partial^2\dot{\bar{\varepsilon}}}{\partial\dot{d}^G{}_i\partial\dot{d}^G{}_j}+\frac{\partial\overline{\sigma}}{\partial\dot{\bar{\varepsilon}}}\frac{\partial\dot{\bar{\varepsilon}}}{\partial\dot{d}^G{}_i}\frac{\partial\dot{\bar{\varepsilon}}}{\partial\dot{d}^G{}_j}\right)d\Omega \\
&\quad+\int_{\Omega^L}\left(\overline{\sigma}\frac{\partial^2\dot{\bar{\varepsilon}}}{\partial\dot{d}^G{}_i\partial\dot{d}^G{}_j}+\frac{\partial\overline{\sigma}}{\partial\dot{\bar{\varepsilon}}}\frac{\partial\dot{\bar{\varepsilon}}}{\partial\dot{d}^G{}_i}\frac{\partial\dot{\bar{\varepsilon}}}{\partial\dot{d}^G{}_j}\right)d\Omega
\end{aligned}
\tag{3.46}
$$

Substitution of eqs. (3.22) and (3.43) into eq. (3.46) yields eq. (3.47).

$$
\begin{aligned}
\frac{\partial^2(\delta\Phi_P)}{\partial\dot{d}^G{}_i\partial\dot{d}^G{}_j} &= \int_{\Omega^G}\frac{\overline{\sigma}}{\dot{\bar{\varepsilon}}}B^G{}_{ki}D'_{kl}B^G{}_{lj}d\Omega \\
&\quad+\int_{\Omega^G}\frac{1}{\dot{\bar{\varepsilon}}^2}\left(\frac{\partial\overline{\sigma}}{\partial\dot{\bar{\varepsilon}}}-\frac{\overline{\sigma}}{\dot{\bar{\varepsilon}}}\right)B^G{}_{ki}D'_{kl}\dot{\varepsilon}^G{}_lB^G{}_{pj}D'_{pq}\dot{\varepsilon}^G{}_qd\Omega \\
&\quad+\int_{\Omega^L}\frac{\overline{\sigma}}{\dot{\bar{\varepsilon}}}B^G{}_{ki}D'_{kl}B^G{}_{lj}d\Omega \\
&\quad+\int_{\Omega^L}\frac{1}{\dot{\bar{\varepsilon}}^2}\left(\frac{\partial\overline{\sigma}}{\partial\dot{\bar{\varepsilon}}}-\frac{\overline{\sigma}}{\dot{\bar{\varepsilon}}}\right)B^G{}_{ki}D'_{kl}(\dot{\varepsilon}^G{}_l+\dot{\varepsilon}^L{}_l)B^G{}_{pj}D'_{pq}(\dot{\varepsilon}^G{}_q+\dot{\varepsilon}^L{}_q)d\Omega
\end{aligned}
\tag{3.47}
$$

Similarly, eqs. (3.48) ~ (3.49) are derived.

$$
\begin{aligned}
\frac{\partial^2(\delta\Phi_P)}{\partial\dot{d}^G{}_i\partial\dot{d}^L{}_j} &= \int_{\Omega^L}\frac{\overline{\sigma}}{\dot{\bar{\varepsilon}}}B^G{}_{ki}D'_{kl}B^L{}_{lj}d\Omega \\
&\quad+\int_{\Omega^L}\frac{1}{\dot{\bar{\varepsilon}}^2}\left(\frac{\partial\overline{\sigma}}{\partial\dot{\bar{\varepsilon}}}-\frac{\overline{\sigma}}{\dot{\bar{\varepsilon}}}\right)B^G{}_{ki}D'_{kl}(\dot{\varepsilon}^G{}_l+\dot{\varepsilon}^L{}_l)B^L{}_{pj}D'_{pq}(\dot{\varepsilon}^G{}_q+\dot{\varepsilon}^L{}_q)d\Omega
\end{aligned}
\tag{3.48}
$$

$$
\begin{aligned}
\frac{\partial^2(\delta\Phi_P)}{\partial\dot{d}^L{}_i\partial\dot{d}^L{}_j} &= \int_{\Omega^L}\frac{\overline{\sigma}}{\dot{\bar{\varepsilon}}}B^L{}_{ki}D'_{kl}B^L{}_{lj}d\Omega \\
&\quad+\int_{\Omega^L}\frac{1}{\dot{\bar{\varepsilon}}^2}\left(\frac{\partial\overline{\sigma}}{\partial\dot{\bar{\varepsilon}}}-\frac{\overline{\sigma}}{\dot{\bar{\varepsilon}}}\right)B^L{}_{ki}D'_{kl}(\dot{\varepsilon}^G{}_l+\dot{\varepsilon}^L{}_l)B^L{}_{pj}D'_{pq}(\dot{\varepsilon}^G{}_q+\dot{\varepsilon}^L{}_q)d\Omega
\end{aligned}
\tag{3.49}
$$

In contrast, the second-order partial derivatives of the external force energy by the global and local nodal velocities become zero.

$$\frac{\partial^2(\delta\Phi_F)}{\partial\dot{d}^G{}_i\partial\dot{d}^G{}_j}=0 \tag{3.50}$$

$$\frac{\partial^2(\delta\Phi_F)}{\partial\dot{d}^G{}_i\partial\dot{d}^L{}_j}=0 \tag{3.51}$$

$$\frac{\partial^2(\delta\Phi_F)}{\partial\dot{d}^L{}_i\partial\dot{d}^L{}_j}=0 \tag{3.52}$$

The second-order partial derivatives of the incompressibility functional by the global and local nodal velocities are expressed as follows:

$$\begin{aligned}\frac{\partial^2(\delta\Phi_V)}{\partial\dot{d}^G{}_i\partial\dot{d}^G{}_j}&=\frac{\partial}{\partial\dot{d}^G{}_j}\left\{\frac{\partial(\delta\Phi_V)}{\partial\dot{d}^G{}_i}\right\}\\&=\lambda\left[\int_{\Omega^G}\frac{\partial}{\partial\dot{d}^G{}_j}\left(\dot{\varepsilon}_V{}^G\frac{\partial\dot{\varepsilon}_V{}^G}{\partial\dot{d}^G{}_i}\right)d\Omega\right.\\&\qquad\left.+\int_{\Omega^L}\frac{\partial}{\partial\dot{d}^G{}_j}\left\{(\dot{\varepsilon}_V{}^G+\dot{\varepsilon}_V{}^L)\frac{\partial\dot{\varepsilon}_V{}^G}{\partial\dot{d}^G{}_i}\right\}d\Omega\right]\\&=\lambda\left(\int_{\Omega^G}\frac{\partial\dot{\varepsilon}_V{}^G}{\partial\dot{d}^G{}_i}\frac{\partial\dot{\varepsilon}_V{}^G}{\partial\dot{d}^G{}_j}d\Omega+\int_{\Omega^L}\frac{\partial\dot{\varepsilon}_V{}^G}{\partial\dot{d}^G{}_i}\frac{\partial\dot{\varepsilon}_V{}^G}{\partial\dot{d}^G{}_j}d\Omega\right)\\&=\lambda\left(\int_{\Omega^G}C^G{}_iC^G{}_jd\Omega+\int_{\Omega^L}C^G{}_iC^G{}_jd\Omega\right)\end{aligned} \tag{3.53}$$

$$\begin{aligned}\frac{\partial^2(\delta\Phi_V)}{\partial\dot{d}^G{}_i\partial\dot{d}^L{}_j}&=\frac{\partial}{\partial\dot{d}^L{}_j}\left\{\frac{\partial(\delta\Phi_V)}{\partial\dot{d}^G{}_i}\right\}\\&=\lambda\int_{\Omega^L}\frac{\partial}{\partial\dot{d}^L{}_j}\left\{(\dot{\varepsilon}_V{}^G+\dot{\varepsilon}_V{}^L)\frac{\partial\dot{\varepsilon}_V{}^G}{\partial\dot{d}^G{}_i}\right\}d\Omega\\&=\lambda\int_{\Omega^L}\frac{\partial\dot{\varepsilon}_V{}^G}{\partial\dot{d}^G{}_i}\frac{\partial\dot{\varepsilon}_V{}^L}{\partial\dot{d}^L{}_j}d\Omega\\&=\lambda\int_{\Omega^L}C^G{}_iC^L{}_jd\Omega\end{aligned} \tag{3.54}$$

$$\frac{\partial^2(\delta\Phi_V)}{\partial\dot{d}^L{}_i\partial\dot{d}^L{}_j} = \frac{\partial}{\partial\dot{d}^L{}_j}\left\{\frac{\partial(\delta\Phi_V)}{\partial\dot{d}^L{}_i}\right\}$$
$$= \lambda\int_{\Omega^L}\frac{\partial}{\partial\dot{d}^L{}_j}\left\{(\dot{\varepsilon}_V{}^G + \dot{\varepsilon}_V{}^L)\frac{\partial\dot{\varepsilon}_V{}^L}{\partial\dot{d}^L{}_i}\right\}d\Omega$$
$$= \lambda\int_{\Omega^L}\frac{\partial\dot{\varepsilon}_V{}^L}{\partial\dot{d}^L{}_i}\frac{\partial\dot{\varepsilon}_V{}^L}{\partial\dot{d}^L{}_j}d\Omega$$
$$= \lambda\int_{\Omega^L}C^L{}_iC^L{}_jd\Omega \tag{3.55}$$

Hence, the stiffness equations based on the Newton-Raphson method are expressed in the matrix description as follows:

$$[K^{G'}]\{\Delta\dot{d}^G\} + [K^{GL'}]\{\Delta\dot{d}^L\} = \{f^{G'}\} \tag{3.56a}$$

$$[K^{GL'}]^T\{\Delta\dot{d}^G\} + [K^{L'}]\{\Delta\dot{d}^L\} = \{f^{L'}\} \tag{3.56b}$$

Here,

$$[K^{G'}] = [K^G] + \int_{\Omega^G}\frac{1}{\dot{\bar{\varepsilon}}^2}\left(\frac{\partial\bar{\sigma}}{\partial\dot{\bar{\varepsilon}}} - \frac{\bar{\sigma}}{\dot{\bar{\varepsilon}}}\right)[B^G]^T[D'](\{\dot{\varepsilon}^G\}\{\dot{\varepsilon}^G\}^T)[D'][B^G]d\Omega$$
$$+ \int_{\Omega^L}\frac{1}{\dot{\bar{\varepsilon}}^2}\left(\frac{\partial\bar{\sigma}}{\partial\dot{\bar{\varepsilon}}} - \frac{\bar{\sigma}}{\dot{\bar{\varepsilon}}}\right)[B^G]^T[D'](\{\dot{\varepsilon}^G\} + \{\dot{\varepsilon}^L\})(\{\dot{\varepsilon}^G\}^T + \{\dot{\varepsilon}^L\}^T)[D'][B^G]d\Omega \tag{3.57a}$$

$$[K^{GL'}] = [K^{GL}]$$
$$+ \int_{\Omega^L}\frac{1}{\dot{\bar{\varepsilon}}^2}\left(\frac{\partial\bar{\sigma}}{\partial\dot{\bar{\varepsilon}}} - \frac{\bar{\sigma}}{\dot{\bar{\varepsilon}}}\right)[B^G]^T[D'](\{\dot{\varepsilon}^G\} + \{\dot{\varepsilon}^L\})(\{\dot{\varepsilon}^G\}^T + \{\dot{\varepsilon}^L\}^T)[D'][B^L]d\Omega \tag{3.57b}$$

$$[K^{L'}] = [K^L]$$
$$+ \int_{\Omega^L}\frac{1}{\dot{\bar{\varepsilon}}^2}\left(\frac{\partial\bar{\sigma}}{\partial\dot{\bar{\varepsilon}}} - \frac{\bar{\sigma}}{\dot{\bar{\varepsilon}}}\right)[B^L]^T[D'](\{\dot{\varepsilon}^G\} + \{\dot{\varepsilon}^L\})(\{\dot{\varepsilon}^G\}^T + \{\dot{\varepsilon}^L\}^T)[D'][B^L]d\Omega \tag{3.57c}$$

$$\{f^{G'}\} = \{f^G\} - \int_{\Omega^G} \frac{\overline{\sigma}}{\dot{\overline{\varepsilon}}} [B^G]^T [D'] \{\dot{\varepsilon}^G\} d\Omega - \int_{\Omega^L} \frac{\overline{\sigma}}{\dot{\overline{\varepsilon}}} [B^G]^T [D'] (\{\dot{\varepsilon}^G\} + \{\dot{\varepsilon}^L\}) d\Omega - \lambda \int_{\Omega} \{C^G\} \dot{\varepsilon}_V{}^G d\Omega - \lambda \int_{\Omega^L} \{C^G\} (\dot{\varepsilon}_V{}^G + \dot{\varepsilon}_V{}^L) d\Omega \quad (3.57d)$$

$$\{f^{L'}\} = \{f^L\} - \int_{\Omega^L} \frac{\overline{\sigma}}{\dot{\overline{\varepsilon}}} [B^L]^T [D'] (\{\dot{\varepsilon}^G\} + \{\dot{\varepsilon}^L\}) d\Omega - \lambda \int_{\Omega^L} \{C^L\} (\dot{\varepsilon}_V{}^G + \dot{\varepsilon}_V{}^L) d\Omega \quad (3.57e)$$

3.2.4 Formulations for Small Local Model

It was noted that the global stiffness matrix $[K^G]$ in the local region Ω^L should be evaluated by the local model for rigid-plastic analysis. However, if the local model is wholly overlaid by one global element, the global stiffness matrix $[K^G]$ can be evaluated by the global model even if the evaluating point is in the local region Ω^L. Such a condition can be assumed when the local model is much smaller than the global model. Additionally, some reports[29),32),46),52),54)] applied the constraint that no local elements are allowed to cover two or more global elements in order to achieve fast convergence or to prevent numerical instability. Under this constraint, the global stiffness matrix $[K^G]$ can be evaluated only by the global model.

In this case, the following simplification can be applied:

$$\int_{\Omega^G} \frac{\overline{\sigma}}{\dot{\overline{\varepsilon}}} B^G{}_{ki} D'_{kl} B^G{}_{lm} d\Omega + \int_{\Omega^L} \frac{\overline{\sigma}}{\dot{\overline{\varepsilon}}} B^G{}_{ki} D'_{kl} B^G{}_{lm} d\Omega \cong \int_{\Omega} \frac{\overline{\sigma}}{\dot{\overline{\varepsilon}}} B^G{}_{ki} D'_{kl} B^G{}_{lm} d\Omega \quad (3.58)$$

This expression contains two simplifications. One is that the resolution of the region covered by the local model becomes coarse because the global Gauss points, instead of the local Gauss points, are used to evaluate the integrated terms in this region. The other is that the equivalent stress and the equivalent strain rate for the global element are used instead of those for the local element. By using eq. (3.58), eq. (3.31) can be modified as follows:

$$\frac{\partial(\delta\Phi_P)}{\partial \dot{d}^G{}_i} \cong \int_{\Omega} \frac{\overline{\sigma}}{\dot{\overline{\varepsilon}}} B^G{}_{ki} D'_{kl} B^G{}_{lm} d\Omega \, \dot{d}^G{}_m + \int_{\Omega^L} \frac{\overline{\sigma}}{\dot{\overline{\varepsilon}}} B^G{}_{ki} D'_{kl} B^L{}_{lm} d\Omega \, \dot{d}^L{}_m \quad (3.59)$$

As similar as the derivation of eq. (3.59), the second term on the right side in eq. (3.33) is evaluated by the global model, as shown in eq. (3.60), in order to simplify the calculation.

$$\int_{\Gamma_t^G} N^G{}_{ki} t_k d\Gamma + \int_{\Gamma_t^L} N^G{}_{ki} t_k d\Gamma \cong \int_{\Gamma_t} N^G{}_{ki} t_k d\Gamma \tag{3.60}$$

By using eq. (3.60), eq. (3.33) is modified to eq. (3.61).

$$\frac{\partial(\delta\Phi_F)}{\partial \dot{d}^G{}_i} \cong -\int_{\Gamma_t} N^G{}_{ki} t_k d\Gamma \tag{3.61}$$

In this case, since the numerical instability due to the indeterminate of the global velocity fields does not occur because no local elements cover two or more global elements, the restriction for the global element deformation is not needed. Hence, the volume constancy condition is defined as follows:

$$\begin{cases} \dot{\varepsilon}_V{}^G = 0 & in \quad \Omega^G \\ \dot{\varepsilon}_V{}^G + \dot{\varepsilon}_V{}^L = 0 & in \quad \Omega^L \end{cases} \tag{3.62}$$

In order to achieve the volume constancy, the following variation of the functional $\delta\Phi_V$ is considered in this case.

$$\delta\Phi_V = \frac{\lambda}{2}\left\{\int_{\Omega^G} (\dot{\varepsilon}_V{}^G)^2 d\Omega + \int_{\Omega^L} (\dot{\varepsilon}_V{}^G + \dot{\varepsilon}_V{}^L)^2 d\Omega\right\} \tag{3.63}$$

Hence, the partial derivative of the variation of the incompressibility functional by the global nodal velocity, eq. (3.35), can be modified as follows:

$$\frac{\partial(\delta\Phi_V)}{\partial \dot{d}^G{}_i} = \lambda\left(\int_\Omega C^G{}_i C^G{}_k d\Omega\, \dot{d}^G{}_k + \int_{\Omega^L} C^G{}_i C^L{}_k d\Omega\, \dot{d}^L{}_k\right) \tag{3.64}$$

As a result, the global stiffness matrix $[K^G]$ and the global force vector $\{f^G\}$, shown in eqs. (3.38a) and (3.38d) respectively, are modified as follows:

$$[K^G] = \int_\Omega \frac{\bar{\sigma}}{\dot{\bar{\varepsilon}}} [B^G]^T [D'][B^G] d\Omega + \lambda \int_\Omega \{C^G\}\{C^G\}^T d\Omega \tag{3.65a}$$

$$\{f^G\} = \int_{\Gamma_t} [N^G]^T \{t\} d\Gamma \tag{3.65d}$$

whereas, the coupled stiffness matrix [K^{GL}], the local stiffness matrix [K^{L}] and the local force vector $\{f^{L}\}$ are the same, as shown in eqs. (3.38b), (3.38c), (3.38e).

In order to achieve fast convergence, Newton-Raphson method can be applied, as well. In the rigid-plastic mesh overlay formulations under Newton-Raphson method, the second and fourth term on the right side in eq. (3.47) are evaluated by the global model for simplifying the computation. Here, the local strain rate is assumed to be zero on the global model.

$$\begin{aligned}
&\int_{\Omega^G} \frac{1}{\dot{\bar{\varepsilon}}^2}\left(\frac{\partial \bar{\sigma}}{\partial \dot{\bar{\varepsilon}}} - \frac{\bar{\sigma}}{\dot{\bar{\varepsilon}}}\right) B^G{}_{ki} D'_{kl} \dot{\varepsilon}^G{}_l B^G{}_{pj} D'_{pq} \dot{\varepsilon}^G{}_q d\Omega \\
&\quad + \int_{\Omega^L} \frac{1}{\dot{\bar{\varepsilon}}^2}\left(\frac{\partial \bar{\sigma}}{\partial \dot{\bar{\varepsilon}}} - \frac{\bar{\sigma}}{\dot{\bar{\varepsilon}}}\right) B^G{}_{ki} D'_{kl} (\dot{\varepsilon}^G{}_l + \dot{\varepsilon}^L{}_l) B^G{}_{pj} D'_{pq} (\dot{\varepsilon}^G{}_q + \dot{\varepsilon}^L{}_q) d\Omega \\
&\qquad \cong \int_{\Omega} \frac{1}{\dot{\bar{\varepsilon}}^2}\left(\frac{\partial \bar{\sigma}}{\partial \dot{\bar{\varepsilon}}} - \frac{\bar{\sigma}}{\dot{\bar{\varepsilon}}}\right) B^G{}_{ki} D'_{kl} \dot{\varepsilon}^G{}_l B^G{}_{pj} D'_{pq} \dot{\varepsilon}^G{}_q d\Omega \qquad (3.66)
\end{aligned}$$

Due to this simplification, eq. (3.47) is modified to eq. (3.67).

$$\frac{\partial^2 (\delta \Phi_P)}{\partial \dot{d}^G{}_i \partial \dot{d}^G{}_j} \cong \int_{\Omega} \frac{\bar{\sigma}}{\dot{\bar{\varepsilon}}} B^G{}_{ki} D'_{kl} B^G{}_{lj} d\Omega + \int_{\Omega} \frac{1}{\dot{\bar{\varepsilon}}^2}\left(\frac{\partial \bar{\sigma}}{\partial \dot{\bar{\varepsilon}}} - \frac{\bar{\sigma}}{\dot{\bar{\varepsilon}}}\right) B^G{}_{ki} D'_{kl} \dot{\varepsilon}^G{}_l B^G{}_{pj} D'_{pq} \dot{\varepsilon}^G{}_q d\Omega \qquad (3.67)$$

Similarly, eq. (3.68) is also derived.

$$\frac{\partial (\delta \Phi)}{\partial \dot{d}^G{}_i} \cong \int_{\Omega} \frac{\bar{\sigma}}{\dot{\bar{\varepsilon}}} B^G{}_{ki} D'_{kl} \dot{\varepsilon}^G{}_l d\Omega - \int_{\Gamma_t} N^G{}_{ki} t_k d\Gamma + \lambda \int_{\Omega} C^G{}_i \dot{\varepsilon}_V{}^G d\Omega \qquad (3.68)$$

Finally, the global stiffness matrix [$K^{G'}$] and the global force vector $\{f^{G'}\}$ based on Newton-Raphson method are modified as follows:

$$[K^{G'}] = [K^G] + \int_{\Omega} \frac{1}{\dot{\bar{\varepsilon}}^2}\left(\frac{\partial \bar{\sigma}}{\partial \dot{\bar{\varepsilon}}} - \frac{\bar{\sigma}}{\dot{\bar{\varepsilon}}}\right) [B^G]^T [D'] \{\dot{\varepsilon}^G\} \{\dot{\varepsilon}^G\}^T [D'] [B^G] d\Omega \qquad (3.69a)$$

$$\{f^{G'}\} = \{f^G\} - \int_{\Omega} \frac{\bar{\sigma}}{\dot{\bar{\varepsilon}}} [B^G]^T [D'] \{\dot{\varepsilon}^G\} d\Omega - \lambda \int_{\Omega} \{C^G\} \dot{\varepsilon}_V{}^G d\Omega \qquad (3.69d)$$

Although the transpose of the coupled stiffness matrix [K^{LG}]^T becomes different from the coupled matrix [K^{GL}] due to the simplification, they are assumed to be the same.

3.2.5 Post Processing at Each Time Step

After acquiring the converged solutions of the stiffness equations at each time step, the strain rate $\dot{\varepsilon}_{ij}$ can be calculated. Then, deviatric stress σ'_{ij} is calculated according to the Levy-Mises flow rule.

$$\sigma'_{ij} = \frac{2\overline{\sigma}}{3\dot{\overline{\varepsilon}}}\dot{\varepsilon}_{ij} \tag{3.70a}$$

or, in the matrix description:

$$\{\sigma'\} = [D]\{\dot{\varepsilon}\} \tag{3.70b}$$

Here,

$$\{\sigma'\} \equiv \{\sigma'_x \quad \sigma'_y \quad \sigma'_z \quad \tau_{xy} \quad \tau_{yz} \quad \tau_{zx}\}^T \tag{3.71}$$

$$[D] = \frac{\overline{\sigma}}{\dot{\overline{\varepsilon}}}[D'] \tag{3.72}$$

Hydro-static stress σ_m is obtained by the following equation:

$$\sigma_m = \lambda\dot{\varepsilon}_V \tag{3.73}$$

Hence, the stress vector $\{\sigma\}$ is represented by eq. (3.74).

$$\{\sigma\} = \sigma_m \begin{Bmatrix} 1 \\ 1 \\ 1 \\ 0 \\ 0 \\ 0 \end{Bmatrix} + [D]\{\dot{\varepsilon}\} \tag{3.74}$$

For two-dimensional analysis, the stress vector $\{\sigma\}$, the deviatoric stress vector $\{\sigma'\}$ and the strain rate vector $\{\dot{\varepsilon}\}$ are modified as follows.

$$\{\sigma\} \equiv \{\sigma_x \quad \sigma_y \quad \tau_{xy}\}^T \tag{3.75}$$

$$\{\sigma'\} \equiv \{\sigma'_x \quad \sigma'_y \quad \tau_{xy}\}^T \tag{3.76}$$

$$\{\dot{\varepsilon}\} \equiv \{\dot{\varepsilon}_x \quad \dot{\varepsilon}_y \quad 2\dot{\varepsilon}_{xy}\}^T \tag{3.77}$$

Since only two dimensions are considered, the following relations can be easily obtained.

$$\tau_{yz} = \tau_{zx} = 0 \tag{3.78}$$

$$\dot{\gamma}_{yz} = \dot{\gamma}_{zx} = 0 \tag{3.79}$$

The following assumption is introduced under the plane strain condition.

$$\dot{\varepsilon}_z = 0 \tag{3.80}$$

By using eqs. (3.78) ~ (3.80), eq. (3.81) can be obtained.

$$\begin{Bmatrix} \dot{\varepsilon}_x \\ \dot{\varepsilon}_y \\ 2\dot{\varepsilon}_{xy} \end{Bmatrix} = \frac{\dot{\bar{\varepsilon}}}{\bar{\sigma}} \begin{bmatrix} 1 & -\frac{1}{2} & 0 \\ -\frac{1}{2} & 1 & 0 \\ 0 & 0 & 3 \end{bmatrix} \begin{Bmatrix} \sigma'_x \\ \sigma'_y \\ \tau_{xy} \end{Bmatrix} \tag{3.81}$$

Equation (3.82) expresses the inverse relation of eq. (3.81).

$$\begin{Bmatrix} \sigma'_x \\ \sigma'_y \\ \tau_{xy} \end{Bmatrix} = \frac{2\bar{\sigma}}{3\dot{\bar{\varepsilon}}} \begin{bmatrix} 2 & 1 & 0 \\ 1 & 2 & 0 \\ 0 & 0 & \frac{1}{2} \end{bmatrix} \begin{Bmatrix} \dot{\varepsilon}_x \\ \dot{\varepsilon}_y \\ 2\dot{\varepsilon}_{xy} \end{Bmatrix} \tag{3.82}$$

Hence, the matrix [*D'*] for the plane strain condition is defined in eq. (3.83).

$$[D'] = \frac{2}{3}\begin{bmatrix} 2 & 1 & 0 \\ 1 & 2 & 0 \\ 0 & 0 & \frac{1}{2} \end{bmatrix} \tag{3.83}$$

On the other hand, the following assumption is introduced under the plane stress condition.

$$\sigma_z = 0 \tag{3.84}$$

The *z*-directional strain rate $\dot{\varepsilon}_z$ is computed by eq. (3.85) under the plane stress condition due to the incompressibility condition.

$$\dot{\varepsilon}_z = -(\dot{\varepsilon}_x + \dot{\varepsilon}_y) \tag{3.85}$$

That is, the *z*-directional strain rate $\dot{\varepsilon}_z$ is a dependent variable of the *x*-directional strain rate $\dot{\varepsilon}_x$ and the *y*-directional strain rate $\dot{\varepsilon}_y$, and is adjusted to make the volumetric strain rate zero. Therefore, the incompressibility constraint does not have to be considered in the stiffness equations under the plane stress condition. Moreover, under the plane stress condition, the stress vector $\{\sigma\}$ itself can be acquired by using eq. (3.86).

$$\begin{Bmatrix} \sigma_x \\ \sigma_y \\ \tau_{xy} \end{Bmatrix} = \frac{2\bar{\sigma}}{3\dot{\bar{\varepsilon}}}\begin{bmatrix} 2 & 1 & 0 \\ 1 & 2 & 0 \\ 0 & 0 & \frac{1}{2} \end{bmatrix}\begin{Bmatrix} \dot{\varepsilon}_x \\ \dot{\varepsilon}_y \\ 2\dot{\varepsilon}_{xy} \end{Bmatrix} \tag{3.86}$$

The geometry should also be updated after acquiring converged solutions for the current time step. The coordinates of the global and local models after the *n*-th time step ${x^G}_i^{(n)}$ and ${x^L}_i^{(n)}$ are computed by using following equations, respectively.

$${x^G}_i^{(n)} = {x^G}_i^{(n-1)} + {\dot{d}^G}_i^{(n)} \cdot \Delta t \tag{3.87}$$

$$x^{L}{}_{i}{}^{(n)} = x^{L}{}_{i}{}^{(n-1)} + (\dot{d}^{L}{}_{i}{}^{(n)} + N^{G}{}_{ik}\dot{d}^{G}{}_{k}{}^{(n)}) \cdot \Delta t \tag{3.88}$$

In this research, in order to avoid the numerical instability due to a zero divide error at the rigid zone, the equivalent strain rate $\dot{\bar{\varepsilon}}^{*}$ is modified as follows[63].

$$\dot{\bar{\varepsilon}}^{*} = \sqrt{\dot{\bar{\varepsilon}}^{2} + (10^{-4}\dot{\bar{\varepsilon}}_{0})^{2}} \tag{3.89}$$

where $\dot{\bar{\varepsilon}}_{0}$ is the maximum value of the equivalent strain rate $\dot{\bar{\varepsilon}}^{*}$ at the previous time step. The initial value of $\dot{\bar{\varepsilon}}_{0}$ as well as $\bar{\varepsilon}$ is set to a small value, say 10^{-2} and 10^{-3}, respectively.

3.2.6 Algorithms

This section explains the algorithms of the rigid-plastic mesh overlay method. **Fig. 3.1** shows the flow chart of the analysis.

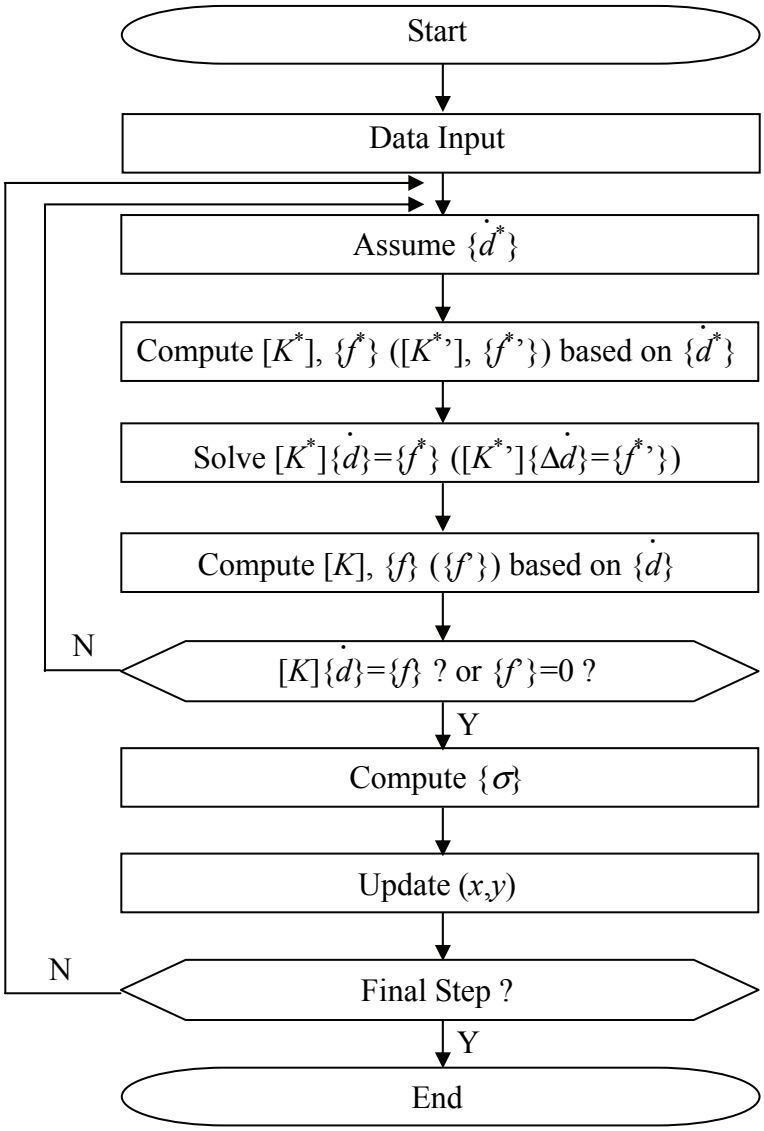

Fig. 3.1 Flow chart of rigid-plastic mesh overlay analysis

The computing conditions －for example, the material constants, the dimensions of the model, and the boundary conditions－ are input. The unknown (the nodal velocity vector) is obtained through the following iterations. First, the nodal velocity vector $\{\dot{d}^*\}$

is assumed. In this research, the initial guesses of the unknown components of the vector are set to zero at the first time step. Then, by using the assumed nodal velocity vector $\{\dot{d}^*\}$, the stiffness matrix [K] and the nodal force vector $\{f\}$ are computed. After this calculation, the stiffness matrix [K] and the nodal force vector $\{f\}$ are modified to consider the velocity boundary conditions. In order to restrain these nodal velocities, the penalty method is adopted in this research. Then, the stiffness equations are solved. In this research, a linear equation solver for a real symmetric indefinite system where the matrix is in the packed storage, called *dspsv*[66], is used. Here, if the assumed nodal velocities are inadequate, divergence of the calculation can easily occur when using Newton-Raphson method. Hence, even though Newton-Raphson method is applied, the successive substitution method is used to obtain the roughly converged solutions of the assumed nodal velocity vector at the first time step. Using the obtained solution, the stiffness matrix [K^*] is computed again, and the error of the nodal velocity assumption is estimated by using the nodal force error norm Δ_f defined by eq. (3.90).

$$\Delta_f \equiv \sqrt{\frac{\delta f_i \delta f_i}{f_j f_j}} \tag{3.90}$$

Here, δf_i is defined in eq. (3.91).

$$\delta f_i = \begin{cases} f_i - K_{ij}\dot{d}_j & \text{for successive substitution method} \\ f_i' & \text{for Newton-Raphson method} \end{cases} \tag{3.91}$$

If the nodal force error norm Δ_f is larger than the convergence criterion δ, the assumed nodal velocity vector $\{\dot{d}^*\}$ is modified, and the iteration is executed again. However, when the nodal force error norm Δ_f becomes smaller than the convergence criterion δ, it is judged that the converged solution has been just achieved. In this research, the convergence criterion δ is set to be 10^{-4}.

After the converged solutions are obtained, the results —nodal velocities, nodal forces, strain rate, stress and so on— are computed as the outputs at the current time step. If the current time step is not the final one, the iteration for the next time step is started. The initial guesses of the nodal velocity vector $\{\dot{d}^*\}$ for the next time step is given by the nodal velocity vector $\{\dot{d}\}$ for the current time step.

3.2.7 Summary

In this section, the formulations of the mesh overlay method for rigid-plastic analysis were newly derived. First, it was shown that the global stiffness matrix and the global force vector in the overlaid region should be evaluated by the local model due to its nonlinearity. Therefore, the rigid-plastic mesh overlay formulations do not apply the simplification that uses the global model instead of the local model to construct the global stiffness matrix and the global force vector in this region. Furthermore, the formulations based on Newton-Raphson method were also derived in order to achieve faster convergence. However, if the local model does not overlay two or more global elements, the simplification mentioned above can be applied. The formulations for such special cases were also derived.

3.3 Numerical Examples of Two-dimensional Analysis

3.3.1 Introduction

In order to verify the accuracy of the rigid-plastic mesh overlay method derived in the previous section, a two-dimensional analysis is first performed.

3.3.2 Computational Conditions

A plane strain plate with a circular inclusion at the center is considered, as shown in **Fig. 3.2**. Here, due to the symmetry of the deformation, one quarter of the model is considered. The length and width of the plate are $2L$ and $2W$, and the diameter of the inclusion is $2r$. The longitudinal displacement rate $\dot{U}$ is given, and no shear forces are applied on this boundary.

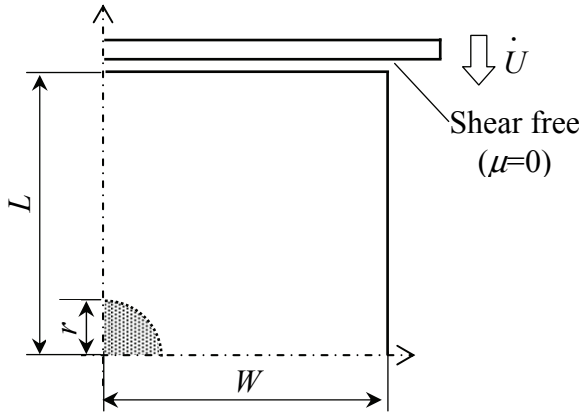

Fig. 3.2 Computational model of rigid-plastic plate compression with inclusion

The following material hardening law is employed.

$$\overline{\sigma} = K\overline{\varepsilon}^{n}\dot{\overline{\varepsilon}}^{m} \tag{3.92}$$

Here, K, n and m represent the material constant of the deformation resistance, the strain hardening index, and the strain rate sensitivity index, respectively.

The computational conditions are shown in **Table 3.1**. Both the initial length $2L$ and width $2W$ of the plate are 60mm, and the initial radius of the diameter $2r$ is 12mm.

Both softer inclusion case (case A) and harder inclusion case (case B) are demonstrated in this research. That is, the material constant of the deformation resistance for the matrix K_0 is 100MPa, whereas that for the inclusion K_1 is 50MPa in case A, and 200MPa in case B. The strain hardening index n for both the matrix and the inclusion is the same, 0.20. The strain rate sensitivity index m for both the matrix and the inclusion is also the same, 0.10. Nominal longitudinal displacement rate $\dot{U}/L$ is 1.0. The time step Δt is 0.02 sec, and the number of the steps N is 15. Therefore, after the final step, the nominal longitudinal displacement U/L becomes 0.30.

Table 3.1 Computational conditions of rigid-plastic plate compression with inclusion

Initial length of plate	$2L$	60	mm
Initial width of plate	$2W$	60	mm
Initial diameter of inclusion	$2r$	12	mm
Nominal longitudinal displacement rate	$\dot{U}/L$	1.0	
Deformation resistance of matrix	K_0	100	MPa
Deformation resistance of inclusion (case A)	K_1	50	MPa
Deformation resistance of inclusion (case B)	K_1	200	MPa
Strain hardening index	n	0.20	
Strain rate sensitivity index	m	0.10	
Time step	Δt	0.02	sec
Number of steps	N	15	

Figure 3.3 shows the mesh discretization of the global and local models for the mesh overlay analysis. The global model, which covers the whole area of the model, is divided into 10×10 meshes. The local model is also divided into 10×10 meshes. Here, two types of the local model are adopted. In addition, the grayed mesh expresses the inclusion. Moreover, conventional analysis is also computed as a reference solution by using 15×15 meshes, as shown in **Fig. 3.4**.

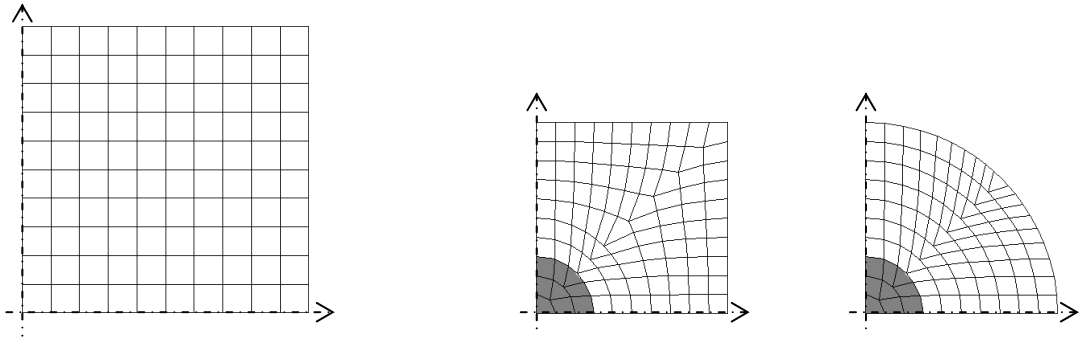

(a) Global model (b) Local model-1 (c) Local model-2

Fig. 3.3 Mesh discretization for mesh overlay method of rigid-plastic plate compression with inclusion

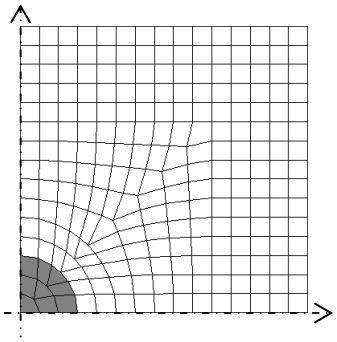

Fig. 3.4 Mesh discretization for conventional method of rigid-plastic plate compression with inclusion

Here, four-node linear isoparametric quadrilateral elements are adopted. The number of Gauss points is 4×4 per element for both the global and local elements, while it is 2×2 for the conventional analysis.

3.3.3 Computational Results (Case A: Softer Inclusion)

First, case A, where the inclusion is softer than the matrix, is considered. **Figure 3.5** shows the longitudinal strain rate $\dot{\varepsilon}_y$ distributions at nominal longitudinal displacement U/L=0.02 (the first step) by the conventional analysis and the mesh overlay analysis, respectively. Both solutions acquired by the mesh overlay method show the closest distributions to the conventional one. That is, the inclusion is significantly deformed since it is softer than the matrix. Strain is concentrated around approximately

a 45-degree direction from the center.

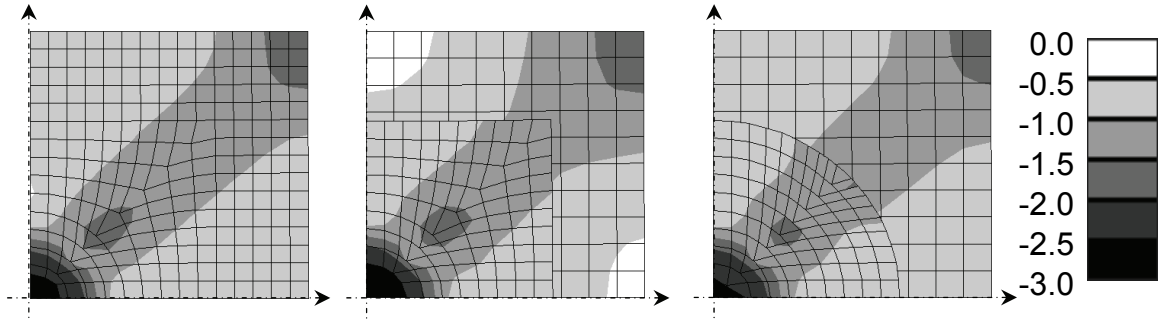

(a) Conventional (b) Mesh Overlay -1 (c) Mesh Overlay -2

Fig. 3.5 Longitudinal strain rate $\dot{\varepsilon}_y$ distributions at U/L=0.02 of rigid-plastic plate compression with softer inclusion

The shear strain rate $\dot{\varepsilon}_{xy}$ distributions at nominal longitudinal displacement U/L=0.02 (the first step) by the conventional analysis and the mesh overlay analysis are shown in **Fig. 3.6**, respectively. The obtained shear strain rate $\dot{\varepsilon}_{xy}$ distributions by the mesh overlay method also agree with the one by the conventional analysis. That is, because of the large inclusion deformation, positive shear strain rate appears near the top of the inclusion, and negative shear strain rate appears near the side of the inclusion.

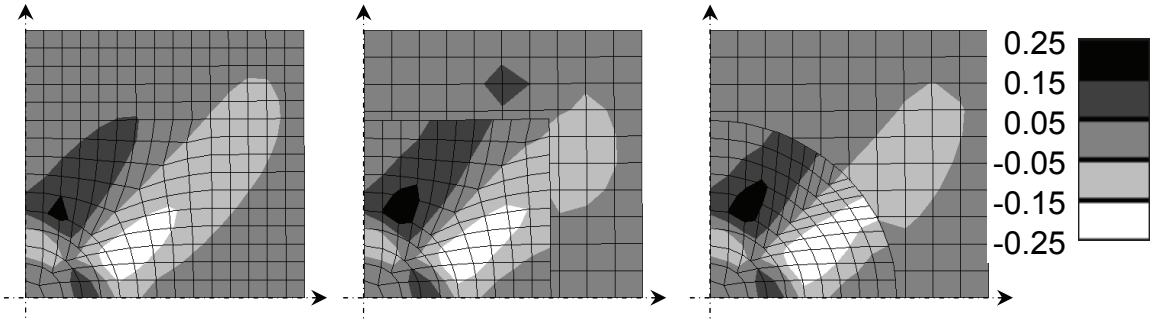

(a) Conventional (b) Mesh Overlay -1 (c) Mesh Overlay -2

Fig. 3.6 Shear strain rate $\dot{\varepsilon}_{xy}$ distributions at U/L=0.02 of rigid-plastic plate compression with softer inclusion

Figure 3.7 shows the equivalent strain rate $\dot{\bar{\varepsilon}}$ distributions at nominal longitudinal displacement U/L=0.02 (the first step) by the conventional analysis and the mesh overlay

analysis, respectively. These distributions are close to each other.

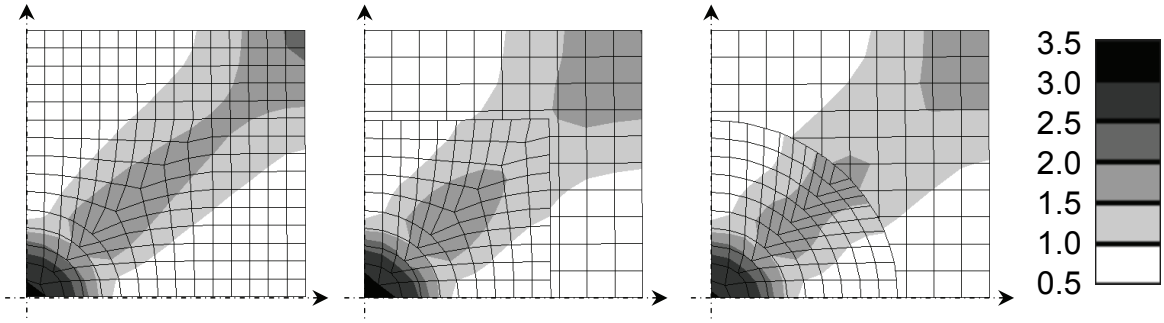

(a) Conventional (b) Mesh Overlay -1 (c) Mesh Overlay -2

Fig. 3.7 Equivalent strain rate $\dot{\bar{\varepsilon}}$ distributions at U/L=0.02 of rigid-plastic plate compression with softer inclusion

Figure 3.8 shows the longitudinal strain rate $\dot{\varepsilon}_y$ distributions at nominal longitudinal displacement U/L=0.10 (the fifth step) by the conventional analysis and the mesh overlay analysis, respectively. Both solutions obtained by the mesh overlay method still show the closest distributions to the conventional one. That is, the inclusion deforms larger than the matrix since the inclusion is softer than the matrix, as observed at nominal longitudinal displacement U/L=0.02.

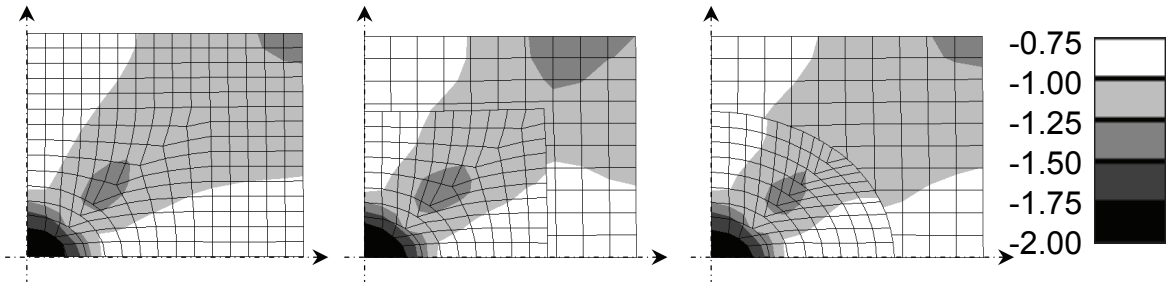

(a) Conventional (b) Mesh Overlay -1 (c) Mesh Overlay -2

Fig. 3.8 Longitudinal strain rate $\dot{\varepsilon}_y$ distributions at U/L=0.10 of rigid-plastic plate compression with softer inclusion

Figure 3.9 represents the shear strain rate $\dot{\varepsilon}_{xy}$ distributions at nominal longitudinal displacement U/L=0.10 (the fifth step) by the conventional analysis and the mesh overlay analysis, respectively. Since the inclusion deforms large, positive shear strain rate

appears near the top of the inclusion, and negative shear strain rate appears near the side of the inclusion, as shown at nominal longitudinal displacement U/L=0.02.

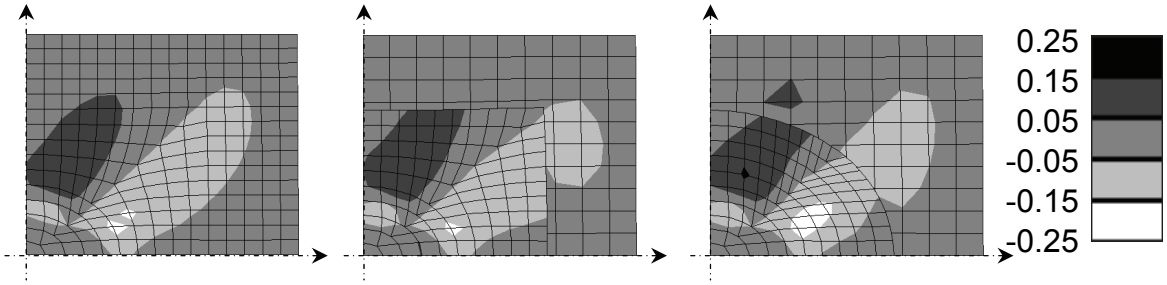

(a) Conventional (b) Mesh Overlay -1 (c) Mesh Overlay -2

Fig. 3.9 Shear strain rate $\dot{\varepsilon}_{xy}$ distributions at U/L=0.10 of rigid-plastic plate compression with softer inclusion

Figure 3.10 shows the equivalent strain rate $\dot{\bar{\varepsilon}}$ distributions at nominal longitudinal displacement U/L=0.10 (the fifth step) by the conventional method and the mesh overlay method, respectively. Again, the solutions obtained by the mesh overlay method show the closest distributions to the conventional one.

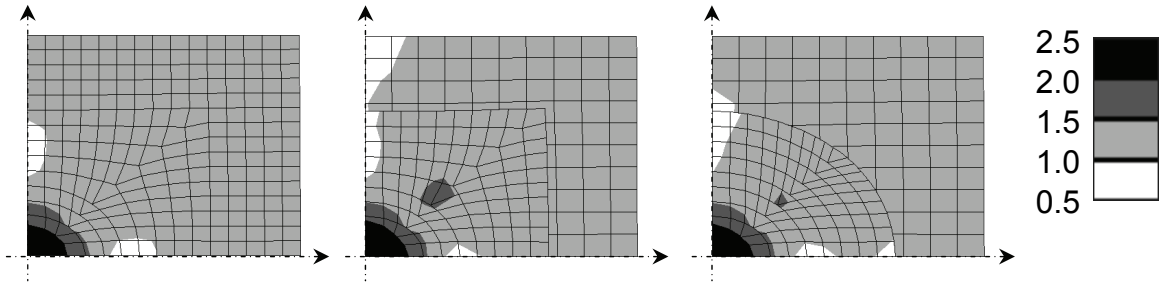

(a) Conventional (b) Mesh Overlay -1 (c) Mesh Overlay -2

Fig. 3.10 Equivalent strain rate $\dot{\bar{\varepsilon}}$ distributions at U/L=0.10 of rigid-plastic plate compression with softer inclusion

Figure 3.11 expresses the equivalent strain $\bar{\varepsilon}$ distributions at nominal longitudinal displacement U/L=0.30 (the last step) by the conventional method and the mesh overlay one, respectively. Closest distribution to the conventional analysis is still obtained by the mesh overlay analysis.

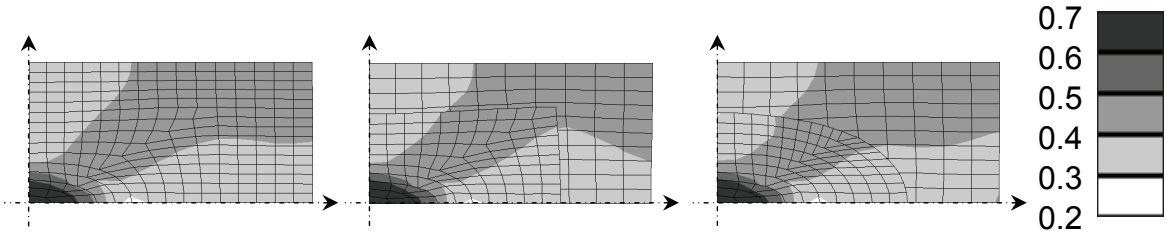

(a) Conventional (b) Mesh Overlay -1 (c) Mesh Overlay -2

Fig. 3.11 Equivalent strain $\bar{\varepsilon}$ distributions at U/L=0.30 of rigid-plastic plate compression with softer inclusion

3.3.4 Computational Results (Case B: Harder Inclusion)

Next, case B, when the inclusion is harder than the matrix, is investigated. **Figure 3.12** shows the longitudinal strain rate $\dot{\varepsilon}_y$ distributions at nominal longitudinal displacement U/L=0.02 (the first step) by the conventional analysis and the mesh overlay analysis, respectively. In this case, the solutions by the mesh overlay method and that by the conventional one practically coincide, while the opposite tendency to the previous case is observed. That is, the inclusion does not deform very much due to its hardness. Hence, the magnitude of the longitudinal strain rate $\dot{\varepsilon}_y$ of the matrix near the x-axis and y-axis becomes large.

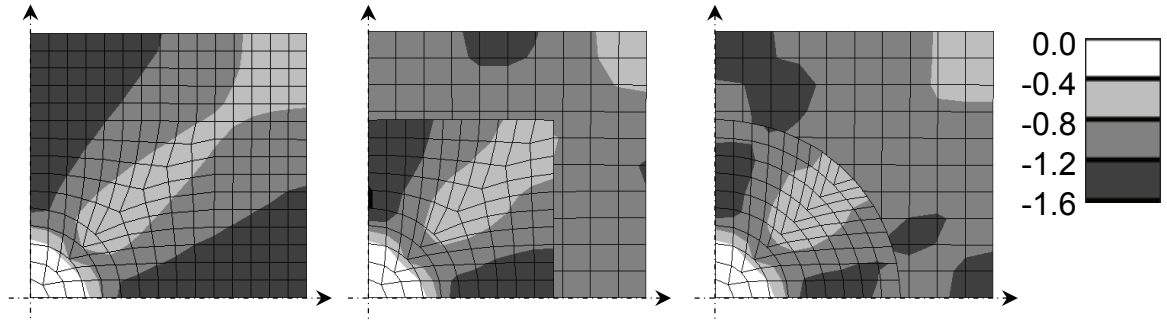

(a) Conventional (b) Mesh Overlay -1 (c) Mesh Overlay -2

Fig. 3.12 Longitudinal strain rate $\dot{\varepsilon}_y$ distributions at U/L=0.02 of rigid-plastic plate compression with harder inclusion

Figure 3.13 represents the shear strain rate $\dot{\varepsilon}_{xy}$ distributions at nominal longitudinal displacement U/L=0.02 (the first step) by the conventional analysis and the mesh overlay

analysis, respectively. Both solutions by the mesh overlay method show good agreement with the one by the conventional method. Because of the small deformation of the inclusion, negative shear strain rate appears on the matrix near the top of the inclusion, and positive shear strain rate appears near the side of the inclusion.

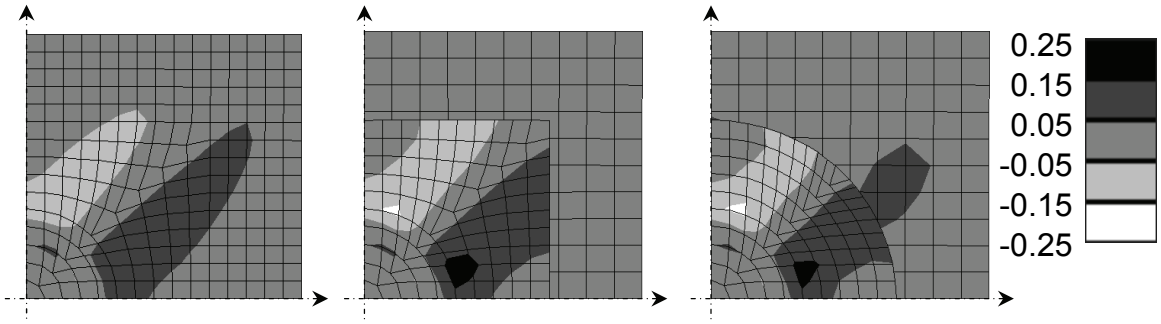

(a) Conventional (b) Mesh Overlay -1 (c) Mesh Overlay -2

Fig. 3.13 Shear strain rate $\dot{\varepsilon}_{xy}$ distributions at U/L=0.02 of rigid-plastic plate compression with harder inclusion

Figure 3.14 shows the equivalent strain rate $\dot{\bar{\varepsilon}}$ distributions at nominal longitudinal displacement U/L=0.02 (the first step) by the conventional analysis and the mesh overlay analysis, respectively. The equivalent strain rate at the region where strain localizes in the previous case becomes smaller than that of the surrounding region, as described above. Moreover, it is also found that the mesh overlay analysis gives results close to the conventional analysis.

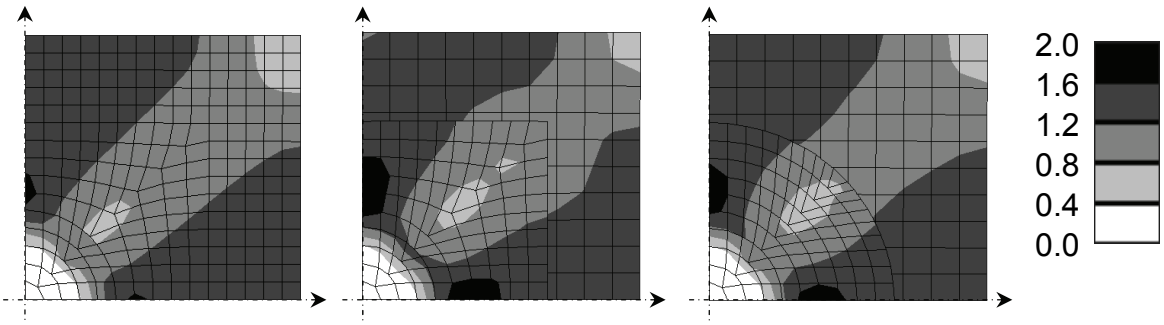

(a) Conventional (b) Mesh Overlay -1 (c) Mesh Overlay -2

Fig. 3.14 Equivalent strain rate $\dot{\bar{\varepsilon}}$ distributions at U/L=0.02 of rigid-plastic plate compression with harder inclusion

Figure 3.15 shows the longitudinal strain rate $\dot{\varepsilon}_y$ distributions at nominal longitudinal displacement U/L=0.10 (the fifth step) by the conventional analysis and the mesh overlay analysis, respectively. Also from these figures, it is observed that the inclusion does not deform very much due to its hardness. Again, the acquired distributions of the mesh overlay analysis and the conventional analysis are close.

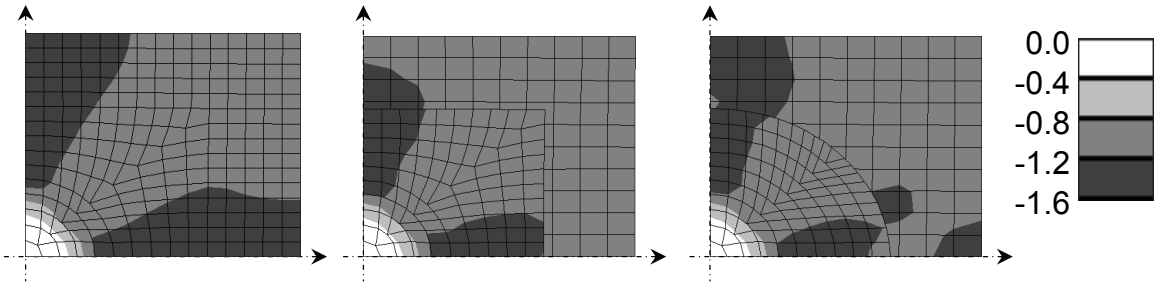

(a) Conventional (b) Mesh Overlay -1 (c) Mesh Overlay -2

Fig. 3.15 Longitudinal strain rate $\dot{\varepsilon}_y$ distributions at U/L=0.10 of rigid-plastic plate compression with harder inclusion

Figure 3.16 shows the shear strain rate $\dot{\varepsilon}_{xy}$ distributions at nominal longitudinal displacement U/L=0.10 (the fifth step) by the conventional analysis and the mesh overlay analysis, respectively. The solutions by the mesh overlay method show good agreement with the one by the conventional one. Because of the small deformation of the inclusion, negative shear strain rate appears on the matrix near the top of the inclusion, and positive shear strain rate appears near the side of the inclusion, as shown at nominal longitudinal displacement U/L=0.02.

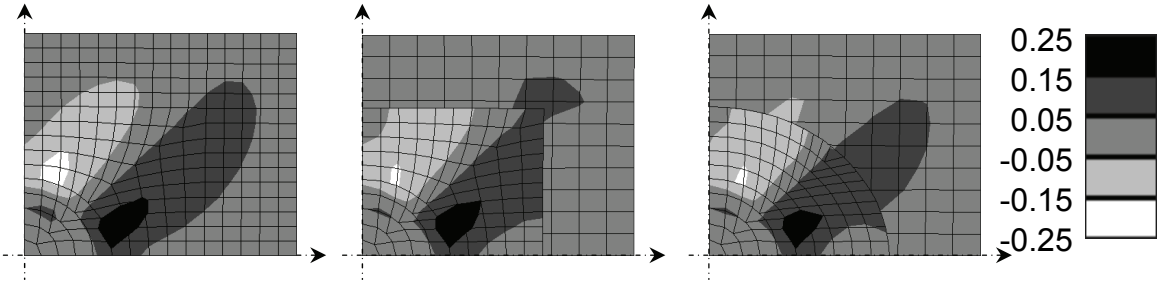

(a) Conventional (b) Mesh Overlay (c) Mesh Overlay -2

Fig. 3.16 Shear strain rate $\dot{\varepsilon}_{xy}$ distributions at U/L=0.10 of rigid-plastic plate compression with harder inclusion

Figure 3.17 shows the equivalent strain rate $\dot{\bar{\varepsilon}}$ distributions at nominal longitudinal displacement U/L=0.10 (the fifth step) by the conventional analysis and the mesh overlay analysis, respectively. Again, both solutions obtained by the mesh overlay method show distribution close to the conventional one.

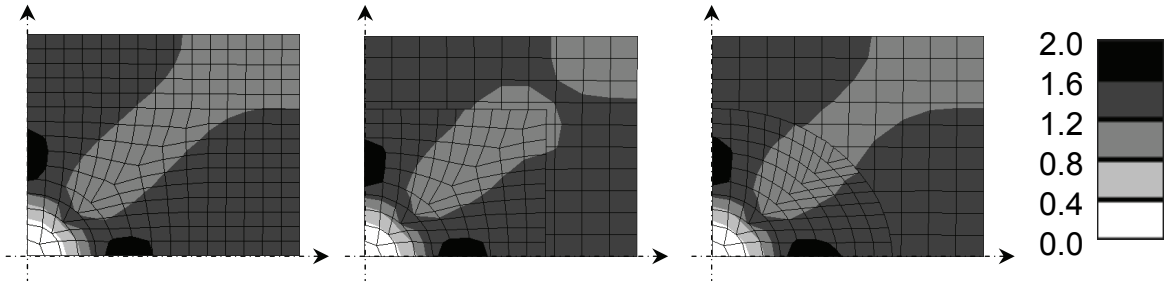

(a) Conventional (b) Mesh Overlay (c) Mesh Overlay -2

Fig. 3.17 Equivalent strain rate $\dot{\bar{\varepsilon}}$ distributions at U/L=0.10 of rigid-plastic plate compression with harder inclusion

Figure 3.18 shows the equivalent strain $\bar{\varepsilon}$ distribution at nominal longitudinal displacement U/L=0.30 (the last step) by the conventional method and the mesh overlay method, respectively. The inclusion does not deform very much since it is harder than the matrix. Close distribution to the conventional method is still acquired by the mesh overlay method.

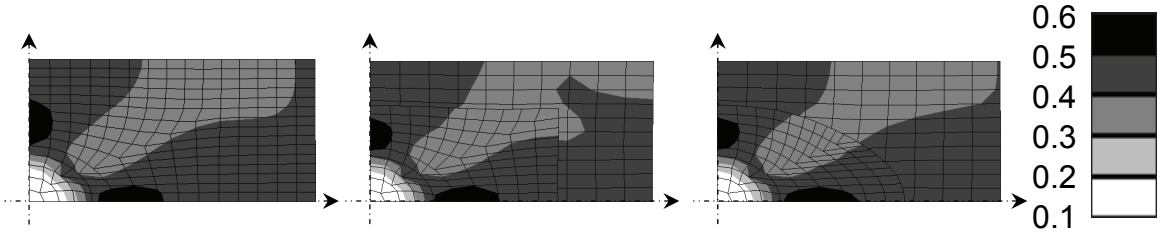

(a) Conventional (b) Mesh Overlay (c) Mesh Overlay -2

Fig. 3.18 Equivalent strain $\bar{\varepsilon}$ distributions at U/L=0.30 of rigid-plastic plate compression with harder inclusion

Additionally, it was shown that there is no guarantee of finding the converged solution for the conventional mesh overlay analysis due to the negative energy when the inclusion in the local model is harder than the matrix in the global model[53]. However,

in the present method, since the material constants of the global model where the local model overlays does not affect the stiffness equations, harder inclusion cases were also computed successfully.

3.3.5 Effect of Volume Constancy Constraints

In the present formulations, the stiffness of the global model where the local model overlays it does not have any effect on the stiffness equations. Therefore, the global velocity in the local region is indeterminate although the velocity in the local region, which is the summation of the global and local velocities, is unique. Actually, if the material constants for the global model and those for the local model are the same, this numerical instability may occur even for elastic analysis. In order to overcome this instability, the order of the global element is set to be different from that of the local model[46),49)]. Or, a different local mesh discretization pattern is used to the global one[54)]. In another solution, the constraints that do not allow the local element that overlays two or more global elements are adopted[29),32),46),52),54)]. These constraints, however, spoil the flexibility of the local model placement, one of the most important features of the mesh overlay method. Additionally, although adding a trivial value to the diagonal components of the stiffness matrix was proposed to increase the numerical stability[53)], the size of the added value is left entirely up to the analyst.

In this research, in order to restrain severe global deformation at the overlaid region, the volume constancy conditions are also imposed for the global model where the local model covers it, as shown in eq. (3.27) on page 75. Since the plastic deformation is incompressible, this constraint would not invite any artifacts. Here, the effectiveness of this constraint is verified through numerical examples for a plane strain compression of a rigid-plastic plate with a rectangular inclusion. Here, the 2×2 elements near the origin in the local model express the inclusion.

If this constraint is not imposed, the volume constancy conditions are expressed in eq. (3.94).

$$\begin{cases} \dot{\varepsilon}_V{}^G = 0 & in \quad \Omega^G \\ \dot{\varepsilon}_V{}^G + \dot{\varepsilon}_V{}^L = 0 & in \quad \Omega^L \end{cases} \tag{3.94}$$

In this case, the first constraint is imposed only in the global model where the local model does not cover. **Figure 3.19** shows the equivalent strain distribution at nominal longitudinal displacement U/L=0.30.

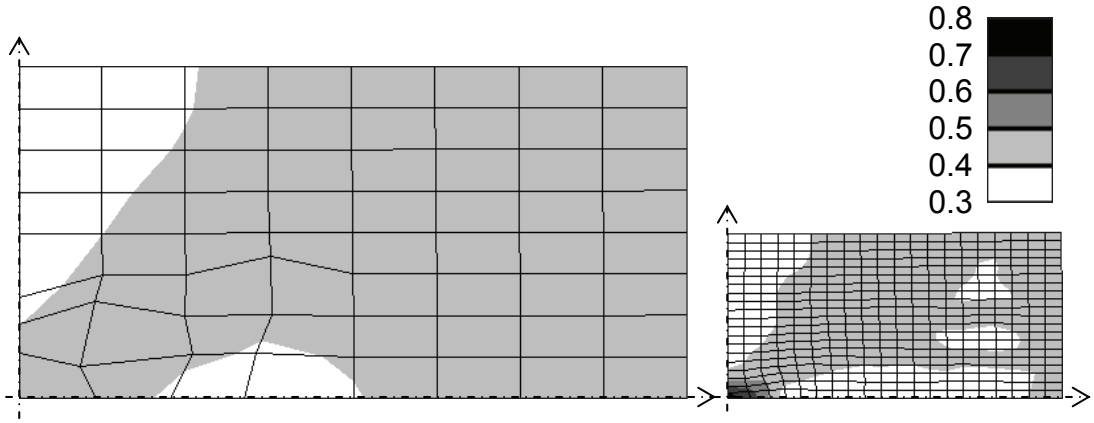

Fig. 3.19 Equivalent strain $\bar{\varepsilon}$ distribution at U/L=0.30 when eq. (3.94) is adopted as volume constancy conditions

It is found that the global element where the local model covers it deforms severely. The local model deformation does not seem to be severe since the local model deformation is represented as the summation of the global and local displacements in this figure. However, the local model itself also deforms severely in order to compensate for the global model deformation. Because these severe deformations invite heavy distortion and degrade the accuracy of the computational simulation, such excessive deformation should be prevented. Therefore, in order to restrain the severe deformation of the global model, the volume constancy conditions are modified in the present formulations, as shown in eq. (3.27). **Figure 3.20** shows the equivalent strain distribution at nominal longitudinal displacement U/L=0.30 under the present constraints.

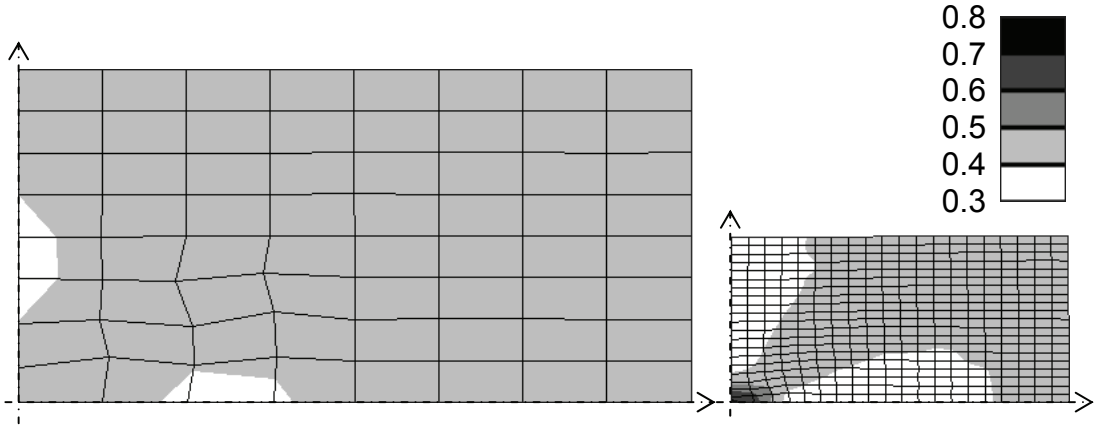

Fig. 3.20 Equivalent strain $\bar{\varepsilon}$ distribution at U/L=0.30 when eq. (3.27) is adopted as volume constancy conditions

Due to the constraints on the global model where the local model covers, global model's affected deformation is reduced. Moreover, the equivalent strain $\bar{\varepsilon}$ in the local model becomes reasonable, because severe shear strain is prevented. However, unnecessary deformation still occurs in the global model where the local model overlays it. Although more improvement to restrain the nonessential deformation in the overlaid region is required, this constraint controls the global model deformation.

3.3.6 Summary

In this section, the deformation behavior of a plane strain plate with a circular inclusion at the center under compression was investigated based on the mesh overlay formulations for rigid-plastic analysis derived in the previous section. Two types of the local model were adopted: one was quadrilateral, and the other was circular. It was verified that the mesh overlay method gives results close to conventional method for either harder inclusion or softer inclusion. Additionally, in order to control severe global element deformation in the local region, imposing the volume constant conditions to these global elements was proposed. Through the numerical examples, it was found that this restraint is efficient in preventing severe deformation of the global model.

3.4 Numerical Examples for Much Small Local Model

3.4.1 Introduction

Surface defects degrade the quality of metal products. Therefore, it is important to clarify the mechanism of surface defect occurrence in order to take preventative measures during the metal forming process. It is said that the metal flow under the rolling process drives inclusions to the surface, and surface defects occur when an inclusion reaches to the surface. Generally, the diameter of an inclusion is 0.1mm (100μm) or less, whereas the initial dimensions of a slab for steel plates/sheets are about 250mm thickness and over 1000mm width. Therefore, if the analyst tried to simulate micro deformation behavior of an inclusion and its vicinity under macro deformation behavior of a slab in order to verify this assumption by conventional FEM, the number of elements would become too many to compute because of the element size. In such cases, the mesh overlay method is effective. Especially when the local model, set on the inclusion and its vicinity, is much smaller than the global element, the mesh overlay formulations can be simplified as shown in subsection 3.2.5.

In this section, the velocity field at the vicinity of the inclusion under simple forging is computed by the mesh overlay method, and it is verified whether the metal flow that makes the inclusion come to the surface is observed.

3.4.2 Computational Conditions

A plane strain plate with a circler inclusion at the center is considered, as shown in **Fig. 3.21**. Here, due to the symmetry of the deformation, one quarter of the model is considered. The length and width of the plate are $2L$ and $2W$, and the diameter of the inclusion is ϕ. The longitudinal displacement rate $\dot{U}$ is given at $y = \pm L$, and no lateral displacement rates are applied on this boundary.

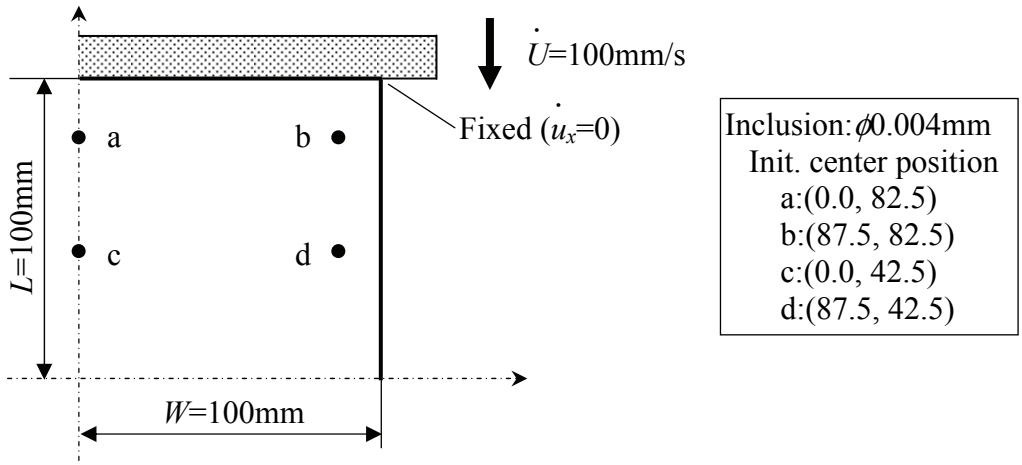

Fig. 3.21 Computational model of rigid-plastic plate compression with much small inclusion

The computational conditions are shown in **Table 3.2**. Both the initial length $2L$ and width $2W$ of the plate are 200mm, and the diameter of the inclusion is 4.0×10^{-3}mm (4.0μm), much smaller when compared to the plate size. The center of the inclusion is set on (a) (x, y)=(0.0, 82.5), (b) (x, y)=(87.5, 82.5), (c) (x, y)=(0.0, 42.5) and (d) (x, y)=(87.5, 42.5). The material hardening law is already shown in eq. (3.92). The material constant of the deformation resistance for the matrix K_0 is 100MPa; that for the inclusion K_1 is 50MPa in case A, and 200MPa in case B. Therefore, the inclusion is twice as soft as the matrix in case A, and twice as hard in case B. The strain hardening index n for both the matrix and the inclusion is the same, 0.20. The strain rate sensitivity index m for both the matrix and the inclusion is also the same, 0.10. Nominal longitudinal displacement rate $\dot{U}/L$ is 1.0. The time step Δt is 0.02 sec, and the number of steps N is 6. Therefore, after the final step, the nominal longitudinal displacement U/L becomes 0.12.

Table 3.2 Computational conditions of rigid-plastic plate compression with much small inclusion

Initial length of plate	$2L$	200	mm
Initial width of plate	$2W$	200	mm
Initial diameter of inclusion	ϕ	0.004	mm
Nominal longitudinal displacement rate	$\dot{U}/L$	1.0	
Deformation resistance of matrix	K_0	100	MPa
Deformation resistance of inclusion (case A)	K_1	50	MPa
Deformation resistance of inclusion (case B)	K_1	200	MPa
Strain hardening index	n	0.20	
Strain rate sensitivity index	m	0.10	
Time step	Δt	0.02	sec
Number of steps	N	6	

Figure 3.22 shows the mesh discretization of the global and local models for the mesh overlay analysis. The global model, which covers the whole area of the model, is divided into 20×20 meshes. The local model is divided into 40×40 meshes. As shown in Fig. 3.22, the local model size is 0.04mm×0.04mm, which is much smaller than the global element that has 5mm×5mm dimensions. Hence, the local model is wholly included in one global element. Here, the grayed mesh means the inclusion.

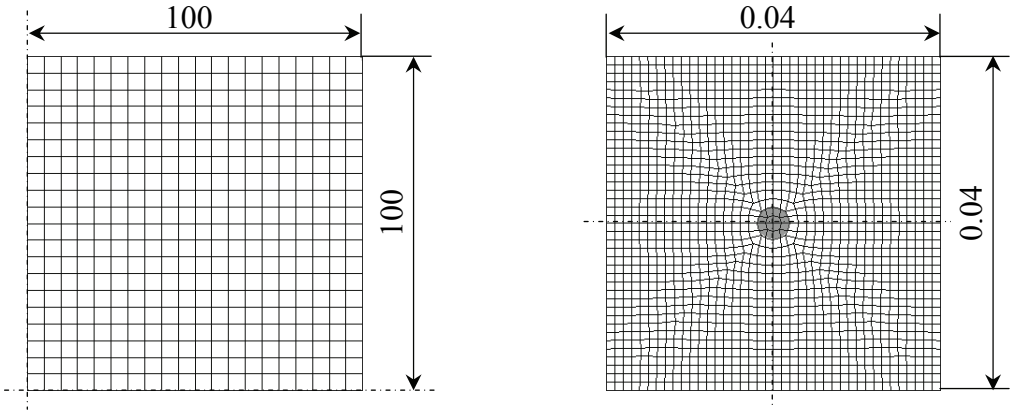

(a) Global model (b) Local model

Fig. 3.22 Mesh discretization for mesh overlay method of rigid-plastic plate compression with much small inclusion

Four-node linear isoparametric quadrilateral elements are adopted. The number of Gauss points is 2×2 per element for both the global and local elements.

3.4.3 Computational Results (Case A: Softer Inclusion)

Figure 3.23 shows the equivalent strain $\bar{\varepsilon}$ distribution at nominal longitudinal displacement U/L=0.12 of the global model. From the figure, point a is in the rigid zone where almost no deformation occurs; point b is in the shear band where severe deformation occurs. Point c and d are close to the shear band.

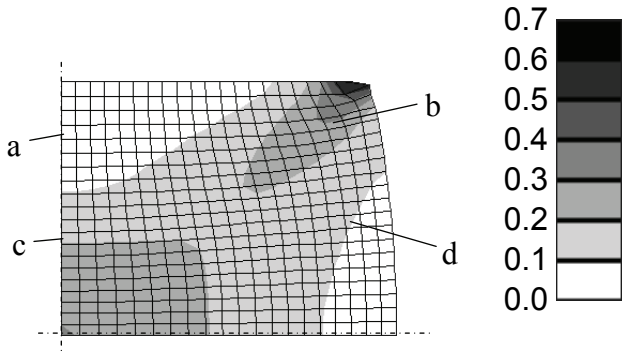

Fig. 3.23 Equivalent strain $\bar{\varepsilon}$ distribution at U/L = 0.12 of rigid-plastic plate compression with much small softer inclusion

The local longitudinal velocity $\dot{u}^L_y$ distributions at nominal longitudinal displacement U/L=0.12 for the local models set on point a, b, c and d are represented in **Fig. 3.24**. At point b and c, the local longitudinal velocity $\dot{u}^L_y$ is negative at the upper region of the inclusion; it is positive at the lower region of the inclusion. Therefore, the metal flow seems to make the inclusion come out to the surface. However, the global longitudinal velocity $\dot{u}^G_y$ at point a, b, c and d are -99.3mm/s, -66.4mm/s, -70.6mm/s and -18.5mm/s, respectively. Hence, as compared to the global longitudinal velocity $\dot{u}^G_y$, the local longitudinal velocity $\dot{u}^L_y$ is small so it can be neglected. Therefore, the metal flow that drives the inclusion to the surface is not observed. This velocity field is supposed to occur due to the following procedures: the inclusion deforms more than the matrix, since the inclusion is softer than the matrix. Therefore, the matrix near the inclusion should have a large deformation. Hence, the local longitudinal velocity $\dot{u}^L_y$ becomes negative at the upper region of the inclusion, and a conflicting local velocity field is observed at the lower region of the inclusion.

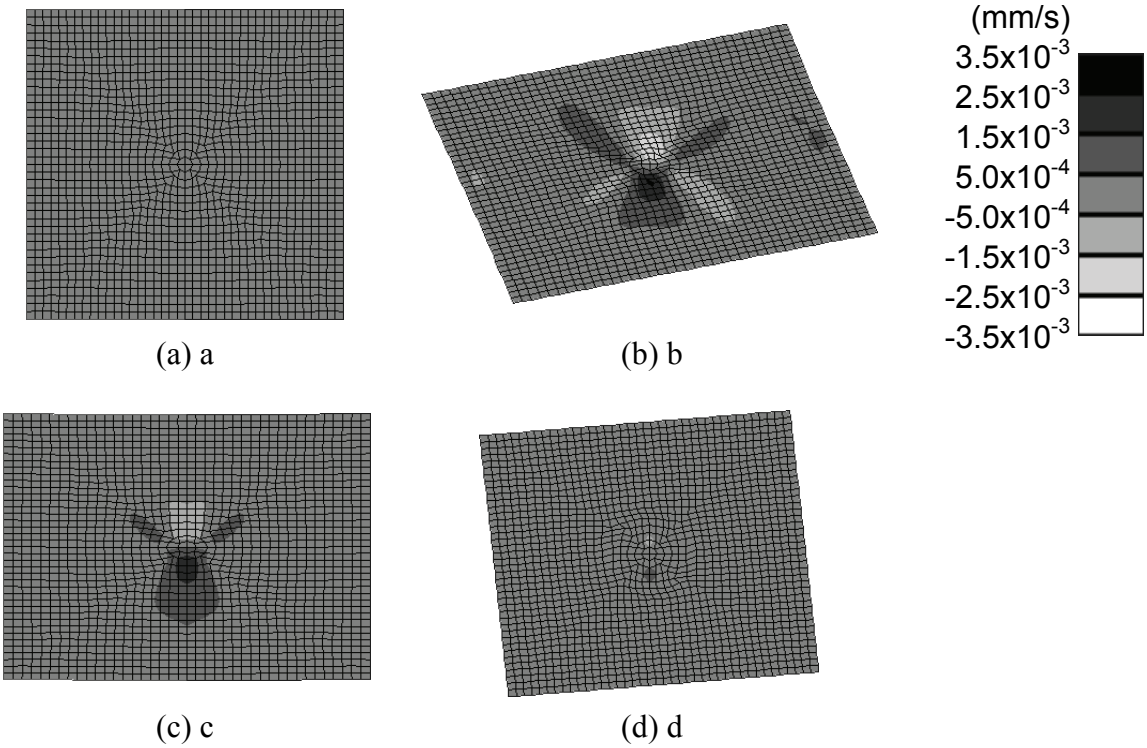

Fig. 3.24 Local longitudinal velocity $\dot{u}^L_y$ distributions at U/L = 0.12 of rigid-plastic plate compression with much small softer inclusion (cf.:$\dot{u}= \dot{u}^G + \dot{u}^L$)

Here, the inclusion seems to rotate at points b and d. However, this phenomenon is observed even when the inclusion has the same material constants as the matrix, as shown in **Fig. 3.25**. Therefore, it is concluded that the inclusion rotation is caused by the mesh discretization, and is not essential.

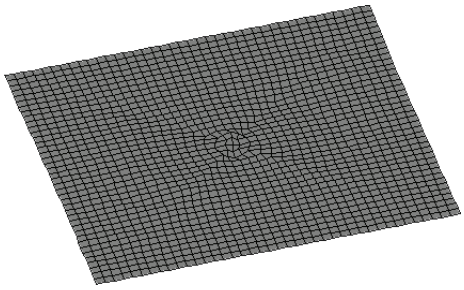

Fig. 3.25 Local longitudinal velocity $\dot{u}^L_y$ distributions at U/L = 0.12 when inclusion has same material constants

3.4.4 Computational Results (Case B: Harder Inclusion)

The equivalent strain $\bar{\varepsilon}$ distribution of the global model at nominal longitudinal displacement U/L=0.12 is shown in **Fig. 3.26**. Similar strain distributions are obtained as in the previous case, since the inclusion is too small to affect the global metal flow.

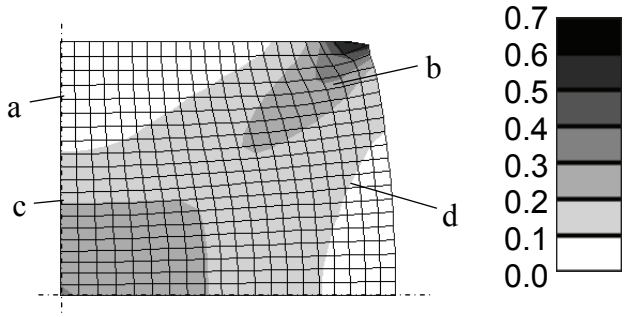

Fig. 3.26 Equivalent strain $\bar{\varepsilon}$ distribution at U/L = 0.12 of rigid-plastic plate compression with much small harder inclusion

Figure 3.27 shows the local longitudinal velocity $\dot{u}^L_y$ distributions at nominal longitudinal displacement U/L=0.12 for the local models set on point a, b, c and d. The global longitudinal velocity $\dot{u}^G_y$ at point a, b, c and d are -99.3mm/s, -66.9mm/s,

-71.6mm/s and -18.5mm/s, respectively. Therefore, the local longitudinal velocity $\dot{u}^L_y$ is so small it can be neglected compared to the global longitudinal velocity $\dot{u}^G_y$. Since the inclusion is harder than the matrix, the local longitudinal velocity $\dot{u}^L_y$ is positive at the upper region of the inclusion, and conflicting local velocity field is observed at the lower region of the inclusion.

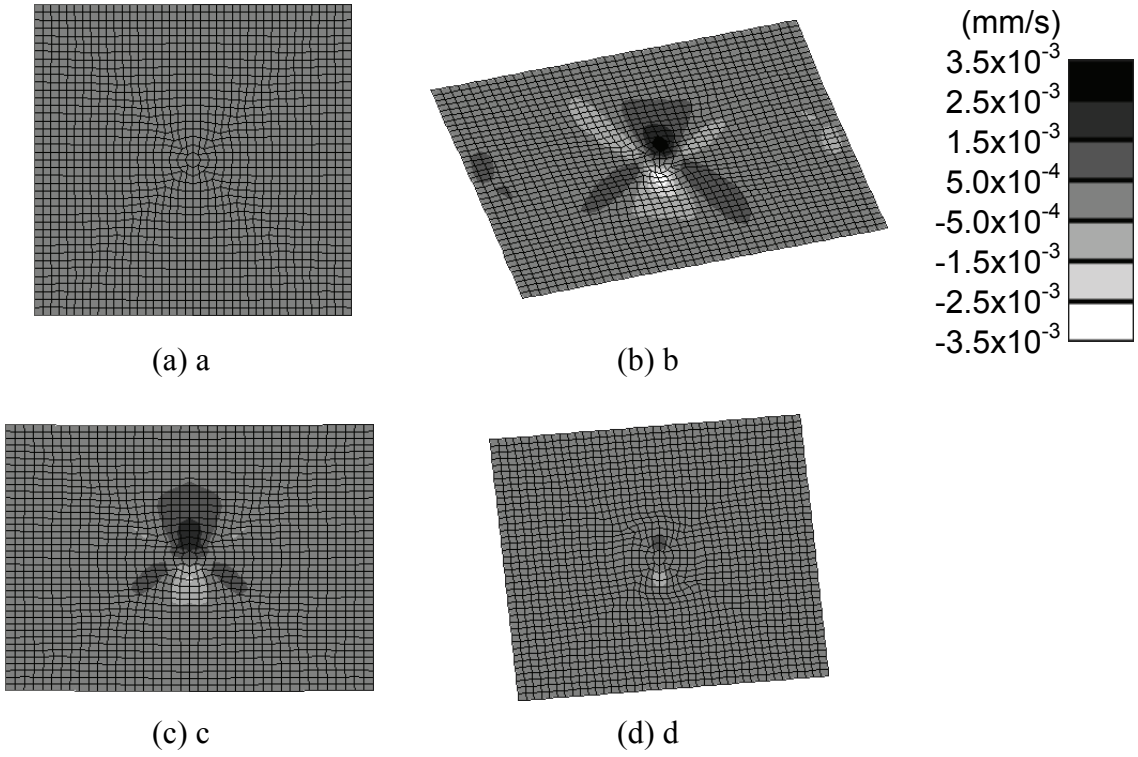

Fig. 3.27 Local longitudinal velocity $\dot{u}^L_y$ distributions at $U/L = 0.12$ of rigid-plastic plate compression with much small harder inclusion (cf.:$\dot{u} = \dot{u}^G + \dot{u}^L$)

3.4.5 Summary

The deformation behavior of a simple forging of a bulk with a small inclusion was investigated using the mesh overlay method. Both softer and harder inclusions were computed. However, the metal flow that raises the inclusion to the surface was not observed. Hence, it was concluded that there is another mechanism for defects due to inclusion appearance at the surface; for example, the affection of the delamination between the matrix and the inclusion[59),67)], or, the inhomogeneity of the matrix due to the temperature distribution in the global metal flow.

3.5 Numerical Examples of Efficient Three-dimensional Analysis -I

3.5.1 Introduction

The combined analysis of a two-dimensional global model and a three-dimensional local model has already been verified in the previous chapter for elastic problems. In this section, this approach is applied to rigid-plastic analysis, and the features of the present mesh overlay analysis are confirmed.

3.5.2 Computational Conditions

A block with a spherical inclusion at the center is considered, as shown in **Fig. 3.28**. Here, due to the symmetry of the deformation, one-eighth of the model is considered. The length, width and thickness of the block are $2L$, $2W$ and $2H$, and the diameter of the inclusion is $2r$. The longitudinal displacement rate $\dot{U}$ is given. As the boundary conditions, $f_x = f_z = 0$ (no shear forces: μ=0) is imposed on the displacement rate boundary ($y = \pm L$). The z-directional displacement rate $\dot{u}_z = 0$ is also applied at $z = \pm H$.

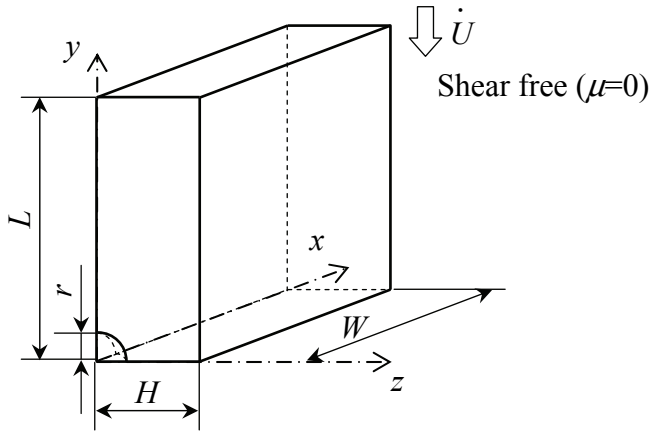

Fig. 3.28 Computational model of rigid-plastic block compression with spherical inclusion

The computational conditions are shown in **Table 3.3**. Both the initial length $2L$ and width $2W$ of the block are 20mm, the initial thickness $2H$ is 10mm, and the initial

diameter of the inclusion $2r$ is 2mm. The material hardening law is already shown in eq. (3.92). The material constant of the deformation resistance for the matrix K_0 is 100MPa; that for the inclusion K_1 is 50MPa in case A, and 200MPa in case B. Therefore, the inclusion is twice softer than the matrix in case A, and twice harder in case B. The strain hardening index n for both the matrix and the inclusion is the same, 0.20. The strain rate sensitivity index m for both the matrix and the inclusion is also the same, 0.10. Nominal longitudinal displacement rate $\dot{U}/L$ is 1.0. The time step Δt is 0.02 sec, and the number of the steps N is 15. Therefore, after the final step, the nominal longitudinal displacement U/L becomes 0.30.

Table 3.3 Computational conditions of rigid-plastic block compression with spherical inclusion

Initial length of block	$2L$	20	mm
Initial width of block	$2W$	20	mm
Initial thickness of block	$2H$	10	mm
Initial diameter of inclusion	$2r$	2	mm
Nominal longitudinal displacement rate	$\dot{U}/L$	1.0	sec^{-1}
Deformation resistance of matrix	K_0	100	MPa
Deformation resistance of inclusion (case A)	K_1	50	MPa
Deformation resistance of inclusion (case B)	K_1	200	MPa
Strain hardening index	n	0.20	
Strain rate sensitivity index	m	0.10	
Time step	Δt	0.02	sec
Number of steps	N	15	

Figure 3.29 shows the mesh discretization of the global and local models for the mesh overlay analysis. The global model, which covers the whole area of the model, is divided into 10×10 meshes. The local model is divided into $10 \times 10 \times 10$ meshes. Here, the grayed mesh represents the inclusion. Moreover, conventional analysis is also computed as a reference solution, as shown in **Fig. 3.30**, where the mesh discretization is $20 \times 20 \times 10$.

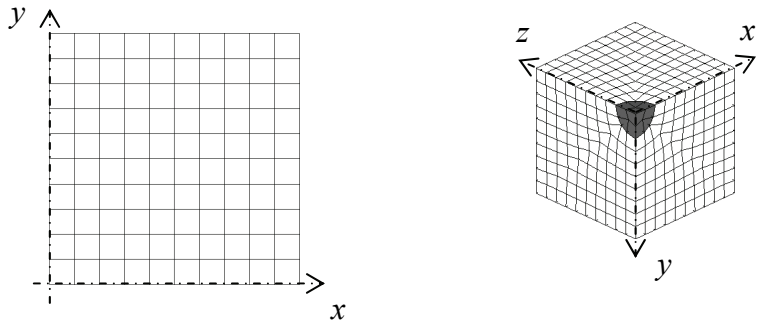

(a) Global model (b) Local model

Fig. 3.29 Mesh discretization for mesh overlay method of rigid-plastic block compression with spherical inclusion

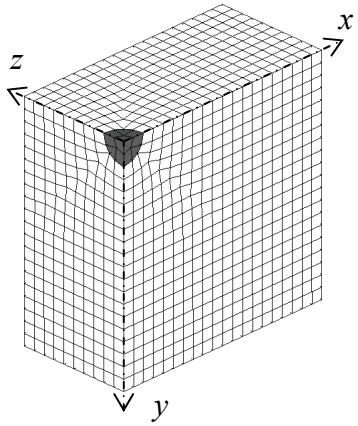

Fig. 3.30 Mesh discretization for conventional method of rigid-plastic block compression with spherical inclusion

Here, four-node linear isoparametric quadrilateral elements are adopted for the global model, and eight-node linear isoparametric hexahedral elements are adopted for the local model and the conventional analysis. The number of Gauss points is 4×4 and $4\times4\times4$ per element for the global and local elements, respectively; it is $2\times2\times2$ for the conventional analysis.

3.5.3 Computational Results (Case A: Softer Inclusion)

Let us consider case A, the softer inclusion case, first. **Figure 3.31** shows the y-directional strain rate $\dot{\varepsilon}_y$ distributions at nominal longitudinal displacement U/L=0.02 (the first step) by conventional method and the mesh overlay method, respectively. The solution acquired by the mesh overlay method shows the closest distributions to the conventional one. That is, the inclusion deforms larger than the matrix since the inclusion is softer than the matrix. Moreover, while the inclusion is largely compressed along the y-direction, the inclusion spreads to the x- and z-direction because the inclusion volume remains constant. Additionally, the magnitude of the y-directional strain rate $\dot{\varepsilon}_y$ at the vicinity region of the inclusion along the x- and y-axis becomes smaller than that of the surrounding region. It is also found that the y-directional strain rate $\dot{\varepsilon}_y$ distributes at the inclusion and its vicinity, though the strain rate distribution becomes uniform at the region farthest from the inclusion. Therefore, a three-dimensional analysis is required at the vicinity of the inclusion.

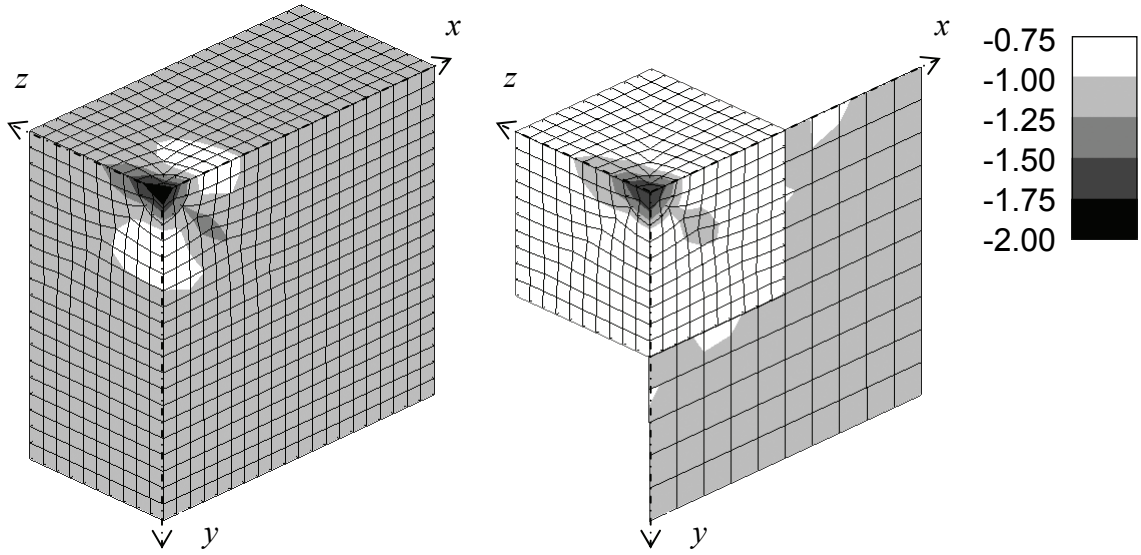

(a) Conventional (b) Mesh Overlay

Fig. 3.31 y-directional strain rate $\dot{\varepsilon}_y$ distributions at U/L=0.02 of rigid-plastic block compression with softer spherical inclusion

Figure 3.32 shows the z-directional strain rate $\dot{\varepsilon}_z$ distributions at nominal longitudinal displacement U/L=0.02 (the first step) by the conventional analysis and the mesh overlay analysis, respectively. Both distributions are similar. Positive z-directional strain rate $\dot{\varepsilon}_z$ is observed at the vicinity of the inclusion along the x-axis and a 45-degree direction on the yz-plane (x=0 plane); negative z-directional strain rate $\dot{\varepsilon}_z$ is also represented along the y-axis and a 45-degree direction on the zx-plane (y=0 plane). The mechanism can be considered as follows: this deformation of the inclusion along the x-axis, described above, causes deformation of the adjacent matrix along the z-axis in order to satisfy the volume constancy conditions. Again, the distribution at the inclusion and its vicinity proves that a three-dimensional analysis is required to analyze the deformation at this region.

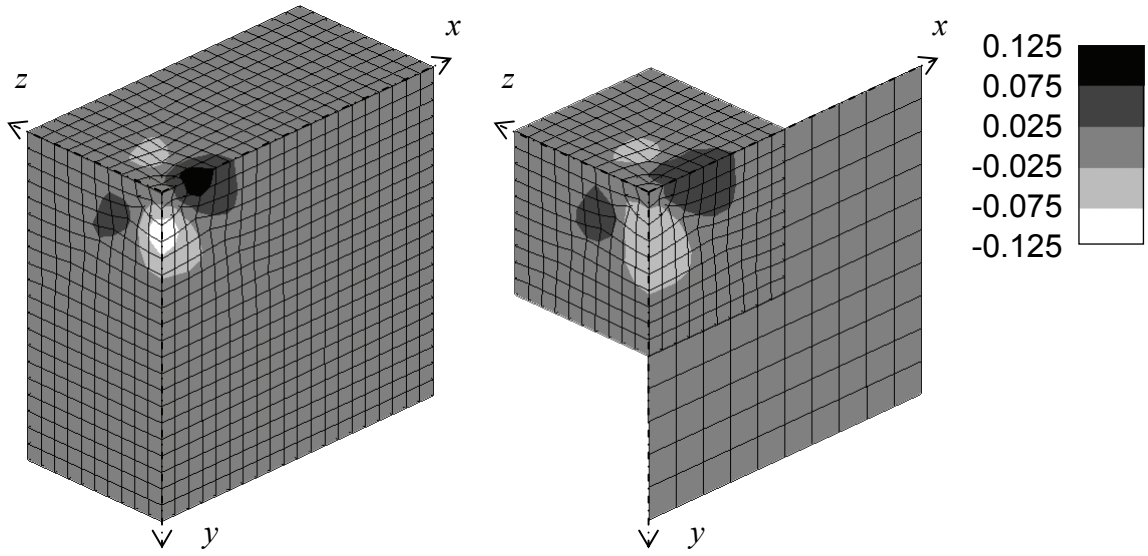

(a) Conventional (b) Mesh Overlay

Fig. 3.32 z-directional strain rate $\dot{\varepsilon}_z$ distributions at U/L=0.02 of rigid-plastic block compression with softer spherical inclusion

Figure 3.33 shows the shear strain rate $\dot{\varepsilon}_{xy}$ distributions at nominal longitudinal displacement U/L=0.02 (the first step) by the conventional analysis and the mesh overlay analysis, respectively. The solution acquired by the mesh overlay method shows the closest distribution to the conventional method. That is, because of the large deformation at the inclusion, positive and negative shear strain appear near the inclusion on the *xy*-plane.

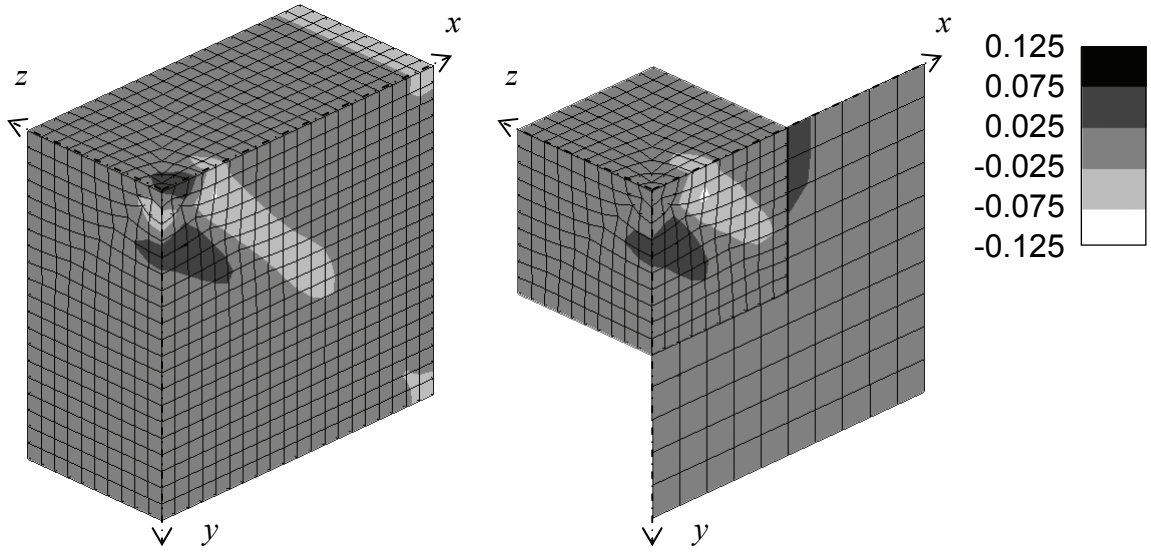

(a) Conventional (b) Mesh Overlay

Fig. 3.33 *xy*-shear strain rate $\dot{\varepsilon}_{xy}$ distributions at U/L=0.02 of rigid-plastic block compression with softer spherical inclusion

Figure 3.34 shows the equivalent strain rate $\dot{\bar{\varepsilon}}$ distributions at nominal longitudinal displacement U/L=0.02 (the first step) by the conventional method and the mesh overlay method, respectively. The mesh overlay analysis gives the closest distribution to the conventional analysis, although the magnitude of the equivalent strain rate at the inclusion identified by the mesh overlay analysis is rather small compared to that found by the conventional analysis.

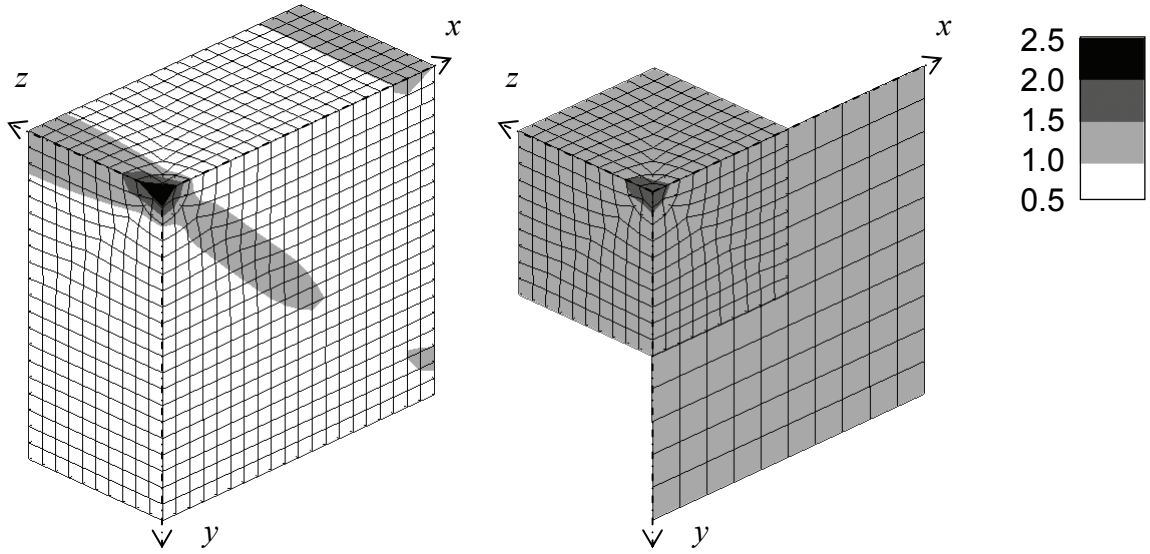

(a) Conventional (b) Mesh Overlay

Fig. 3.34 Equivalent strain rate $\dot{\bar{\varepsilon}}$ distributions at U/L=0.02 of rigid-plastic block compression with softer spherical inclusion

Figures 3.35~38 show the y-directional strain rate $\dot{\varepsilon}_y$, the z-directional strain rate $\dot{\varepsilon}_z$, the shear strain rate $\dot{\varepsilon}_{xy}$ and the equivalent strain rate $\dot{\bar{\varepsilon}}$ distributions at nominal longitudinal displacement U/L=0.10 (the fifth step) by the conventional analysis and the mesh overlay analysis, respectively. Both distributions show good agreement with each other, and the same tendency as observed at nominal longitudinal displacement U/L=0.02 is recognized.

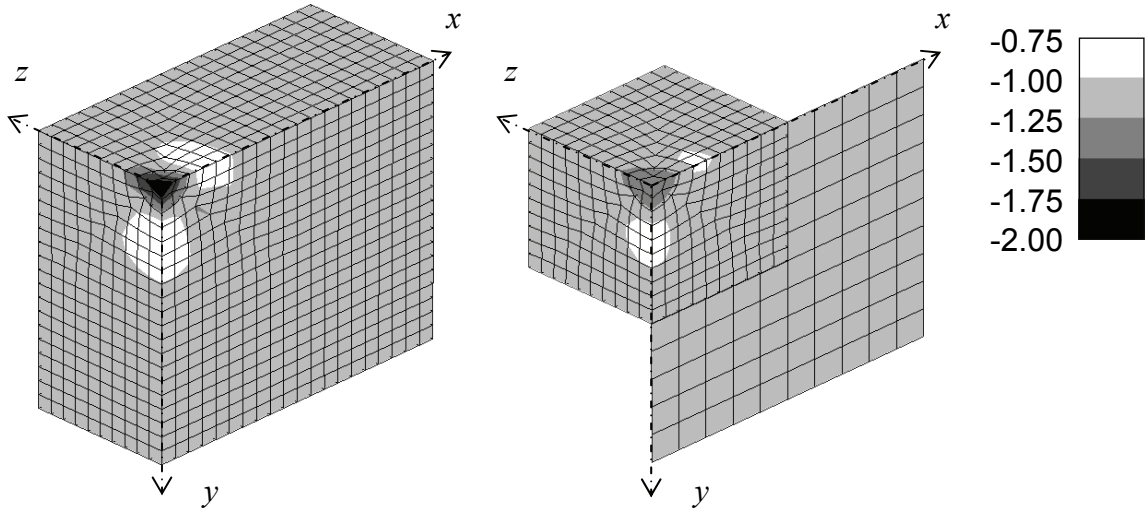

(a) Conventional (b) Mesh Overlay

Fig. 3.35 y-directional strain rate $\dot{\varepsilon}_y$ distributions at U/L=0.10 of rigid-plastic block compression with softer spherical inclusion

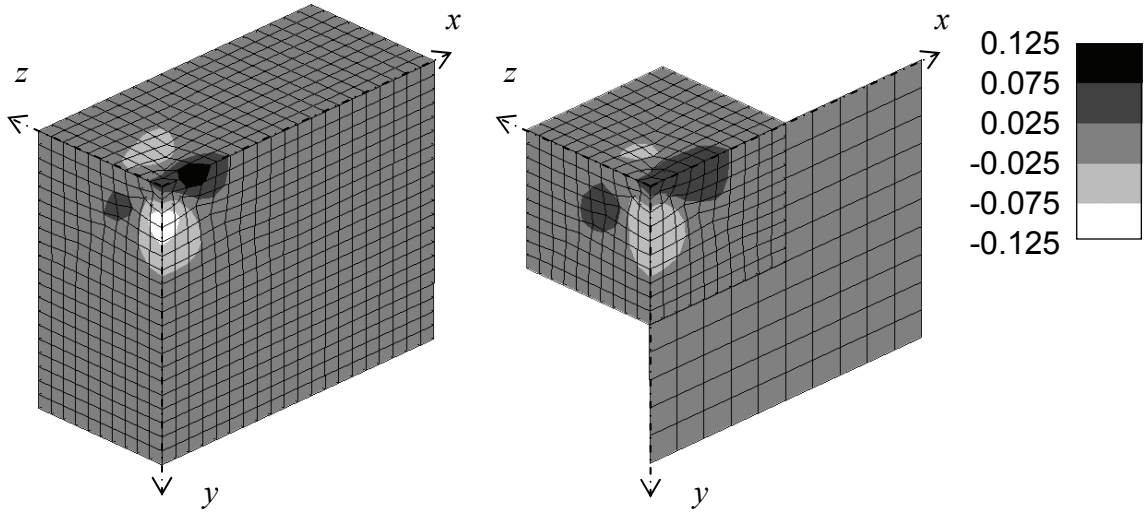

(a) Conventional (b) Mesh Overlay

Fig. 3.36 z-directional strain rate $\dot{\varepsilon}_z$ distributions at U/L=0.10 of rigid-plastic block compression with softer spherical inclusion

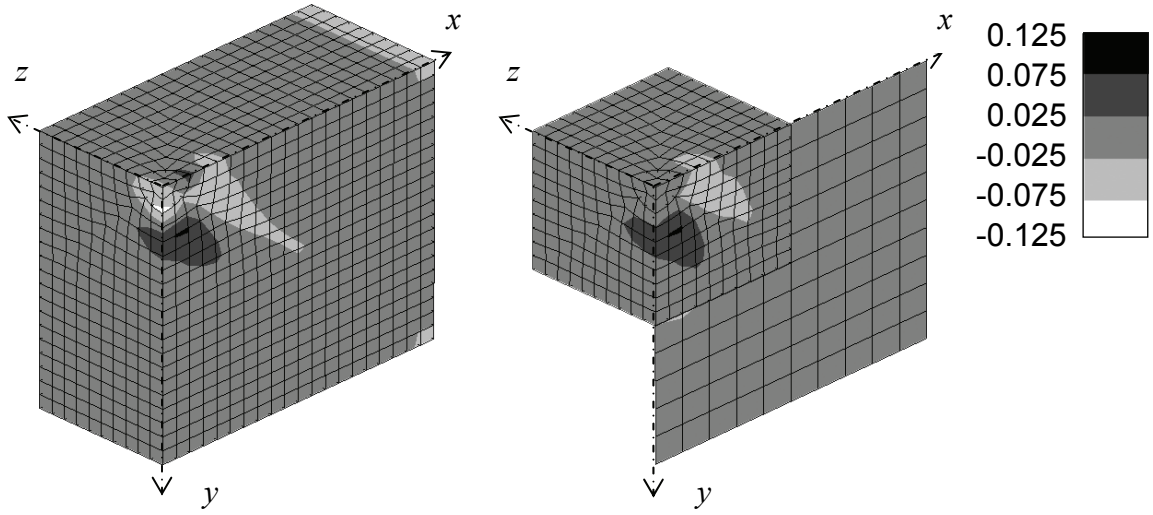

(a) Conventional (b) Mesh Overlay

Fig. 3.37 *xy*-shear strain rate $\dot{\varepsilon}_{xy}$ distributions at U/L=0.10 of rigid-plastic block compression with softer spherical inclusion

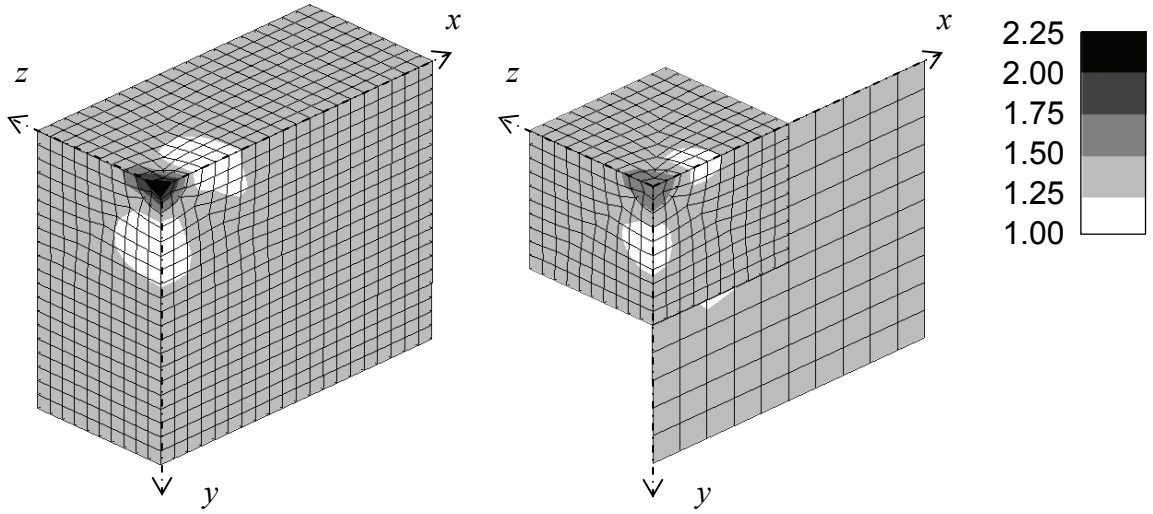

(a) Conventional (b) Mesh Overlay

Fig. 3.38 Equivalent strain rate $\dot{\bar{\varepsilon}}$ distributions at U/L=0.10 of rigid-plastic block compression with softer spherical inclusion

Figure 3.39 shows the equivalent strain $\bar{\varepsilon}$ distributions at nominal longitudinal displacement U/L=0.30 (the final step) by the conventional analysis and the mesh overlay analysis, respectively. The obtained strain distribution by the mesh overlay method is

similar to the conventional one. These figures also indicate that the inclusion deformation is larger than that of the matrix because it is relatively softer.

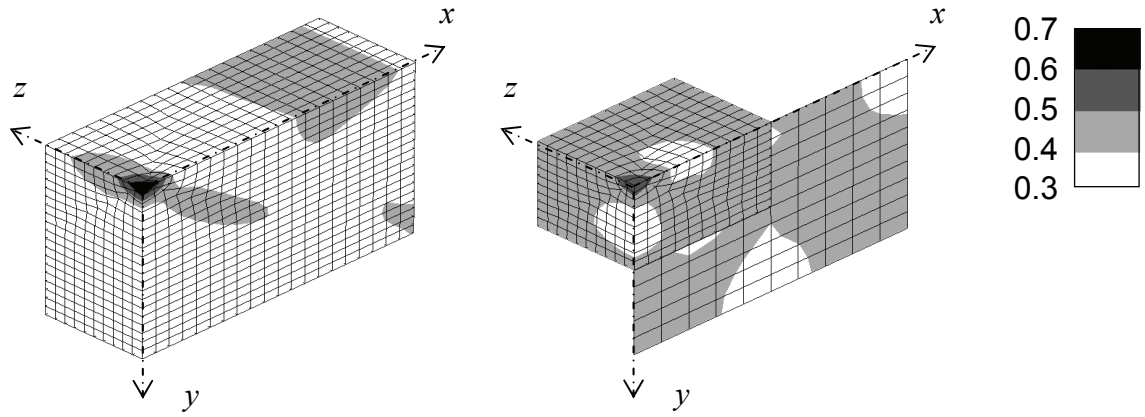

(a) Conventional (b) Mesh Overlay

Fig. 3.39 Equivalent strain $\bar{\varepsilon}$ distributions at U/L=0.30 of rigid-plastic block compression with softer spherical inclusion

Figure 3.40 shows the traces of the standard deviation of each strain rate component. The standard deviation is already defined in eq. (2.57). Each standard deviation is small compared to the magnitude of the nominal lateral strain rate $\dot{U}/L$=1.

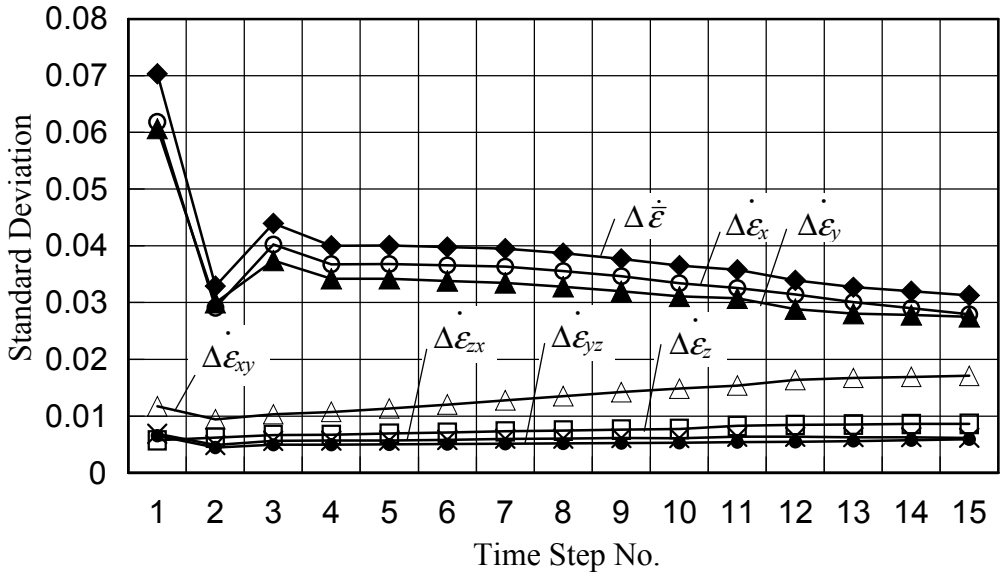

Fig. 3.40 Standard deviation traces of strain rate in local model of rigid-plastic block compression with softer spherical inclusion

3.5.4 Computational Results (Case B: Harder Inclusion)

Next, the harder inclusion case, case B, is investigated. **Figure 3.41** shows the y-directional strain rate $\dot{\varepsilon}_y$ distributions at nominal longitudinal displacement U/L=0.02 (the first step) by the conventional method and the mesh overlay method, respectively. In this case, the inclusion does not deform very much since the inclusion is harder than the matrix. Therefore, large deformation occurs at the vicinity of the inclusion along the x- and y-axis. On the other hand, the deformation at its vicinity along the z-axis and a 45-degree direction on the xy-plane (z=0 plane) becomes smaller than the averaged deformation. Both results show good agreement. Additionally, the farther the distance from the inclusion, the milder the distribution becomes. That is, the deformation characteristic in a certain region including the inclusion shows a three-dimensional flow. Hence, a three-dimensional approach is necessary to investigate the deformation behavior around the inclusion.

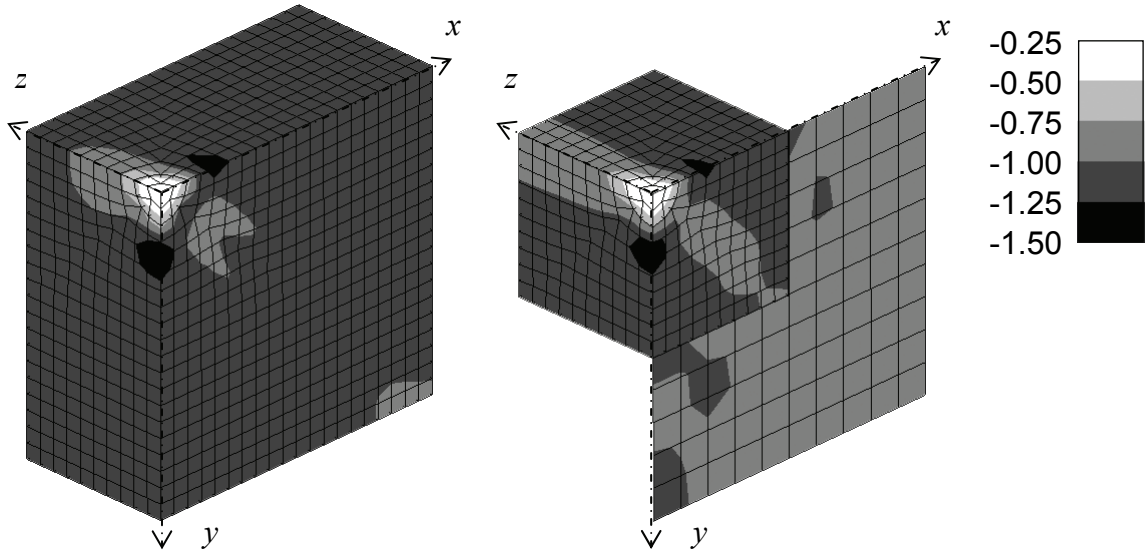

(a) Conventional (b) Mesh Overlay

Fig. 3.41 y-directional strain rate $\dot{\varepsilon}_y$ distributions at U/L=0.02 of rigid-plastic block compression with harder spherical inclusion

Figure 3.42 shows the z-directional strain rate $\dot{\varepsilon}_z$ distributions at nominal longitudinal displacement U/L=0.02 (the first step) by the conventional analysis and the mesh overlay analysis, respectively. Positive large z-directional strain rate $\dot{\varepsilon}_z$ is observed at the vicinity of the inclusion along the y-axis and 45-degree direction on the zx-plane (y=0 plane), while negative z-directional strain rate $\dot{\varepsilon}_z$ is also observed along the x-axis and a 45-degree direction on the yz-plane (x=0 plane). The distributions become gradual with increasing distance from the inclusion. Both figures show these features well. Positive z-directional strain rate $\dot{\varepsilon}_z$ along the y-axis is caused in order to compensate large y-directional strain rate $\dot{\varepsilon}_y$, owing to the volume constancy conditions. Similarly, negative z-directional strain rate $\dot{\varepsilon}_z$ along the x-axis is observed due to large x-directional strain rate $\dot{\varepsilon}_x$ compensation.

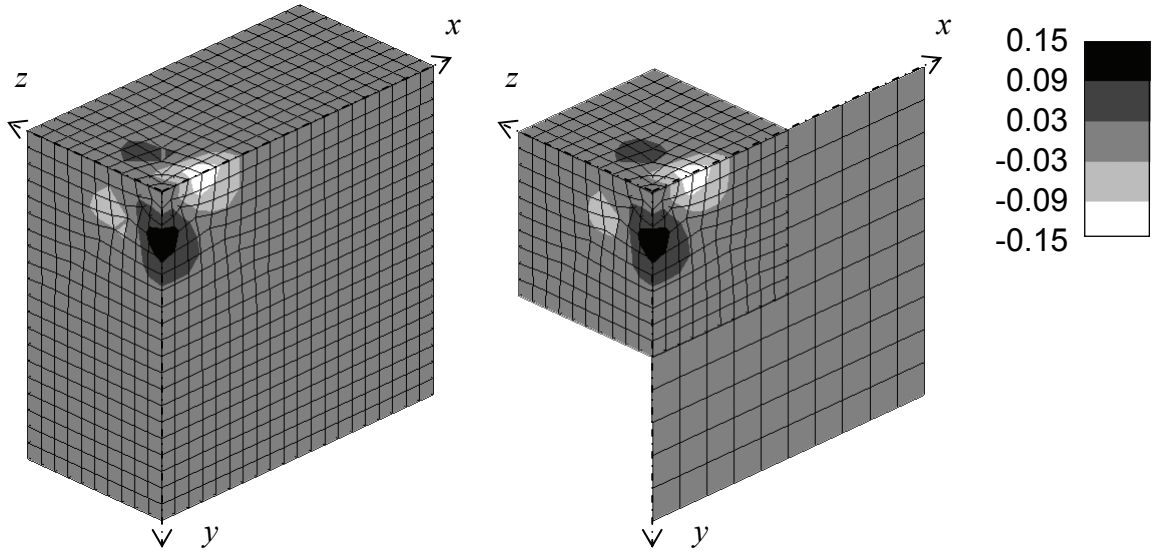

(a) Conventional (b) Mesh Overlay

Fig. 3.42 z-directional strain rate $\dot{\varepsilon}_z$ distributions at U/L=0.02 of rigid-plastic block compression with harder spherical inclusion

Figure 3.43 shows the shear strain rate $\dot{\varepsilon}_{xy}$ distributions at nominal longitudinal displacement U/L=0.02 (the first step) by the conventional method and the mesh overlay method, respectively. The distribution by the mesh overlay analysis agrees with that by the conventional analysis.

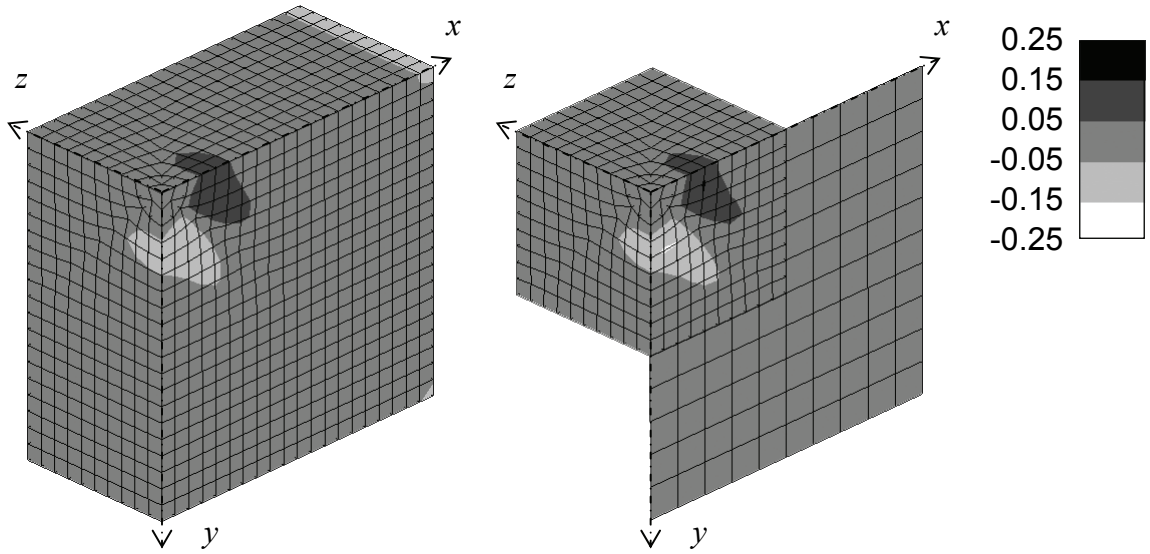

(a) Conventional (b) Mesh Overlay

Fig. 3.43 *xy*-shear strain rate $\dot{\varepsilon}_{xy}$ distributions at U/L=0.02 of rigid-plastic block compression with harder spherical inclusion

Figure 3.44 shows the equivalent strain rate $\dot{\bar{\varepsilon}}$ distributions at nominal longitudinal displacement U/L=0.02 (the first step) by the conventional analysis and the mesh overlay analysis, respectively. Similar distributions are achieved by the mesh overlay method and the conventional method.

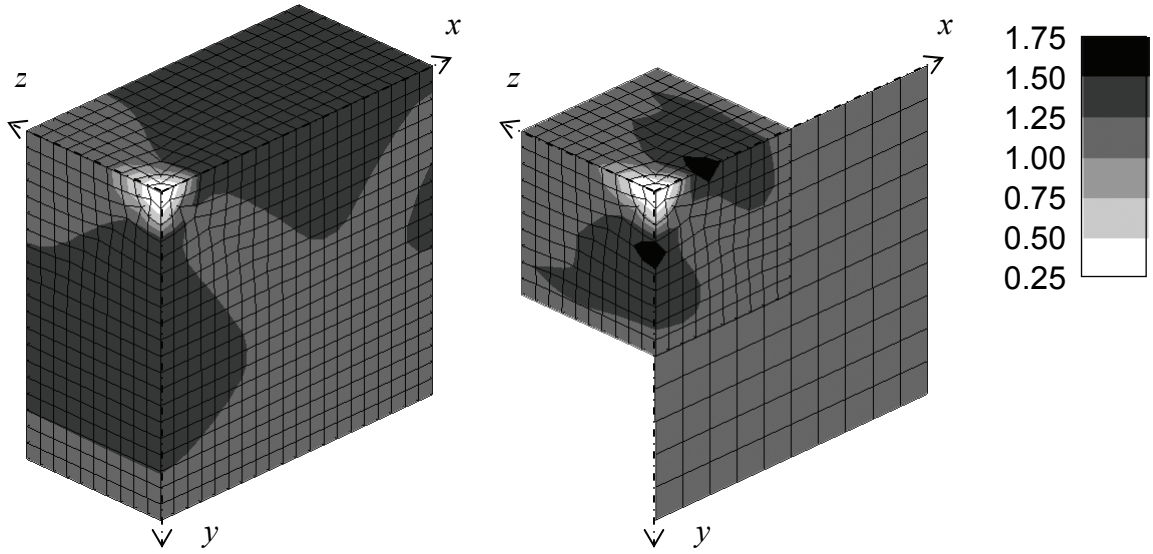

(a) Conventional (b) Mesh Overlay

Fig. 3.44 Equivalent strain rate $\dot{\bar{\varepsilon}}$ distributions at U/L=0.02 of rigid-plastic block compression with harder spherical inclusion

Figures 3.45~3.48 show the y-directional strain rate $\dot{\varepsilon}_y$, the z-directional strain rate $\dot{\varepsilon}_z$, the shear strain rate $\dot{\varepsilon}_{xy}$ and the equivalent strain rate $\dot{\bar{\varepsilon}}$ distributions at nominal longitudinal displacement U/L=0.10 (the fifth step) by the conventional method and the mesh overlay method, respectively. Both distributions still show good agreement, and the same tendency observed at nominal longitudinal displacement U/L=0.02 is represented.

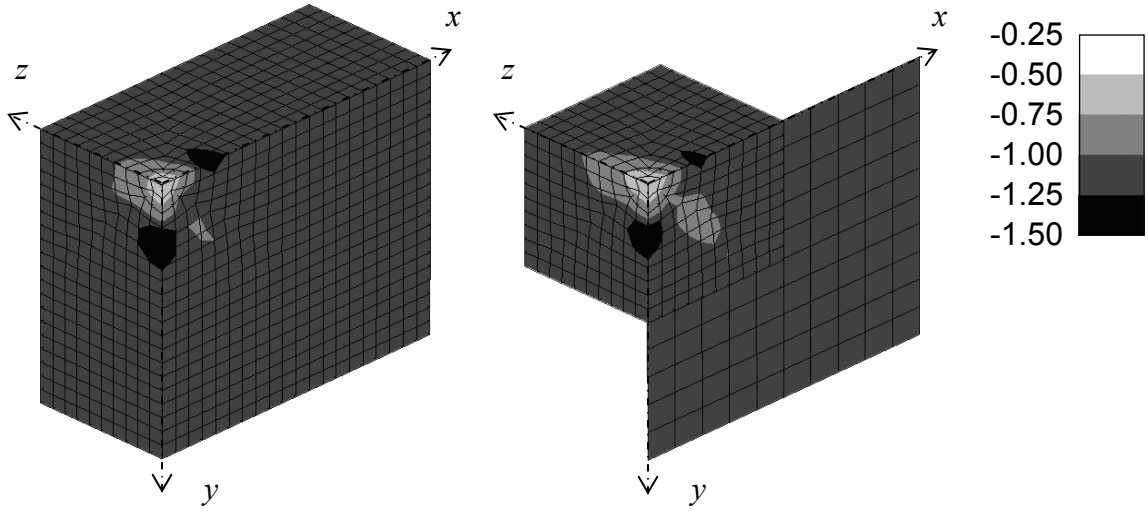

(a) Conventional (b) Mesh Overlay

Fig. 3.45 y-directional strain rate $\dot{\varepsilon}_y$ distributions at U/L=0.10 of rigid-plastic block compression with harder spherical inclusion

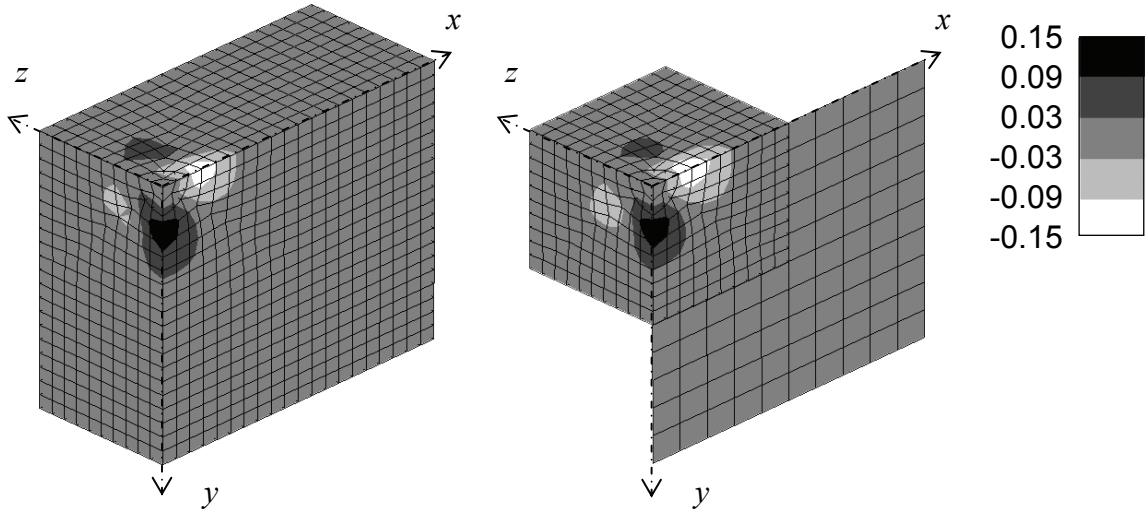

(a) Conventional (b) Mesh Overlay

Fig. 3.46 z-directional strain rate $\dot{\varepsilon}_z$ distributions at U/L=0.10 of rigid-plastic block compression with harder spherical inclusion

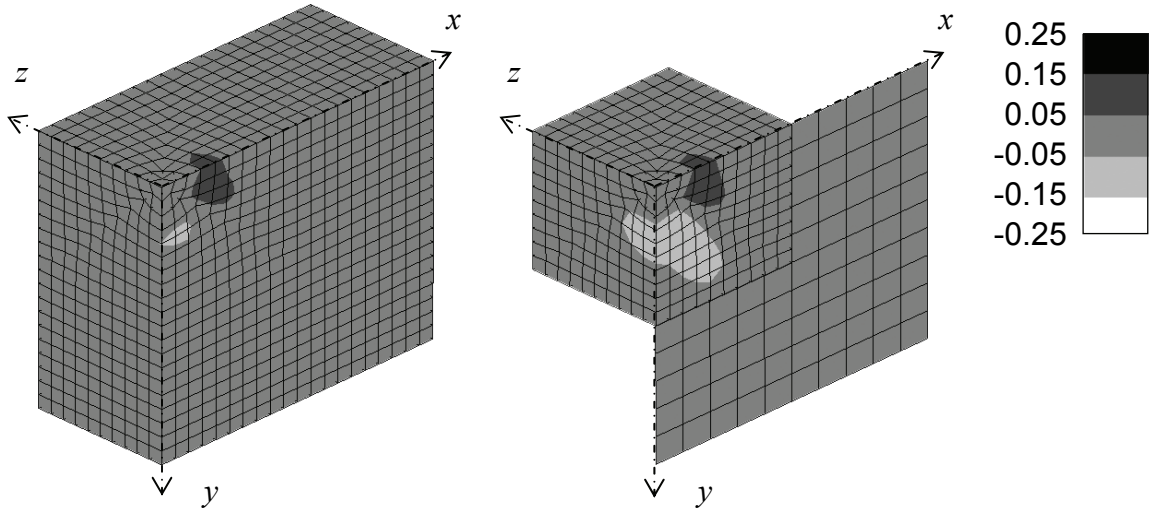

(a) Conventional (b) Mesh Overlay

Fig. 3.47 *xy*-shear strain rate $\dot{\varepsilon}_{xy}$ distributions at U/L=0.10 of rigid-plastic block compression with harder spherical inclusion

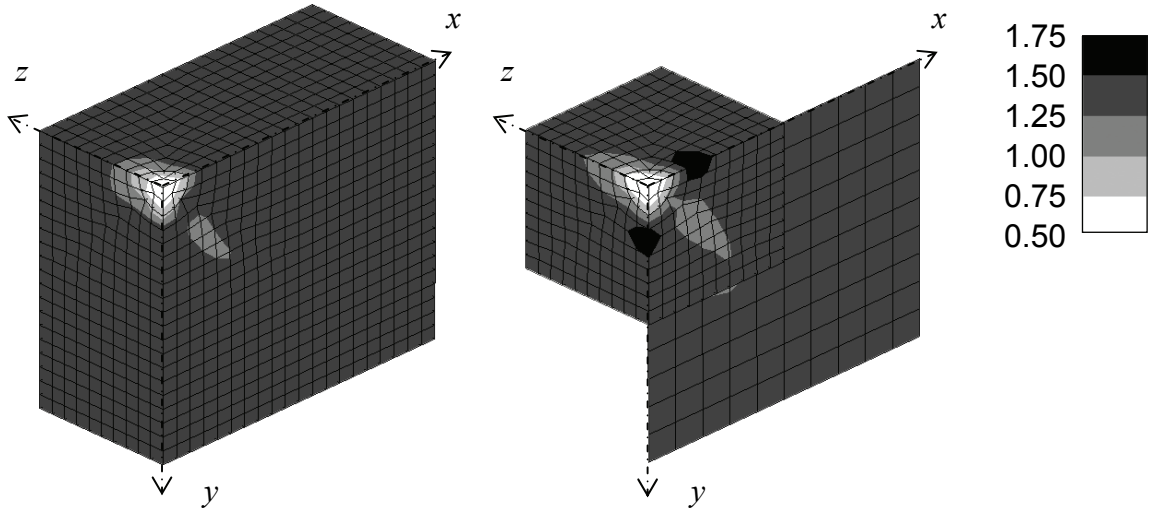

(a) Conventional (b) Mesh Overlay

Fig. 3.48 Equivalent strain rate $\dot{\bar{\varepsilon}}$ distributions at U/L=0.10 of rigid-plastic block compression with harder inclusion

Figure 3.49 shows the equivalent strain $\bar{\varepsilon}$ distributions at nominal longitudinal displacement U/L=0.30 (the final step) by the conventional method and the mesh overlay one, respectively. The obtained distribution by the mesh overlay method shows good

agreement with that by the conventional analysis.

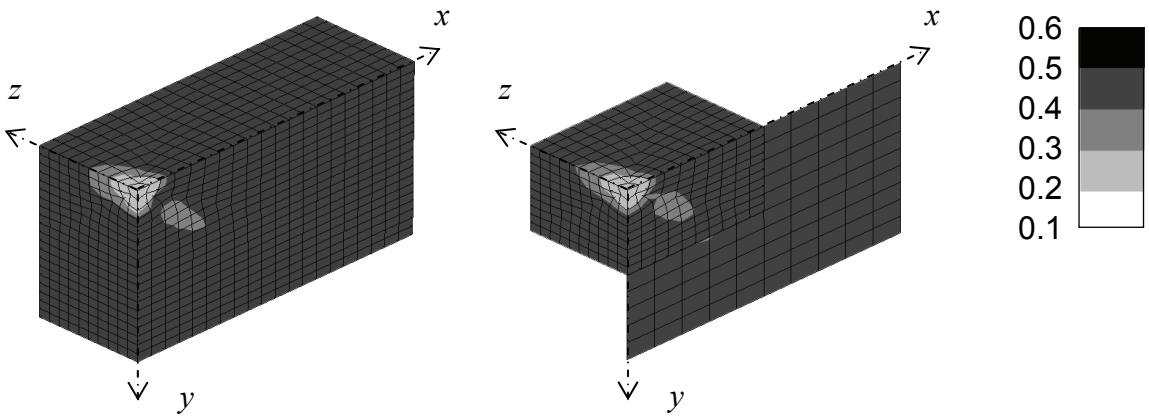

(a) Conventional (b) Mesh Overlay

Fig. 3.49 Equivalent strain $\bar{\varepsilon}$ distributions at U/L=0.30 of rigid-plastic block compression with harder spherical inclusion

Figure 3.50 shows the traces of the standard deviation of each strain rate component. Each standard deviation is small compared to the magnitude of the nominal lateral strain rate $\dot{U}/L$=1.

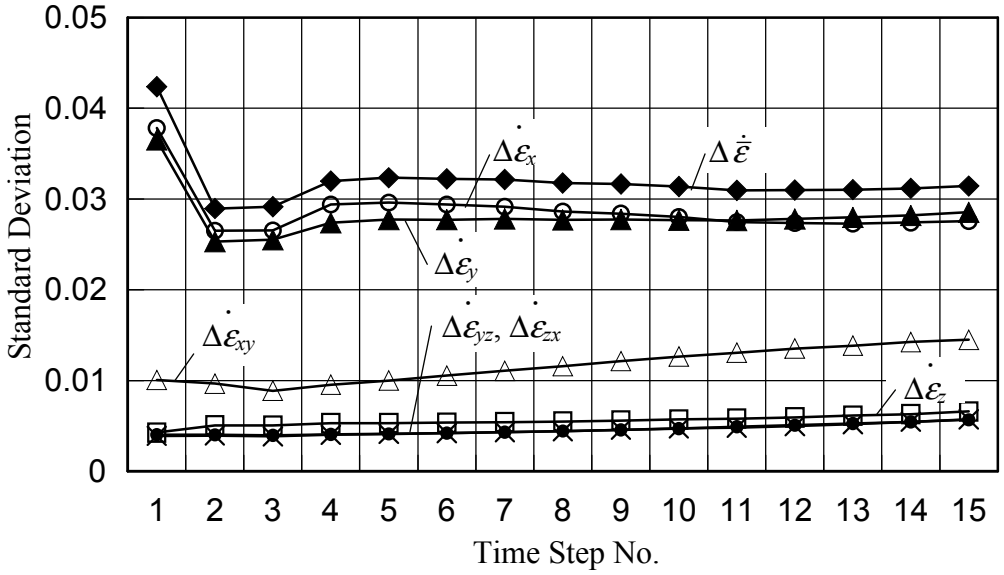

Fig. 3.50 Standard deviation traces of strain rate in local model of rigid-plastic block compression with harder spherical inclusion

3.5.5 Summary

The efficient three-dimensional simulation method, applying the mesh overlay method with a two-dimensional global model and a three-dimensional local model, was applied for rigid-plastic analysis. The deformation behavior of a block including softer/harder spherical inclusion at the center under compression was investigated to verify the present method. High accuracy with the present method was confirmed through comparison with conventional three-dimensional analysis. In addition, the deformation behavior at the inclusion and its vicinity shows not two-dimensional but three-dimensional deformation. Therefore, conventional approaches that assume two-dimensional conditions may fail to grasp the quantitative deformation characteristics, although the qualitative nature could be clarified. There are various metal forming processes in which the macro deformation behavior can be assumed to be two-dimensional although its micro behavior should be regarded as three-dimensional. For instance, the deformation behavior of the inclusion in a slab during the plate rolling process can be quoted. The present method will quantitatively clarify such deformation mechanisms with lower computing costs.

3.6 Numerical Examples of Efficient Three-dimensional Analysis -II

3.6.1 Introduction

In the previous section, the deformation behavior of the block with a spherical inclusion was investigated. Besides, a void in a bulk metal also causes various defects. The mesh overlay method has already been applied to the void closure problem under three-dimensional condition[33], but the reported example was for elastic deformation behavior. In this section, the deformation behavior of a rigid-plastic block with a void under compression is performed by using the mesh overlay method with a two-dimensional global model and a three-dimensional local model.

3.6.2 Computational Conditions

A block with a spherical void at the center is considered, as shown in **Fig. 3.51**. The dimension is the same as the previous condition. However, not an inclusion but a void exists at the center. Due to the symmetry of the deformation, one-eighth of the model is considered. The length, width and thickness of the plate are $2L$, $2W$ and $2H$, and the diameter of the void is $2r$. The longitudinal displacement rate $\dot{U}$ is given. As the boundary conditions, (A) $f_x=f_z=0$ (no shear forces: $\mu=0$), and (B) $\dot{u}_x=\dot{u}_z=0$ are imposed on the displacement rate boundary ($y=\pm L$). The z-directional displacement rate $\dot{u}_z=0$ is also applied at $z=\pm H$.

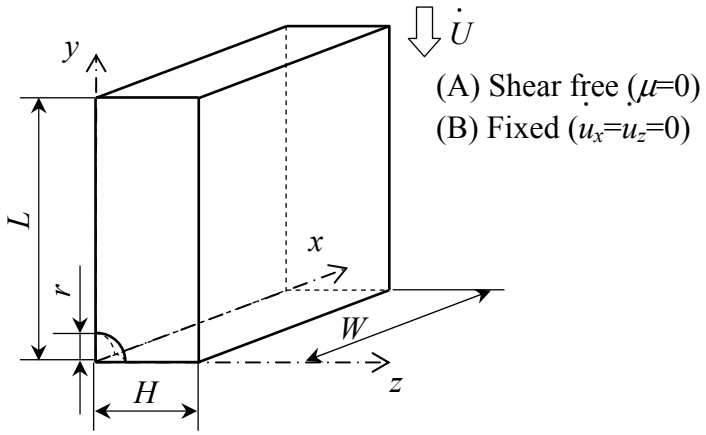

Fig. 3.51 Computational model of rigid-plastic block compression with spherical void

The computational conditions are shown in **Table 3.4**. The initial length $2L$ and width $2W$ of the plate are 20mm, the initial thickness $2H$ is 10mm, and the initial diameter of the void $2r$ is 2mm. The material hardening law is already shown in eq. (3.92) where the material constant of the deformation resistance for the matrix K_0 is 100MPa, the strain hardening index n is 0.20, and the strain rate sensitivity index m is 0.10. In order to decrease the deformation resistance of the void, the deformation resistance for the void K_1 is 0.1MPa. Moreover, in order to allow volume reduction of the void, the penalty constant for the void λ_1 is 1, whereas that for the matrix λ_0 is 10^4. Nominal longitudinal displacement rate $\dot{U}/L$ is 1.0. The time step Δt is 0.02 sec, and the number of steps N is 10 in case A, and 6 in case B. Therefore, after the final step, the nominal longitudinal displacement U/L becomes 0.20 in case A, and 0.12 in case B, respectively.

Table 3.4 Computational conditions of rigid-plastic block compression with spherical void

Initial length of plate	$2L$	20	mm
Initial width of plate	$2W$	20	mm
Initial thickness of plate	$2H$	10	mm
Initial diameter of void	$2r$	2	mm
Nominal longitudinal displacement rate	$\dot{U}/L$	1.0	sec^{-1}
Deformation resistance of matrix	K_0	100	MPa
Deformation resistance of inclusion	K_1	0.1	MPa
Penalty constant for matrix	λ_0	10^4	
Penalty constant for void	λ_1	1	
Strain hardening index	n	0.20	
Strain rate sensitivity index	m	0.10	
Time step	Δt	0.02	sec
Number of steps (case A)	N	10	
Number of steps (case B)	N	6	

The mesh discretization is the same as the previous case, as shown in **Fig. 3.52** for the present mesh overlay analysis, and **Fig. 3.53** for conventional three-dimensional analysis. Here, the grayed element means the void. However, if the global model is not allowed to change the volume, the volume of the local model can not change, because in the mesh overlay method the global and local velocity fields at the global-local boundaries must match. Hence, the global model also has an element that is regarded as a void. Additionally, a two-dimensional plane strain model, shown in **Fig. 3.54**, is also computed as a conventional method to verify the validity of the two-dimensional assumption for the void closure characteristics.

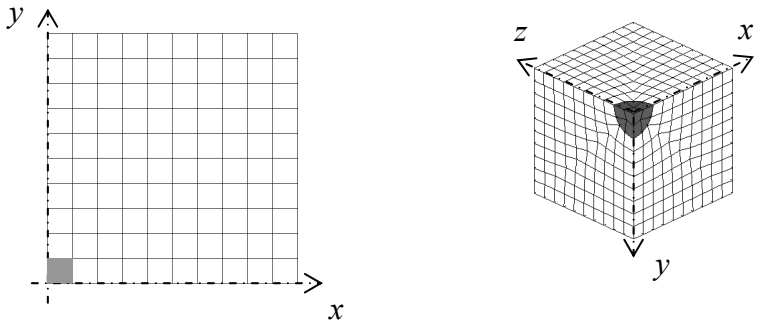

(a) Global model (b) Local model

Fig. 3.52 Mesh discretization for present mesh overlay method of rigid-plastic block compression with spherical void

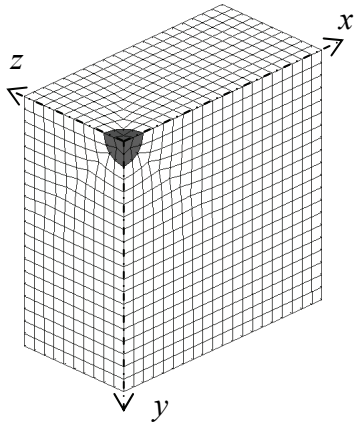

Fig. 3.53 Mesh discretization for three-dimensional conventional method of rigid-plastic block compression with spherical void

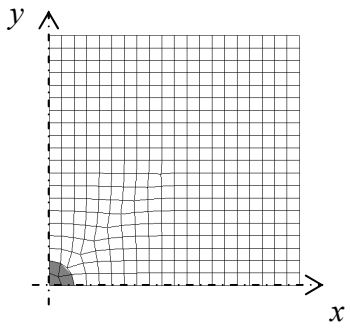

Fig. 3.54 Mesh discretization for two-dimensional conventional method of rigid-plastic block compression with void

Here, four-node linear isoparametric quadrilateral elements are adopted for the global model and the two-dimensional conventional analysis, and eight-node linear isoparametric hexahedral elements are adopted for the local model and the conventional three-dimensional analysis. The number of Gauss points is 4×4 and $4\times4\times4$ per element for the global and local elements, and 2×2 and $2\times2\times2$ Gauss points per element for the two-dimensional and three-dimensional conventional analysis, respectively.

3.6.3 Computational Results (Case A: Shear Free B. C.)

Case A, where the boundary condition is the shear free condition at the velocity assigned plane, is investigated first. **Figure 3.55** shows the y-directional strain rate $\dot{\varepsilon}_y$ distributions at nominal longitudinal displacement U/L=0.02 (the first step) by the conventional method (two-dimensional and three-dimensional) and the present mesh overlay method, respectively. The solution acquired by the present mesh overlay method shows the distributions closest to the conventional distribution. That is, the void and its vicinity deform large, and strain localization is observed about a 45-degree direction from the center on the xy-plane (z=0 plane). However, the deformation of the inclusion for the two-dimensional analysis is larger than that for the three-dimensional analysis or the present mesh overlay analysis. The three-dimensional analysis as well as the present mesh overlay analysis considers the obstructing effect of the metal behind the void along the z-axis to the void closure. The void is, however, expressed as a penetrated hole along the z-axis under two-dimensional conditions. Hence, the void

deforms easier, and under two-dimensional analysis the void closure may be overestimated.

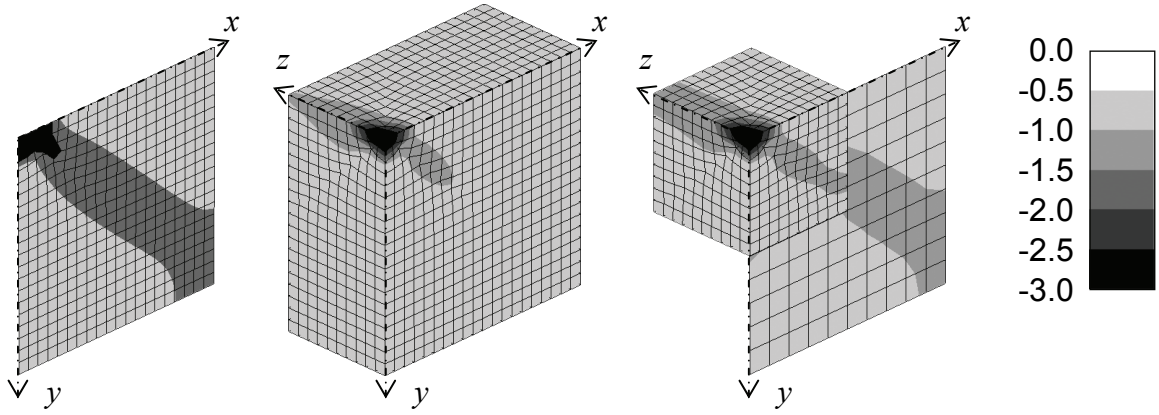

(a) Conventional (2D) (b) Conventional (3D) (c) Present (Mesh Overlay)

Fig. 3.55 y-directional strain rate $\dot{\varepsilon}_y$ distributions at U/L=0.02 of rigid-plastic block compression with void under shear free boundary condition

Figure 3.56 shows the xy-shear strain rate $\dot{\varepsilon}_{xy}$ distributions at nominal longitudinal displacement U/L=0.02 (the first step) by the conventional analysis (two-dimensional and three-dimensional) and the present mesh overlay analysis, respectively. The present mesh overlay analysis closely follows the conventional three-dimensional analysis. However, the two-dimensional analysis overestimates the xy-shear deformation, since the void is regarded as a penetrated hole and the deformation easily occurs, as described above. This fact implies that the discussion about the void closure effect of the shear strain based on the two-dimensional analysis[57] may fail to grasp its quantitative evaluation.

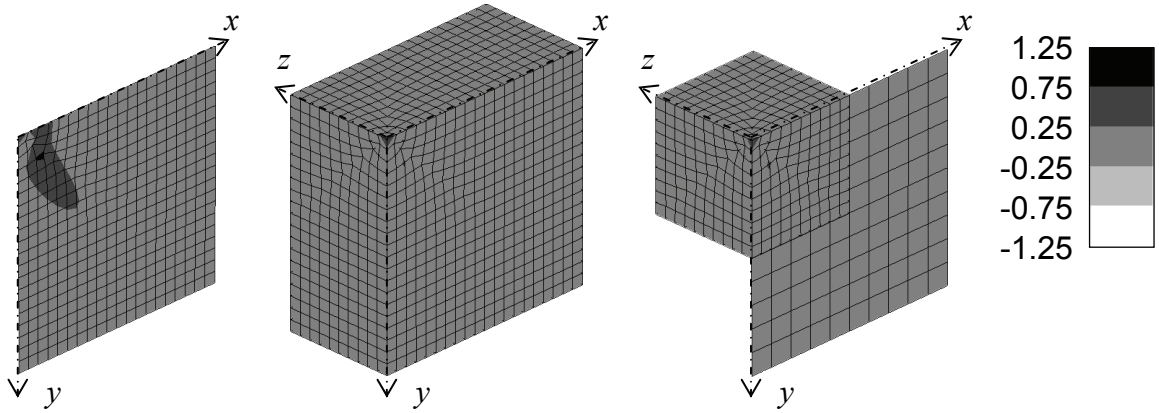

(a) Conventional (2D) (b) Conventional (3D) (c) Present (Mesh Overlay)

Fig. 3.56 *xy*-shear strain rate $\dot{\varepsilon}_{xy}$ distributions at U/L=0.02 of rigid-plastic block compression with void under shear free boundary condition

Figure 3.57 shows the *yz*-shear strain rate $\dot{\varepsilon}_{yz}$ distributions at nominal longitudinal displacement U/L=0.02 (the first step) by the conventional analysis (two-dimensional and three-dimensional) and the present mesh overlay analysis, respectively. As represented in the conventional three-dimensional analysis and the present mesh overlay analysis, the *yz*-shear strain rate $\dot{\varepsilon}_{yz}$, which is assumed to be zero in the two-dimensional analysis, is not small enough to ignore at the void and its vicinity. The obtained result by the present mesh overlay analysis agrees well with that by the conventional three-dimensional analysis.

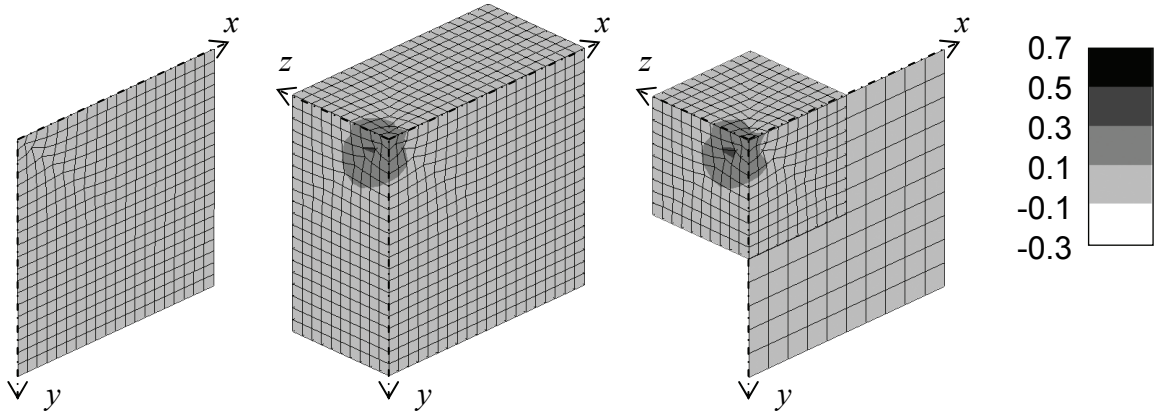

(a) Conventional (2D) (b) Conventional (3D) (c) Present (Mesh Overlay)

Fig. 3.57 *yz*-shear strain rate $\dot{\varepsilon}_{yz}$ distributions at U/L=0.02 of rigid-plastic block compression with void under shear free boundary condition

Figure 3.58 shows the z-directional strain rate $\dot{\varepsilon}_z$ distributions at nominal longitudinal displacement U/L=0.02 (the first step) by the conventional method (two-dimensional and three-dimensional) and the present mesh overlay method, respectively. Here, it is found that the z-directional strain rate $\dot{\varepsilon}_z$, which is ignored under the two-dimensional plane strain analysis, can not be ignored at the inclusion and its vicinity through the three-dimensional conventional analysis as well as the present mesh overlay analysis. In addition, it is shown that the void closure is also caused by the bulging behavior of the metal behind the void along the z-axis toward the void. Therefore, a three-dimensional analysis is necessary to consider these behaviors around the inclusion. The present mesh overlay results and the conventional three-dimensional results are similar.

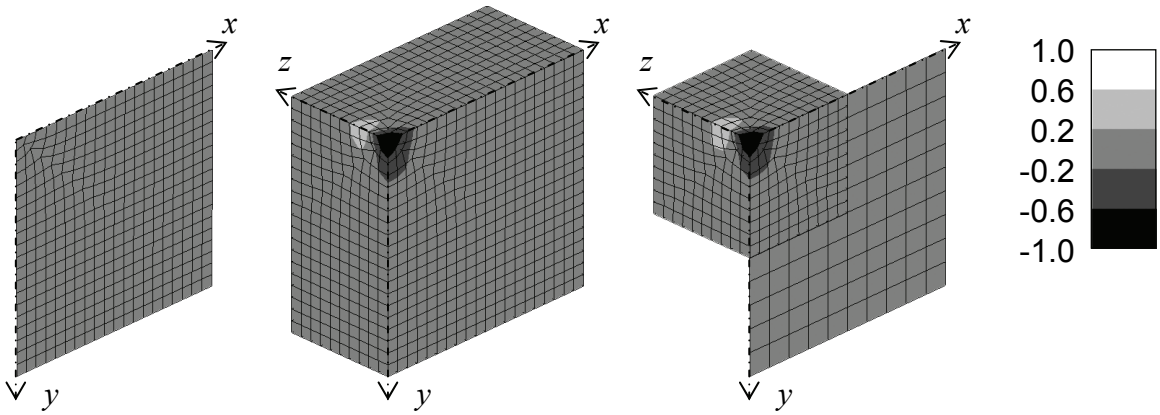

(a) Conventional (2D) (b) Conventional (3D) (c) Present (Mesh Overlay)

Fig. 3.58 z-directional strain rate $\dot{\varepsilon}_z$ distributions at U/L=0.02 of rigid-plastic block compression with void under shear free boundary condition

Figure 3.59 shows the equivalent strain rate $\dot{\bar{\varepsilon}}$ distributions at nominal longitudinal displacement U/L=0.02 (the first step) by the conventional method (two-dimensional and three-dimensional) and the present mesh overlay method, respectively. Large equivalent strain rate is noticed along a 45-degree direction on the xy-plane (z=0 plane) because of large shear deformation in the two-dimensional analysis. On the other hand, strain concentration is restrained when a three-dimensional analysis is applied. Again, the present mesh overlay method shows good agreement with the three-dimensional conventional analysis.

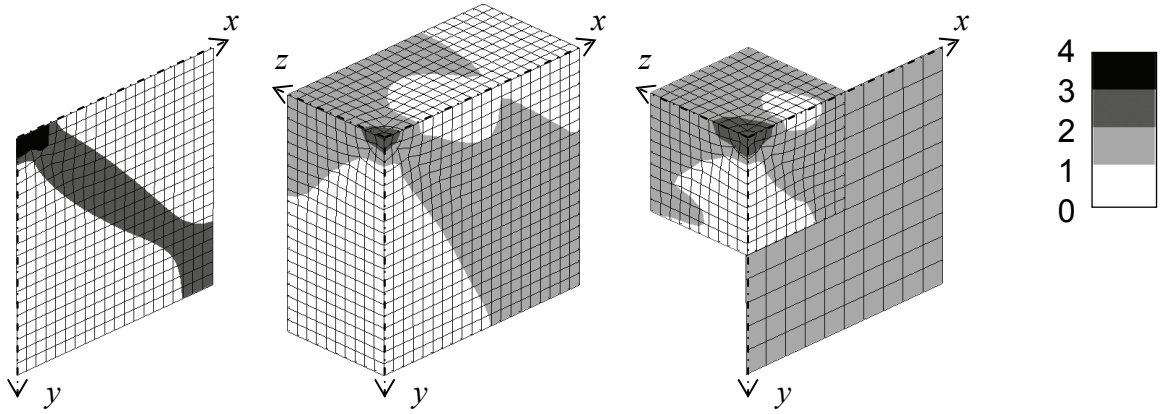

(a) Conventional (2D) (b) Conventional (3D) (c) Present (Mesh Overlay)

Fig. 3.59 Equivalent strain rate $\dot{\bar{\varepsilon}}$ distributions at U/L=0.02 of rigid-plastic block compression with void under shear free boundary condition

Figure 3.60 shows the y-directional stress σ_y distributions at nominal longitudinal displacement U/L=0.02 (the first step) by the conventional analysis (two-dimensional and three-dimensional) and the present mesh overlay analysis, respectively. The present mesh overlay analysis also gives close stress distribution to the conventional three-dimensional analysis.

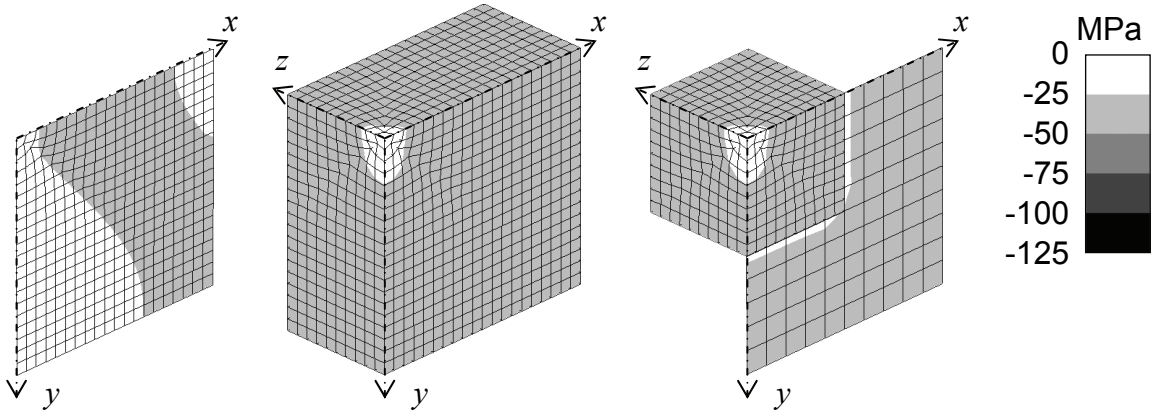

(a) Conventional (2D) (b) Conventional (3D) (c) Present (Mesh Overlay)

Fig. 3.60 y-directional stress σ_y distributions at U/L=0.02 of rigid-plastic block compression with void under shear free boundary condition

Figure 3.61 shows the equivalent stress $\bar{\sigma}$ distributions at nominal longitudinal displacement U/L=0.02 (the first step) by the conventional analysis (two-dimensional and

three-dimensional) and the present mesh overlay analysis, respectively. The equivalent stress distribution by the present mesh overlay analysis and that by the conventional three-dimensional analysis are similar.

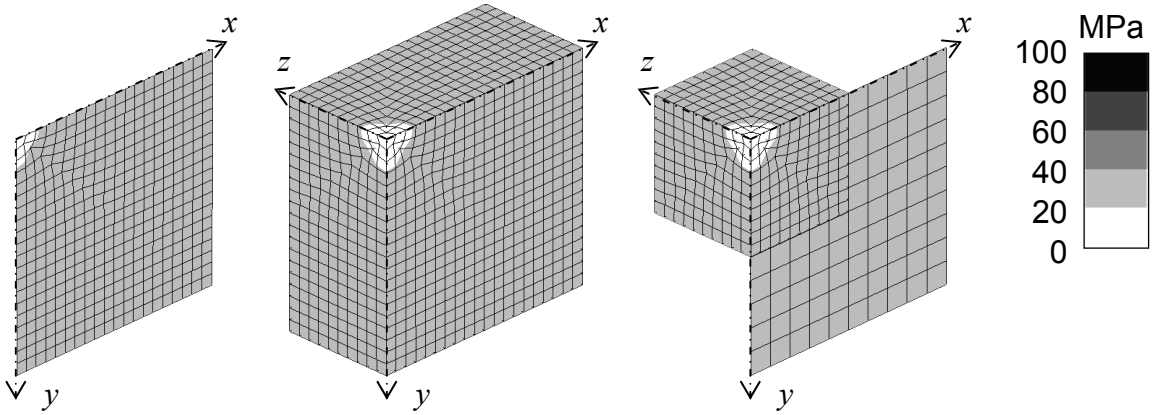

(a) Conventional (2D) (b) Conventional (3D) (c) Present (Mesh Overlay)

Fig. 3.61 Equivalent stress $\bar{\sigma}$ distributions at U/L=0.02 of rigid-plastic block compression with void under shear free boundary condition

Figure 3.62 shows the y-directional strain rate $\dot{\varepsilon}_y$ distributions at nominal longitudinal displacement U/L=0.10 (the fifth step) by the conventional method (two-dimensional and three-dimensional) and the present mesh overlay method, respectively. The two-dimensional analysis also reveals large deformation at the shear band also at nominal longitudinal displacement U/L=0.10. Still, the present mesh overlay method gives results close to the conventional three-dimensional analysis.

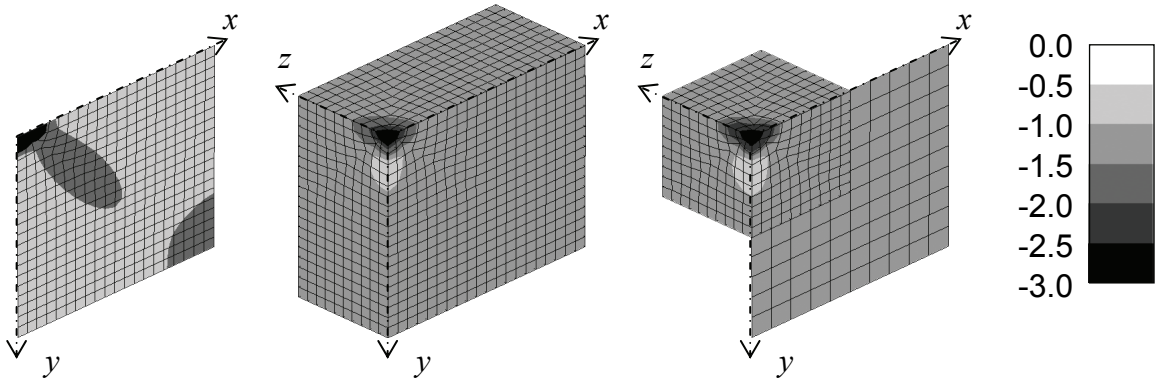

(a) Conventional (2D) (b) Conventional (3D) (c) Present (Mesh Overlay)

Fig. 3.62 y-directional strain rate $\dot{\varepsilon}_y$ distributions at U/L=0.10 of rigid-plastic block compression with void under shear free boundary condition

Figure 3.63 shows the xy-shear strain rate $\dot{\varepsilon}_{xy}$ distributions at nominal longitudinal displacement U/L=0.10 (the fifth step) by the conventional analysis (two-dimensional and three-dimensional) and the present mesh overlay analysis, respectively. Overestimation of the xy-shear deformation still remains in the two-dimensional analysis. On the other hand, the present mesh overlay analysis agrees with the conventional three-dimensional analysis.

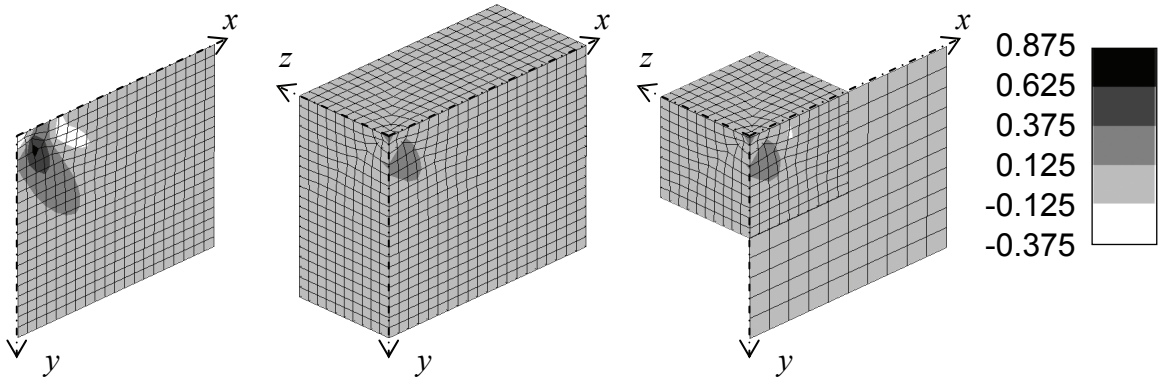

(a) Conventional (2D) (b) Conventional (3D) (c) Present (Mesh Overlay)

Fig. 3.63 xy-shear strain rate $\dot{\varepsilon}_{xy}$ distributions at U/L=0.10 of rigid-plastic block compression with void under shear free boundary condition

Figure 3.64 shows the yz-shear strain rate $\dot{\varepsilon}_{yz}$ distributions at nominal longitudinal displacement U/L=0.10 (the fifth step) by the conventional method (two-dimensional and three-dimensional) and the present mesh overlay one, respectively. These figures also show that the yz-shear strain rate $\dot{\varepsilon}_{yz}$, assumed to be zero in the two-dimensional analysis, can not be ignored.

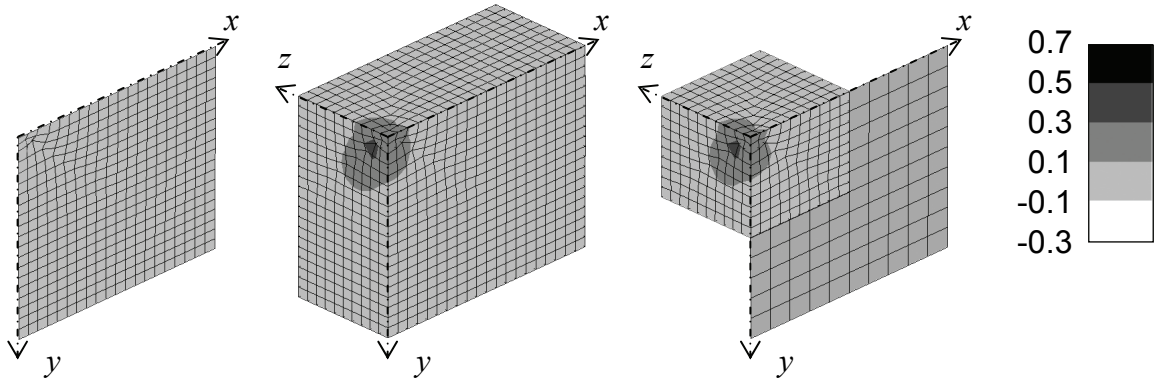

(a) Conventional (2D) (b) Conventional (3D) (c) Present (Mesh Overlay)

Fig. 3.64 *yz*-shear strain rate $\dot{\varepsilon}_{yz}$ distributions at U/L=0.10 of rigid-plastic block compression with void under shear free boundary condition

Figure 3.65 shows the *z*-directional strain rate $\dot{\varepsilon}_z$ distributions at nominal longitudinal displacement U/L=0.10 (the fifth step) by the conventional method (two-dimensional and three-dimensional) and the present mesh overlay method, respectively. These distributions also indicate that the *z*-directional strain rate $\dot{\varepsilon}_z$, which is ignored in a two-dimensional plane strain analysis, has a great influence on the void closure behavior. The present mesh overlay method gives results close to the conventional three-dimensional analysis.

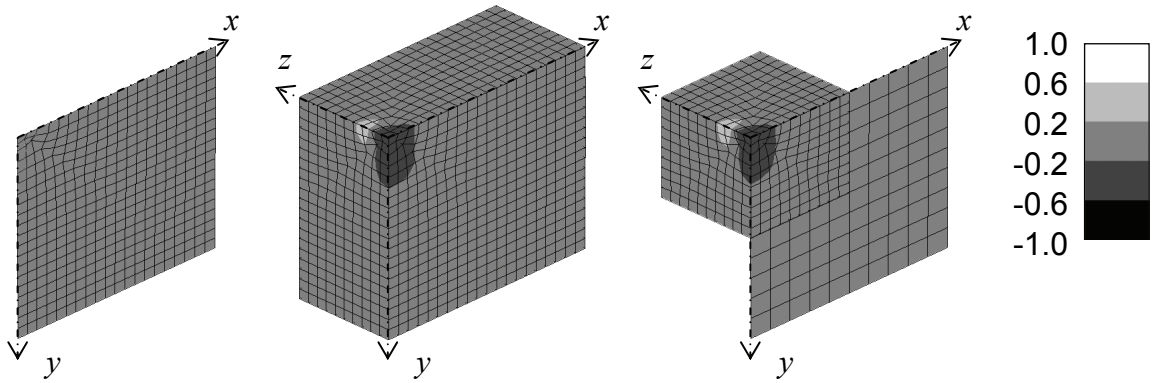

(a) Conventional (2D) (b) Conventional (3D) (c) Present (Mesh Overlay)

Fig. 3.65 *z*-directional strain rate $\dot{\varepsilon}_z$ distributions at U/L=0.10 of rigid-plastic block compression with void under shear free boundary condition

Figure 3.66 shows the equivalent strain rate $\dot{\bar{\varepsilon}}$ distributions at nominal longitudinal displacement U/L=0.10 (the fifth step) by the conventional method (two-dimensional and three-dimensional) and the present mesh overlay method, respectively. Large deformation at the void and its vicinity along a 45-degree direction on the xy-plane is observed when the two-dimensional analysis is applied; the deformation spreads when the three-dimensional conventional analysis or the present mesh overlay analysis is adopted. As described before, the potential of the metal behind the void along the z-axis to obstruct the void closure is not considered in the two-dimensional analysis. Therefore, the deformation behavior in the two-dimensional analysis is different from that in the three-dimensional analysis.

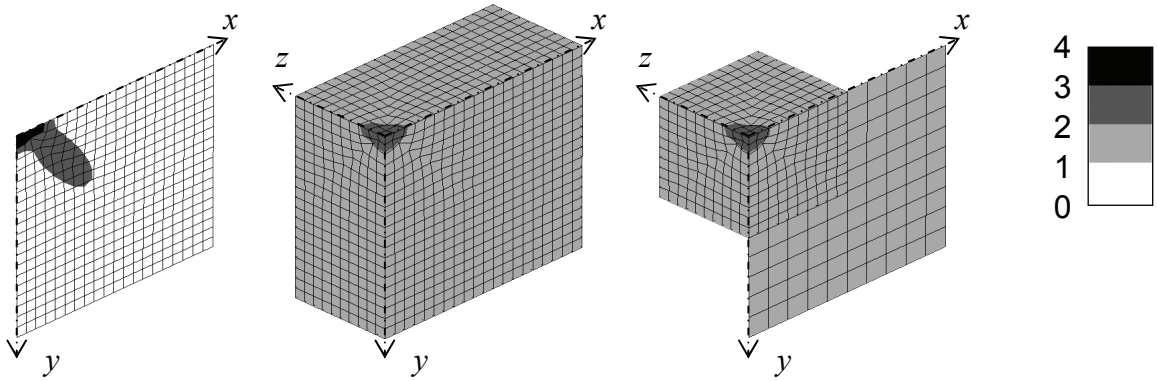

(a) Conventional (2D) (b) Conventional (3D) (c) Present (Mesh Overlay)

Fig. 3.66 Equivalent strain rate $\dot{\bar{\varepsilon}}$ distributions at U/L=0.10 of rigid-plastic block compression with void under shear free boundary condition

Figure 3.67 shows the y-directional stress σ_y distributions at nominal longitudinal displacement U/L=0.10 (the fifth step) by the conventional analysis (two-dimensional and three-dimensional) and the present mesh overlay analysis, respectively. Large stress concentration at the vicinity of the void along the x-axis is observed in the two-dimensional analysis. Such large stress concentration is not shown in the three-dimensional conventional analysis and the present mesh overlay analysis. Since in the three-dimensional analysis the void is a sphere and not a hole as in the two-dimensional analysis, the stress disperses not only to the x-direction but also in all radial directions. The distribution of the present mesh overlay analysis and that of the

three-dimensional conventional analysis are similar.

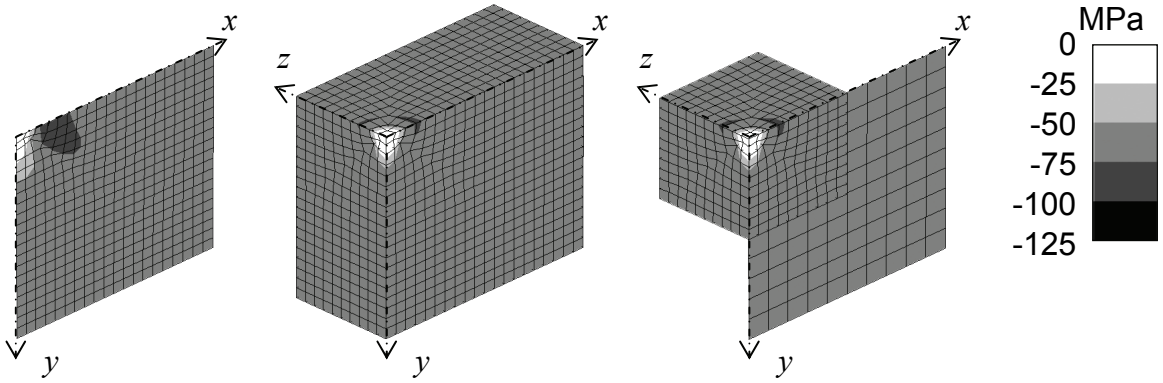

(a) Conventional (2D) (b) Conventional (3D) (c) Present (Mesh Overlay)

Fig. 3.67 *y*-directional stress σ_y distributions at U/L=0.10 of rigid-plastic block compression with void under shear free boundary condition

Figure 3.68 shows the equivalent stress $\bar{\sigma}$ distributions at nominal longitudinal displacement U/L=0.10 (the fifth step) by the conventional analysis (two-dimensional and three-dimensional) and the present mesh overlay analysis, respectively. These distributions also show that the present mesh overlay method gives properly accurate results.

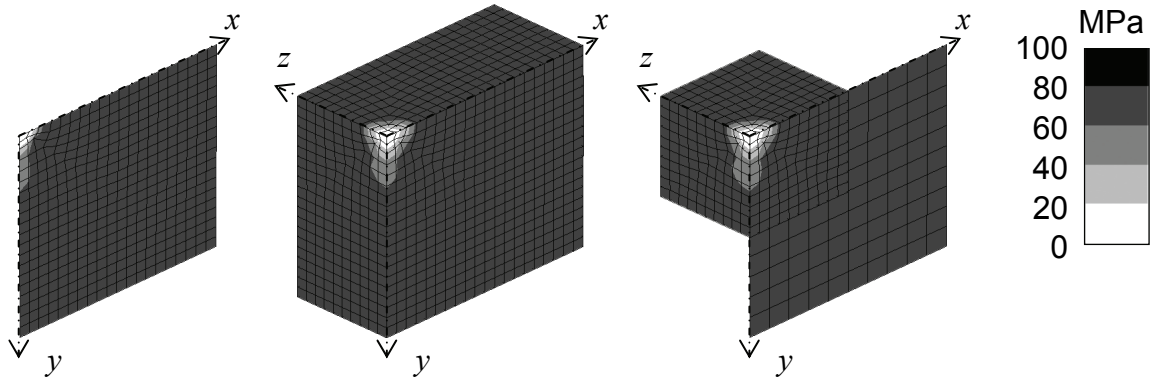

(a) Conventional (2D) (b) Conventional (3D) (c) Present (Mesh Overlay)

Fig. 3.68 Equivalent stress $\bar{\sigma}$ distributions at U/L=0.10 of rigid-plastic block compression with void under shear free boundary condition

Figures 3.69~3.76 show the y-directional strain rate $\dot{\varepsilon}_y$, the xy-shear strain rate $\dot{\varepsilon}_{xy}$, the yz-shear strain rate $\dot{\varepsilon}_{yz}$, the z-directional strain rate $\dot{\varepsilon}_z$, the equivalent strain rate $\dot{\bar{\varepsilon}}$, the equivalent strain $\bar{\varepsilon}$, the y-directional stress σ_y and the equivalent stress $\bar{\sigma}$ distributions at nominal longitudinal displacement U/L=0.20 (the tenth step) by the conventional method (two-dimensional and three-dimensional) and the present mesh overlay method, respectively. The deformation behavior at nominal longitudinal displacement U/L=0.02 or U/L=0.10 is still observed at nominal longitudinal displacement U/L=0.20. Additionally, the present mesh overlay analysis and the conventional three-dimensional analysis show good agreement.

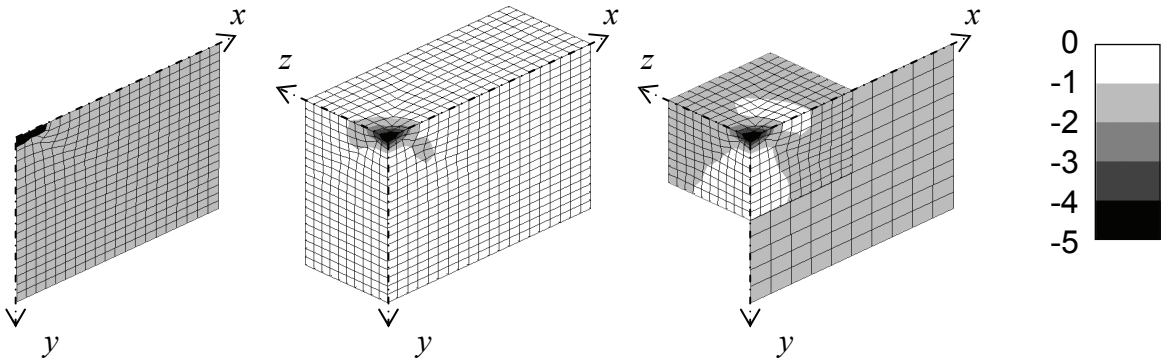

(a) Conventional (2D) (b) Conventional (3D) (c) Present (Mesh Overlay)

Fig. 3.69 y-directional strain rate $\dot{\varepsilon}_y$ distributions at U/L=0.20 of rigid-plastic block compression with void under shear free boundary condition

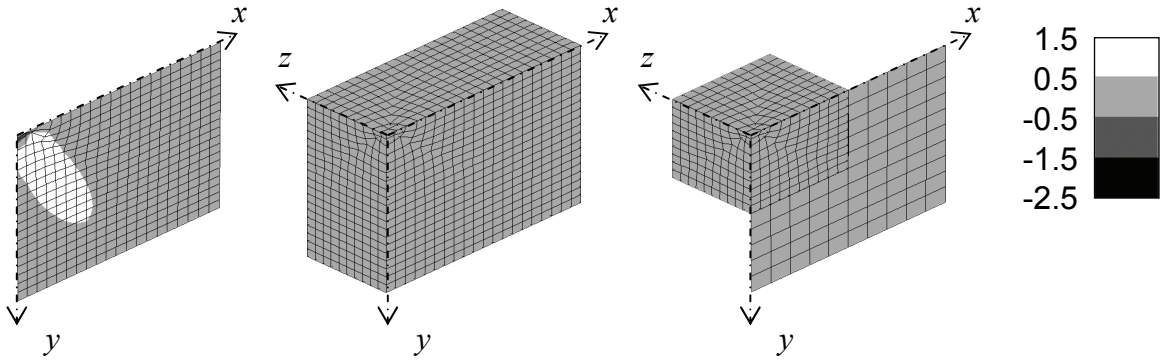

(a) Conventional (2D) (b) Conventional (3D) (c) Present (Mesh Overlay)

Fig. 3.70 xy-shear strain rate $\dot{\varepsilon}_{xy}$ distributions at U/L=0.20 of rigid-plastic block compression with void under shear free boundary condition

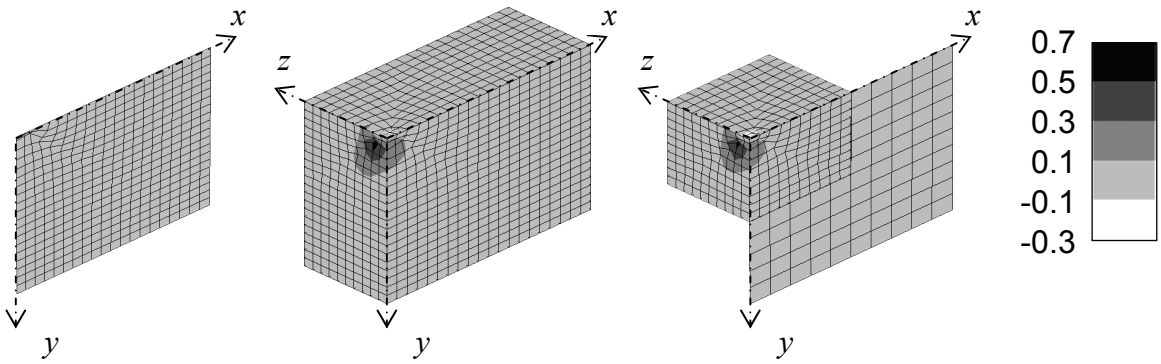

(a) Conventional (2D) (b) Conventional (3D) (c) Present (Mesh Overlay)

Fig. 3.71 *yz*-shear strain rate $\dot{\varepsilon}_{yz}$ distributions at U/L=0.20 of rigid-plastic block compression with void under shear free boundary condition

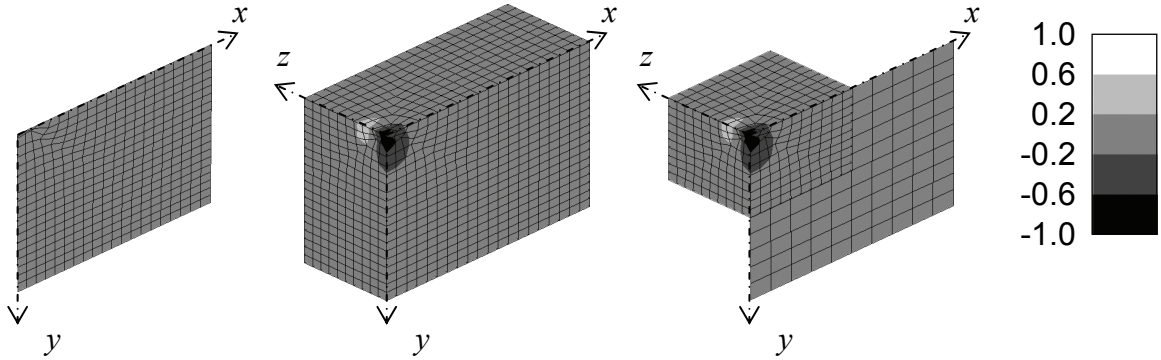

(a) Conventional (2D) (b) Conventional (3D) (c) Present (Mesh Overlay)

Fig. 3.72 *z*-directional strain rate $\dot{\varepsilon}_z$ distributions at U/L=0.20 of rigid-plastic block compression with void under shear free boundary condition

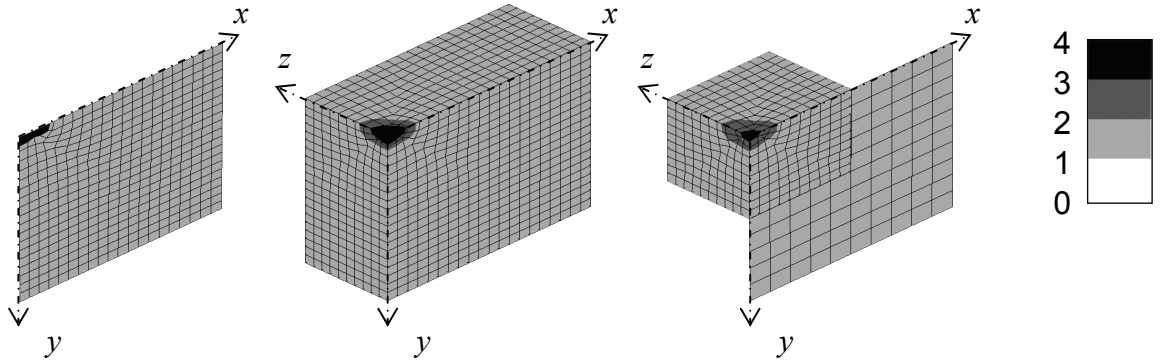

(a) Conventional (2D) (b) Conventional (3D) (c) Present (Mesh Overlay)

Fig. 3.73 Equivalent strain rate $\dot{\bar{\varepsilon}}$ distributions at U/L=0.20 of rigid-plastic block compression with void under shear free boundary condition

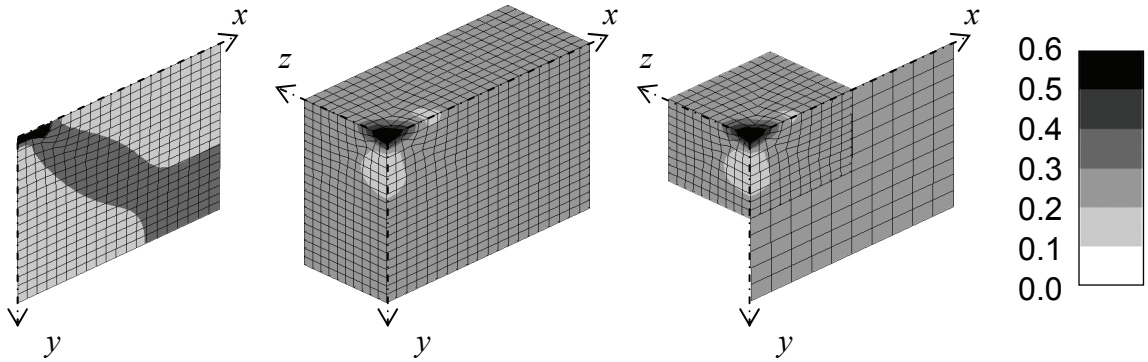

(a) Conventional (2D) (b) Conventional (3D) (c) Present (Mesh Overlay)

Fig. 3.74 Equivalent strain $\bar{\varepsilon}$ distributions at U/L=0.20 of rigid-plastic block compression with void under shear free boundary condition

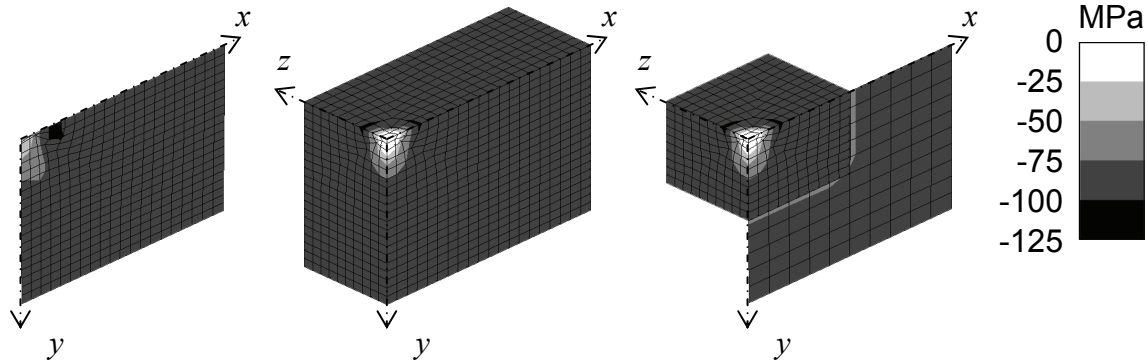

(a) Conventional (2D) (b) Conventional (3D) (c) Present (Mesh Overlay)

Fig. 3.75 y-directional stress σ_y distributions at U/L=0.20 of rigid-plastic block compression with void under shear free boundary condition

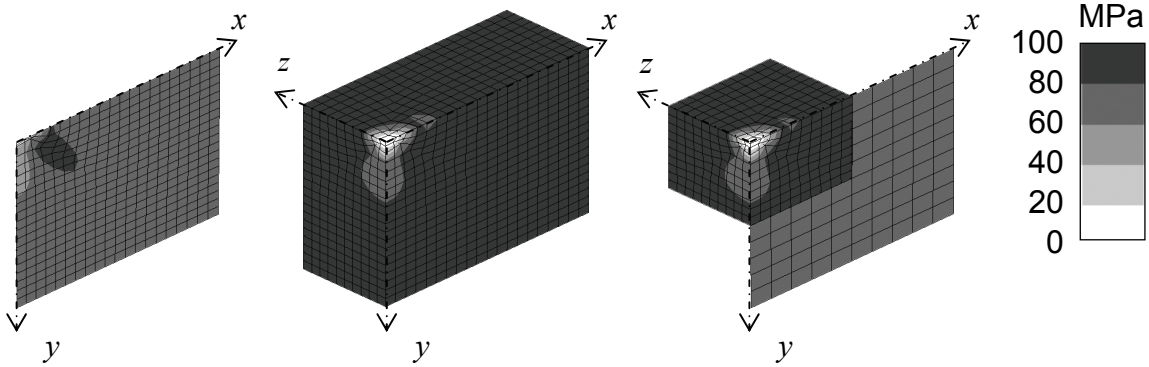

(a) Conventional (2D) (b) Conventional (3D) (c) Present (Mesh Overlay)

Fig. 3.76 Equivalent stress $\bar{\sigma}$ distributions at U/L=0.20 of rigid-plastic block compression with void under shear free boundary condition

Figure 3.77 shows the mesh deformation on the *xy*-plane (*z*=0 plane) at nominal longitudinal displacement *U*/*L*=0.20 (the tenth step) by the conventional method (two-dimensional and three-dimensional) and the present mesh overlay method, respectively. The void almost closes in the two-dimensional analysis. In the three-dimensional analysis as well as in the present mesh overlay analysis, the void is not fully closed. Therefore, it is found that the two-dimensional assumption overestimates the void closure. The present mesh overlay method gives results close to the three-dimensional conventional analysis.

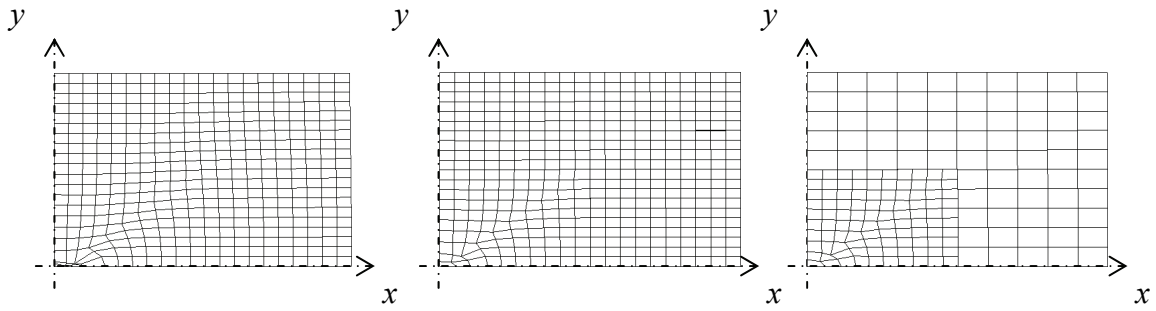

(a) Conventional (2D) (b) Conventional (3D) (c) Present (Mesh Overlay)

Fig. 3.77 Mesh deformation (*z*=0 plane) at *U*/*L*=0.20 of rigid-plastic block compression with void under shear free boundary condition

Additionally, **Fig. 3.78** shows the axial strain ε_x, ε_y and ε_z, and the volumetric strain ε_V of the void at nominal longitudinal displacement *U*/*L*=0.20 (the tenth step) by the conventional method (two-dimensional and three-dimensional) and the present mesh overlay method, respectively. This figure also shows that two-dimensional analysis overestimates the *y*-directional strain ε_y as well as the volumetric strain ε_V at the void. In the three-dimensional analysis, the effect of the *z*-directional strain ε_z on the void closure is precisely considered. Moreover, it is also verified that the present mesh overlay analysis quantitatively agrees with the conventional three-dimensional analysis.

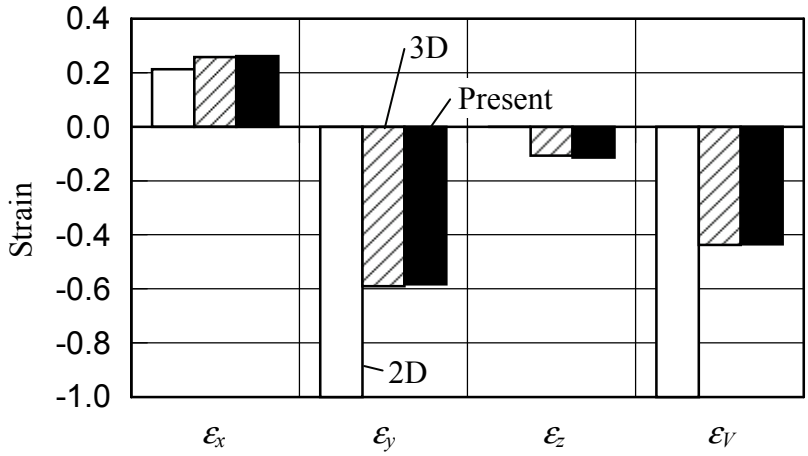

Fig. 3.78 Axial strain ε_x, ε_y, ε_z and volumetric strain ε_V of the inclusion at U/L=0.20 of rigid-plastic block compression with void under shear free boundary condition

The computing time of the present mesh overlay analysis was about 28 times shorter than that of the three-dimensional conventional analysis for this condition. This represents one of the features of the present mesh overlay method, although the fact that the banded matrix solver was not applied to this numerical code is one reason why the computing speed for the three-dimensional conventional analysis was so slow.

If faster computing time is not required, this example can be solved even by conventional three-dimensional analysis as investigated above. However, real problems for the metal forming process often require analyzing much smaller void deformation behavior in much larger bulk metal. In such cases, conventional method becomes impractical due to the huge number of elements and nodes. The accuracy of the present mesh overlay analysis is comparable to that with three-dimensional conventional analysis. Hence, it is concluded that applying the present mesh overlay method to practical problems will assist in clarifying the mechanism of micro deformation behaviors under macro metal flow, and in developing fundamental improvement for the metal forming process.

3.6.4 Computational Results (Case B: Fixed B. C.)

Next, the deformation behavior when the boundary conditions at the velocity assigned plane is the fixed boundary condition is performed. **Figure 3.79** shows the y-directional strain rate $\dot{\varepsilon}_y$ distributions at nominal longitudinal displacement U/L=0.02 (the first step) by the conventional method (two-dimensional and three-dimensional) and the present mesh overlay method, respectively. The solution acquired by the present mesh overlay method shows the closest distribution to the conventional one. In addition, the global model expresses the macro strain rate distributions, although the coarser mesh discretization is applied. Moreover, the same tendency of the deformation behavior as shown under the shear free boundary conditions is also confirmed. However, the obtained strain rate distributes more widely, and the magnitude of the strain rate at the void becomes larger under the fixed boundary conditions.

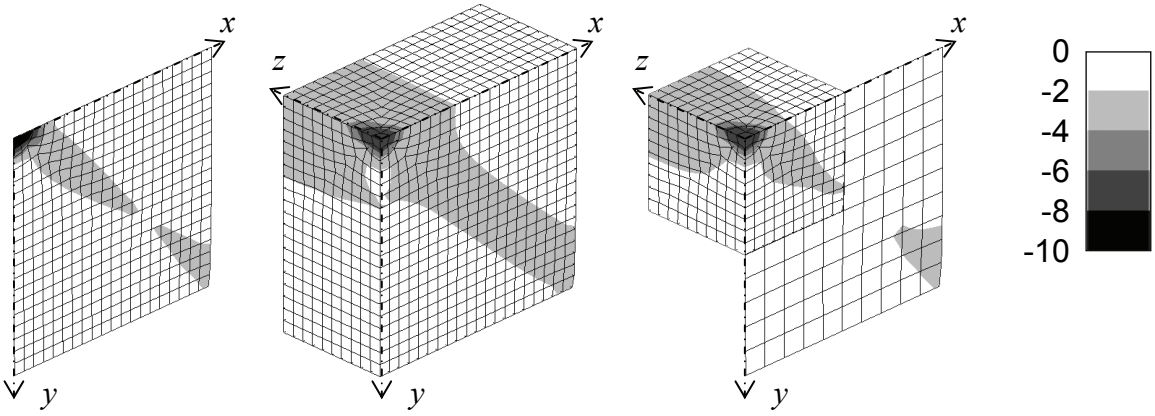

(a) Conventional (2D) (b) Conventional (3D) (c) Present (Mesh Overlay)

Fig. 3.79 y-directional strain rate $\dot{\varepsilon}_y$ distributions at U/L=0.02 of rigid-plastic block compression with void under fixed boundary condition

Figure 3.80 shows the xy-shear strain rate $\dot{\varepsilon}_{xy}$ distributions at nominal longitudinal displacement U/L=0.02 (the first step) by the conventional analysis (two-dimensional and three-dimensional) and the present mesh overlay analysis, respectively. As shown in case A that imposes the shear free boundary conditions, large xy-shear strain rate $\dot{\varepsilon}_{xy}$ is observed in the two-dimensional analysis, whereas in the three-dimensional analysis and the present mesh overlay analysis, such large shear deformation is not observed except at

the corner of the displacement rate assigned plane. The reason for such large shear deformation is that the void deforms easier under two-dimensional condition since the void is regarded as a penetrated hole along the *z*-direction.

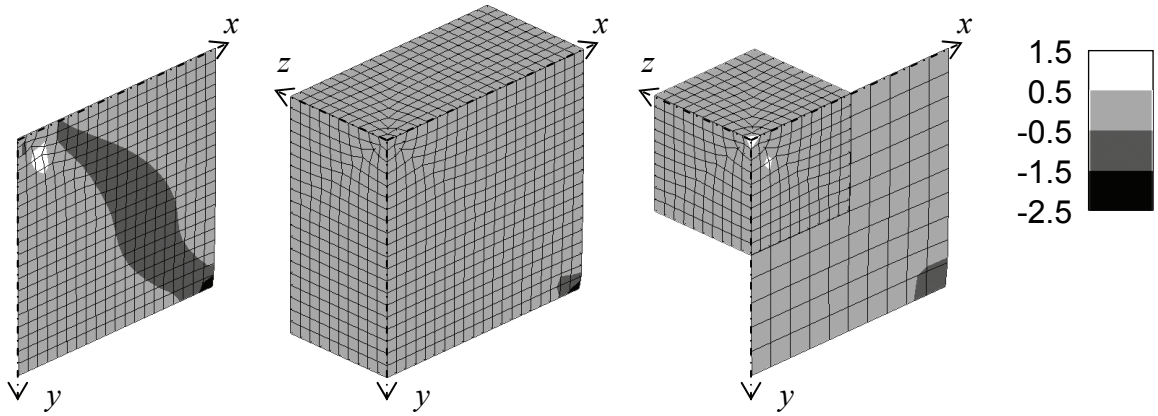

(a) Conventional (2D) (b) Conventional (3D) (c) Present (Mesh Overlay)

Fig. 3.80 *xy*-shear strain rate $\dot{\varepsilon}_{xy}$ distributions at U/L=0.02 of rigid-plastic block compression with void under fixed boundary condition

Figure 3.81 shows the *yz*-shear strain rate $\dot{\varepsilon}_{yz}$ distributions at nominal longitudinal displacement U/L=0.02 (the first step) by the conventional analysis (two-dimensional and three-dimensional) and the present mesh overlay analysis, respectively. Again, it is recognized that the *yz*-shear strain rate $\dot{\varepsilon}_{yz}$, assumed to be zero in two-dimensional analysis, can not be ignored at the void and its vicinity through three-dimensional analysis. Additionally, the present mesh overlay method gives results close to the three-dimensional conventional analysis.

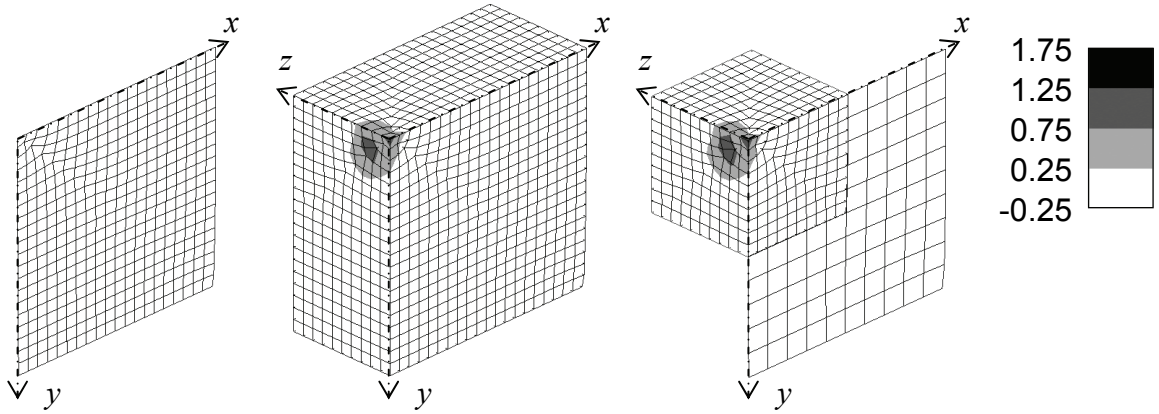

(a) Conventional (2D) (b) Conventional (3D) (c) Present (Mesh Overlay)

Fig. 3.81 yz-shear strain rate $\dot{\varepsilon}_{yz}$ distributions at U/L=0.02 of rigid-plastic block compression with void under fixed boundary condition

Figure 3.82 shows the z-directional strain rate $\dot{\varepsilon}_z$ distributions at nominal longitudinal displacement U/L=0.02 (the first step) by the conventional method (two-dimensional and three-dimensional) and the present mesh overlay method, respectively. Nonzero z-directional strain rate $\dot{\varepsilon}_z$ at the void and its vicinity is acquired through the three-dimensional conventional analysis since the metal behind the void along the z-direction protrudes into the void, although two-dimensional analysis assumes it to be zero. The results obtained by the present mesh overlay method are close to those obtained by the conventional three-dimensional analysis.

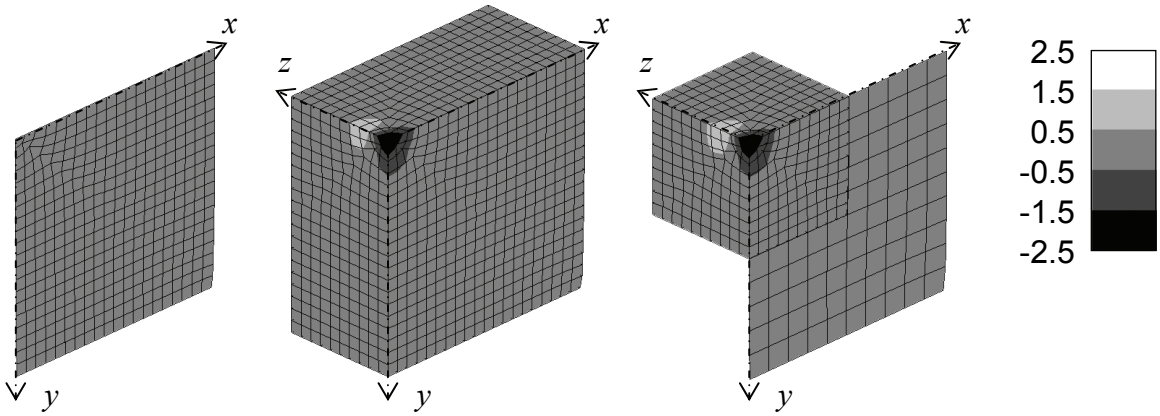

(a) Conventional (2D) (b) Conventional (3D) (c) Present (Mesh Overlay)

Fig. 3.82 z-directional strain rate $\dot{\varepsilon}_z$ distributions at U/L=0.02 of rigid-plastic block compression with void under fixed boundary condition

Figure 3.83 shows the equivalent strain rate $\dot{\bar{\varepsilon}}$ distributions at nominal longitudinal displacement U/L=0.02 (the first step) by the conventional method (two-dimensional and three-dimensional) and the present mesh overlay method, respectively. The equivalent strain rate $\dot{\bar{\varepsilon}}$ distributions on the xy-plane (z=0 plane) are similar, although their value at the void is slightly larger in the two-dimensional analysis. However, at the void and its vicinity, the equivalent strain rate $\dot{\bar{\varepsilon}}$ distributes along the z-axis. Hence, three-dimensional analysis is required at least at and around the void to analyze the deformation behavior in this region.

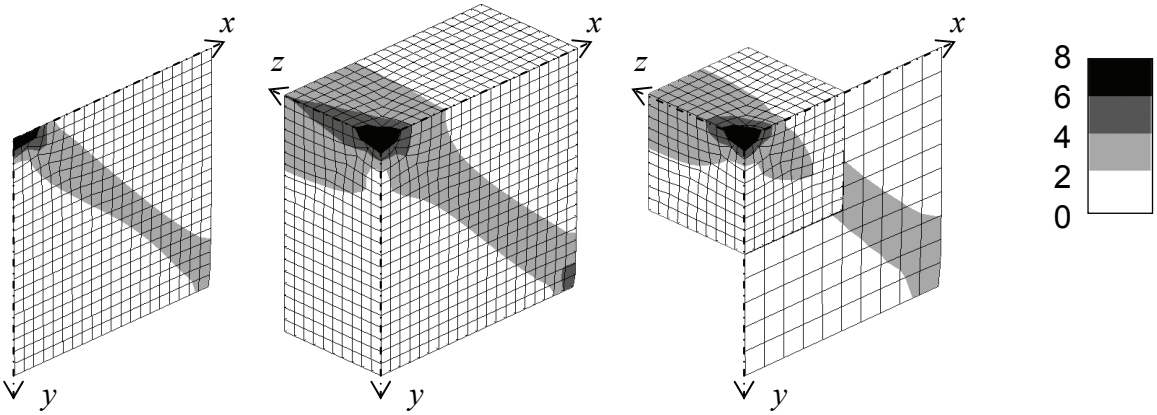

(a) Conventional (2D) (b) Conventional (3D) (c) Present (Mesh Overlay)

Fig. 3.83 Equivalent strain rate $\dot{\bar{\varepsilon}}$ distributions at U/L=0.02 of rigid-plastic block compression with void under fixed boundary condition

Figure 3.84 shows the y-directional stress σ_y distributions at nominal longitudinal displacement U/L=0.02 (the first step) by the conventional analysis (two-dimensional and three-dimensional) and the present mesh overlay analysis, respectively. These figures also exhibit close y-directional stress σ_y distributions on the xy-plane (z=0 plane). However, the y-directional stress σ_y distributions along the z-direction demonstrate that three-dimensional analysis is necessary to perform the deformation characteristics of the void and its vicinity. The present mesh overlay analysis shows good agreement with the conventional three-dimensional analysis.

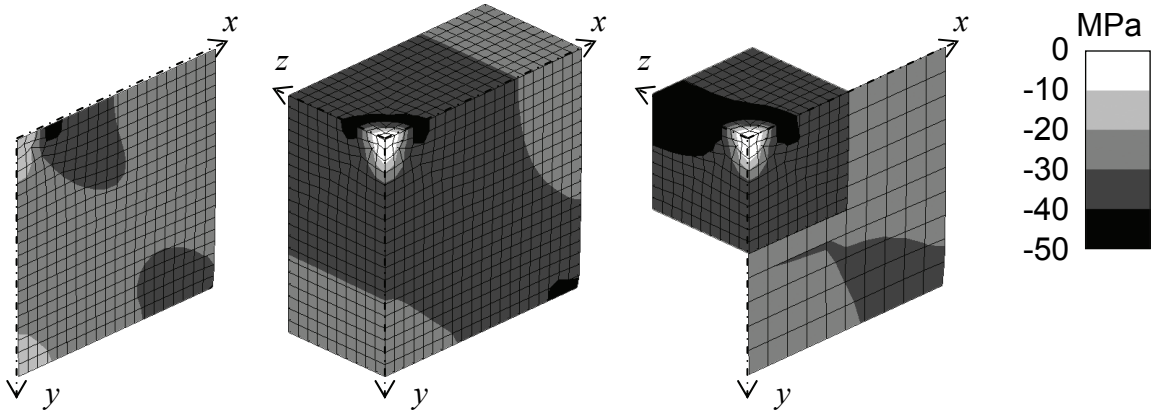

(a) Conventional (2D) (b) Conventional (3D) (c) Present (Mesh Overlay)

Fig. 3.84 y-directional stress σ_y distributions at U/L=0.02 of rigid-plastic block compression with void under fixed boundary condition

Figure 3.85 shows the equivalent stress $\bar{\sigma}$ distributions at nominal longitudinal displacement U/L=0.02 (the first step) by the conventional analysis (two-dimensional and three-dimensional) and the present mesh overlay analysis, respectively. Similar to the y-directional stress σ_y distributions, the equivalent stress $\bar{\sigma}$ distributions on the xy-plane (z=0 plane) are close to each other, and it is also found that three-dimensional analysis is necessary to simulate the deformation behavior at and around the void. The present mesh overlay results and the conventional three-dimensional results agree well.

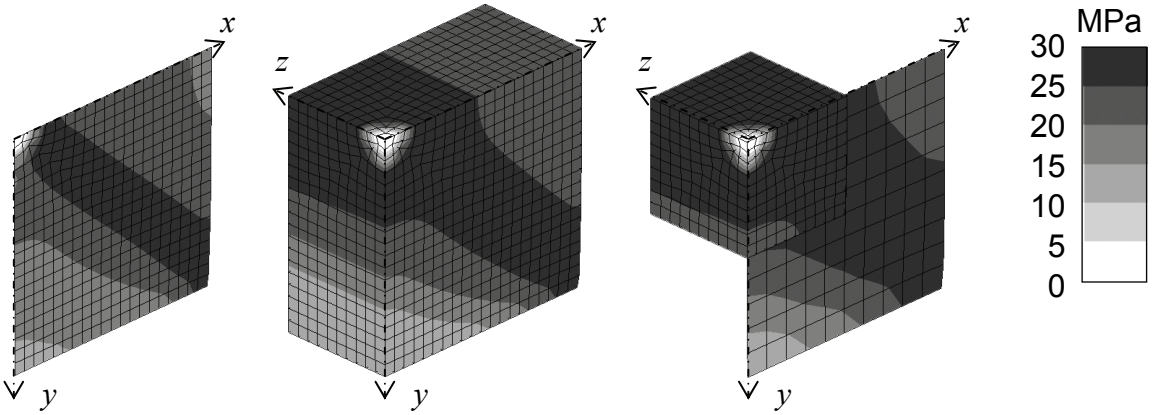

(a) Conventional (2D) (b) Conventional (3D) (c) Present (Mesh Overlay)

Fig. 3.85 Equivalent stress $\bar{\sigma}$ distributions at U/L=0.02 of rigid-plastic block compression with void under fixed boundary condition

Figures 3.86~3.93 show the y-directional strain rate $\dot{\varepsilon}_y$, the xy-shear strain rate $\dot{\varepsilon}_{xy}$, the yz-shear strain rate $\dot{\varepsilon}_{yz}$, the z-directional strain rate $\dot{\varepsilon}_z$, the equivalent strain rate $\dot{\bar{\varepsilon}}$, the equivalent strain $\bar{\varepsilon}$, the y-directional stress σ_y and the equivalent stress $\bar{\sigma}$ distributions at nominal longitudinal displacement U/L=0.12 (the final step) by the conventional method (two-dimensional and three-dimensional) and the present mesh overlay method, respectively. It is identified that the yz-shear strain rate $\dot{\varepsilon}_{yz}$ and the z-directional strain rate $\dot{\varepsilon}_z$ have considerable effects on the deformation behavior at the void and its vicinity at the nominal longitudinal displacement U/L=0.12. Moreover, the y-directional strain rate $\dot{\varepsilon}_y$, the xy-shear strain rate $\dot{\varepsilon}_{xy}$, the equivalent strain rate $\dot{\bar{\varepsilon}}$, the equivalent strain $\bar{\varepsilon}$, the y-directional stress σ_y and the equivalent stress $\bar{\sigma}$ distributions at the region also vary along the z-direction. Hence, three-dimensional analysis is indispensable to analyze the deformation behavior of the void and its vicinity. Additionally, the present mesh overlay method gives results close to the conventional three-dimensional analysis.

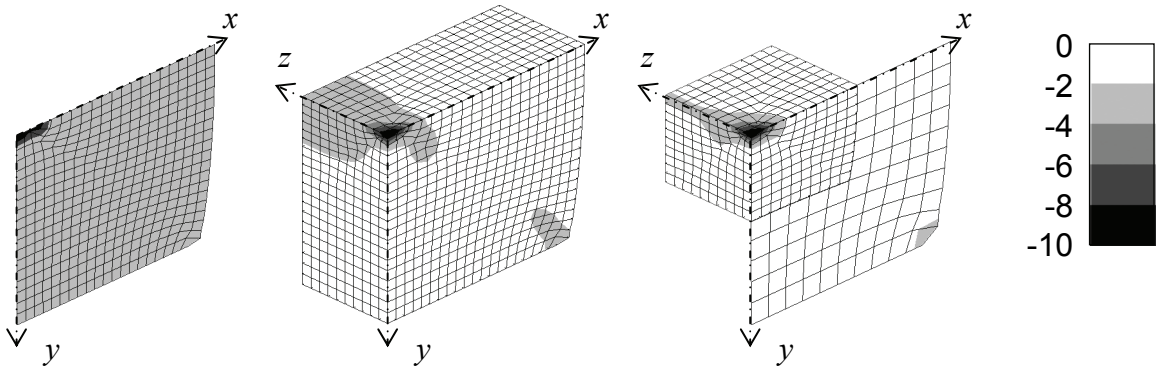

(a) Conventional (2D) (b) Conventional (3D) (c) Present (Mesh Overlay)

Fig. 3.86 y-directional strain rate $\dot{\varepsilon}_y$ distributions at U/L=0.12 of rigid-plastic block compression with void under fixed boundary condition

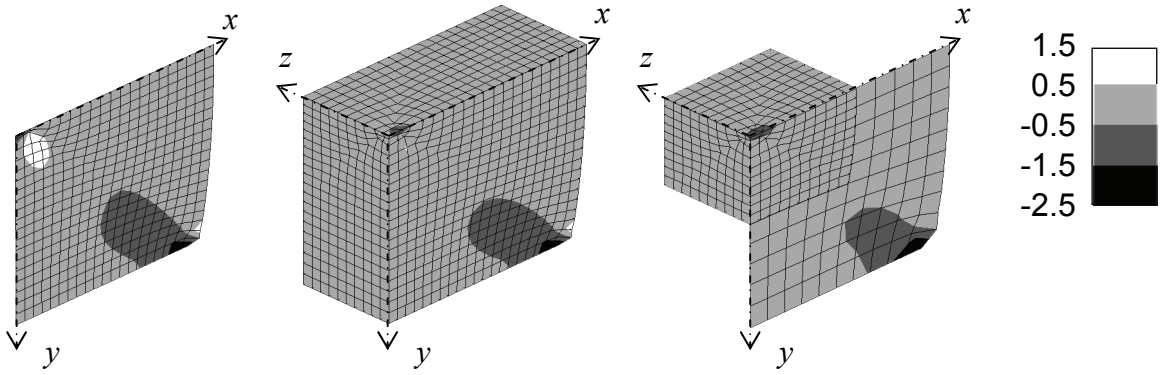

(a) Conventional (2D) (b) Conventional (3D) (c) Present (Mesh Overlay)

Fig. 3.87 *xy*-shear strain rate $\dot{\varepsilon}_{xy}$ distributions at U/L=0.12 of rigid-plastic block compression with void under fixed boundary condition

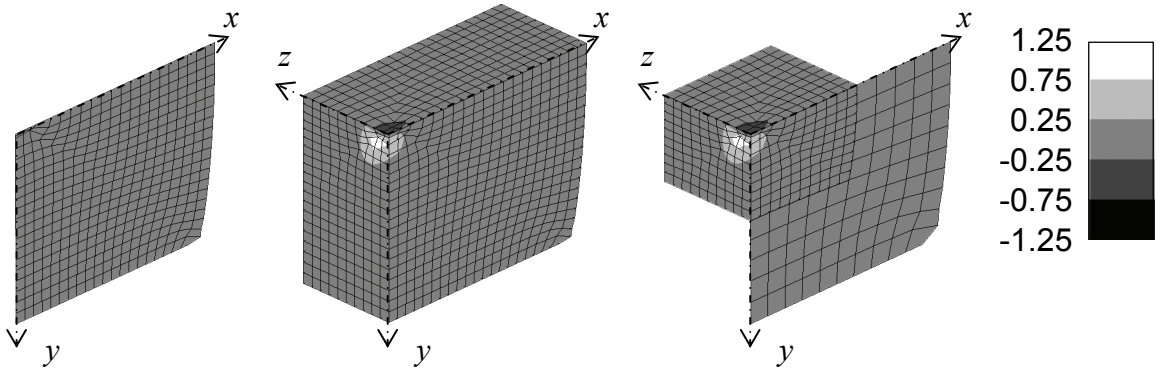

(a) Conventional (2D) (b) Conventional (3D) (c) Present (Mesh Overlay)

Fig. 3.88 *yz*-shear strain rate $\dot{\varepsilon}_{yz}$ distributions at U/L=0.12 of rigid-plastic block compression with void under fixed boundary condition

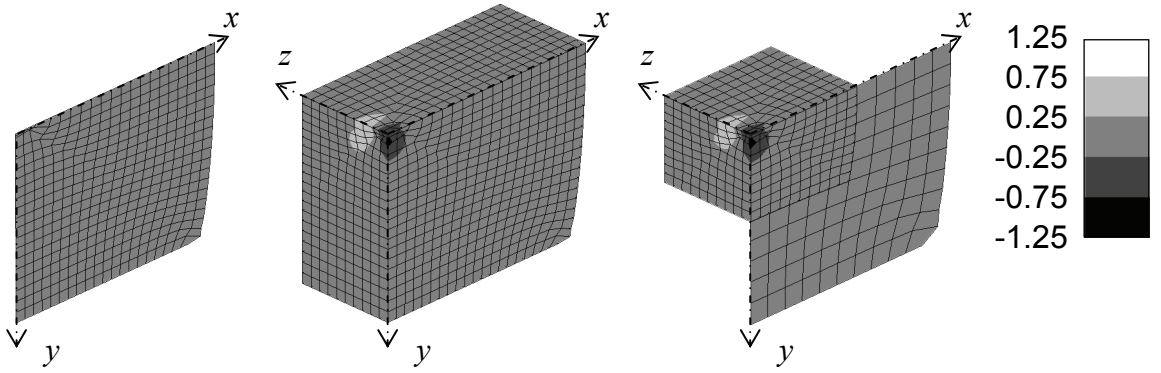

(a) Conventional (2D) (b) Conventional (3D) (c) Present (Mesh Overlay)

Fig. 3.89 *z*-directional strain rate $\dot{\varepsilon}_z$ distributions at U/L=0.12 of rigid-plastic block compression with void under fixed boundary condition

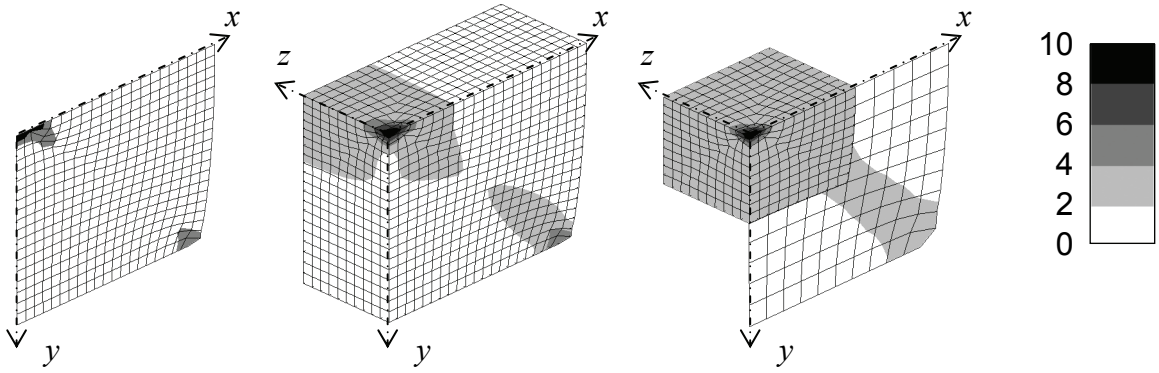

(a) Conventional (2D) (b) Conventional (3D) (c) Present (Mesh Overlay)

Fig. 3.90 Equivalent strain rate $\dot{\bar{\varepsilon}}$ distributions at U/L=0.12 of rigid-plastic block compression with void under fixed boundary condition

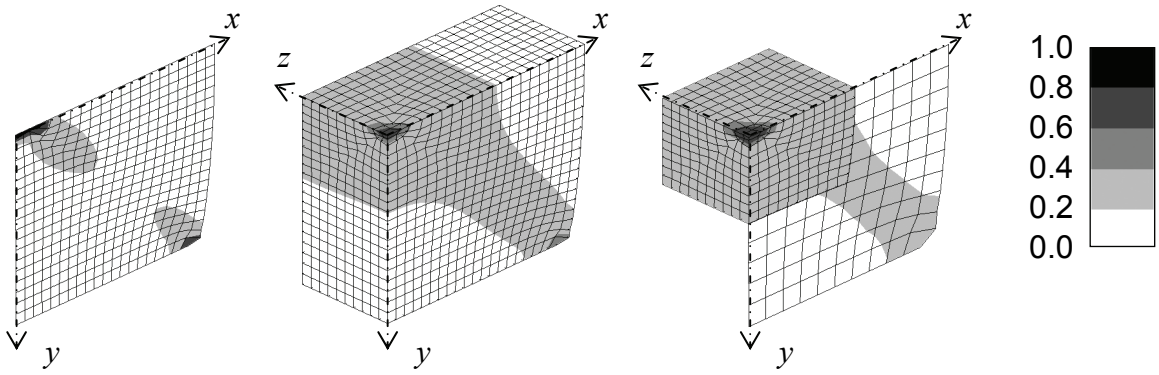

(a) Conventional (2D) (b) Conventional (3D) (c) Present (Mesh Overlay)

Fig. 3.91 Equivalent strain $\bar{\varepsilon}$ distributions at U/L=0.12 of rigid-plastic block compression with void under fixed boundary condition

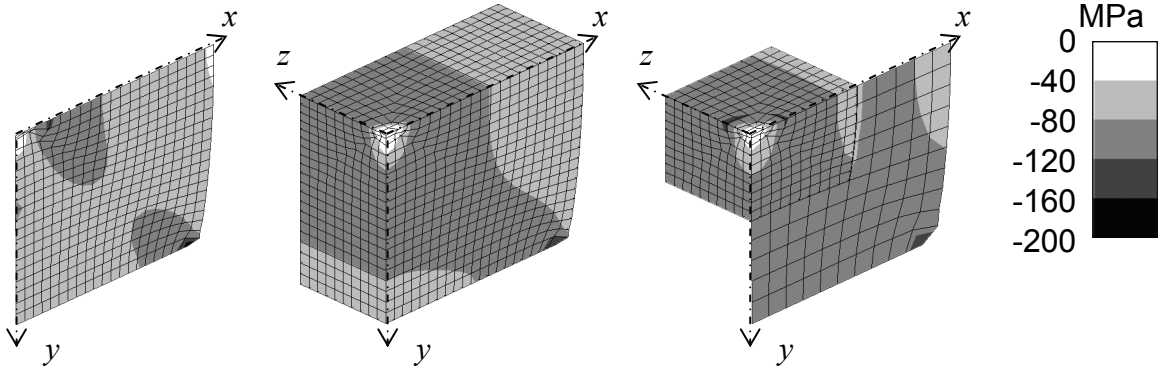

(a) Conventional (2D) (b) Conventional (3D) (c) Present (Mesh Overlay)

Fig. 3.92 y-directional stress σ_y distributions at U/L=0.12 of rigid-plastic block compression with void under fixed boundary condition

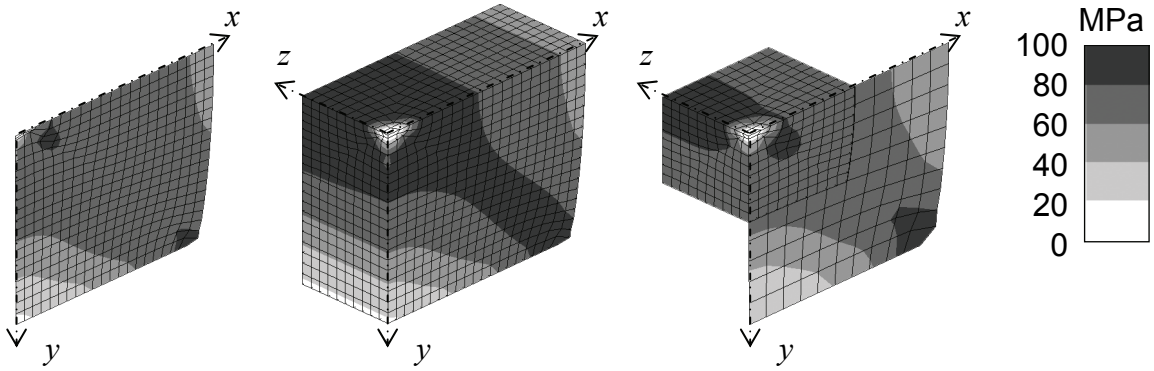

(a) Conventional (2D) (b) Conventional (3D) (c) Present (Mesh Overlay)

Fig. 3.93 Equivalent stress $\bar{\sigma}$ distributions at U/L=0.12 of rigid-plastic block compression with void under fixed boundary condition

Figure 3.94 shows the mesh deformation on the xy-plane (z=0 plane) at the nominal longitudinal displacement U/L=0.12 (the final step) by the conventional method (two-dimensional and three-dimensional) and the present mesh overlay method, respectively. The void mostly closes at the nominal longitudinal displacement U/L=0.12 when the two-dimensional conditions are assumed. However, the void does not fully close when the three-dimensional analysis is applied. The present mesh overlay method expresses deformation of the void similar to the conventional three-dimensional analysis.

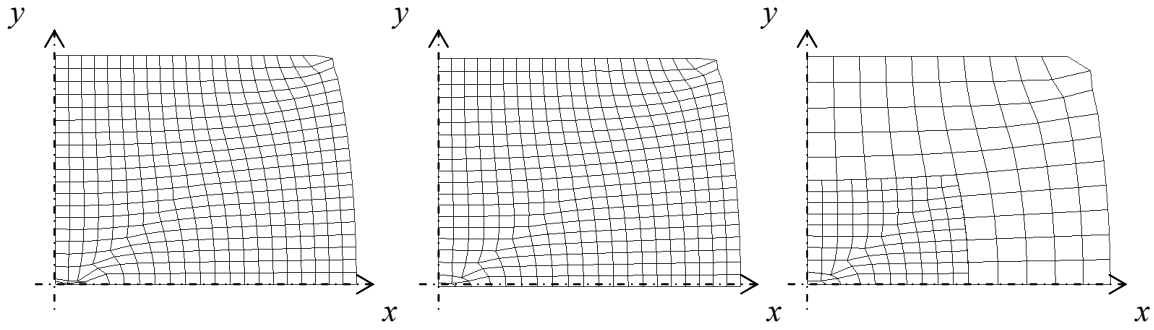

(a) Conventional (2D) (b) Conventional (3D) (c) Present (Mesh Overlay)

Fig. 3.94 Mesh deformation (z=0 plane) at U/L=0.12 of rigid-plastic block compression with void under fixed boundary condition

Additionally, **Fig. 3.95** shows the axial strain ε_x, ε_y and ε_z, and the volumetric strain ε_V of the void at nominal longitudinal displacement U/L=0.12 (the final step) by the conventional method (two-dimensional and three-dimensional) and the present mesh overlay method, respectively. The conventional three-dimensional result when the shear free boundary conditions are imposed, which is performed in the previous subsection, is also shown in this figure. Similar to the previous case, the two-dimensional analysis overestimates the volumetric strain ε_V due to overestimation of the y-directional strain ε_y. Additionally, the z-directional strain ε_z, which is ignored in two-dimensional analysis, has some effect on the void closure. Moreover, it is also shown that the void closes more easily when the fixed boundary conditions are applied than when the shear free boundary conditions are imposed. Hence, the boundary conditions also have an influence on the void closure. Of course, the macro deformation is not uniform under the fixed boundary conditions. Therefore, the position of the void may also have a great influence on the void closure. When considering the plate rolling process, this fact suggests that the void closure is not defined only by the reduction ratio of the rolling pass if the boundary conditions, like the friction coefficient and/or the position of the void, are not appropriate.

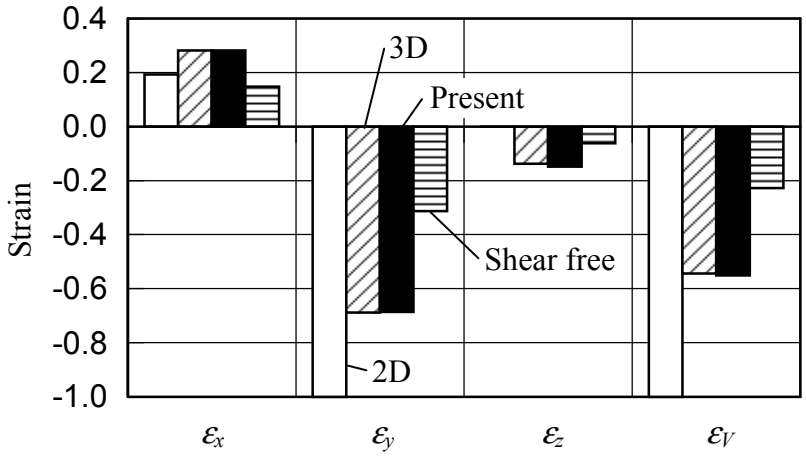

Fig. 3.95 Axial strain ε_x, ε_y, ε_z and volumetric strain ε_V of the inclusion at U/L=0.12 of rigid-plastic block compression with void under fixed boundary condition

3.6.5 Summary

As with other numerical examples for applying the efficient three-dimensional analysis, the deformation behavior of the block with a spherical void at the center under compression was investigated to verify its versatility. A two-dimensional analysis was also computed as a conventional analysis to verify the validity of the two-dimensional assumption. Since the two-dimensional analysis regards a void as a penetrated hole, the void deforms easier than with the three-dimensional analysis. Moreover, it was also confirmed that strain and stress distributes along the z-direction at the void and its vicinity, and the void deformation along the z-direction that affects the void closure is also observed. Therefore, it was concluded that a three-dimensional analysis is required at least at and around the void in order to achieve the quantitative analysis. It was also verified that the present mesh overlay analysis gives results close to the three-dimensional analysis with vastly reduced computing cost. Therefore, the practicality of the present mesh overlay method that applies a two-dimensional global model with a three-dimensional local model was demonstrated. Additionally, the boundary conditions as well as the position of the void also have an influence on the void closure. Therefore, nominal strain or reduction ratio is not a universal parameter to presume void closure during the metal forming process.

3.7 Conclusions

In this chapter, the rigid-plastic mesh overlay formulations were newly derived. Moreover, the stiffness equations based on Newton-Raphson method were also developed in order to increase the computing speed. The features of the present formulations are as follows:

1) The mesh overlay method describes velocity at any point as the summation of the global velocity and the local velocity. In order to satisfy the C^0 continuity of velocity, the local velocity on the global-local boundary is set to zero as the boundary conditions.

2) The volume constancy conditions are also imposed on the global model where the local model overlays it in order to control severe deformation of the global model.

3) In the local region, the global stiffness matrix $[K^G]$ ($[K^{G'}]$ for Newton-Raphson method) should be evaluated by the local Gauss points because of the nonlinearity of rigid-plastic problems.

4) However, if the local model covers only one global element, the formulations can be simplified like the elastic mesh overlay formulations.

Due to these features, the rigid-plastic mesh overlay analysis can be successfully performed even when the local model covers two or more global elements.

Numerical examples were investigated to verify the rigid-plastic mesh overlay method derived in this research. Numerical results for a plane strain plate compression with a circular inclusion at the center represented that the mesh overlay method gives results close to conventional method with both a harder inclusion case and a softer inclusion case. Furthermore, it was also confirmed that severe global element deformation in the local region could be controlled by imposing the volume constant conditions on the whole global elements. The small inclusion deformation behavior under the bulk metal was also demonstrated. The obtained results showed that the metal flow that drives an inclusion to the surface, which is said to induce a surface scratch in the metal forming process, can not be observed.

Finally, the efficient three-dimensional approach that combines a three-dimensional local model with a two-dimensional global model, which was newly proposed in this research and performed for elastic problems in the previous chapter, was applied to rigid-plastic analysis. The deformation behavior of a block with a small inclusion or void under simple compression was investigated using the present mesh overlay method. These numerical examples represented that the inclusion or void and its vicinity shows three-dimensional deformation. Therefore, simplified approaches that assume two-dimensional conditions may fail to grasp the quantitative deformation characteristics. It was confirmed that the accuracy of the present method compares with that of conventional three-dimensional analysis through the numerical examples. Moreover, the computing cost significantly decreases with the present method application. There are various metal forming processes in which the macro deformation behavior can be assumed to be two-dimensional although its micro behavior should be regarded as three-dimensional. Hence, the present method will quantitatively clarify such deformation mechanisms with lower computing costs.

Chapter 4

Conclusions

In order to develop a rational numerical method for analyzing micro behavior under macro deformation, the fundamental research needed to apply the mesh overlay method to the metal forming process was performed.

In Chapter 2, the formulations of the mesh overlay method for elastic problem were reviewed first. The features of the mesh overlay method are (1) the coupled analysis between the global and local models, and (2) the flexibility of mesh discretization. Then, the relation between solution accuracy and convergence criterion when the iterative method is applied to solve the simultaneous linear equations was also investigated to consider the suitability of the iterative method for the mesh overlay analysis. This research concluded that the iterative method might fail to acquire accurate solutions when the convergence criterion is inadequate, especially when the size of the elements in one computational model widely distributes, which is an advantage of the mesh overlay method. Hence, from the standpoint on the accuracy, the direct method is adopted to solve the stiffness equations in this research. Then, the features of the mesh overlay method were verified through numerical examples, including a center-holed plane strain tension and an application to the homogenization problems. Moreover, the mesh overlay method that applies a three-dimensional local model with a two-dimensional global model was newly proposed as an efficient three-dimensional analysis. A simple compression problem of a block that contains a small spherical inclusion at the center was considered to verify the present method. According to the numerical simulation, it was shown that the present mesh overlay analysis gives close results to conventional FE analysis.

In Chapter 3, in order to extend the mesh overlay method to rigid-plastic analysis, the following research was performed. First, it was certified that the global stiffness

matrix in the local region should be evaluated by the local model due to the material nonlinearity of rigid-plastic deformation. Based on this conclusion, the rigid-plastic mesh overlay formulations were newly derived. Furthermore, the stiffness equations based on Newton-Raphson method were also developed in order to increase the computing speed. Additionally, the volume constancy conditions are also imposed on the global element where it is overlaid by the local model in order to control its severe deformation. Through the numerical simulations for the deformation behavior of a plane strain plate with a circular inclusion at the center under the compression, it was verified that the mesh overlay method gives results close to the ordinary method with either harder inclusion or softer inclusion. Moreover, it was also confirmed that severe global element deformation in the region where the local model overlays it could be controlled by imposing the volume constancy conditions to the whole global elements.

The efficient three-dimensional approach that combines a two-dimensional global model with a three-dimensional local model was also applied to rigid-plastic analysis. The deformation behavior of a simple compression of a block with a small spherical inclusion or void was investigated using the present mesh overlay method. These numerical examples represented that the deformation at the inclusion or void and its vicinity is three-dimensional. Therefore, conventional approaches that assume two-dimensional condition may fail to grasp the quantitative deformation characteristics. It was also confirmed that the accuracy of the present method is high enough through the comparison with the conventional three-dimensional analysis. In addition, the computing cost vastly improved due to the application of the present method. There are various metal forming processes in which the macro deformation behavior can be assumed to be two-dimensional although its micro behavior should be regarded as three-dimensional. Hence, the present method will quantitatively clarify such deformation mechanisms with lower computing costs.

In conclusion, this report devotes the fundamental research to applying the mesh overlay method for the metal forming process. Through this research, the following facts were newly derived:

(1) The direct method is suitable for the stiffness equation solver of the mesh overlay

method due to its high accuracy.

(2) The mesh overlay method was successfully extended to rigid-plastic (nonlinear) problems.

(3) An efficient three-dimensional analysis not only for elastic problem but also for rigid-plastic problem was proposed that couples a two-dimensional global model with a three-dimensional local model by employing the mesh overlay method.

However, the following issues still remain in order to improve the practicality of the mesh overlay method:

(1) How to decide the size of the local model as well as the resolution of the global model is still left to the analyst. Therefore, some universal guidelines to decide these parameters and/or establishments of accuracy evaluation of the mesh overlay analysis are needed.

(2) More effective restraint to control undesirable global deformation in the local region for the rigid-plastic mesh overlay analysis is demanded.

(3) It will be required to contain the surfaces in the local model when the deformation behavior of the surface microasperity[21),68),69)] , or one of the surface defects[22),70)~73)] is analyzed by the mesh overlay method. Under such conditions, the surface topology can not be expressed by the global model due to its rough resolution. Therefore, developing a mesh overlay strategy when the local model protrudes outside the global model[74)] will be required.

Of course, the application of the mesh overlay method to actual metal forming processes is the most challenging work for this research. For example, if the present method is applied in analyzing the deformation behavior of internal inclusions/voids in the stock during the rolling pass, the apperance mechanism of the surface scratches on the surface will be clarified. Moreover, by quantifying the topology transfer effect between the roll and stock during the rolling process, surface roughness, one of the most important quality factors of the rolled material, can be controlled as needed. Therefore, different desirable outcomes can be achieved through applying the rigid-plastic mesh overlay

method, newly derived in this research, to industrial metal forming process.

Appendices

Appendix A

Mesh Overlay Formulations by Principle of Virtual Work

A.1 Introduction

The mesh overlay formulations can be also derived by using the principle of virtual work. In this appendix, the procedures for deriving the mesh overlay formulations for elastic materials using the principle of virtual work are reviewed.

A.2 Formulations

As shown in Chapter 2, two models, the global and local models, are defined. The global model covers the whole region Ω, whereas the local model, which overlays the global model, covers only the local region Ω^L. The region covered only by the global model is named the global region Ω^G, and the boundary between the global region Ω^G and the local region Ω^L is named the global-local boundary Γ^{GL}.

$$\Omega = \Omega^G \cup \Omega^L \tag{A.1a}$$

$$\Omega^G \cap \Omega^L = 0 \tag{A.1b}$$

In the mesh overlay method, displacement u_i is defined by eq. (A.2), where ${u^G}_i$ and ${u^L}_i$ denote the global and local displacements, respectively.

$$u_i \equiv \begin{cases} {u^G}_i & in \quad \Omega^G \\ {u^G}_i + {u^L}_i & in \quad \Omega^L \end{cases} \tag{A.2}$$

In order to satisfy the C^0 continuity of displacement u_i, the local displacement ${u^L}_i$ is set to be zero on the global-local boundary Γ^{GL}.

$${u^L}_i = 0 \qquad on \quad \Gamma^{GL} \tag{A.3}$$

Then, strain ε_{ij} is expressed by eq. (A.4).

$$\varepsilon_{ij} = \begin{cases} \dfrac{\partial u^G{}_i}{\partial x_j} \equiv \varepsilon^G{}_{ij} & in \quad \Omega^G \\ \dfrac{\partial u^G{}_i}{\partial x_j} + \dfrac{\partial u^L{}_i}{\partial x_j} \equiv \varepsilon^G{}_{ij} + \varepsilon^L{}_{ij} & in \quad \Omega^L \end{cases} \tag{A.4}$$

Stress σ_{ij} is expressed by eq. (A.5) where $D^G{}_{ijkl}$ and $D^L{}_{ijkl}$ denote the elastic deformation tensor for the global and local elements, respectively.

$$\sigma_{ij} = \begin{cases} D^G{}_{ijkl}\varepsilon^G{}_{kl} & in \quad \Omega^G \\ D^L{}_{ijkl}(\varepsilon^G{}_{kl} + \varepsilon^L{}_{kl}) & in \quad \Omega^L \end{cases} \tag{A.5}$$

Now, let us consider that the body force b_i acts on the whole region Ω and the external force t_i acts on the boundary Γ_t. The principle of virtual work for linear elastic materials is expressed by eq. (A.6).

$$\int_\Omega \delta\varepsilon_{ij} D_{ijkl} \varepsilon_{kl} d\Omega - \int_\Omega \delta u_i b_i d\Omega - \int_{\Gamma_t} \delta u_i t_i d\Gamma = 0 \tag{A.6}$$

Substitution of eqs. (A.2) and (A.4) into eq. (A.6) yields eq. (A.7a).

$$\begin{aligned} &\int_{\Omega^G} \delta\varepsilon^G{}_{kl} D^G{}_{ijkl} \varepsilon^G{}_{kl} d\Omega + \int_{\Omega^L} (\delta\varepsilon^G{}_{ij} + \delta\varepsilon^L{}_{ij}) D^L{}_{ijkl} (\varepsilon^G{}_{kl} + \varepsilon^L{}_{kl}) d\Omega \\ &\quad = \int_{\Omega^G} \delta u^G{}_i b_i d\Omega + \int_{\Omega^L} (\delta u^G{}_i + \delta u^L{}_i) b_i d\Omega \\ &\qquad + \int_{\Gamma^G{}_t} \delta u^G{}_i t_i d\Gamma + \int_{\Gamma^L{}_t} (\delta u^G{}_i + \delta u^L{}_i) t_i d\Gamma \end{aligned} \tag{A.7a}$$

Then, eq. (A.7b) is derived from eq. (A.7a).

$$\begin{aligned} &\int_{\Omega^G} \delta\varepsilon^G{}_{ij} D^G{}_{ijkl} \varepsilon^G{}_{kl} d\Omega + \int_{\Omega^L} \delta\varepsilon^G{}_{ij} D^L{}_{ijkl} \varepsilon^G{}_{kl} d\Omega + \int_{\Omega^L} \delta\varepsilon^G{}_{ij} D^L{}_{ijkl} \varepsilon^L{}_{kl} d\Omega \\ &\quad + \int_{\Omega^L} \delta\varepsilon^L{}_{ij} D^L{}_{ijkl} \varepsilon^G{}_{kl} d\Omega + \int_{\Omega^L} \delta\varepsilon^L{}_{ij} D^L{}_{ijkl} \varepsilon^L{}_{kl} d\Omega \\ &\quad = \int_{\Omega^G} \delta u^G{}_i b_i d\Omega + \int_{\Omega^L} \delta u^G{}_i b_i d\Omega + \int_{\Omega^L} \delta u^L{}_i b_i d\Omega \\ &\qquad + \int_{\Gamma^G{}_t} \delta u^G{}_i t_i d\Gamma + \int_{\Gamma^L{}_t} \delta u^G{}_i t_i d\Gamma + \int_{\Gamma^L{}_t} \delta u^L{}_i t_i d\Gamma \end{aligned} \tag{A.7b}$$

In order to simplify the calculation, eq. (A.8) is assumed, in which the global elastic deformation tensor D^G_{ijkl} is used instead of the local elastic deformation tensor D^L_{ijkl}.

$$\int_{\Omega^L} \delta\varepsilon^G{}_{ij} D^L{}_{ijkl} \varepsilon^G{}_{kl} d\Omega \approx \int_{\Omega^L} \delta\varepsilon^G{}_{ij} D^G{}_{ijkl} \varepsilon^G{}_{kl} d\Omega \tag{A.8}$$

Substitution of eq. (A.8) into eq. (A.7b) yields eq. (A.9) where $\Omega = \Omega^G + \Omega^L$ and $\Gamma_t = \Gamma^G{}_t + \Gamma^L{}_t$ are used.

$$\begin{aligned}
&\int_{\Omega} \delta\varepsilon^G{}_{ij} D^G{}_{ijkl} \varepsilon^G{}_{kl} d\Omega + \int_{\Omega^L} \delta\varepsilon^G{}_{ij} D^L{}_{ijkl} \varepsilon^L{}_{kl} d\Omega \\
&\quad + \int_{\Omega^L} \delta\varepsilon^L{}_{ij} D^L{}_{ijkl} \varepsilon^G{}_{kl} d\Omega + \int_{\Omega^L} \delta\varepsilon^L{}_{ij} D^L{}_{ijkl} \varepsilon^L{}_{kl} d\Omega \\
&\quad = \int_{\Omega} \delta u^G{}_i b_i d\Omega + \int_{\Omega^L} \delta u^L{}_i b_i d\Omega + \int_{\Gamma_t} \delta u^G{}_i t_i d\Gamma + \int_{\Gamma^L{}_t} \delta u^L{}_i t_i d\Gamma
\end{aligned} \tag{A.9a}$$

Equation (A.9b) denotes matrix notation of eq. (A.9a)

$$\begin{aligned}
&\int_{\Omega} \{\delta\varepsilon^G\}^T [D^G] \{\varepsilon^G\} d\Omega + \int_{\Omega^L} \{\delta\varepsilon^G\}^T [D^L] \{\varepsilon^L\} d\Omega \\
&\quad + \int_{\Omega^L} \{\delta\varepsilon^L\}^T [D^L] \{\varepsilon^G\} d\Omega + \int_{\Omega^L} \{\delta\varepsilon^L\}^T [D^L] \{\varepsilon^L\} d\Omega \\
&\quad = \int_{\Omega} \{\delta u^G\}^T \{b\} d\Omega + \int_{\Omega^L} \{\delta u^L\}^T \{b\} d\Omega \\
&\qquad + \int_{\Gamma_t} \{\delta u^G\}^T \{t\} d\Gamma + \int_{\Gamma^L{}_t} \{\delta u^L\}^T \{t\} d\Gamma
\end{aligned} \tag{A.9b}$$

The global and local displacement vectors $\{u^G\}$ and $\{u^L\}$ at arbitrary points are expressed by the nodal displacement vectors $\{d^G\}$ and $\{d^L\}$ for the global and local nodes, and the shape function matrix $[N^G]$ and $[N^L]$ for the global and local elements, respectively.

$$\{u^G\} = [N^G] \{d^G\} \tag{A.10a}$$

$$\{u^L\} = [N^L] \{d^L\} \tag{A.10b}$$

Moreover, the global and local strain vectors $\{\varepsilon^G\}$ and $\{\varepsilon^L\}$ are denoted in eq. (A.11) where $[B^G]$ and $[B^L]$ denote the strain-nodal displacement matrix for the global and local elements, respectively.

$$\{\varepsilon^G\} = [B^G]\{d^G\} \tag{A.11a}$$

$$\{\varepsilon^L\} = [B^L]\{d^L\} \tag{A.11b}$$

Substitution of eqs. (A.10) ~ (A.11) into eq. (A.9) results in eq. (A.12a).

$$\begin{aligned}
&\int_\Omega ([B^G]\{\delta d^G\})^T [D^G]([B^G]\{d^G\}) d\Omega + \int_{\Omega^L} ([B^G]\{\delta d^G\})^T [D^L]([B^L]\{d^L\}) d\Omega \\
&\quad + \int_{\Omega^L} ([B^L]\{\delta d^L\})^T [D^L]([B^G]\{d^G\}) d\Omega + \int_{\Omega^L} ([B^L]\{\delta d^L\})^T [D^L]([B^L]\{d^L\}) d\Omega \\
&\quad = \int_\Omega ([N^G]\{\delta d^G\})^T \{b\} d\Omega + \int_{\Omega^L} ([N^L]\{\delta d^L\})^T \{b\} d\Omega \\
&\quad\quad + \int_{\Gamma_t} ([N^G]\{\delta d^G\})^T \{t\} d\Gamma + \int_{\Gamma^L_t} ([N^L]\{\delta d^L\})^T \{t\} d\Gamma
\end{aligned} \tag{A.12a}$$

Then, eq. (A.12b) is easily derived.

$$\begin{aligned}
&\{\delta d^G\}^T \left(\int_\Omega [B^G]^T [D^G][B^G] d\Omega \{d^G\} + \int_{\Omega^L} [B^G]^T [D^L][B^L] d\Omega \{d^L\} \right) \\
&\quad + \{\delta d^L\}^T \left(\int_{\Omega^L} [B^L]^T [D^L][B^G] d\Omega \{d^G\} + \int_{\Omega^L} [B^L]^T [D^L][B^L] d\Omega \{d^L\} \right) \\
&\quad = \{\delta d^G\}^T \left(\int_\Omega [N^G]^T \{b\} d\Omega + \int_{\Gamma_t} [N^G]^T \{t\} d\Gamma \right) \\
&\quad\quad + \{\delta d^L\}^T \left(\int_{\Omega^L} [N^L]^T \{b\} d\Omega + \int_{\Gamma^L_t} [N^L]^T \{t\} d\Gamma \right)
\end{aligned} \tag{A.12b}$$

Equations (A.13a) ~ (A.13b) are required in order to satisfy eq. (A.12b) for arbitrary global and local virtual displacement vectors $\{\delta d^G\}$ and $\{\delta d^L\}$.

$$\begin{aligned}
&\int_\Omega [B^G]^T [D^G][B^G] d\Omega \{d^G\} + \int_{\Omega^L} [B^G]^T [D^L][B^L] d\Omega \{d^L\} \\
&\quad = \int_\Omega [N^G]^T \{b\} d\Omega + \int_{\Gamma_t} [N^G]^T \{t\} d\Omega
\end{aligned} \tag{A.13a}$$

$$\begin{aligned}
&\int_{\Omega^L} [B^L]^T [D^L][B^G] d\Omega \{d^G\} + \int_{\Omega^L} [B^L]^T [D^L][B^L] d\Omega \{d^L\} \\
&\quad = \int_{\Omega^L} [N^L]^T \{b\} d\Omega + \int_{\Gamma^L_t} [N^L]^T \{t\} d\Omega
\end{aligned} \tag{A.13b}$$

Hence, eqs. (A.13a) ~ (A.13b) are modified as follows:

$$[K^G]\{d^G\}+[K^{GL}]\{d^L\}=\{f^G\} \tag{A.14a}$$

$$[K^{LG}]\{d^G\}+[K^L]\{d^L\}=\{f^L\} \tag{A.14b}$$

Here, the global stiffness matrix $[K^G]$, the coupled stiffness matrix $[K^{GL}]$, the local stiffness matrix $[K^L]$, the global force vector $\{f^G\}$ and the local force vector $\{f^L\}$ are defined as follows.

$$[K^G]=\int_\Omega [B^G]^T[D^G][B^G]d\Omega \tag{A.15a}$$

$$[K^{GL}]=[K^{LG}]^T=\int_{\Omega^L}[B^G]^T[D^L][B^L]d\Omega \tag{A.15b}$$

$$[K^L]=\int_{\Omega^L}[B^L]^T[D^L][B^L]d\Omega \tag{A.15c}$$

$$\{f^G\}=\int_\Omega [N^G]^T\{b\}d\Omega+\int_{\Gamma_t}[N^G]^T\{t\}d\Omega \tag{A.15d}$$

$$\{f^L\}=\int_{\Omega^L}[N^L]^T\{b\}d\Omega+\int_{\Gamma^L{}_t}[N^L]^T\{t\}d\Omega \tag{A.15e}$$

Appendix B

Conjugate Gradient Method

B.1 Introduction

Recently, the conjugate gradient (CG) method has often been adopted to solve a system of linear equations. The most important feature of the CG method is its fast computing speed because there are no matrix inner products requiring long calculating time. In this appendix, the algorithm of the CG method is reviewed.

B.2 Formulations[75)~77)]

Consider the system of linear equations given by eq. (B.1).

$$[A]\{x\} = \{b\} \tag{B.1}$$

Here, the matrix $[A]$ and the vector $\{b\}$ are known, but the vector $\{x\}$ is unknown. Moreover, $[A]$ is assumed to be a symmetric matrix.

Since the CG method is an iterative method, the unknown vector $\{x\}$ is guessed and revised until it converges. In order to judge the convergence, the residual vector $\{r\}$ is defined by eq. (B.2).

$$\{r\} \equiv \{b\} - [A]\{x\} \tag{B.2}$$

Clearly, when the guess of the unknown vector $\{x\}$ is correct, the residual vector $\{r\}$ becomes a zero vector. Hence, the norm of the residual vector $\{r\}$ can be used to evaluate the accuracy of the guess of the unknown vector $\{x\}$.

In order to improve the converging speed, scaling is often effective. Here, a scaling matrix $[W]$ is assumed to be expressed as follows:

$$[W] = [w]^T[w] \tag{B.3}$$

By multiplying eq. (B.1) by $[w]^{-T}$ from the left, eq. (B.4) is derived.

$$[w]^{-T}[A]\{x\} = [w]^{-T}\{b\} \tag{B.4}$$

Since $[w]^{-1}[w]$ is a unit matrix, eq. (B.5) can be obtained.

$$[w]^{-T}[A][w]^{-1}[w]\{x\} = [w]^{-T}\{b\} \tag{B.5}$$

Here, $[\widetilde{A}]$, $\{\widetilde{x}\}$ and $\{\widetilde{b}\}$ are defined as follows:

$$[\widetilde{A}] \equiv [w]^{-T}[A][w]^{-1} \tag{B.6}$$

$$\{\widetilde{x}\} \equiv [w]\{x\} \tag{B.7}$$

$$\{\widetilde{b}\} \equiv [w]^{-T}\{b\} \tag{B.8}$$

By using eqs. (B.6) ~ (B.8), eq. (B.5) is modified to eq. (B.9).

$$[\widetilde{A}]\{\widetilde{x}\} = \{\widetilde{b}\} \tag{B.9}$$

First, the formulations to solve eq. (B.9) by the CG method are reviewed. The residual vector $\{\widetilde{r}\}$ is defined in eq. (B.10).

$$\{\widetilde{r}\} \equiv \{\widetilde{b}\} - [\widetilde{A}]\{\widetilde{x}\} \tag{B.10}$$

The initial guess of the unknown vector $\{\widetilde{x}\}$ is set to a zero vector.

The (k+1)-th assumption of the unknown vector $\{\widetilde{x}\}$ is renewed in accordance with eq. (B.11).

$$\{\widetilde{x}^{(k+1)}\} = \{\widetilde{x}^{(k)}\} + \alpha^{(k)}\{\widetilde{p}^{(k)}\} \tag{B.11}$$

Here, $\{\widetilde{x}^{(k)}\}$ denotes the guess of the unknown vector $\{\widetilde{x}\}$ at the k-th iteration, $\{\widetilde{p}\}$ denotes the directional correction vector, and α denotes the quantity of the correction. Initially, the directional correction vector $\{\widetilde{p}\}$ is set to the residual vector $\{\widetilde{r}\}$.

$$\{\tilde{p}\} = \{\tilde{r}\} \tag{B.12}$$

Equation (B.13) gives the residual vector at the (k+1)-th iteration $\{\tilde{r}^{(k+1)}\}$.

$$\{\tilde{r}^{(k+1)}\} = \{\tilde{b}\} - [\tilde{A}]\{\tilde{x}^{(k+1)}\} \tag{B.13}$$

Substitution of eq. (B.13) into eq. (B.11) yields eq. (B.14).

$$\begin{aligned}\{\tilde{r}^{(k+1)}\} &= \{\tilde{b}\} - [\tilde{A}](\{\tilde{x}^{(k)}\} + \alpha^{(k)}\{\tilde{p}^{(k)}\}) \\ &= \{\tilde{b}\} - [\tilde{A}]\{\tilde{x}^{(k)}\} - \alpha^{(k)}[\tilde{A}]\{\tilde{p}^{(k)}\} \\ &= \{\tilde{r}^{(k)}\} - \alpha^{(k)}[\tilde{A}]\{\tilde{p}^{(k)}\}\end{aligned} \tag{B.14}$$

Equation (B.15) defines the function Q, where $(\{X\}, \{Y\})$ means the inner product of a vector $\{X\}$ and $\{Y\}$.

$$Q(\{\tilde{r}\}) = (\{\tilde{r}\}, [\tilde{A}]^{-1}\{\tilde{r}\}) \tag{B.15}$$

By substituting eq. (B.14) into eq. (B.15), eq. (B.16) is derived.

$$\begin{aligned}Q(\{\tilde{r}^{(k+1)}\}) &= (\{\tilde{r}^{(k+1)}\}, [\tilde{A}]^{-1}\{\tilde{r}^{(k+1)}\}) \\ &= (\{\tilde{r}^{(k)}\} - \alpha^{(k)}[\tilde{A}]\{\tilde{p}^{(k)}\}, [A]^{-1}(\{\tilde{r}^{(k)}\} - \alpha^{(k)}[\tilde{A}]\{\tilde{p}^{(k)}\})) \\ &= (\{\tilde{r}^{(k)}\} - \alpha^{(k)}[\tilde{A}]\{\tilde{p}^{(k)}\}, [A]^{-1}\{\tilde{r}^{(k)}\} - \alpha^{(k)}\{\tilde{p}^{(k)}\})\end{aligned} \tag{B.16}$$

Equation (B.17) expresses the derivative of the function Q by $\alpha^{(k)}$.

$$\begin{aligned}\frac{dQ}{d\alpha^{(k)}} &= \frac{\partial}{\partial\alpha^{(k)}}(\{\tilde{r}^{(k)}\} - \alpha^{(k)}[\tilde{A}]\{\tilde{p}^{(k)}\}, [A]^{-1}\{\tilde{r}^{(k)}\} - \alpha^{(k)}\{\tilde{p}^{(k)}\}) \\ &= (-[\tilde{A}]\{\tilde{p}^{(k)}\}, [A]^{-1}\{\tilde{r}^{(k)}\} - \alpha^{(k)}\{\tilde{p}^{(k)}\}) \\ &\quad + (\{\tilde{r}^{(k)}\} - \alpha^{(k)}[\tilde{A}]\{\tilde{p}^{(k)}\}, -\{\tilde{p}^{(k)}\}) \\ &= -([\tilde{A}]\{\tilde{p}^{(k)}\}, [A]^{-1}\{\tilde{r}^{(k)}\}) + \alpha^{(k)}([\tilde{A}]\{\tilde{p}^{(k)}\}, \{\tilde{p}^{(k)}\}) \\ &\quad - (\{\tilde{r}^{(k)}\}, \{\tilde{p}^{(k)}\}) + \alpha^{(k)}([\tilde{A}]\{\tilde{p}^{(k)}\}, \{\tilde{p}^{(k)}\}) \\ &= 2\alpha^{(k)}([\tilde{A}]\{\tilde{p}^{(k)}\}, \{\tilde{p}^{(k)}\}) - 2(\{\tilde{r}^{(k)}\}, \{\tilde{p}^{(k)}\})\end{aligned} \tag{B.17}$$

Note that $(\{X\}, \{Y\}) = (\{Y\}, \{X\})$, $([A]\{X\}, \{Y\}) = (\{X\}, [A]^T\{Y\})$, and $[A]^T$=$[A]$ are used to derive eq. (B.17). $\alpha^{(k)}$ that minimizes the function Q is given by eq. (B.18).

$$\alpha^{(k)} = \frac{\left(\{\tilde{r}^{(k)}\}, \{\tilde{p}^{(k)}\}\right)}{\left([\tilde{A}]\{\tilde{p}^{(k)}\}, \{\tilde{p}^{(k)}\}\right)} \tag{B.18}$$

The directional correction vector at the (k+1)-th iteration, $\{\tilde{p}^{(k+1)}\}$, is defined by eq. (B.19).

$$\{\tilde{p}^{(k+1)}\} = \{\tilde{r}^{(k+1)}\} + \beta^{(k)}\{\tilde{p}^{(k)}\} \tag{B.19}$$

Then, the inner product of $\{\tilde{p}^{(k+1)}\}$ and $[\tilde{A}]\{\tilde{p}^{(k)}\}$ is expressed by eq. (B.20).

$$\begin{aligned}\left(\{\tilde{p}^{(k+1)}\}, [\tilde{A}]\{\tilde{p}^{(k)}\}\right) &= \left(\{\tilde{r}^{(k+1)}\} + \beta^{(k)}\{\tilde{p}^{(k)}\}, [\tilde{A}]\{\tilde{p}^{(k)}\}\right) \\ &= \left(\{\tilde{r}^{(k+1)}\}, [\tilde{A}]\{\tilde{p}^{(k)}\}\right) + \beta^{(k)}\left([\tilde{A}]\{\tilde{p}^{(k)}\}, \{\tilde{p}^{(k)}\}\right)\end{aligned} \tag{B.20}$$

Since $\{\tilde{p}^{(k+1)}\}$ is perpendicular to $[\tilde{A}]\{\tilde{p}^{(k)}\}$, their inner product becomes zero. Hence, eq. (B.21) can be derived.

$$\beta^{(k)} = -\frac{\left(\{\tilde{r}^{(k+1)}\}, [\tilde{A}]\{\tilde{p}^{(k)}\}\right)}{\left([\tilde{A}]\{\tilde{p}^{(k)}\}, \{\tilde{p}^{(k)}\}\right)} \tag{B.21}$$

In order to solve a system of linear equations, shown in eq. (B.9), the unknown vector $\{\tilde{x}\}$ is renewed in accordance with eq. (B.11) by using eqs. (B.18) ~ (B.19) and (B.21) until it converges. However, one should avoid obtaining $[\tilde{A}]$ by using eq. (B.6), since the inner product of matrix takes long computing time. Therefore, the following procedure, which is called the preconditioned CG method, is often adopted.

First, substitution of eqs. (B.6) ~ (B.8) into eq. (B.10) yields eq. (B.22).

$$\begin{aligned}\{\tilde{r}\} &= [w]^{-T}\{b\} - [w]^{-T}[A][w]^{-1}[w]\{\tilde{x}\} \\ &= [w]^{-T}\{b\} - [w]^{-T}[A][\{\tilde{x}\} \\ &= [w]^{-T}\left(\{b\} - [A][\{\tilde{x}\}\right) \\ &= [w]^{-T}\{r\}\end{aligned} \tag{B.22}$$

Equation (B.23) defines $\{\tilde{p}\}$.

$$\{\tilde{p}\} \equiv [w]\{p\} \tag{B.23}$$

Then, substituting eqs. (B.22) ~ (B.23) into eq. (B.12) yields eq. (B.24a).

$$[w]\{p\} = [w]^{-T}\{r\} \tag{B.24a}$$

Equation (B.24b), which gives the initial guess of $\{p\}$, is obtained by modifying eq.(B.24a).

$$\begin{aligned}\{p\} &= [w]^{-1}[w]^{-T}\{r\} \\ &= [W]^{-1}\{r\}\end{aligned} \tag{B.24b}$$

Substitution of eqs. (B.7) and (B.23) into eq. (B.11) yields eq. (B.25a).

$$[w]\{x^{(k+1)}\} = [w]\{x^{(k)}\} + \alpha^{(k)}[w]\{p^{(k)}\} \tag{B.25a}$$

By modifying eq. (B.25a), eq. (B.25b) is derived.

$$\{x^{(k+1)}\} = \{x^{(k)}\} + \alpha^{(k)}\{p^{(k)}\} \tag{B.25b}$$

Equation (B.26a) is derived by substituting eqs. (B.7) ~ (B.8) and (B.22) into eq. (B.13).

$$[w]^{-T}\{r^{(k+1)}\} = [w]^{-T}\{b\} - [w]^{-T}[A][w]^{-1}[w]\{x^{(k+1)}\} \tag{B.26a}$$

Equation (B.26b) can be derived from eq. (B.26a).

$$\{r^{(k+1)}\} = \{b\} - [A]\{x^{(k+1)}\} \tag{B.26b}$$

By substituting eqs. (B.6) ~ (B.8) and (B.22) ~ (B.23) into eq. (B.14), eq. (B.27a) can be obtained.

$$\begin{aligned}[w]^{-T}\{r^{(k+1)}\} &= [w]^{-T}\{b\} - [w]^{-T}[A][w]^{-1}([w]\{x^{(k)}\} + \alpha^{(k)}[w]\{p^{(k)}\}) \\ &= [w]^{-T}\{b\} - [w]^{-T}[A]\{x^{(k)}\} - \alpha^{(k)}[w]^{-T}[A]\{p^{(k)}\}\end{aligned} \tag{B.27a}$$

Hence, the residual vector $\{r^{(k+1)}\}$ is expressed by eq. (B.27b).

$$\begin{aligned}\{r^{(k+1)}\} &= \{b\} - [A]\{x^{(k)}\} - \alpha^{(k)}[A]\{p^{(k)}\} \\ &= \{r^{(k)}\} - \alpha^{(k)}[A]\{p^{(k)}\}\end{aligned} \tag{B.27b}$$

Equations (B.28) ~ (B.29) are derived by using eqs. (B.6), (B.22) and (B.23).

$$\begin{aligned}\left(\{\widetilde{r}^{(k)}\}, \{\widetilde{p}^{(k)}\}\right) &= \left([w]^{-T}\{r^{(k)}\}, [w]\{p^{(k)}\}\right) \\ &= \left(\{r^{(k)}\}, [w]^{-1}[w]\{p^{(k)}\}\right) \\ &= \left(\{r^{(k)}\}, \{p^{(k)}\}\right)\end{aligned} \tag{B.28}$$

$$\begin{aligned}\left([\widetilde{A}]\{\widetilde{p}^{(k)}\}, \{\widetilde{p}^{(k)}\}\right) &= \left([w]^{-T}[A][w]^{-1}[w]\{p^{(k)}\}, [w]\{p^{(k)}\}\right) \\ &= \left([w]^{-T}[A]\{p^{(k)}\}, [w]\{p^{(k)}\}\right) \\ &= \left([A]\{p^{(k)}\}, [w]^{-1}[w]\{p^{(k)}\}\right) \\ &= \left([A]\{p^{(k)}\}, \{p^{(k)}\}\right)\end{aligned} \tag{B.29}$$

Substitution of eqs. (B.28) ~ (B.29) into eq. (B.18) yields eq. (B.30).

$$\alpha^{(k)} = \frac{\left(\{r^{(k)}\}, \{p^{(k)}\}\right)}{\left([A]\{p^{(k)}\}, \{p^{(k)}\}\right)} \tag{B.30}$$

Similarly, eq. (B.31) can be derived by using eqs. (B.3), (B.6) and (B.22) ~ (B.23).

$$\begin{aligned}\left(\{\widetilde{r}^{(k+1)}\}, [\widetilde{A}]\{\widetilde{p}^{(k)}\}\right) &= \left([w]^{-T}\{r^{(k+1)}\}, [w]^{-T}[A][w]^{-1}[w]\{p^{(k)}\}\right) \\ &= \left([w]^{-T}\{r^{(k+1)}\}, [w]^{-T}[A]\{p^{(k)}\}\right) \\ &= \left([w]^{-1}[w]^{-T}\{r^{(k+1)}\}, [A]\{p^{(k)}\}\right) \\ &= \left([W]^{-1}\{r^{(k+1)}\}, [A]\{p^{(k)}\}\right)\end{aligned} \tag{B.31}$$

Substitution of eqs. (B.29) ~ (B.30) into eq. (B.21) yields eq. (B.32).

$$\beta^{(k)} = -\frac{\left([W]^{-1}\{r^{(k+1)}\}, [A]\{p^{(k)}\}\right)}{\left([A]\{p^{(k)}\}, \{p^{(k)}\}\right)} \tag{B.32}$$

By substituting eqs. (B.22) ~ (B.23) into eq. (B.19), and using eq. (B.3), eq. (B.33a) can be derived.

$$[w]\{p^{(k+1)}\} = [w]^{-T}\{r^{(k+1)}\} + \beta^{(k)}[w]\{p^{(k)}\} \tag{B.33a}$$

Hence,

$$\begin{aligned}\{p^{(k+1)}\} &= [w]^{-1}[w]^{-T}\{r^{(k+1)}\} + \beta^{(k)}[w]^{-1}[w]\{p^{(k)}\} \\ &= [W]^{-1}\{r^{(k+1)}\} + \beta^{(k)}\{p^{(k)}\}\end{aligned} \tag{B.33b}$$

Figure B.1 shows the flow chart to solve a system of linear equations based on the preconditioned CG method, as shown in eqs. (B.22) ~ (B.33).

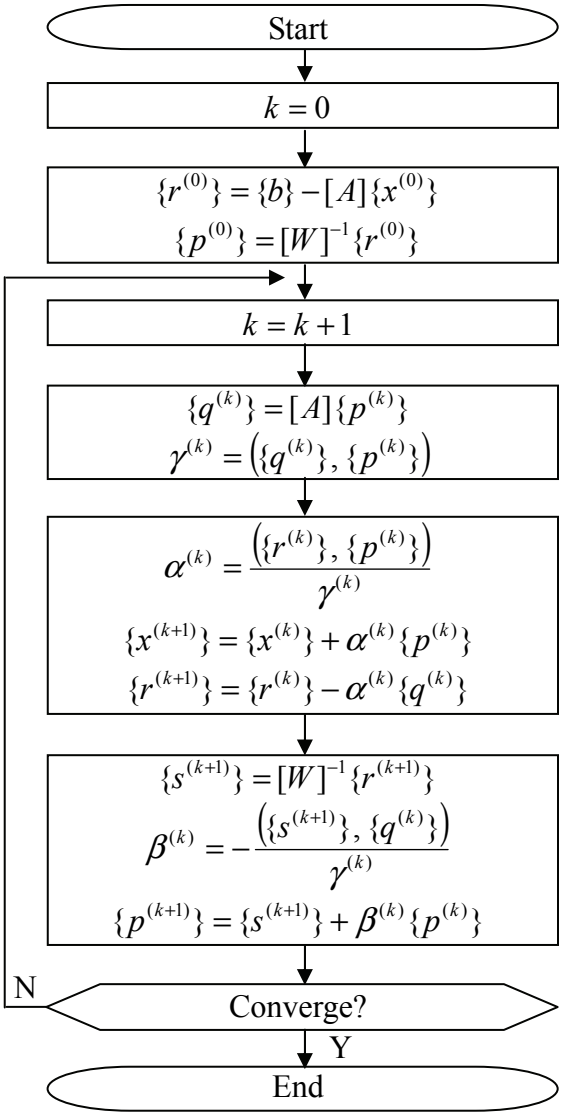

Fig. B.1 Flow chart of preconditioned CG method to solve a system of linear equations

The norm $\delta^{(k)}$, defined by eq. (B.34), is used to judge convergence.

$$\delta^{(k)} = \sqrt{\left(\{r^{(k)}\}, \{r^{(k)}\}\right)} \tag{B.34}$$

When the ratio of the norm for the k-th iteration to the initial norm, $\Delta^{(k)}$, defined by eq. (B.35), becomes small enough, say less than the CG convergence criterion Δ, the k-th assumption of the unknowns $\{x^{(k)}\}$ is regarded as the converged solution.

$$\Delta^{(k)} = \frac{\delta^{(k)}}{\delta^{(0)}} \tag{B.35}$$

Furthermore, the diagonal matrix, defined by eq. (B.36), was used as the scaling matrix $[W]$ in this research. Due to this scaling, the diagonal components of $[\widetilde{A}]$ become unity.

$$W_{ij} = \begin{cases} A_{ij} & if\ i = j \\ 0 & if\ i \neq j \end{cases} \tag{B.36}$$

This preconditioner is known as *diagonal preconditioning* or *Jacobi preconditioning*[75].

Appendix C

Homogenization Method

C.1 Introduction

The homogenization method is used to obtain a homogenized (effective) value of a parameter for heterogeneous media. The original idea was to give the upper and lower boundary value of the homogenized parameter[10]. By adopting acceptable assumptions, the range of the homogenized parameter is narrowed or converges.

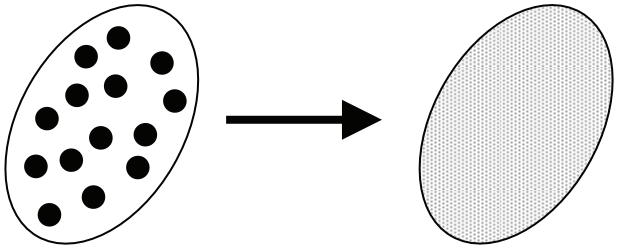

Fig. C.1 Schematic figure of the concept of the homogenization method

J. M. Guedes et al.[78] introduced the homogenization method into the FEM and numerous FE analyses have been reported. For example, S. J. Hollister et al.[79] investigated the influence of the number of unit cell. Furthermore, S. Jansson[11] examined the homogenized behavior of a fiber reinforced metal matrix composite as the first application of the homogenization method for nonlinear problems. This formulation, however, was based on the asymptotic expansion method, as an extension of linear formulations. In this method, the unknowns are assumed to be expressed in asymptotic expansion form, and then, the solution is derived according to this assumption. However, there are no guarantees that the unknowns can be expressed in such form, although some applications[80] followed this method. Therefore, a proof of the assumption's requisite expressibility is needed. Then, in order to resolve the lack of the proof of the convergence, the formulations of the homogenization method for nonlinear problems were derived based on the generalized variational principle[81].

However, another issue arises when the homogenization method is applied for nonlinear problems. As shown in **Fig. C.2**, the purpose of the homogenization method is to obtain the homogenized deformation matrix (D-matrix) of the micro model that considers the heterogeneity of the material. In order to acquire the homogenized deformation matrix $[D^H]$, the micro model is analyzed where the macro strain rate vector $\{\dot{E}\}$, which is the result of the macro analysis, is applied as an input. Then, the homogenized deformation matrix is used to analyze the macro model deformation as the deformation matrix of corresponding global Gauss point. In elastic analysis, when the homogenized deformation matrix $[D^H]$ is once calculated, further calculation to obtain the homogenized deformation matrix $[D^H]$ is not needed due to the problem's linearity. However, in plastic analysis, the homogenized deformation matrix $[D^H]$ is a function of the equivalent strain rate and the equivalent stress that is also a function of the equivalent strain rate and the equivalent strain. Therefore, the homogenized deformation matrix $[D^H]$ must be computed at each time step. Moreover, deformation distributes from point to point. Therefore, in order to obtain the homogenized deformation matrix $[D^H]$, the strain distributions of each micro model, which corresponds to each Gauss point on the macro element, are necessary. Hence, it is required to memorize the equivalent strain of each micro element that composes the micro model. In order to memorize the equivalent strain of all micro elements, extensive computer memory capacity is needed. In order to disperse memory capacity and to shorten the computing time, parallel processing[82)] was applied to nonlinear homogenization problems[83)]. However, parallel processing generally requires a huge computer system. In fact, though 38 CPUs were used, about one day computing time was still required to compute the micro structure evolution during the steel rolling process with adopting nonlinear homogenization theory[84)], even for a two-dimensional dynamic explicit analysis. As other approaches to reduce computing costs for applying the homogenization method to the nonlinear FE analysis, some researches employed the database of the homogenized properties[85)] or the mode superposition technique[86)].

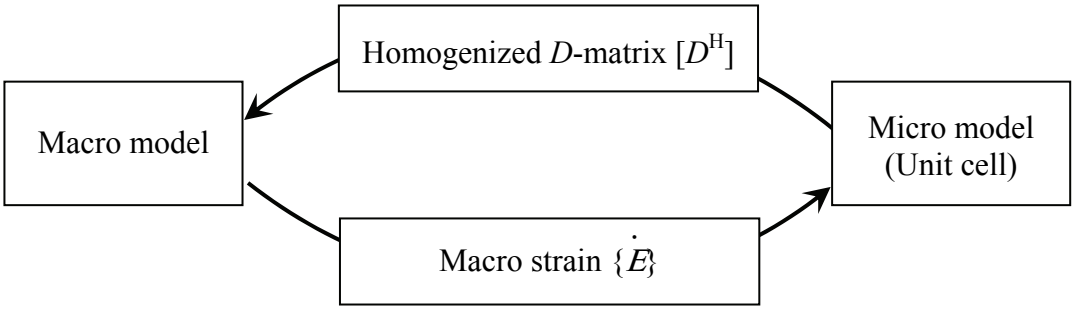

Fig. C.2 Inputs and outputs of the macro and micro models

In this appendix, since the homogenization method helps to clarify the relation between macro and micro behavior, formulations based on the asymptotic expansions are reviewed.

C.2 Formulations[87)]

Macro coordinate x_i and micro coordinate y_i are considered in the homogenization method. Equation (C.1) expresses the relation between these two coordinates where Δ is a positive real parameter.

$$y_i = \frac{x_i}{\Delta} \tag{C.1}$$

Now, the differentiation is done by using the chain rule.

$$\frac{d}{dx^{\Delta}{}_i} = \frac{d}{dx_i} + \frac{1}{\Delta}\frac{d}{dy_i} \tag{C.2}$$

Then, displacement $u^{\Delta}{}_i$ is assumed to be expressed by eq. (C.3).

$$u^{\Delta}{}_i = u^{(0)}{}_i + \Delta u^{(1)}{}_i + \Delta^2 u^{(2)}{}_i + \cdots \tag{C.3}$$

Here, $u^{(0)}{}_i$, $u^{(1)}{}_i$, $u^{(2)}{}_i$, $\cdots$ satisfy eq. (C.4), where $|Y|$ denotes the volume of the unit cell.

$$\frac{1}{|Y|}\int_Y u^{(k)}{}_i dy = 0 \tag{C.4}$$

The condition expressed by eq. (C.4) is called "Y-periodic."

Strain $\varepsilon^{\Delta}_{ij}$ is denoted by eq. (C.5).

$$\begin{aligned}\varepsilon^{\Delta}{}_{ij} &= \frac{du^{\Delta}{}_{i}}{dx^{\Delta}{}_{j}} \\ &= \left(\frac{d}{dx_j} + \frac{1}{\Delta}\frac{d}{dy_j}\right)(u^{(0)}{}_{i} + \Delta u^{(1)}{}_{i} + \Delta^2 u^{(2)}{}_{i} + \cdots) \\ &= \frac{1}{\Delta}\frac{du^{(0)}{}_{i}}{dy_j} + \left(\frac{du^{(0)}{}_{i}}{dx_j} + \frac{du^{(1)}{}_{i}}{dy_j}\right) + \Delta\left(\frac{du^{(1)}{}_{i}}{dx_j} + \frac{du^{(2)}{}_{i}}{dy_j}\right) + \cdots \\ &= \frac{1}{\Delta}\varepsilon^{(-1)}{}_{ij} + \varepsilon^{(0)}{}_{ij} + \Delta\varepsilon^{(1)}{}_{ij} + \cdots \end{aligned} \tag{C.5}$$

Here $\varepsilon^{(-1)}{}_{ij}$, $\varepsilon^{(0)}{}_{ij}$, $\varepsilon^{(1)}{}_{ij}, \cdots$ are defined by eq. (C.6).

$$\varepsilon^{(-1)}{}_{ij} \equiv \frac{du^{(0)}{}_{i}}{dy_j} \tag{C.6a}$$

$$\varepsilon^{(0)}{}_{ij} \equiv \frac{du^{(0)}{}_{i}}{dx_j} + \frac{du^{(1)}{}_{i}}{dy_j} \tag{C.6b}$$

$$\varepsilon^{(1)}{}_{ij} \equiv \frac{du^{(1)}{}_{i}}{dx_j} + \frac{du^{(2)}{}_{i}}{dy_j} \tag{C.6c}$$

Then, stress $\sigma^{\Delta}{}_{ij}$ is expressed by eq. (C.7) by using the elastic deformation tensor D_{ijkl}.

$$\begin{aligned}\sigma^{\Delta}{}_{ij} &= \frac{1}{\Delta}D_{ijkl}\varepsilon^{(-1)}{}_{kl} + D_{ijkl}\varepsilon^{(0)}{}_{kl} + \Delta D_{ijkl}\varepsilon^{(1)}{}_{kl} + \cdots \\ &= \frac{1}{\Delta}\sigma^{(-1)}{}_{ij} + \sigma^{(0)}{}_{ij} + \Delta\sigma^{(1)}{}_{ij} + \cdots \end{aligned} \tag{C.7}$$

Here $\sigma^{(-1)}{}_{ij}$, $\sigma^{(0)}{}_{ij}$, $\sigma^{(1)}{}_{ij}, \cdots$ are defined by eq. (C.8).

$$\sigma^{(-1)}{}_{ij} \equiv D_{ijkl}\varepsilon^{(-1)}{}_{kl} \tag{C.8a}$$

$$\sigma^{(0)}{}_{ij} \equiv D_{ijkl}\varepsilon^{(0)}{}_{kl} \tag{C.8b}$$

$$\sigma^{(1)}{}_{ij} \equiv D_{ijkl}\varepsilon^{(1)}{}_{kl} \tag{C.8c}$$

Let us consider the equilibrium, where b_i denotes the body force.

$$\frac{d\sigma^{\Delta}{}_{ij}}{dx^{\Delta}{}_{j}} + b_i = 0 \tag{C.9}$$

Substitution of eq. (C.7) into eq. (C.9) yields eq. (C.10) by using the chain rule, eq. (C.2).

$$\frac{1}{\Delta^2}\frac{d\sigma^{(-1)}{}_{ij}}{dy_j} + \frac{1}{\Delta}\left(\frac{d\sigma^{(-1)}{}_{ij}}{dx_j} + \frac{d\sigma^{(0)}{}_{ij}}{dy_j}\right) + \left(\frac{d\sigma^{(0)}{}_{ij}}{dx_j} + \frac{d\sigma^{(1)}{}_{ij}}{dy_j}\right) + \cdots + b_i = 0 \tag{C.10}$$

Since Δ is arbitrary positive value, eq. (C.11) is derived.

$$\frac{d\sigma^{(-1)}{}_{ij}}{dy_j} = 0 \tag{C.11a}$$

$$\frac{d\sigma^{(-1)}{}_{ij}}{dx_j} + \frac{d\sigma^{(0)}{}_{ij}}{dy_j} = 0 \tag{C.11b}$$

$$\frac{d\sigma^{(0)}{}_{ij}}{dx_j} + \frac{d\sigma^{(1)}{}_{ij}}{dy_j} + b_i = 0 \tag{C.11c}$$

Equation (C.11c) denotes the macro equilibrium.

Now, let us consider the strain energy Q. The strain energy Q (per unit volume) for the domain Y is expressed by eq. (C.12).

$$
\begin{aligned}
Q &= \frac{1}{2}\frac{1}{|Y|}\int_Y \sigma^{\Delta}{}_{ij}\varepsilon^{\Delta}{}_{ij}dy \\
&= \frac{1}{2}\frac{1}{|Y|}\int_Y \left(\frac{1}{\Delta}\sigma^{(-1)}{}_{ij} + \sigma^{(0)}{}_{ij} + \Delta\sigma^{(1)}{}_{ij} + \cdots\right) \\
&\qquad \times\left(\frac{1}{\Delta}\varepsilon^{(-1)}{}_{ij} + \varepsilon^{(0)}{}_{ij} + \Delta\varepsilon^{(1)}{}_{ij} + \cdots\right)dy \\
&= \frac{1}{2}\frac{1}{|Y|}\int_Y \left\{\frac{1}{\Delta^2}\sigma^{(-1)}{}_{ij}\varepsilon^{(-1)}{}_{ij} + \frac{1}{\Delta}(\sigma^{(-1)}{}_{ij}\varepsilon^{(0)}{}_{ij} + \sigma^{(0)}{}_{ij}\varepsilon^{(-1)}{}_{ij})\right. \\
&\qquad \left. + (\sigma^{(-1)}{}_{ij}\varepsilon^{(1)}{}_{ij} + \sigma^{(0)}{}_{ij}\varepsilon^{(0)}{}_{ij} + \sigma^{(1)}{}_{ij}\varepsilon^{(-1)}{}_{ij}) + \cdots\right\}dy
\end{aligned}
\tag{C.12}
$$

Due to the uniqueness of the strain energy Q for arbitrary Δ, eq. (C.13) is obtained.

$$\int_Y \sigma^{(-1)}{}_{ij}\varepsilon^{(-1)}{}_{ij}dy = 0 \tag{C.13a}$$

$$\int_Y (\sigma^{(-1)}{}_{ij}\varepsilon^{(0)}{}_{ij} + \sigma^{(0)}{}_{ij}\varepsilon^{(-1)}{}_{ij})dy = 0 \tag{C.13b}$$

$$Q = \frac{1}{2}\frac{1}{|Y|}\int_Y (\sigma^{(-1)}{}_{ij}\varepsilon^{(1)}{}_{ij} + \sigma^{(0)}{}_{ij}\varepsilon^{(0)}{}_{ij} + \sigma^{(1)}{}_{ij}\varepsilon^{(-1)}{}_{ij})dy \tag{C.13c}$$

Now, substitution of eq. (C.13a) into eq. (C.8a) yields eq. (C.14).

$$\int_Y \sigma^{(-1)}{}_{ij}\varepsilon^{(-1)}{}_{ij}dy = \int_Y D_{ijkl}\varepsilon^{(-1)}{}_{kl}\varepsilon^{(-1)}{}_{ij}dy = 0 \tag{C.14}$$

Since each component of the elastic deformation tensor D_{ijkl} has a positive value, eq. (C.15) is derived.

$$\varepsilon^{(-1)}{}_{ij} = 0 \tag{C.15}$$

Then, substitution of eq. (C.15) into eq. (C.6a) yields eq. (C.16).

$$\varepsilon^{(-1)}{}_{ij} = \frac{du^{(0)}{}_i}{dy_j} = 0 \tag{C.16}$$

Hence, displacement $u^{(0)}{}_i$ is not a function of micro coordinate y_i but a function of macro coordinate x_i. Then, substitution of eq. (C.15) into eq. (C.8a) yields eq. (C.17).

$$\sigma^{(-1)}{}_{ij} = 0 \tag{C.17}$$

Equation (C.13b) is automatically satisfied by eqs. (C.15) and (C.17). Then, substitution of eqs. (C.15) and (C.17) into eq. (C.13c) leads to eq. (C.18).

$$Q = \frac{1}{2}\frac{1}{|Y|}\int_Y \sigma^{(0)}{}_{ij}\varepsilon^{(0)}{}_{ij}\,dy \tag{C.18}$$

On the other hand, the strain energy Q as shown in eq. (C.18) should be equal to the one obtained from the macro strain E_{ij} and the macro stress Σ_{ij}, which are the average strain and stress in the domain Y.

$$Q = \frac{1}{2}\Sigma_{ij}E_{ij} = \frac{1}{2}\frac{1}{|Y|}\int_Y \sigma^{(0)}{}_{ij}\varepsilon^{(0)}{}_{ij}\,dy \tag{C.19}$$

Then, eq. (C.20) is derived.

$$\Sigma_{ij}E_{ij} = \frac{1}{|Y|}\int_Y \sigma^{(0)}{}_{ij}\varepsilon^{(0)}{}_{ij}\,dy \tag{C.20}$$

Let us go back to the equilibrium. Equation (C.17) satisfies eq. (C.11a) and substitution of eq. (C.17) into eq. (C.11b) yields eq. (C.21), the micro equilibrium.

$$\frac{d\sigma^{(0)}{}_{ij}}{dy_j} = 0 \tag{C.21}$$

Now, eq. (C.22) is easily derived by using eqs. (C.6b) and (C.8b).

$$\sigma^{(0)}{}_{ij} = D_{ijkl}\left(\frac{du^{(0)}{}_k}{dx_l} + \frac{du^{(1)}{}_k}{dy_l}\right) \tag{C.22}$$

As the macro strain E_{ij} is defined as the average of the micro strain ε_{ij} in the domain Y, eq. (C.23) is derived by using the fact that $u^{(0)}{}_i$ is not a function of the micro coordinate y_i as written in eq. (C.16).

$$
\begin{aligned}
E_{ij} &= \frac{1}{|Y|}\int_Y \varepsilon^{(0)}{}_{ij}\, dy \\
&= \frac{1}{|Y|}\int_Y \left(\frac{du^{(0)}{}_i}{dx_j} + \frac{du^{(1)}{}_i}{dy_j} \right) dy \\
&= \frac{1}{|Y|}\int_Y \frac{du^{(0)}{}_i}{dx_j}\, dy + \frac{1}{|Y|}\int_Y \frac{du^{(1)}{}_i}{dy_j}\, dy \\
&= \frac{du^{(0)}{}_i}{dx_j} + \frac{1}{|Y|}\int_Y \frac{du^{(1)}{}_i}{dy_j}\, dy
\end{aligned}
\tag{C.23}
$$

Now, let us consider the second term. Adopting the divergence theorem where n_j is the unit outer normal vector and using the facts that $u^{(1)}{}_i$ is "Y-periodic" and n_i is "Y-antiperiodic," eq. (C.24) can be derived.

$$
\int_Y \frac{du^{(1)}{}_i}{dy_j}\, dy = \int_\Gamma u^{(1)}{}_i n_j\, d\Gamma = 0 \tag{C.24}
$$

Substitution of eq. (C.24) into eq. (C.23) yields eq. (C.25).

$$
E_{ij} = \frac{du^{(0)}{}_i}{dx_j} \tag{C.25}
$$

Then, substitution of eq. (C.25) into eq. (C.6b) leads to eq. (C.26).

$$
\varepsilon^{(0)}{}_{ij} = E_{ij} + \frac{du^{(1)}{}_i}{dy_j} \tag{C.26}
$$

Moreover, substitution of eq. (C.26) into eq. (C.22) results in eq. (C.27).

$$
\sigma^{(0)}{}_{ij} = D_{ijkl}\left(E_{kl} + \frac{du^{(1)}{}_k}{dy_l} \right) \tag{C.27}
$$

Equation (C.28a) expresses the weak form of eq. (C.21).

$$
\int_Y \delta u^{(1)}{}_i \frac{d\sigma^{(0)}{}_{ij}}{dy_j}\, dy = 0 \tag{C.28a}
$$

Rewrite this equation using integration by parts.

$$\int_Y \frac{d}{dy_j}(\delta u^{(1)}{}_i \sigma^{(0)}{}_{ij})dy - \int_Y \frac{d\delta u^{(1)}{}_i}{dy_j}\sigma^{(0)}{}_{ij}dy = 0 \tag{C.28b}$$

Applying the divergence theorem to the first term in eq. (C.28b) yields eq. (C.28c).

$$\int_\Gamma \delta u^{(1)}{}_i \sigma^{(0)}{}_{ij} n_j dS - \int_Y \frac{d\delta u^{(1)}{}_i}{dy_j}\sigma^{(0)}{}_{ij}dy = 0 \tag{C.28c}$$

Here, since $\sigma^{(0)}{}_{ij}n_j$ is "Y-antiperiodic," the first term becomes zero. Hence,

$$\int_Y \frac{d\delta u^{(1)}{}_i}{dy_j}\sigma^{(0)}{}_{ij}dy = 0 \tag{C.28d}$$

Let us consider the matrix notation of eq. (C.28d). Now, the micro stress σ_{ij} and the micro strain ε_{ij} as well as the macro stress Σ_{ij} and the macro strain E_{ij} are expressed as a column vector. That is, eqs. (C.29a) ~ (C.29d) denote the micro stress vector $\{\sigma\}$, the micro strain vector $\{\varepsilon\}$, the macro stress vector $\{\Sigma\}$ and the macro strain vector $\{E\}$.

$$\{\sigma\} = \{\sigma_x \quad \sigma_y \quad \sigma_z \quad \sigma_{xy} \quad \sigma_{yz} \quad \sigma_{zx}\}^T \tag{C.29a}$$

$$\{\varepsilon\} = \{\varepsilon_x \quad \varepsilon_y \quad \varepsilon_z \quad 2\varepsilon_{xy} \quad 2\varepsilon_{yz} \quad 2\varepsilon_{zx}\}^T \tag{C.29b}$$

$$\{\Sigma\} = \{\Sigma_x \quad \Sigma_y \quad \Sigma_z \quad \Sigma_{xy} \quad \Sigma_{yz} \quad \Sigma_{zx}\}^T \tag{C.29c}$$

$$\{E\} = \{E_x \quad E_y \quad E_z \quad 2E_{xy} \quad 2E_{yz} \quad 2E_{zx}\}^T \tag{C.29d}$$

The purpose of these notations is to simplify the elastic deformation matrix notation. In fact, the elastic deformation matrix [D] becomes a 6×6 matrix, as shown in eq. (C.30).

$$[D]=\frac{E}{(1+\nu)(1-2\nu)}\begin{bmatrix} 1-\nu & \nu & \nu & 0 & 0 & 0 \\ \nu & 1-\nu & \nu & 0 & 0 & 0 \\ \nu & \nu & 1-\nu & 0 & 0 & 0 \\ 0 & 0 & 0 & \frac{1-2\nu}{2} & 0 & 0 \\ 0 & 0 & 0 & 0 & \frac{1-2\nu}{2} & 0 \\ 0 & 0 & 0 & 0 & 0 & \frac{1-2\nu}{2} \end{bmatrix} \tag{C.30}$$

Now, the following relations are used.

$$\frac{d}{dy_j} \rightarrow [B] \tag{C.31a}$$

$$\frac{du^{(1)}{}_i}{dy_j} \rightarrow [B]\{d^{(1)}\} \tag{C.31b}$$

$$\varepsilon^{(0)}{}_{ij} \rightarrow \{E\}+[B]\{d^{(1)}\} \tag{C.31c}$$

$$\sigma^{(0)}{}_{ij} \rightarrow [D](\{E\}+[B]\{d^{(1)}\}) \tag{C.31d}$$

Substitution of eqs. (C.31a) ~ (C.31d) into eq. (C.28d) and consideration of arbitrariness of the virtual displacement vector $\{\delta d^{(1)}\}$ yield eq. (C.32).

$$\int_Y [B]^T[D][B]dy\ \{d^{(1)}\} = -\int_Y [B]^T[D]dy\{E\} \tag{C.32}$$

Now, when the lateral macro strain E_x is set to unity while other macro strain components are set to zero, the obtained macro stress vector $\{\Sigma\}$ is equal to the first column components of the homogenized elastic deformation matrix $[D^H]$. Therefore, the homogenized elastic deformation matrix $[D^H]$ can be obtained by computing six modes of deformation, unit macro strain E_x=1, E_y=1, E_z=1, $2E_{xy}$=1, $2E_{yz}$=1 and $2E_{zx}$=1.

References

References

1) I. Pillinger, P. Hartley, C. E. N. Sturgess & G. W. Rowe; *Finite-element Modelling of Metal Flow in Three-dimensional Forming*, International Journal for Numerical Methods in Engineering, **25**(1988), 87-97.
2) S. E. Clift, P. Hartley, C. E. N. Sturgess & G. W. Rowe; *Fracture Prediction in Plastic Deformation Process*, International Journal of Mechanical Sciences, **32**-1(1990), 1-17.
3) Z. Peng & T. Sheppard; *Study of Surface Cracking During Extrusion of Aluminum Alloy AA2014*, Materials Science and Technology, **20**(2004), 1179-1191.
4) W. Liansheng, C. Qixiang & L. Zhuang; *Numerical Simulation and Experimental Verification of Microstructure Evolution in a Three-dimensional Hot-upsetting Process*, Journal of Materials Processing Technology, **58**(1996), 331-336.
5) J. Yanagimoto; *FE-based Analysis for the Prediction of Microstructure Evolution in Hot Rolling*, Modelling and Simulation in Materials Science and Engineering, **12**(2004), S47-S58.
6) T. Belytschko & T. Black; *Elastic Crack Growth in Finite Elements with Minimal Remeshing*, International Journal for Numerical Methods in Engineering, **45**(1999), 601-620.
7) F. Cleri, S. R. Phillpot, D. Wolf & S. Yip; *Atomistic Simulations of Materials Fracture and the Link between Atomic and Continuum Length Scales*, Journal of American Ceramic Society, **81**-3(1998), 501-516.
8) Y. C. Fung; *A First Course in Continuum Mechanics 2nd edition*, (1977), Prentice-Hall, ISBN: 0-1331-8311-4.
9) Y. Tomita; *An Introduction to Continuum Mechanics*, (1995), Yokendo, ISBN: 4-8425-9511-6. (in Japanese)
10) J. L. Lions; *Some Methods in the Mathematical Analyses of Systems and Their Control*, (1981), Gordon and Breach, Science Publisher Inc. & Science Press, ISBN: 0-677-60200-6.
11) S. Jansson ; *Mechanical Characterization and Modeling of Non-linear Deformation and Fracture of a Fiber Reinforced Metal Matrix Composite*, Mechanics of Materials, **12**(1991), 47-62.

12) M. Pietrzyk, J. Kusiak, H. Kusiak & F. Grosman; *Fields of Strains around the Inclusion of Second Phase in a Uniform Matrix undergoing Plastic Deformation*, Steel Research, **62**-11(1991), 507-511.
13) M. Ichishima, Y. Yokouchi & T. Izumi; *Processing of Transition Region from a Fine to a Coarse Mesh in Finite-element Analysis*, Journal of the Japan Society for Technology of Plasticity, **41**-471(2000), 395-399. (in Japanese)
14) A. K. Gupta; *A Finite Element for Transition from a Fine to a Coarse Grid*, International Journal for Numerical Methods in Engineering, **12**-1(1978), 35-45.
15) S. McCormick & J. Thomas; *The Fast Adaptive Composite Grid (FAC) Method for Elliptic Equations*, Mathematics of Computation, **46**-174(1986), 439-456.
16) J. H. Bramble, R. E. Ewing, J. E. Pasciak & A. H. Schatz; *A Preconditioning Technique for the Efficient Solution of Problems with Local Grid Refinement*, Computer Methods in Applied Mechanics and Engineering, **67**(1988), 149-159.
17) K. Muramatsu, T. Nakata, N. Takahashi & K. Fujiwara; *Investigation of Effectiveness of 3-D Nonconforming Mesh*, IEEE Transactions on Magnetics, **27**-6(1991), 5211-5213.
18) J. Fish & S. Markolefas; *Adaptive Global-local Refinement Strategy Based on the Interior Error Estimates of the h-method*, International Journal for Numerical Methods in Engineering, **37**-5(1994), 827-838.
19) MSC. Software Corp.; *MSC. Marc® and MSC. Marc® Mentat® Release Guide Version 2005*, (2005), http://www.mscsoftware.com/support/prod_support/marc/hw_specs/Marc2005_ReleaseGuide.pdf
20) I. Hirai, B. P. Wang & W. D. Pilkey; *An Efficient Zooming Method for Finite Element Analysis*, International Journal for Numerical Methods in Engineering, **20**(1984), 1671-1683.
21) N. Yukawa, T. Akiyama, Y. Yoshida & K. Ishikawa; *Analysis of Surface Roughness Transcription in Skin-pass Rolling Using Zooming Method*, Tetsu-to-Hagané, **94**-10(2008), 399-404. (in Japanese)
22) M. Krzyzanowski, J. H. Beynon & C. M. Sellars; *Analysis of Secondary Oxide Scale Failure at Entry into the Roll Gap*, Metallurgical & Materials Transactions B, **31**(2000), 1483-1490.

23) C. Luo & U. Ståhlberg; *Deformation of Inclusions During Hot Rolling of Steels*, Journal of Materials Processing Technology, **114**(2001), 87-97.

24) J. D. Whitcomb; *Iterative Global / Local Finite Element Analysis*, Computers & Structures, **40**-4(1991), 1027-1031.

25) J. Fish; *The S-version of the Finite Element Method*, Computers & Structures, **43**-3(1992), 539-547.

26) K. Suzuki, H. Ohtsubo, S. Min & T. Shiraishi; *Multi Scale Analysis of Ship Structure Using Overlaying Mesh Method*, Transactions of the Japan Society for Computational Engineering and Science, **1**(1999), 155-160. (in Japanese)

27) H. Okada, S. Endoh & M. Kikuchi; *On Fracture Analysis Using an Element Overlay Technique*, Engineering Fracture Mechanics, **72**(2005), 773-789.

28) N. Takano, M. Zako & M. Ishizono; *Global / Local Modeling of Structures with Local Heterogeneity*, Transactions of the Japan Society of Mechanical Engineers Series A, **66**-642(2000), 220-226. (in Japanese)

29) S. Wang & M. Y. Wang; *A Moving Superimposed Finite Element Method for Structural Topology Optimization*, International Journal for Numerical Methods in Engineering, **65**(2006), 1892-1922.

30) M. Yoshida, S. Fujino & H. Okada; *Effectiveness of Masking Preconditioner of CG Method for Linear Systems in the Composite Materials Analysis by s-version FEM Analysis*, Transactions of the Japan Society for Computational Engineering and Science, (2006), 20060010. (in Japanese)

31) Y. Okuno, N. Takano & M. Zako; *Three-dimensional Multi-scale Stress Analysis of Heterogeneous Media by Finite Element Mesh Superposition Method and Homogenization Method*, Transactions of the Japan Society of Mechanical Engineers Material and Mechanics Division, (2003), 987-988. (in Japanese)

32) J. W. Park, J. W. Hwang & Y. H. Kim; *Efficient Finite Element Analysis Using Mesh Superposition Technique*, Finite Elements in Analysis and Design, **39**(2003), 619-638.

33) H. Okada, C. T. Liu, T. Ninomiya, Y. Fukui & N. Kumazawa; *Analysis of Particulate Composite Materials Using an Element Overlay Technique*, Computer Modeling in Engineering & Sciences, **6**-4(2004), 333-347.

34) N. Takano, Y. Uetsuji, Y. Kashiwagi & M. Zako; *Hierarchical Modelling of Textile Composite Materials and Structures by the Homogenization Method*, Modelling and Simulation in Materials Science and Engineering, **7**(1999), 207-231.

35) N. Takano, M. Zako & T. Okazaki; *Efficient Modeling of Microscopic Heterogeneity and Local Crack in Composite Materials by Finite Element Mesh Superposition Method*, JSME International Journal A, **44**-4(2001), 602-609.

36) S. J. Hollister & N. Kikuchi; *Homogenization Theory and Digital Imaging: A Basis for Studying the Mechanics and Design Principles of Bone Tissue*, Biotechnology and Bioengineering, **43**-7, (1994), 586-596.

37) J. Fish & R. Guttal; *The s-version of Finite Element Method for Laminated Composites*, International Journal for Numerical Methods in Engineering, **39**(1996), 3641-3662.

38) S. Nakasumi, K. Suzuki, H. Ohtsubo & D. Fujii; *Mixed Analysis of Shell and Solid Elements Using Overlaying Mesh Method*, Journal of the Society of Naval Architects of Japan, **189**(2001), 219-224. (in Japanese)

39) H. Okada, S. Endoh & M. Kikuchi; *Application of S-version Finite Element Method to Two Dimensional Fracture Mechanics Problems*, Transactions of the Japan Society of Mechanical Engineers series A, **71**-704(2005), 677-684. (in Japanese)

40) S. Nakasumi, K. Suzuki, D. Fujii & H. Ohtsubo; *An Elastic and Elasto-Plastic Mixed Analysis Using Overlaying Mesh Method*, Transactions of the Japan Society of Mechanical Engineers Series A, **68**-668(2002), 603-610. (in Japanese)

41) T. Belytschko, J. Fish & A. Bayliss; *The Spectral Overlay on Finite Elements for Problems with High Gradients*, Computer Methods in Applied Mechanics and Engineering, **81**(1990), 71-89.

42) J. Fish, S. Markolefas, R. Guttal & P. Nayak; *On Adaptive Multilevel Superposition of Finite Element Meshes for Linear Elastostatics*, Applied Numerical Mathematics, **14**(1994), 135-164.

43) O. C. Zienkiewicz & R. L. Taylor; *Finite Element Method Fifth Edition*, Butterworth-Heinemann, (2000), ISBN: 0-7506-5049-4.

44) Y. Seguchi, H. Kitagawa & Y. Tomita; *YUUGEN-YOUSO-HOU NO KISO*, The Nikkan Kogyo Shimbun Ltd., (1983), ISBN: 4-526-01526-1. (in Japanese)

45) D. H. Robbins Jr. & J. N. Reddy; *Efficient Computational Model for the Stress Analysis of Smart Plate Structures*, Smart Materials and Structures, **5**-3(1996), 353-360.

46) E. Rank & R. Krause; *A Multiscale Finite-element Method*, Computers & Structures, **64**(1997), 139-144.

47) R. Krause & E. Rank; *Multiscale Computations with a Combination of the h- and p-versions of the Finite-element Method*, Computer Methods in Applied Mechanics and Engineering, **192**(2003), 3959-3983.

48) K. Ozaki, T. Ogita, S. M. Rump & S. Oishi; *Fast and Robust Algorithm for Geometric Predicates Using Floating-Point Arithmetic*, Transaction of the Japan Society for Industrial and Applied Mechanics, **16**-4(2006), 553-562. (in Japanese)

49) J. Fish & S. Markolefas; *Adaptive s-method for Linear Elastostatics*, Computer Methods in Applied Mechanics and Engineering, **104**(1993), 363-396.

50) M. Kakihara & S. Fujino; *Estimation of Diagonally Relaxed Quasi Robust ICCG Method for Linear Systems in Structural Analysis*, Transactions of the Japan Society for Computational Engineering and Science, (2004), Paper No.20040020. (in Japanese)

51) VINAS Co., Ltd.; *Super Matrix Solver Product Introduction and Business Outline*, http://www.vinas.com/jp/en/seihin/pdf/SMS_Product_Introduction040823.pdf, (2004)

52) N. Takano & M. Zako; *Microscopic Stress Analysis of Heterogeneous Media by Finite Element Mesh Superposition Method*, Transactions of the Japan Society of Mechanical Engineers Series A, **67**-656(2001), 603-610. (in Japanese)

53) S. Nakasumi; *JUUGOU-mesh-HOU WO MOCHI-ITA KOUZOU KAISEKI SYUHOU NI KANSURU KENKYUU*, Doctoral Dissertation Report No.18991, (2004), The University of Tokyo. (in Japanese)

54) Z. Yue & D. H. Robbins Jr.; *Adaptive Superposition of Finite Element Meshes in Elastodynamic Problems*, International Journal for Numerical Methods in Engineering, **63**(2005), 1604-1635.

55) M. Tanaka, S. Ono & M. Tsuneno; *Factors Contributing to Crushing of Voids during Forging*, Journal of the Japan Society for Technology of Plasticity, **27**-306(1986), 852-859. (in Japanese)

56) A. Wang, P. F. Thomson & P. D. Hodgson; *A Study of Pore Closure and Welding in Hot Rolling Process*, Journal of Materials Processing Technology, **60**(1996), 95-102.

57) T. Uchino & M. Sese; *FEM Analysis on a Study of Blister Appearance Mechanism*, Current Advances in Materials and Processes -Report of the Iron and Steel Institute of Japan Meeting (CAMP-ISIJ), **16**(2003), 1414. (in Japanese)

58) M. Fukumura, M. Horie, K. Hirata & S. Tomita; *Pore Closure Simulation during the Rolling Process*, Current Advances in Materials and Processes -Report of the Iron and Steel Institute of Japan Meeting (CAMP-ISIJ), **11**(1998), 1007. (in Japanese)

59) H. L. Yu, X. H. Liu & X. W. Li; *FE Analysis of Inclusion Deformation and Crack Generation During Cold Rolling with a Transition Layer*, Materials Letters, **62**(2008), 1595-1598.

60) S. Nakasumi, K. Suzuki, D. Fujii & H. Ohtsubo; *Mixed Analysis of Shell and Solid Elements Using Overlaying Mesh Method (Part 2)*, Journal of the Society of Naval Architects of Japan, **190**(2001), 655-662. (in Japanese)

61) S. Kobayashi, S.-I. Oh & T. Altan; *Metal Forming and the Finite-Element Method*, Oxford University Press, New York, (1989), ISBN: 0-19-504402-9.

62) B. S. Kang, L. P. Lei & S. M. Hwang; *Rigid-plastic Finite Element Method and Its Implementation in the Hydroforming Processes*, Proceedings of the 8th International Conference on Metal Forming, (2000), 171-178.

63) K. Osakada, J. Nakano & K. Mori; *Finite Element Method for Rigid-plastic Analysis of Metal Forming -Formulation for Finite Deformation*, International Journal of Mechanical Sciences, **24**-8(1982), 459-468.

64) N. Takano & Y. Okuno; *Three-scale Finite Element Analysis of Heterogeneous Media by Asymptotic Homogenization and Mesh Superposition Methods*, International Journal of Solids and Structures, **41**(2004), 4121-4135.

65) D. S. Malkus & T. J. R. Hughes; *Mixed Finite Element Methods -Reduced and Selective Integration Techniques: A Unification of Concepts*; Computer Methods in Applied Mechanics and Engineering, **15**(1978), 63-81.

66) E. Anderson, Z. Bai, C. Bischof, S. Blackford, J. Demmel, J. Dongarra, J. Du Croz, A. Greenbaum, S. Hammarling, A. McKenney & D. Sorensen; *LAPACK User's Guide Third Edition*, (1999), Society for Industrial and Applied Mathematics, ISBN: 0-89871-447-8.

67) E. Ervasti & U. Ståhlberg; *Void Initiation Close to a Macro-inclusion During Single Pass Reductions in the Hot Rollng of Steel Slabs: A Numerical Study*, Journal of Materials Processing Technology, **170**(2005), 142-150.

68) Y. F. Al-Obaid; *Three-dimensional Dynamic Finite Element Analysis for Shot-peening Mechanics*, Computers & Structures, **36**-4(1990), 681-689.

69) K. Mori, K. Osakada & N. Matsuoka; *Finite Element Analysis of Peening Process with Plastically Deforming Shot*, Journal of Materials Processing Technology, **45**(1994), 607-612.

70) E. Ervasti & U. Ståhlberg; *Behavior of Longitudinal Surface Cracks in the Hot Rolling of Steel Slabs*, Journal of Materials Processing Technology, **94**(1999), 141-150.

71) J. Tang, A. K. Tieu & Z. Jiang; *Modeling of the Development of Initial Crack under Hot Rolling Condition*, Materials Science Forum, **505-507**(2006), 1291-1296.

72) H. -L. Yu, X. -H. Liu & G. -D. Wang; *Analysis of Crack Tip Stress of Transversal Crack on Slab Corner During Vertical-Horizontal Rolling Process by FEM*, Journal of Iron and Steel Research International, **15**-3(2008), 19-26.

73) I. H. Son, J. D. Lee, S. Choi, D. L. Lee & Y. T. Im; *Deformation Behavior of the Surface Defects of Low Carbon Steel in Wire Rod Rolling*, Journal of Materials Processing Technology, **201**(2008), 91-96.

74) K. Suzuki, A. Sando, D. Shimamura & H. Ohtsubo; *Study on the Local Area Exceeding Global Area in Mesh Superposition Method*, Journal of Applied Mechanics Japan Society of Civil Engineers, **7**(2004), 383-389. (in Japanese)

75) J. R. Shewchuk; *An Introduction to the Conjugate Gradient Method Without the Agonizing Pain Edition 1 1/4*, School of Computer Science Carnegie Mellon University, (1994).

76) I. Kawakami; *Fundamentals of Numerical Computation*, (2005), http://www7.ocn.ne.jp/~kawa1/ (in Japanese)

77) H. Matsumoto; *Computer-NI-YORU JISSEN SUUCHI KEISAN-HOU*, Kyusyu University Press, (1999), ISBN: 4-87378-600-2. (in Japanese)
78) J. M. Guedes & N. Kikuchi; *Preprocessing and Postprocessing for Materials Based on the Homogenization Method with Adaptive Finite Element Methods*, Computer Methods in Applied Mechanics and Engineering, **83**(1990), 143-198.
79) S. J. Hollister & N. Kikuchi; *A Comparison of Homogenization and Standard Mechanics Analyses for Periodic Porous Composites*, Computational Mechanics, **10**(1992), 73-95.
80) For example, Y.-M. Yi, S.-H. Park & S.-K. Youn; *Asymptotic Homogenization of Viscoelastic Composites with Periodic Microstructures*, International Journal of Solids and Structures, **35**-17(1998), 2039-2055.
81) K. Terada & N. Kikuchi; *A Class of General Algorithms for Multi-scale Analyses of Heterogeneous Media*, Computer Methods in Applied Mechanics and Engineering, **190**(2001), 5427-5464.
82) A. Matsuda, T. Kato, Y. Miyakawa, T. Kawabe & A. Nagaoka; *Parallelization of Finite Element Analysis Using Broadcast on Workstation Cluster*, Japan Society of Mechanical Engineers International Journal Series A, **44**-1(2001), 144-151.
83) K. Matsui, K. Terada & K. Yuge; *Parallelized Two-Scale Analysis with a PC Cluster for Elastic-Plastic Heterogeneous Media*, Japan Society of Mechanical Engineers International Journal Series A, **44**-4(2001), 584-593.
84) S. Takahashi, N. N. Tam, K. Tanaka, T. Katayama, E. Nakamachi & H. Kuramae; *Analyses of Texture Evolution in Asymmetric Rolling Process by Using Dynamic Explicit Crystallographic Homogenized Elasto/viscoplastic Finite Element Method*, Japan Society of Mechanical Engineers 20th Computational Mechanics Conference, (2007), 151-152. (in Japanese)
85) N. Takano, Y. Ohnishi, M. Zako & K. Nishiyabu; *Microstructure-based Deep-drawing Simulation of Knitted Fabric Reinforced Thermoplastics by Homogenization Theory*, International Journal of Solids and Structures, **38**(2001), 6333-6356.
86) J. Okada, T. Washio & T. Hisada; *Nonlinear Homogenization Algorisms with Low Computing Cost*, Transactions of the Japan Society of Mechanical Engineers series A, **74**-738(2008), 191-200. (in Japanese)

87) K. Terada & N. Kikuchi (edited by the Japan Society for Computational Engineering and Science); *KINSHITSU-KA-HOU NYUUMON*, Maruzen Co. Ltd., (2003), ISBN: 4-621-07256-0. (in Japanese)